THE UNIVERSITY OF CALGARY

Seismic Methods for Heavy Oil Reservoir Monitoring and Characterization

by

Zandong Sun

A DISSERTATION

SUBMITTED TO THE FACULTY OF GRADUATE STUDIES

IN PARTIAL FULFILLMENT OF THE REQUIREMENTS FOR THE

DEGREE OF DOCTOR OF PHILOSOPHY

DEPARTMENT OF GEOLOGY AND GEOPHYSICS

CALGARY, ALBERTA

February, 1999

Abstract

Extracted seismic attributes from time-lapse 3-D seismic data has been used extensively to map steam areal conformance by using statistical analysis in the development and monitoring of follow-up processes at Imperial Oil's Cold Lake production project.

In this dissertation, a quantitative cross-calibration scheme between time-lapse seismic surveys has been developed using data normalization. It was found that a significant difference results from using a different calibration set; and that time-lapse data cross-calibration provides better, more stable and consistent results.

Attributes from principal component decomposition of seismic data compensate for the redundancy of conventional seismic attributes in statistical analysis and provide better well-to-seismic ties when a full set of principal component attributes are used.

Vertical steam conformance can be established through post-stack inversion to provide 3-D visualization of the impact of lithologic control on steam distribution and steam migration pathway. The vertical conformance reveals that sequence architecture has a significant influence on steam migration. A sequence with high mud content tends to limit or slow both vertical and lateral migration of the steam chambers.

Shear-wave information is useful for both reservoir characterization and monitoring fluid movement. Integrated surface 2-D seismic and borehole VSP *P*- and *S*-wave studies have illustrated that the task of differentiating lithology and identifying fluid can be achieved by integrating *P*- and *S*-wave information. However, when compared with *P*-*P* wave, the surface *P*-*S* wave lacks the resolution at Cold Lake area. 3-D 3-component VSP is the tool that will meet this need. A 3-D VSP survey design and processing stream have been developed in this dissertation.

The functional relation of *P*- to *S*-wave velocities, called the mud-rock line, plays an important rule in extracting *S*-wave information from pre-stack data. An optimized mud-rock line for Cold Lake clastic rocks is an exponential relationship between *P*- and *S*-

wave velocities. With an optimized mud-rock line and high frequency seismic data, the inverted psuedo *S*-wave from AVO analysis has much higher resolution than the *P-S* wave data. The reservoir heterogeneity can be well defined by fluid factor alone. The application of this technique to reservoir monitoring defines steam channels and identifies lithologic barriers within the reservoir.

Acknowledgements

Dr. Rob Stewart, my dissertation supervisor, has provided guidance and contributed many useful suggestions to this dissertation. I appreciate his patient proofreading of this dissertation while he was teaching overseas. The CREWES group that he created provided much convenience for this dissertation work. Imperial Oil Resources very generously provided the data used in the dissertation and approved the release of the work. Strong support of this research was provided by Dr. Jim Hawkins the manager of oil sands research with Imperial Oil Resources. His promotion of the research for this dissertation, his patient review of every piece of work in this dissertation, and proofreading the first draft helped shaped its quality, contents, and appearance. Many discussions between him and myself were appreciated in balancing the business needs of Imperial Oil and scientific advances presented in this dissertation.

The time-lapse cross-calibration program extended the discriminant analysis program that was originally coded by Dr. John E. Eastwood using computer-based statistical analysis programs. Dr. John E. Eastwood, Glen W. Bishop, and Gary D. Mann provided many suggestions for the analysis of principal component attributes. Yong Xu provided some coding for algorithms used in the AVO analysis. Many programs for 3-D VSP analysis were created as a joint effort by Qi Zhang and myself. The data used in this dissertation was mostly processed by Dr. Mark P. Harrison with Matrix Geoservices Ltd. Thanks also go to Shane D. Stark and Dr. Tom J. Boone for discussions relating seismic results to oil production data. Their feedback links between the geophysics and reservoir disciplines is much appreciated. Some helps on proofreading from Dr. Cheryl Trudell and Herold Gutek are very much appreciated.

I thank my daughter Lisa who missed the attendance of her dad so much during the past year. Through all this time she hasn't complained and waited patiently until all this work was done. Most of all, I appreciate the support, encouragement, and love from my wife Qi. Her very hard work looking after our newborn son Mark enabled me to focus on completing this work.

Dedication

This dissertation is dedicated to my parents whose encouragement and belief in me will live on forever through steps like this one in my quest of lifelong learning.

Table of Content

List of Tables

List of Figures

Chapter 1 – Introduction

1.1 General

The Lower Cretaceous (Albian) Clearwater Formation is the most prolific heavy oil bitumen reservoir at Cold Lake, Alberta. In 1998 the average production rate at Cold Lake was approximately 135,000 bbl (22,000 m^3) per day which represented approximately 7% of Canada's total petroleum production (Rolheiser, 1998). The oil is produced by a process called cyclic steam stimulation (CSS) which involves injection of steam at high temperatures and pressures (as high as 310 °C and 10 MPa), followed by the production of bitumen from the same injection wells.

Follow-up processes, or FUPs, is a technology designed to be implemented near the end of the life of the CSS process. The objective of a FUP is to achieve an improvement in steam efficiency, as measured by an uplift in the oil-steam-ratio (OSR), relative to a continuation of the CSS process.

Time-lapse 3-D seismic methods have been used to create an image of steam conformance for reservoir monitoring to assist implementing FUPs by better placement of infill wells and adjustments to steaming strategy. This seismic technology is also used for steam performance evaluation during early cycles of CSS, reservoir characterization, and for monitoring the performance of CSS using horizontal wells.

1.2 Geology

The Clearwater Formation was deposited during maximum transgression of the Mannville Group (see Figure 1.1, modified after Potocki and Hutcheon (1992), Leckie and Smith (1992) and Cant (1996)). The Clearwater Formation at Cold Lake was fed by a large fluvial system that probably originated in highlands to the south where contemporaneous arc-related volcanism contributed rock fragments. Today, that volcanic system is preserved as Cretaceous batholiths. The main reservoir units of the Clearwater Formation consist of unconsolidated very fine- to medium-grained feldspathic litharenite

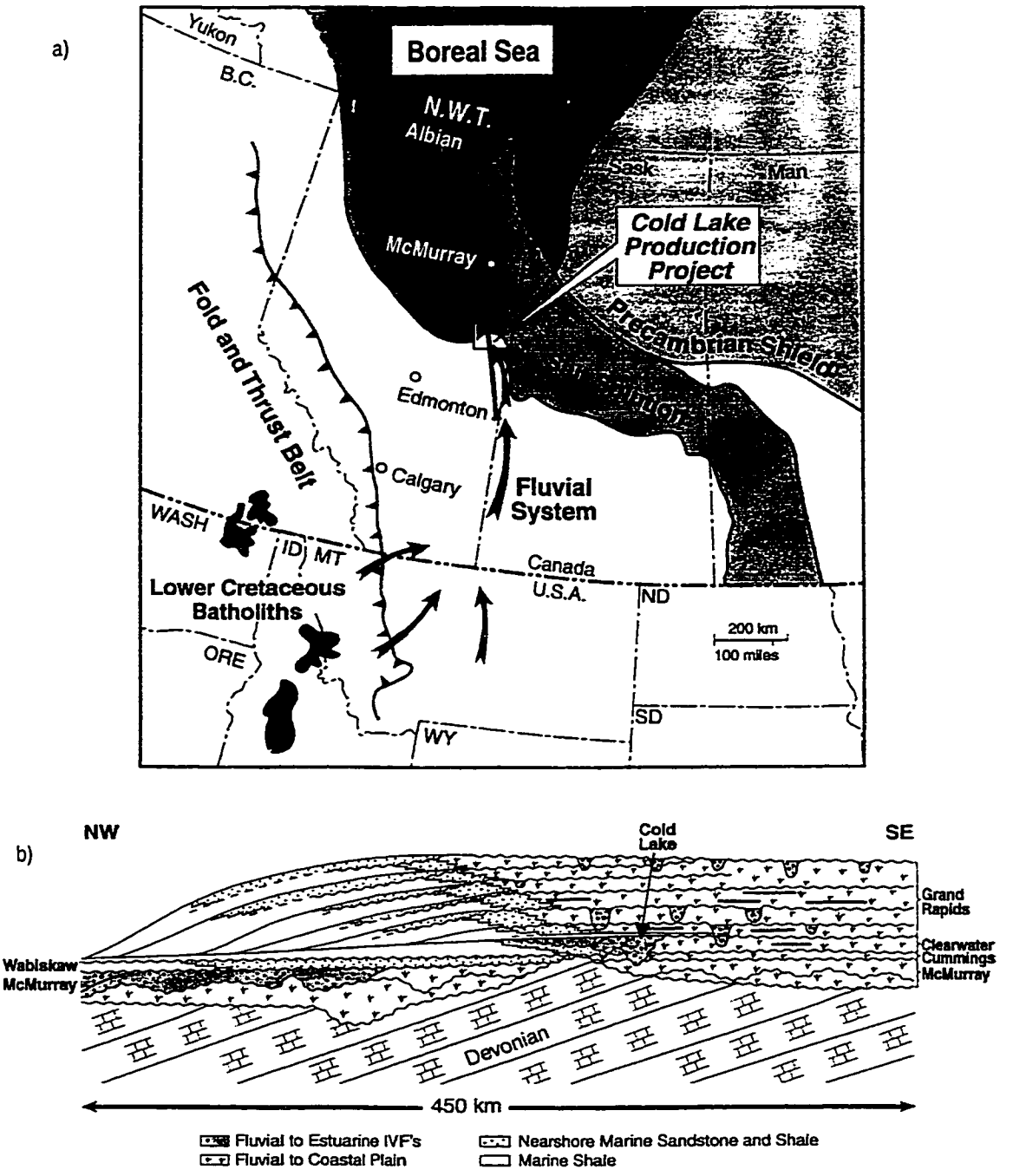

FIG. 1.1. (a) Generalized paleogeography during Clearwater Formation deposition (modified after Potocki and Hutcheon (1992) and Leckie and Smith (1992), (b) Schematic dip section of the Mannville Group (see (a) for section location, modified after Cant (1996)).

and shale deposited near the southern edge of the Boreal Sea (Figure 1.1). Rivers that incised valleys in the Cold Lake area originated in mountains to the south where active volcanoes provided abundant feldspathic rock fragments. High frequency sea-level cycles caused multiple episodes of valley incision and filling along the very low relief siliciclastic ramp.

The analysis of the Clearwater Formation at Cold Lake has revealed a complex array of facies within nested incised valleys. Many sequences have been correlated within the 50

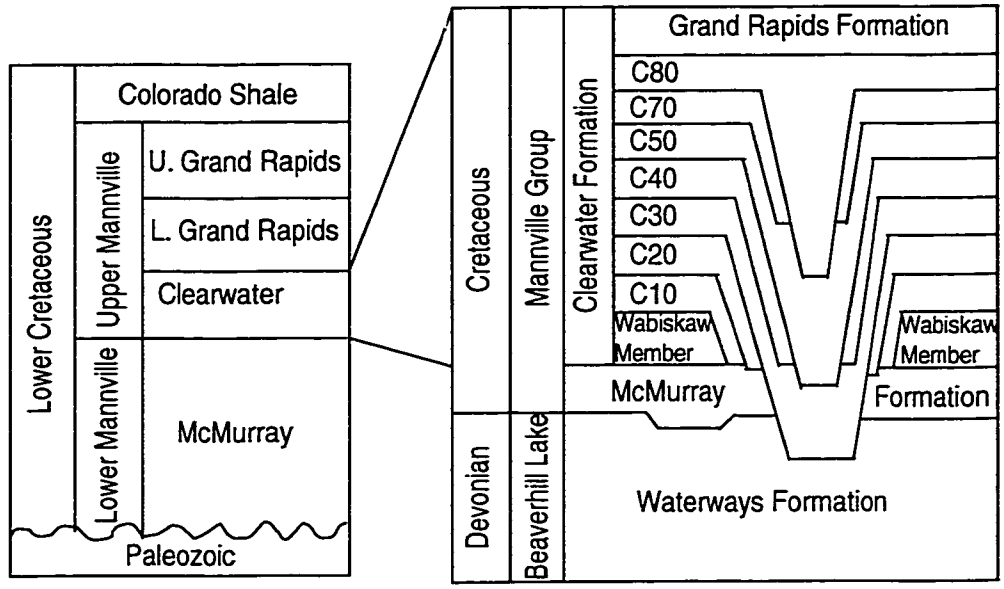

FIG. 1.2. Local stratigraphic nomenclature for the Cold Lake area. Several sequences of strata (C10 to C80) are recognized in the Clearwater Formation at Cold Lake. Modified after McCrimmon and Cheadle (1997).

m thick Clearwater Formation at Cold Lake (Figure 1.2, McCrimmon and Cheadle, 1997). This model has revealed that all of the Cold Lake reservoir occurs within incised valley infills; however, not every incised valley contains reservoir, and the muddier valley fills act as barriers to the fluid flow. Figure 1.3 shows a cross section of the Clearwater Formation illustrating two major sequence sets (C80 and C70 for upper sequence set and the rest for lower sequence set). Each sequence contains a lower muddy incised valley fill (either C30 or C70) and upper sandy incised valley fills (C80 and C50). Sequences C80 and C60 are fluvial lowstand system tract (LST) facies. Sequences C50, C40, and

southwest part of C20 are high energy estuarine LST facies. Sequences C30 and C70 are low energy estuarine LST facies. Sequences C10 and northeast part of C20 are a muddy transgressive system tract (TST) or a highstand system tract (HST) facies. Sequences C80, C50, and part of C20 are good reservoir. However, C70, C10, and part of C20 are usually low energy muddy TST/HST, and they are barriers. The location of the cross

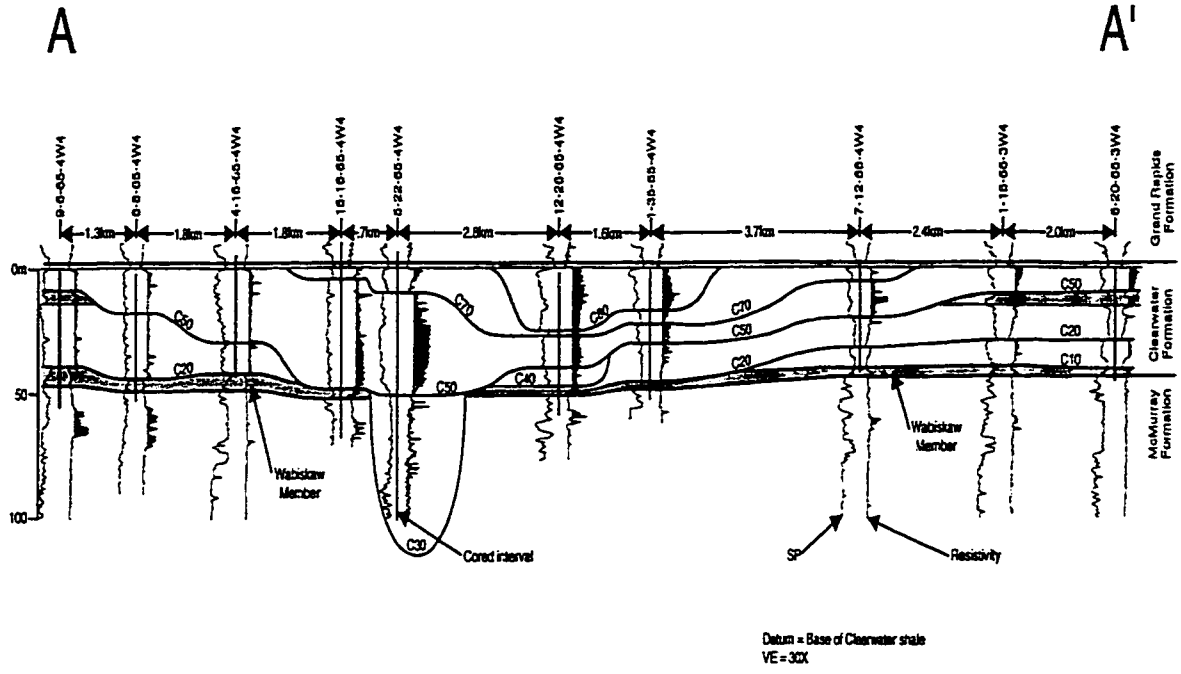

FIG. 1.3. Stratigraphic cross-section showing the relationship between regional Clearwater Formation marker units (shaded) and the incised-valley successions at Cold Lake. Sequence boundaries in the Clearwater Formation are labeled C10 to C80 (not including the Wabiskaw Member). After McCrimmon and Cheadle (1997).

section is shown in Figure 2.1.

1.3 Reservoir and fluids

The Clearwater Formation at Cold Lake is about 420 m below the surface. The gross thickness of oil sands is from 40 m to 75 m. The average net pay is about 45 m. The bitumen weight percentage saturation varies from 0 to 12% with an average of

approximately 10%. The reservoir's average porosity is 32%. The permeability varies from 0.5 to 4 darcies. The bitumen viscosity at reservoir pressure and temperature is rather high ranging from 10^4 to 10^6 cp. Reservoir parameters are listed in Table 1.1. The

Table 1.1. Cold Lake oil sand reservoir parameters

Net pay	45 m
Typical wt. % bitumen	10.5
% sand	>90
Porosity	0.30-0.36
% fine (<44 microns)	<5
Grain size	.17 mm
Reservoir temperature	13 deg C
Oil Viscosity (@ 13 deg C)	10,000-1,000,000 cp
Reservoir pressure	3 MPa
Permeability	0.5 to 4 darcies

Table 1.2. Grain composition of Cold Lake oil sands

minerals	%
quartz	21
feldspar	28
volcanics	23
chert	20
argillite	3
metasediments	5

sands of the Clearwater Formation are a complex assemblage of minerals which are texturally immature. The minerals are highly reactive due to the nature of their volcanic source sediments and because the sands are unconsolidated. The grain composition is listed in Table 1.2.

The Clearwater Formation gas caps are structurally controlled and restricted in localized areas. Gas caps can be up to 4 m thick and are sealed by a 2 to 5 m shale interval above the Clearwater Formation. The gas saturation is typically over 70% by pore volume. It is postulated that these gas sands could act as a steam thief zone. Such a loss of steam into the gas cap could lead to a loss of energy into the overlying shales and reduce the volume of heated bitumen.

In some areas the oil sands are positioned directly or indirectly on permeable water sands. These sands are referred to as a bottom water zone. The bottom water sands can act as a thief zone for steam because of their high transmissibility, thus limiting heat transfer into the oil sands. The water sands are permeable and can attain thicknesses in excess of 50 m.

1.4 Description of Cyclic Steam Stimulation (CSS) process and CSS pad

Since heat can be used to reduce bitumen viscosity, cyclic steam stimulation (CSS) is one of the techniques that can be used to realize bitumen production. Conceptually, the CSS process has three phases: steam injection phase (steam injected into the reservoir), soak phase (steam and condensed water heat the viscous oil), and the production phase (heated oil and water flow are pumped to the surface). The schematic diagram in Figure 1.4 displays the CSS process. During the CSS steam injection cycles, pressure increases and reaches a level where the Formation approaches a zero net effective stress state. The Formation dilates allowing some of the injected steam and condensate steam to penetrate into the cold reservoir. Reservoir pressures become uniformly elevated and can exceed the minimum *in-situ* stress, 10 MPa, while far exceeding the initial bitumen bubble point pressure, 3 MPa. At this point there are only two phases present in the bitumen, water and bitumen. At equilibrium, any existing gas saturation will either have condensed (steam) or been dissolved (solution gas), into the bitumen phase. Temperatures are highest near

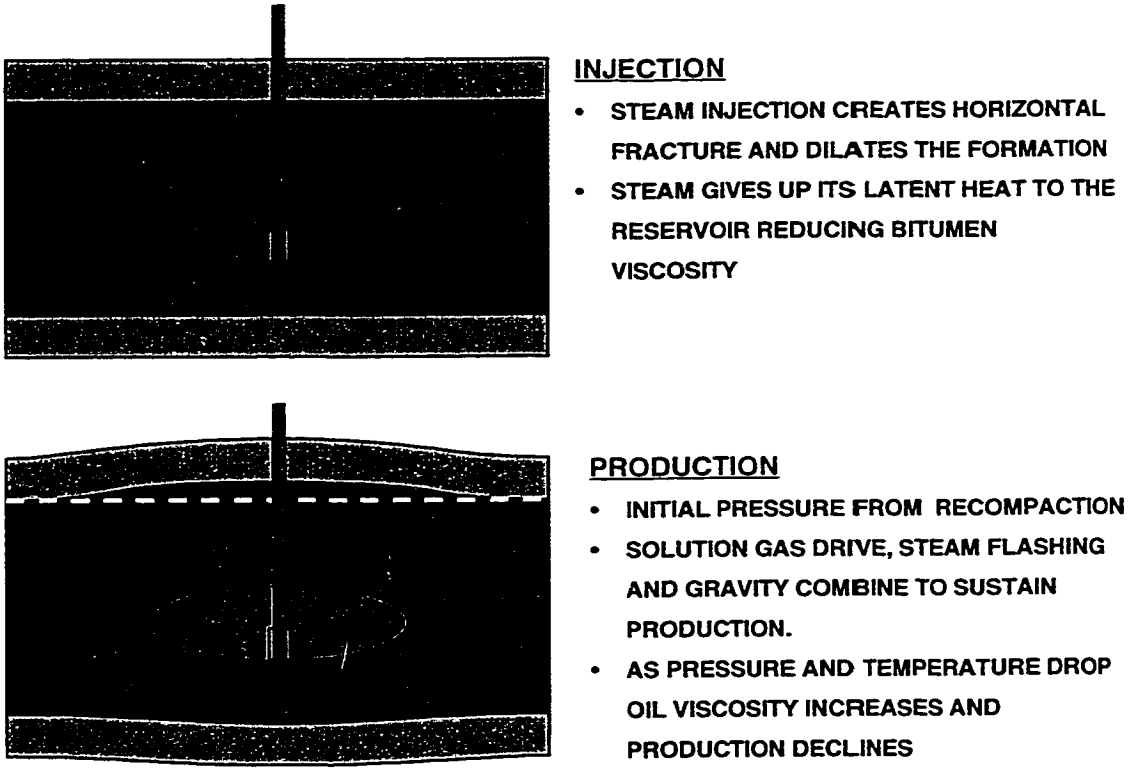

FIG. 1.4. Reservoir mechanics of Cyclic Steam Stimulation (courtesy of J. P. Lebel).

the wellbore, decreasing only slowly with distance. To sustain the CSS process, injected steam volumes are sized so that heat from the injected fluids contacts previously unheated bitumen during the sequential injection cycle rather than just re-stimulating the wellbore region.

The steam chamber around the wellbore is subdivided into three zones: the heated zone, transition (impedance) zone, and cold zone (Batycky et al., 1997). The transition zone is relative narrow and characterized by intermediate temperatures and significant gas evolution and foaming. As the number of CSS cycles increases and steam migrates along lateral fractures; inter-well communication occurs; and thereafter, steam channels are formed.

The CSS is implemented in the field with regular well configurations referred to as pads. A typical production pad is a 20-well-block with dimensions of 485 m by 668 m (4 acre well spacing). Twenty directionally-drilled wells form this single reservoir production unit.

1.5 Follow-up processes

Late cycle CSS reaches its economic recovery limit due to a decline in OSR. The Follow-up processes (FUPs) program is targeted at increasing economic recovery at Cold Lake beyond the 25% average recovery expected with CSS. This increase will be achieved through infill drilling. The first follow-up process implemented at Cold Lake was the BB/W injector-only-infill (IOI) pilot, started in late 1988. Findings from this first FUP have led to further IOI piloting at B2/B5 pads and a horizontal injector, M-H1, also at BB/W (see Figure 1.5). FUP pilots involving horizontal well producers have been piloted at AA, B03, and C03 pads. Horizontal-injector-producers (HIP) build on the findings of all previous FUP pilots that have been implemented.

Time-lapse 3-D seismic played a key role in placing infill locations and also in evaluation of steam performance in these FUPs programs.

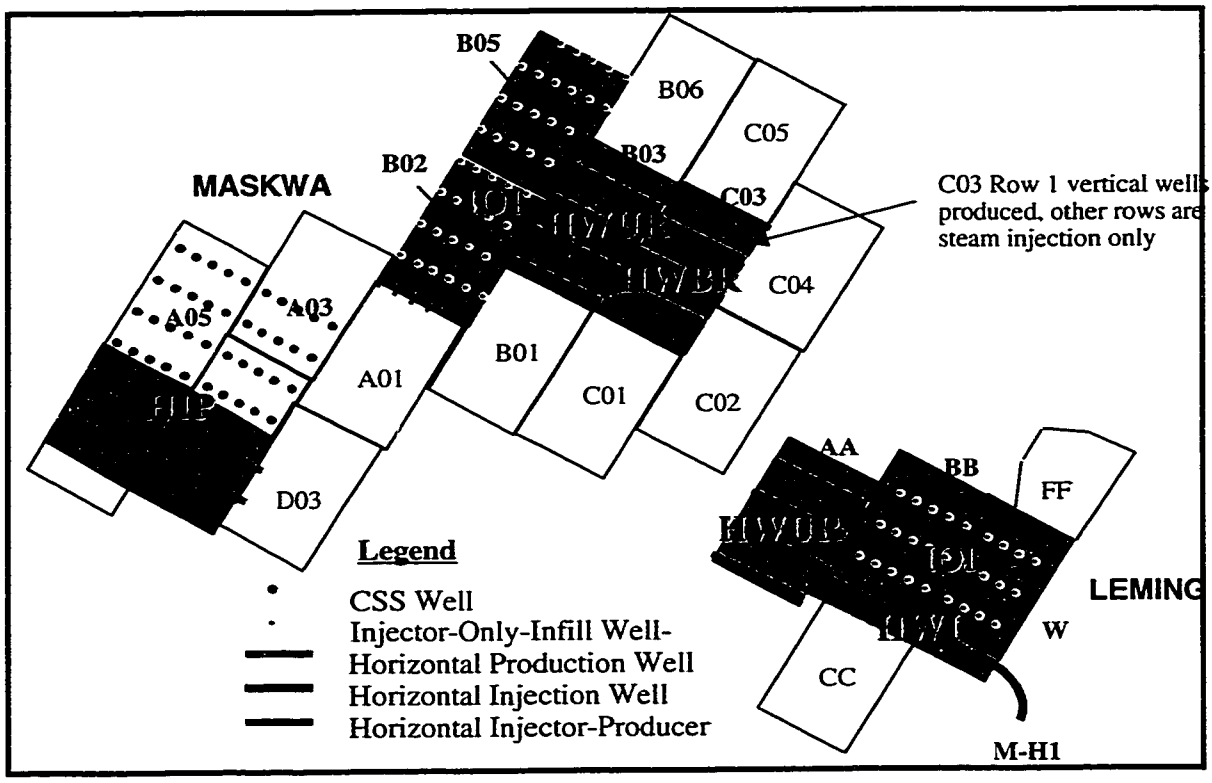

FIG. 1.5. Locations of Follow-up processes pilots at Cold Lake including injector-only-infills (IOI), horizontal wells under rows (HWUR), horizontal wells between rows (HWBR), and horizontal-injector-producer (HIP) pilots.

1.6 Reservoir monitoring - the role of Geophysics in bitumen recovery

Time-lapse 3-D seismic surveys have been successfully used to map and monitor steam conformance. These steam conformance maps have been used extensively in the development and monitoring of follow-up processes. Seismic waves can recognize the steam zone for three major reasons. The most critical reason is that natural gas (CH_4 or methane) evolves from bitumen when the reservoir pressure drops below its bubble point at a particular temperature (2 to 3 MPa). In particular, the *P*-wave velocity drops from 2300 m/s in oil sands with 0% gas saturation to 1850 m/s with 2-5% gas saturation. Increasing the rock temperature also decreases the rock velocity. In the situation of high temperature and low pressure water vapor exists in the heated zone, which causes a seismic response similar to gas.

As CSS is a dynamic process, to monitor steam conformance the timing of seismic data acquisition has to fall into the reservoir pressure window of 2 to 3 MPa. Figure 1.6 shows the reservoir pressure curve of two CSS cycles and seismic survey acquisition window. For the purpose of steam conformance mapping and monitoring, the seismic survey should be conducted during the production phase (i.e., pressure slowly declining).

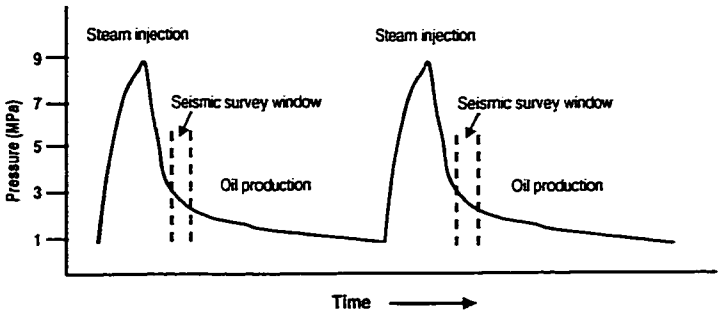

FIG. 1.6. Schematic diagram showing reservoir pressure state and 3-D seismic acquisition window.

1.7 Previous work

Three key seismic attributes were used for the monitoring of reservoir bitumen recovery in the early stages of this technology development (Eastwood, 1994). The delay time (sag) is generated by mapping the relative time difference of reflections from horizons above and below the reservoir between repeated (time-lapse) surveys. The amplitudes of horizons above, below and within the reservoir between repeated (time-lapse) surveys were also used for the monitoring. Frequency attenuation within the reservoir is the third attribute used for monitoring. Statistics such as discriminant analysis for a large number of attributes analysis were introduced (Eastwood, 1996). Isaac (1996) further combined 2-D compressional-wave and converted shear-wave with 3-D seismic data to illustrate that V_p/V_s can be used to distinguish heated from cold reservoir. Her amplitude-versus-offset (AVO) analysis confirmed the amplitude anomalies were caused by low velocity intervals (heated reservoir). The previous work mostly focused on mapping areal steam conformance and treated the reservoir as a single unit. The AVO analysis focused on the single event amplitude anomaly. The AVO inversion was not introduced.

1.8 Dissertation objectives

The main objectives of this dissertation are to develop new reservoir characterization and monitoring technologies by using different seismic data and analysis methods.

To understand reservoir heterogeneity, shear-wave information is critical. The first objective is to conduct a converted shear-wave feasibility study through the 3-component acquisition, processing, and interpretation including 3-component vertical seismic profiling (VSP) data.

The second objective is to develop a 3-D VSP survey design and processing (mapping) technique as VSP can provide converted shear-wave (*P-S* wave) data with better quality. Also, it is advantageous (cost effective) to use 3-D VSP at Cold Lake for reservoir monitoring and characterization because the well and vertical geophone arrays are usually available from passive seismic monitoring programs.

The third objective of this dissertation is to develop the concept of quantitative cross-calibration or cross-training for time-lapse seismic data and further to assess time-lapse seismic data normalization routines. This quantitative approach will address the issue of consistency between the results of time-lapse seismic surveys. It is useful to predict the reservoir status using cross calibration and data normalization as a bridge between time-lapse surveys.

The fourth objective of the dissertation is to develop analysis techniques that compensate for the redundancy of conventional seismic attributes as these attributes have some degree of correlation. Conventional attributes such as average amplitude, isochron, peak amplitude, central frequency, etc. are readily extracted from a data volume and can be related to reservoir properties in many instances. However, these attributes do not necessarily capture the entire variance of the reservoir property of interest. Seismic attributes calculated from principal component decomposition of the seismic data are orthogonal to each other and the full suite of principal components contains all the variance in the seismic data.

The fifth objective of this dissertation is to create the detailed 3-D models of steam chambers through post-stack inversion. This will provide insight into the impact of lithology controls on steam chamber and steam migration. The Clearwater sequence stratigraphy will be tied to the steam chambers to determine if the internal boundaries within sequences can influence steam migration.

The sixth objective of this dissertation is to develop an AVO inversion algorithm that is suitable for the Cold Lake area for reservoir quality (heterogeneity) studies and reservoir monitoring. To achieve this objective a mud-rock line that is suitable for Cold Lake must be established via V_p and V_s analysis using dipole sonic logs. With the limitation of availability and resolution of shear-wave data pseudo-shear information can be obtained through the pre-stack attribute - AVO inversion. Time-lapse AVO inversion will also be carried out by applying this technique to define steam distribution and relate it to lithology controls such as tight streaks or muddy channels.

1.9 Hardware and software used

All the seismic interpretation of data used in this dissertation was performed using a Geoquest IESX interpretation system that is operating on a Sun Sparc 20 workstation. Basic processing was performed using the ProMax processing package developed by Advance Geophysical Inc. This processing package is also operating on a Sun Sparc 20 workstation. The 3-D VSP processing software was developed into the ProMax system. Seismic attributes were extracted by using the software developed by Exxon Production Research Co. The discriminant analysis was implemented with a SAS statistics package. This SAS package was also used for log statistic analysis and display. Some displays were created using a MATLAB package. Most contouring and areal mapping of steam conformance were created using a Z-MAP plus software package. Seismic inversion was performed using both Hampson-Russell STRATA and the Jason Geosystem Workbench. The Jason Geosystem was also used for tying the deviated well logs to seismic related results. The AVO inversion algorithm was developed using FORTRAN 77 and C++ on a Sun Sparc 20 workstation. Synthetics were made using GMA LogM on a PC computer and a MATLAB software developed by the CREWES project at the University of

Calgary. All figures were made electronically by importing CGM files into Microsoft PowerPoint® on a PC computer. All text processing was done with Microsoft Word®.

Chapter 2 – Seismic methods and characterization at Cold Lake

2.1 Introduction

The purpose of this chapter is to introduce seismic methods used at Cold Lake for reservoir monitoring and characterization. The chapter emphasizes building a relationship between compressional and shear velocities and 3-component studies from surface to borehole VSP methods. Shear-waves (*S*-waves) information has the potential to improve reservoir characterization and monitoring as shear-wave can differentiate some lithologies that compressional-waves (*P*-waves) can not. Also, the fluid content in rock formation is better understood when integrating *P*-wave with *S*-wave information. For borehole seismic *S*-wave resolution is usually higher than *P*-wave resolution, while for most surface data *S*-wave resolution is about the same or lower than *P*-wave resolution.

Shear-wave information can be obtained in many ways. Shear-wave information obtained from AVO inversion process is not a direct measurement, but rather a calculated one; therefore it is called pseudo shear-wave or indirect shear-wave. However, it is probably the most cost-effective way to obtain shear-wave information. But poor amplitude recovery and erroneous relationships between *P*- and *S*-wave velocities can significantly alter the results. The functional relation of *P*- to *S*-wave velocities plays an important rule in extracting *S*-wave information. This functional relation is called mud-rock line (Castagna et al., 1985; Gidlow et al., 1992; Goodway, 1997). The first part of this chapter calculates an optimized mud-rock line for Cold Lake clastic rocks.

Shear-wave information obtained from 3-component acquisition and converted-wave processing is much more cost-effective as compared to using a direct shear source. Furthermore, near surface attenuation of *S*-wave energy is problematic. The second part of this chapter discuss as the integrated analysis of *P*- and *S*-waves including both surface seismic and borehole seismic data.

Finally this chapter introduces surface 3-D seismic data acquisition and discusses processing for preparation of 3-D data analysis in subsequent chapters. A 3-D VSP dataset from D3 pad is also introduced.

2.2 Borehole compressional- and shear-wave information in Cold Lake

One compressional-wave (*P*-wave) sonic log is available on each of 200 production pads. Each pad has 20 production wells (see Figure 2.1). The wells with sonic log data available are almost all near vertical. Sonic logs are also always available at observation vertical (OV) wells. *P*-wave data, therefore, is widely available in Cold Lake. However, shear-wave (*S*-wave) information is quite limited. Table 2.1 lists the wells with both *P*-wave and *S*-wave logs (e.g. dipole sonic) available in the CLPP area. There are 14 wells with dipole sonic data available, and six are shallow shale evaluation wells which do not penetrate the Clearwater reservoir (see Figure 2.1 for the areal distribution of all the dipole sonic wells). Wells B5-28 and B2-32 have the most complete log interval for both

Table 2.1. List of wells with *P*- and *S*-wave logs available at Cold Lake.

common name	well identifier	log interval	logging date	edited length
B2-32	116121306504W400	76-467(P,S)	10/27/95	25 m
B2-34	118121306504W400	63-426(P), 382-456(S)		
B5-28	113032406504W400	27-470(P,S)	11/13/95	35 m
B5-33	114141306504W400	16-469(P), 392-469(S)	11/26/95	35 m
BB-13A	110110706503W400	285-468(P,S)	01/06/93	40 m
P2-05	111092606504W400	177-284(P,S)		
OV11-17	1AA111706503W400	173-540(P), 155-548(S)	03/20/97	
LL-16	100110606503W400			
DMT-01	1AB160206504W400	shale evaluation (<300 m)		
DMT-02	1AA150206504W400	shale evaluation (<300 m)		
DMT-04	100130706503W400	shale evaluation (<300 m)		
DMT-05	112152606504W400	shale evaluation (<300 m)		
DMT-06	111062606504W400	shale evaluation (<300 m)		
DMT-08	110082606504W400	shale evaluation (<300 m)		

P- and *S*-wave data, which were run from shallow glacial till through Colorado shale to Clearwater reservoir.

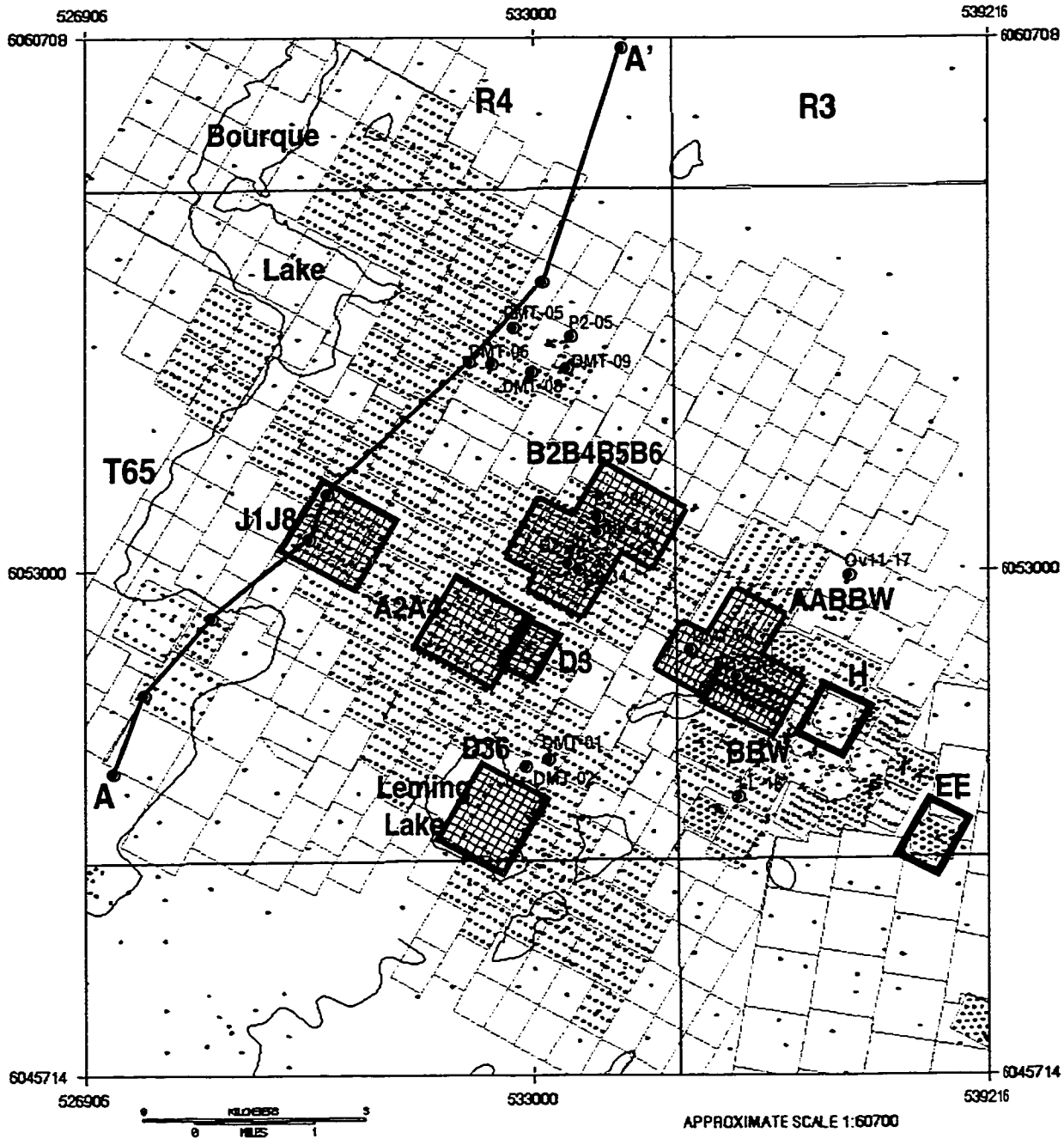

FIG. 2.1. Cold Lake Production Project (CLPP) showing wells with dipole sonic logs (green dots and red dots), 3-D seismic acquisition 1990s (red grids), 3-D seismic acquisition 1980s (blue rectangles), The light blue grids outline CLPP pads. The black dots regular acre grid are productions wells.

2.3 Relationships between *P*- and *S*-wave velocities in Cold Lake clastic rocks

The ratio of compressional to shear wave velocities (V_p/V_s) has been used as a lithology indicator (Pickett, 1963). Cold Lake oil sands (Clearwater reservoir) are clastic rocks. The V_p/V_s for mixtures of quartz, clays, and other rock-forming minerals is significant in reflection seismology. The V_p/V_s relationships established in this chapter is mainly based on in-situ well log data.

Figure 2.2 shows the velocity data from well B5-28. The logs were run from shallow glacial till to Clearwater reservoir, including only clastic rock. The glacial till is poorly consolidated or unconsolidated conglomerate and clays, saturated with water. The Colorado shale zone is well compacted and consolidated. Grand Rapids Formation is sandstone interbeded with shale or muddy layers. The Grand Rapids sandstone is well consolidated except where oil sands are present. The Clearwater Formation is mostly unconsolidated oil sands with thickness from 30 m to 50 m. The V_p-versus-V_s plot (Figure 2.2b) shows that the data are scattered, which suggests that a simple linear relationship of V_p and V_s as published by Castagna (1985) can not be extracted. The scatter plot can be grouped into three different linear trends denoted by red, green, and purple in color. The linear relationships extracted from these three groups represent the mud-rock line for glacier till, Colorado shale, and Grand Rapids and Clearwater sandstone. Points denoted by blue color are tight streaks. Tight streaks are calcified high velocity thin layers (lenses) formed due by diagenesis process. A single linear relationship between V_p and V_s is not observed in Cold Lake clastic rock as the rock from near surface to reservoir experience different compactions. However, if the V_p/V_s is cross-plotted versus V_s a power trend regression (least-square best fit) can be extracted for the rock from all depth (see Figure 2.2c).

$$\frac{V_p}{V_s} = 291 V_s^{-0.6967} \tag{2.1}$$

Solving for V_p in terms of V_s gives:

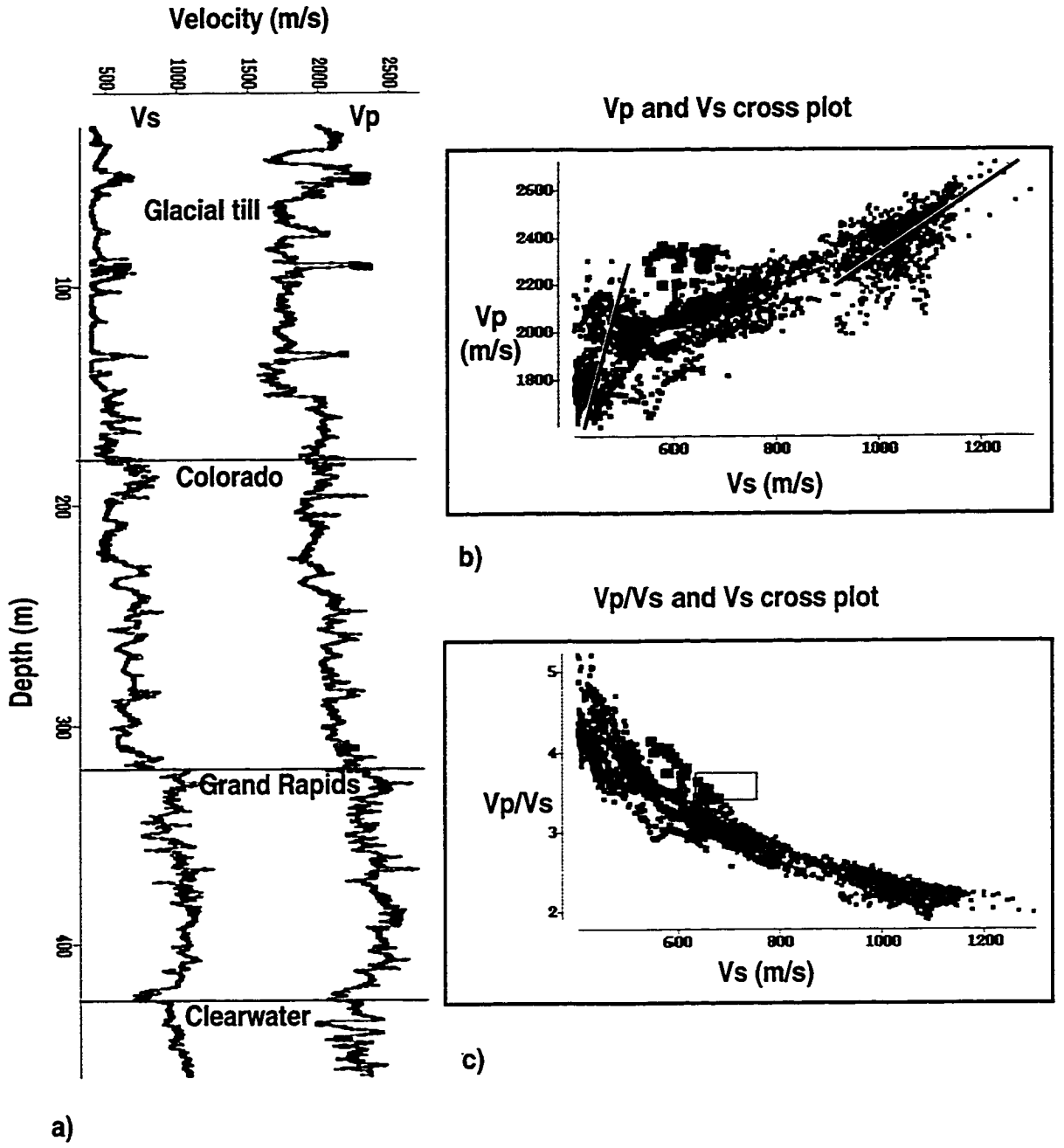

FIG. 2.2. Velocity data from well B5-28 in Cold Lake: (a) Compressional and shear wave velocity logs, (b) cross plot of V_p versus V_s, (c) cross plot of V_p/V_s versus V_s. Data denoted in red are mostly from shallow glacial till; the data denoted in green are mostly from Colorado shale, the data denoted in purple are from Grand Rapids and Clearwater sandstone.

$$V_p = 291 V_s^{0.3033}. \quad (2.2)$$

This relationship can not be derived from the cross-plot of V_p/V_s versus V_p as the data are widely scattered (see Figure 2.3). The compressional wave velocity data is scattered in larger in extend than shear wave velocity data within zones of glacial till (red) and sandstone (pink).

Well ov11-17 is an observation vertical well, drilled to the top of Devonian (see Table 2.1 and Figure 2.1). The dipole sonic log was conducted from Colorado shale to the top of Devonian. Many thin tight streak layers were encountered in the Grand Rapids and Clearwater Formations. Figure 2.4 shows the V_p and V_s velocity logs, cross-plots of V_p, V_s velocities with the tight steaks and Devonian Formation (carbonate) are excluded (Figure 2.4 b and c).

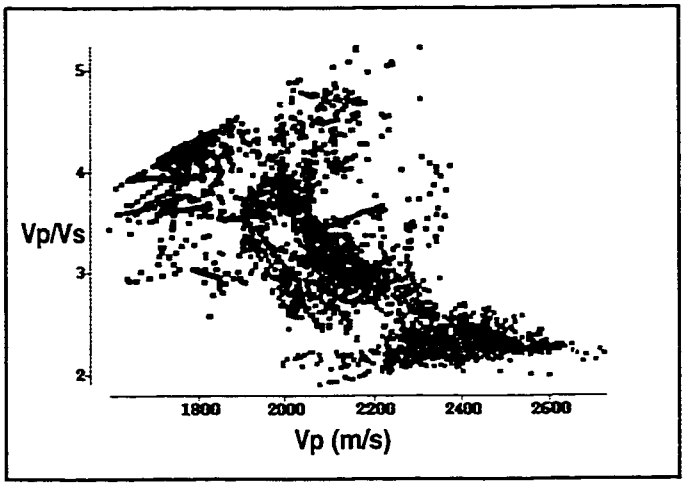

FIG. 2.3. Cross plot of V_p/V_s versus V_p from well B5-28 in Cold Lake. Red - glacier till, green - Colorado shale, purple - Grand Rapids and Clearwater sandstone.

Comparing with Figure 2.2 only two major zones are present as there is no data available in the glacial till. The relationship between V_p and V_s is closer to a linear function. However, if the linear regression is applied to the two groups (green and red) separately the relationship between V_p and V_s is similar to Figure 2.2. A power trend regression applied to the cross-plot of V_p/V_s versus V_s (Figure 2.4c) yields:

$$V_p = 199 V_s^{0.3543}. \quad (2.3)$$

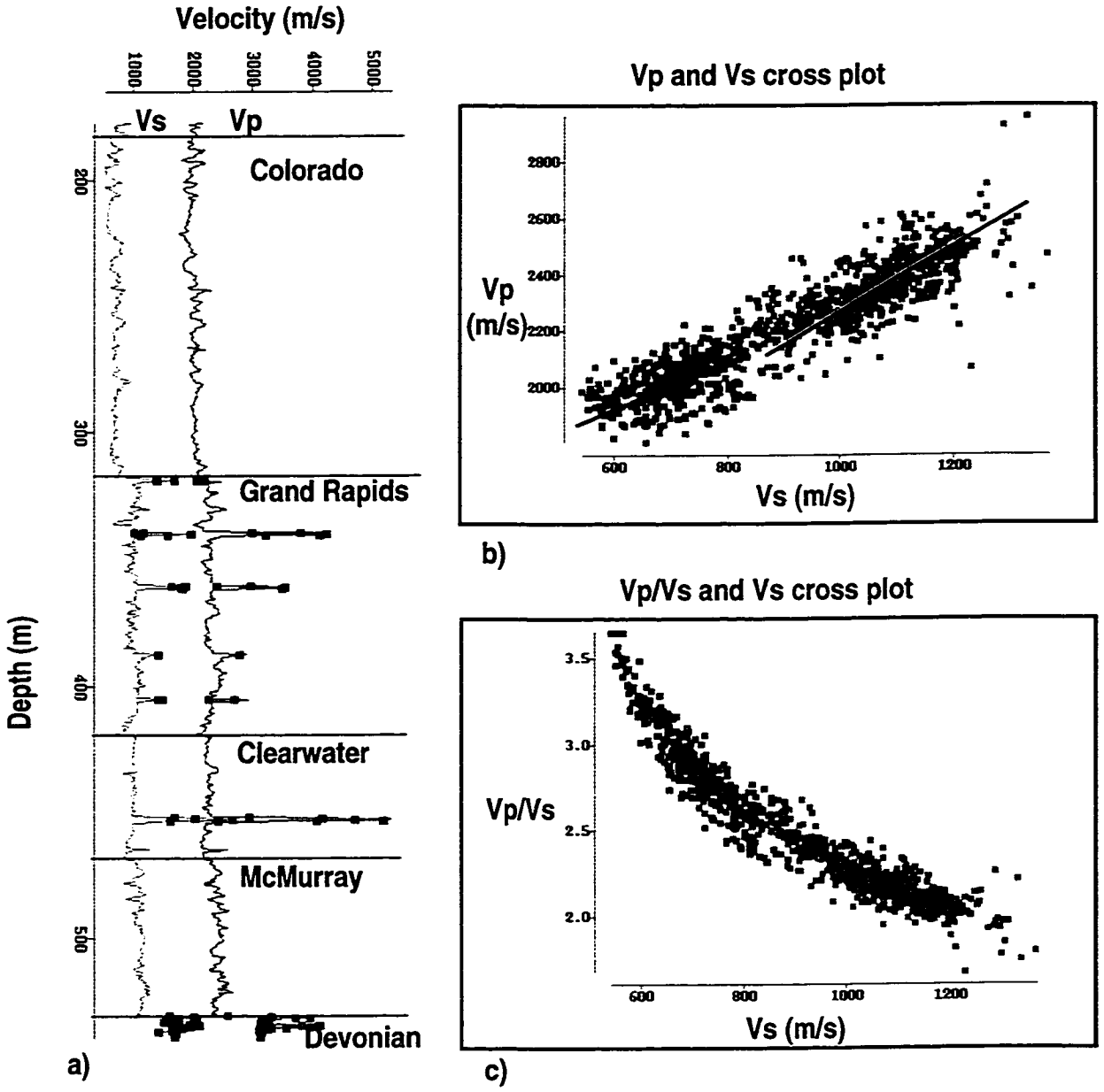

FIG. 2.4. Velocity data of well OV11-17 (1AA111706503W400) at Cold Lake: (a) Compressional and shear wave velocity logs, (b) cross plot of V_p versus V_s, (c) cross plot of V_p/V_s versus V_s. The data denoted in green are mostly from Colorado shale, the data denoted in red are from Grand Rapids, Clearwater, and McMurray sandstone. Tight streaks and Devonian Formation (carbonate) are excluded in cross-plot.

The two functions are plotted together in Figure 2.5. There is no data in the shallow glacial till zone in well OV11-17. So the extracted relationship between V_p and V_s is biased to higher shear wave velocity in the low velocity zone (the majority of low velocity data are associated with shallow zone). This is clearly illustrated in Figure 2.5 where orange curve (equation 2.3) is above red curve (equation 2.2) for lower V_p as well change in geology. As indicated in Figure 2.1 well B5-28 is several kilometers away from well OV11-17.

The V_p-versus-V_s relation forms the base for the mud-rock line in AVO analysis (Smith and Gidlow, 1987). If these functions are used as mud-rock line for AVO inversion analysis then equation (2.2) is more general, while equation (2.3) represents the mud-rock line for shale and sandstone from Colorado shale to the top of Devonian.

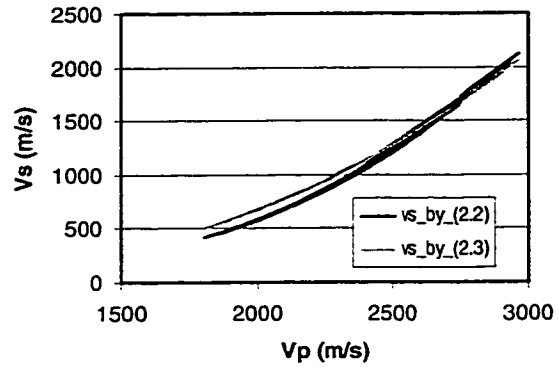

FIG. 2.5. Theoretical plots of two V_p-V_s functions (equation 2.2 and 2.3).

Figure 2.6 shows the velocity logs from well OV11-17 and predicted compressional wave velocities from the shear wave velocity using the two equations discussed above. Obviously equation (2.3) gives better prediction as it is extracted from the data of this well. But the relative error of prediction has very minor difference in reservoir (Clearwater Formation) and Grand Rapids Formation (compare red and orange curves in Figure 2.6b). The relative error of prediction is less than 5% greater in Colorado shale using equation (2.2) than using equation (2.3). The relative error of prediction is calculated as follow:

$$Er = \frac{V_m - V_{prd}}{V_m} \times 100 \qquad (2.4)$$

where E_r is the relative error, V_m is the measured velocity, V_{prd} is the predicted velocity. So the negative error represents the over prediction of velocity, and positive error represents under prediction of velocity.

For a given shear wave velocity equation (2.2) predicts a higher value of V_p than equation (2.3) (Figure 2.5) for shear wave velocity less than 1500 m/s (Cold lake clastic rocks.)

It is important to note that the direction of relative error (positive or negative) is an indicator of lithology or reservoir quality using mud-rock line as a reference. First of all, all tight streaks correspond to positive error. The V_p of tight streaks is under estimated when shear wave velocity is used for prediction (see Figure 2.6a and compare black curve with red and orange ones). The shale and poor reservoir quality zones correspond to positive error (see the shale zone above Clearwater Formation and shaly zones in McMurray Formation. The reservoir oil sands and sandstone correspond to the negative error (see Clearwater Formation). For either mud-rock line this general trend is very similar (compare red and curves in Figure 2.6b). These rules are not applicable to Colorado shale.

The tight streaks are over estimated when using compressional wave velocity to predict shear wave velocity (see Figure 2.7a and compare black curve with red and orange curves). In this case the relative error is generally higher as the magnitude of shear wave velocity is much smaller than compressional wave velocity. The errors are confined within ±20% except tight streak zones. The direction of relative error as an indicator of lithology or reservoir quality is opposite. Tight streaks and shale are associated with negative error. Good reservoir sandstone is associated with positive error.

Figure 2.8 shows the in-situ velocity measurement from well BB-13A. The well was drilled to a hot gas zone (denoted in red color on the plots). The cross-plots of V_p-versus-V_s and V_p/V_s-versus-V_s show a similar feature as previous well data (Figures 2.2 and 2.4). However, the velocities from hot gas zone are significantly different. It is distinctly

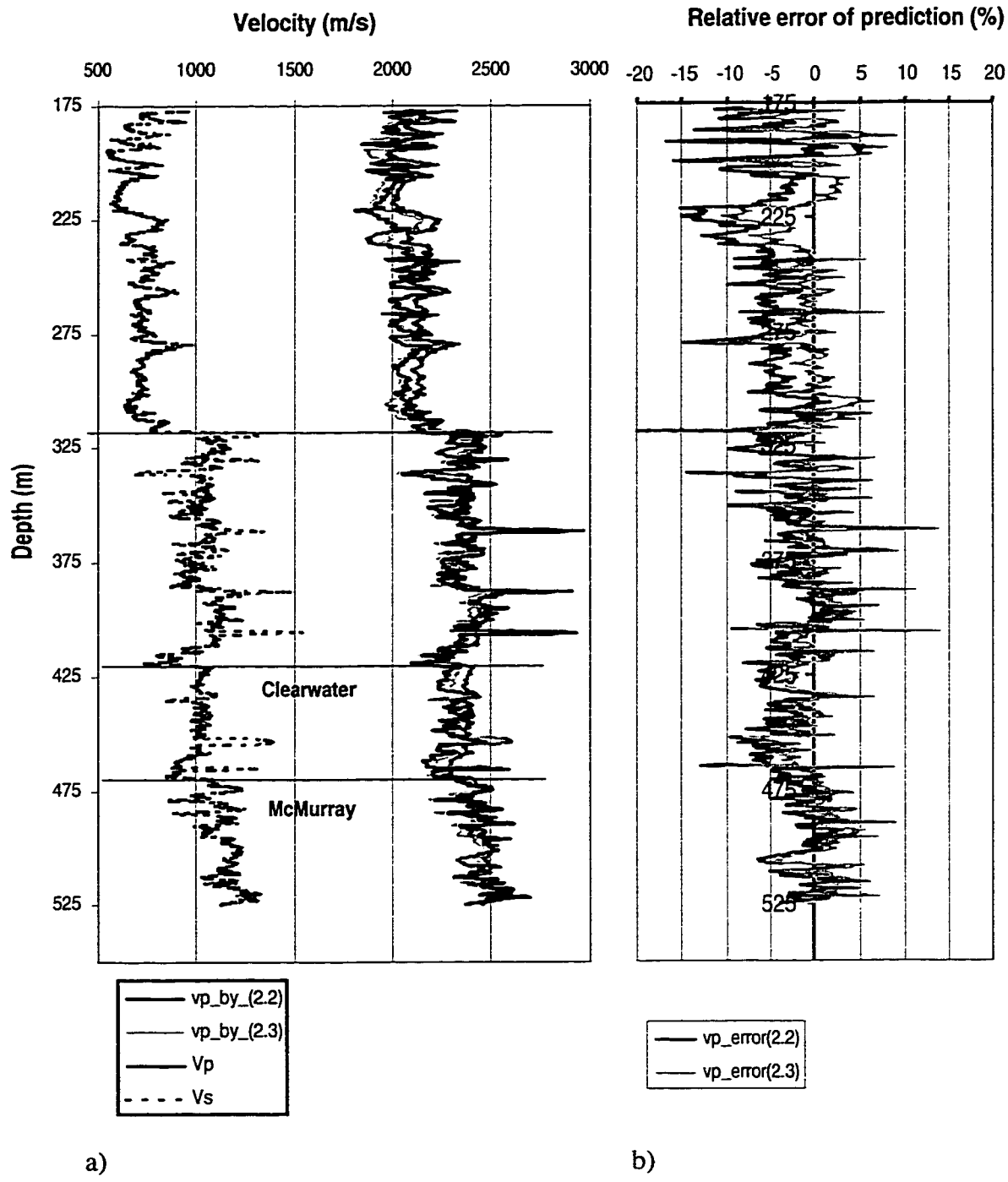

FIG. 2.6. Well OV11-17 compressional wave velocity prediction: (a) Velocity logs (V_p and V_s) and predicted compressional wave velocity by equations (2.2 and 2.3), (b) relative error of different prediction.

separated from best-fit power trend regression line (see Figure 2.8c). This indicates that the 'steam' invaded zone can be well differentiated from the surrounding rocks by using power trend regression line as mud-rock line through AVO inversion analysis.

By integrating all the available V_p and V_s data (excluding shale evaluation wells) a more general relationship between V_p and V_s can be extracted (see Figure 2.9) as follows:

$$V_p = 333.5 V_s^{0.2826}. \tag{2.5}$$

Figure 2.9 also illustrates that the power trend regression gives the best fit to the data, and other regressions (log and exponential) produce inferior results.

This general relationship (mud-rock line) between V_p and V_s is useful for AVO inversion analysis in the area where borehole shear wave data is not available. The theoretical curves of equations (2.2), (2.3), and (2.5) and other mud-rock lines extracted from other wells are plotted in Figure 2.10. They are similar with the exception of well P02-05 that has data available only in Colorado shale (see Table 2.1 and yellow curve in Figure 2.10). Although some discrepancies are observed among these mud-rock lines, the differences are minor in the reservoir zone where the compressional wave velocity ranges from 2000 m/s to 2500 m/s (for both sandstone and shale).

Though the general mud-rock line is useful and important a local mud-rock line is usually more accurate for local AVO analysis. It is better to establish the local mud-rock line if the data is available. However, a mud-rock line only based on the data from shallow Formations such as Colorado shale is not applicable. The mud-rock line should be established based on the data mostly from target study zone such as reservoir Formation if the purpose of AVO inversion is for reservoir heterogeneity study such as differentiating sandstone from shale and delineating reservoir geometry. The general mud-rock line can be used to balance the whole section. Further discussions can be found in chapter 7.

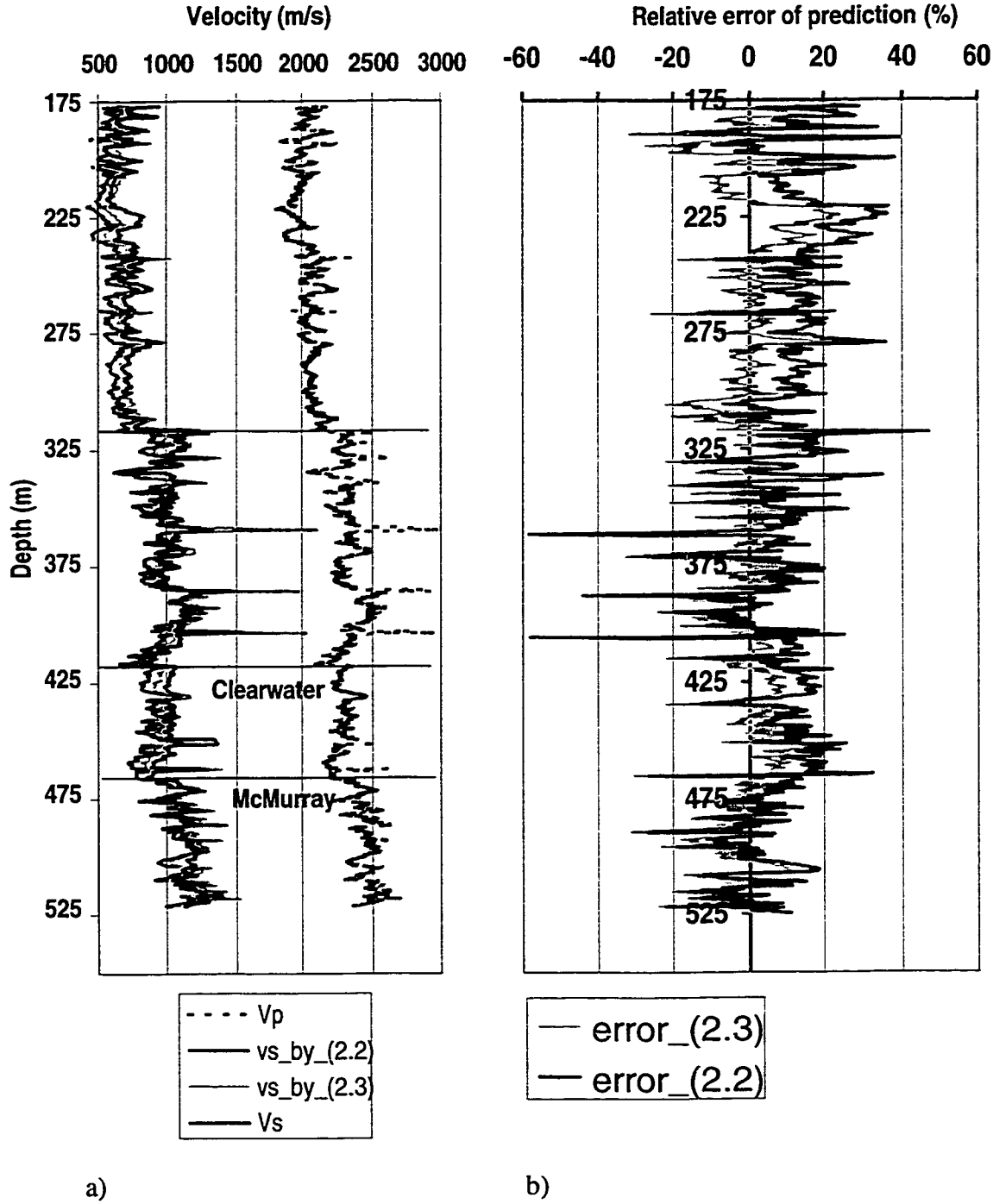

FIG. 2.7. Well OV11-17 shear wave velocity prediction: (a) Velocity logs (V_p and V_s) and predicted shear wave velocity by different equations (2.2 and 2.3), (b) relative error of different prediction.

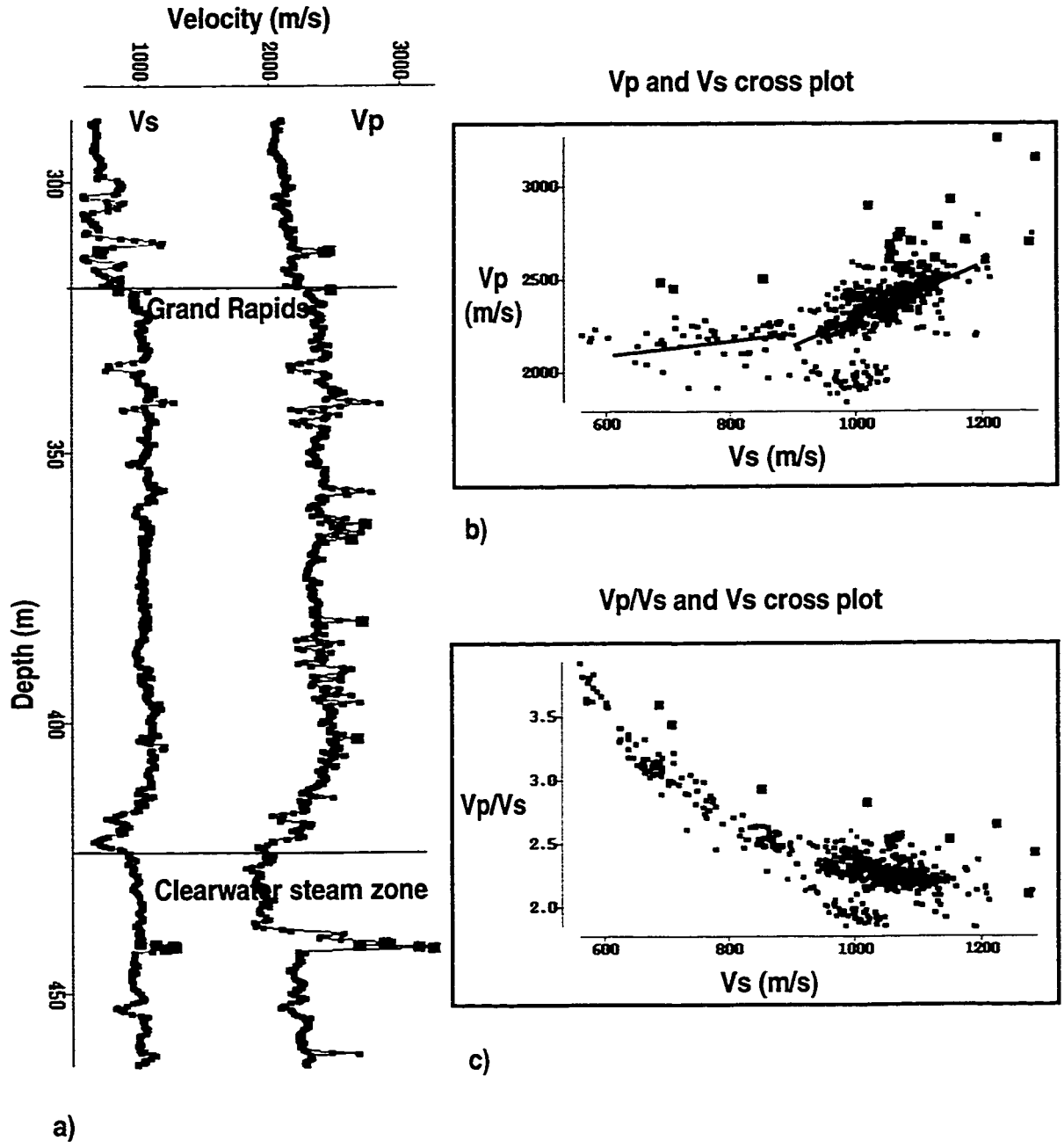

FIG. 2.8. Velocity data of well BB-13A at Cold Lake showing steam response on velocity: (a) V_p and V_s logs, (b) cross plot of V_p versus V_s, (c) cross plot of V_p/V_s versus V_s. The red is steam-flooded zone, the purples are tight streaks. There are very few data points from Colorado shale (above Grand Rapids).

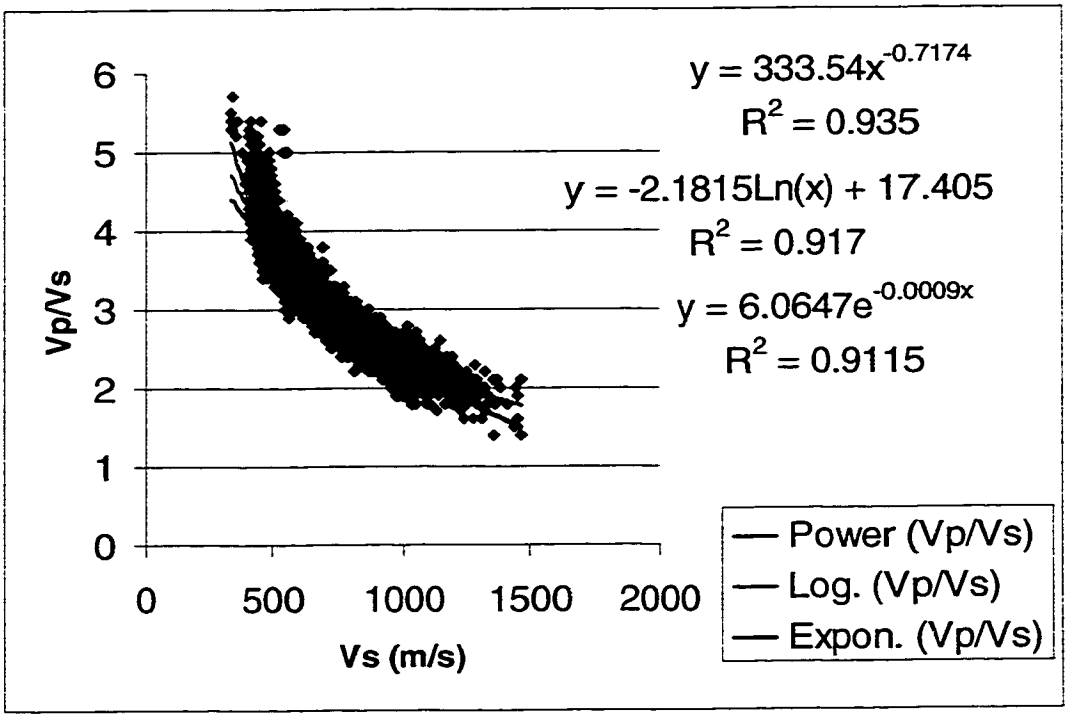

FIG. 2.9. Cross-plot of V_p/V_s versus V_s using all available V_p and V_s data excluding dipole sonic from shale evaluation wells.

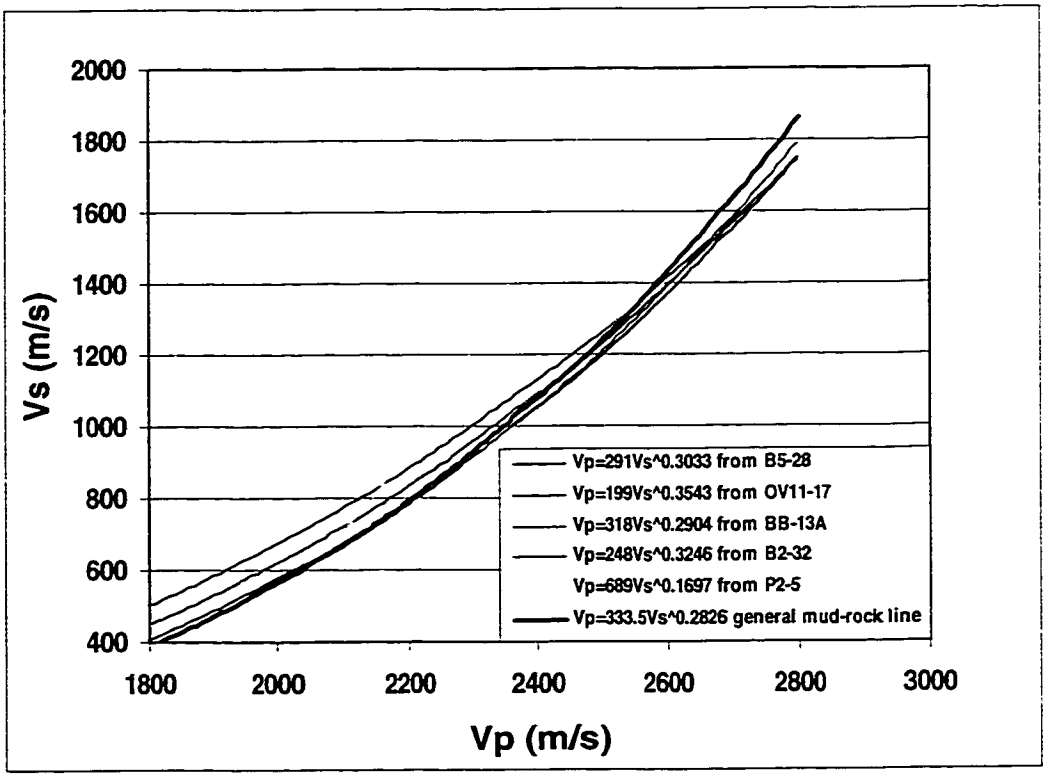

FIG. 2.10. Plots of different mud-rock lines (curves).

2.4 Lame's parameter and velocities

Different elastic parameters have different sensitivity for discrimination of lithology and fluid content in reservoir. The compressional and shear wave velocities are very common parameters, but they may not be the most sensitive ones in some circumstances. Lame's elastic parameters λ and μ are related to velocities as the follows:

$$\lambda = \rho(V_p^2 - 2V_s^2), \tag{2.6}$$

$$\mu = \rho V_s^2, \tag{2.7}$$

where ρ is the density.

The sensitivity of Lame's parameter for fluid detection has been studied by Goodway et al. (1997). Comparisons of V_s, V_p, λ, μ, Vp/Vs, and λ/μ can be easily made when dipole sonic data are available. Figure 2.11 shows the comparisons for well BB-13A in which

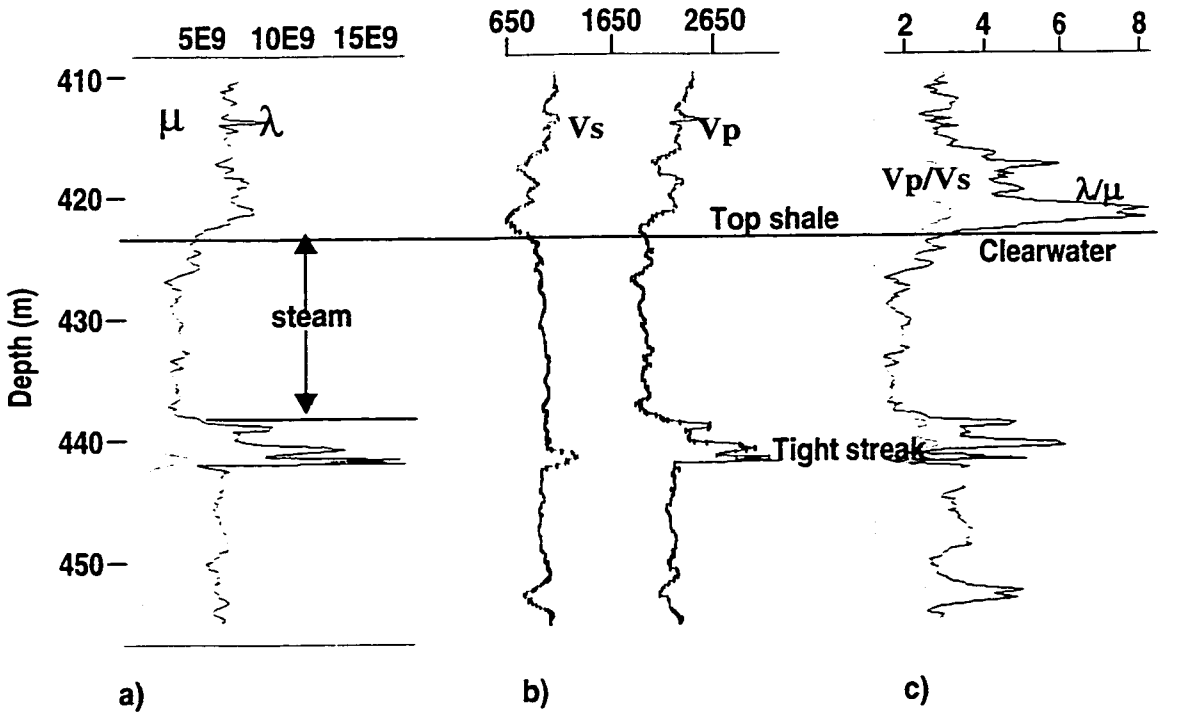

FIG. 2.11. Sensitivity of velocities (Vp and Vs) and Lame parameters (λ and μ) to steam flooded zone of well BB-13A; (a) The curves of λ and μ, (b) The curves of V_p and V_s, (c) The curves of λ/μ and V_p/V_s.

the reservoir interval is steam flooded. The compressional wave (V_p) is more sensitive to the steam-invaded zone than shear wave (V_s). But V_s is more sensitive to shale than V_p, for example, more velocity change is seen on the V_s of the shale layer immediately above Clearwater reservoir (top shale in Figure 2.11b). The different response of compressional- and shear-wave to lithology and fluid is reflected very well by the V_p/V_s ratio (see Figure 2.11c). So V_p/V_s ratio is a lithology and fluid indicator. The Lame's parameters (λ and μ) are elastic parameters contains properties of both velocities and density. The μ has similar sensitivity as V_s to lithology. But the λ is more sensitive to the steam-invaded zone than V_p. However, the λ/μ ratio is much more sensitive than V_p/V_s to both lithology and fluid content (see Figure 2.11c). It has much higher contrast from steam zone (red in Figure 2.11b) to non-steam zone (green in Figure 2.11) in the reservoir interval and similarly from sand to shale (above Clearwater from gray to dark green). It should be a very good indicator of both fluid (steam zone) and lithology (shale versus sandstone).

Figure 2.12 shows the well logs of an observation vertical well 11-17-65-3W4, with lithologic annotations. The calculated logs of λ, μ, and λ/μ are shown in Figure 2.13. Comparing with V_p/V_s ratio, the λ/μ is much more sensitive to lithology change. The V_p/V_s ratio increases in the shale layer (top shale) above Clearwater reservoir; but the contrast of λ/μ is much more significant. The shaly zones identified on Gamma Ray and SP logs in C10 sequence and McMurray Formation (Figure 2.12) are not clear on V_p and V_s logs or even the V_p/V_s log. But they are very clear on λ/μ log. Relative to the surroundings the tight streaks show a significant decrease of λ/μ.

The λ/μ is actually directly related to V_p/V_s as follows (take equation (2.6) divided by equation (2.7)),

$$\frac{\lambda}{\mu}=\left(\frac{V_p}{V_s}\right)^2-2. \qquad (2.8)$$

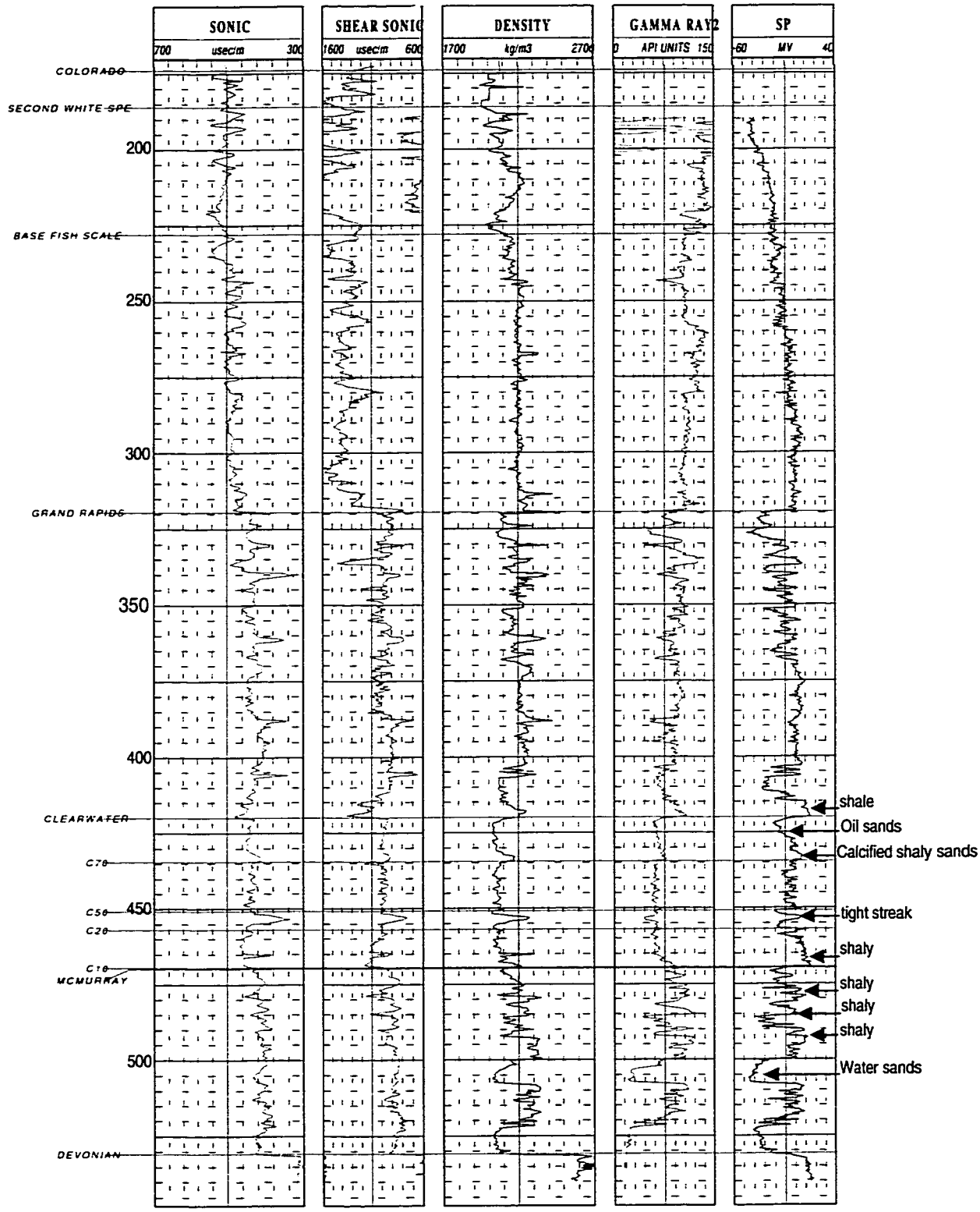

FIG 2.12. Well logs of OV11-17 (1AA111706503W400) showing lithologies in the reservoir formation (Clearwater) and the surroundings.

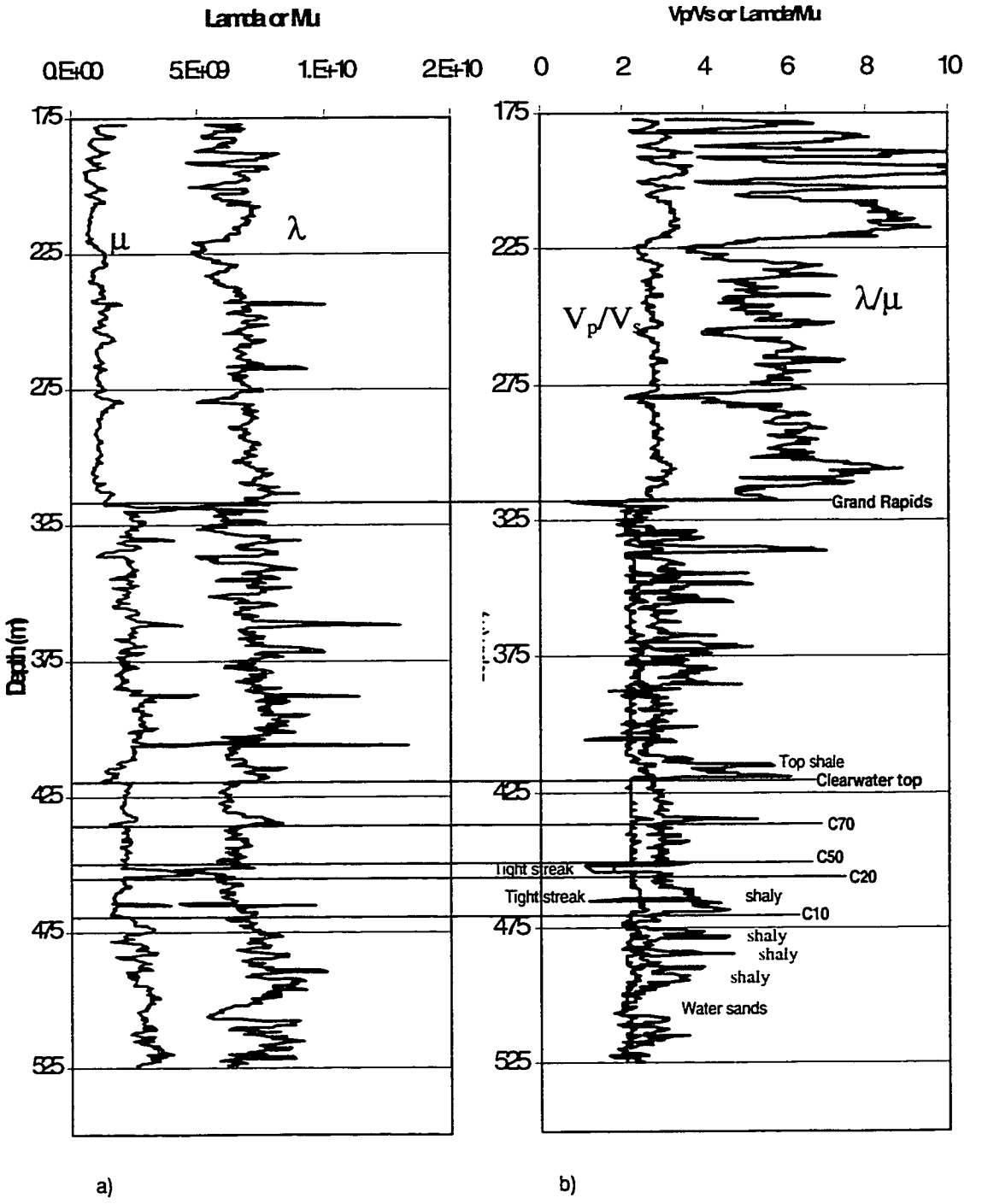

FIG. 2.13. Sensitivity of λ, μ, and λ/μ to different lithologies and comparison to V_p/V_s ratio for well OV11-17.

The λ/μ is plotted as a function of V_p/V_s in Figure 2.14 (dark blue curve). Also, a straight line ($\lambda/\mu=V_p/V_s$) is plotted in pink color as a reference line. The plot illustrates that a small change on V_p/V_s causes a big change on λ/μ. The only point that V_p/V_s and λ/μ are the same is when the V_p/V_s equals 2, and this point is called the lithology indicator transition point in this dissertation. For tight streaks and carbonate rocks V_p/V_s is usually less than 2, and the λ/μ drops much faster. For most sandstone and shale in Cold Lake area the V_p/V_s is higher than 2 and the λ/μ is dramatically higher. This explains why λ/μ is more sensitive to lithology change and fluid content in the Formations. So converting velocity measurements to Lame's moduli parameters of rigidity (μ) and incompressibility (λ) offers new insight into the rock property and fluid content.

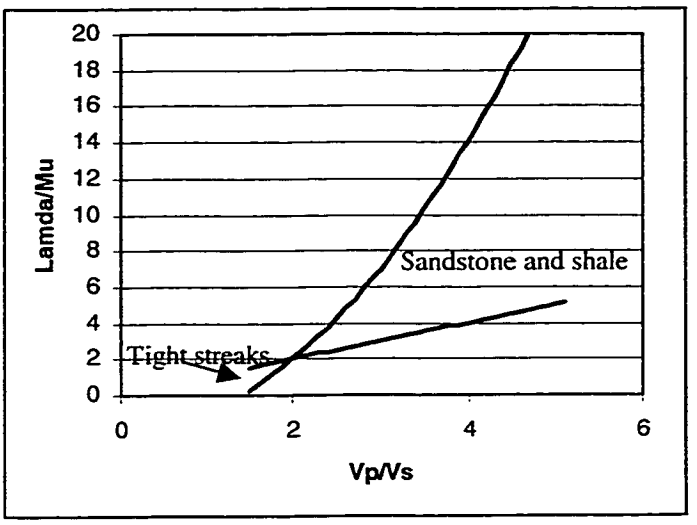

FIG. 2.14. Plot of the λ/μ as a function of V_p/V_s showing λ/μ more sensitive to lithology change V_p/V_s.

2.5 Surface 2-D 3-component study

It is usually difficult for a compressional-waves (*P*-waves) to differentiate shale from a non gas-bearing sandstone as the impedance contrast between them is not high enough. Figure 2.15 shows the cross plot of *P*-wave and *S*-wave impedance (Is) from well OV11-17. It is seen that both shale and permeable sands have similar range of *P*-wave impedance (Ip). However, their shear-wave impedance is different enough to enable us to separate shale from permeable sands. This is one of the key reasons for motivation of shear-wave study. Also, better understanding about reservoir fluid can be obtained by combining *S*-wave with *P*-wave data as *S*-wave does not respond to fluid compressibility changes, hence they respond only to the changes related to rock matrix and density. The

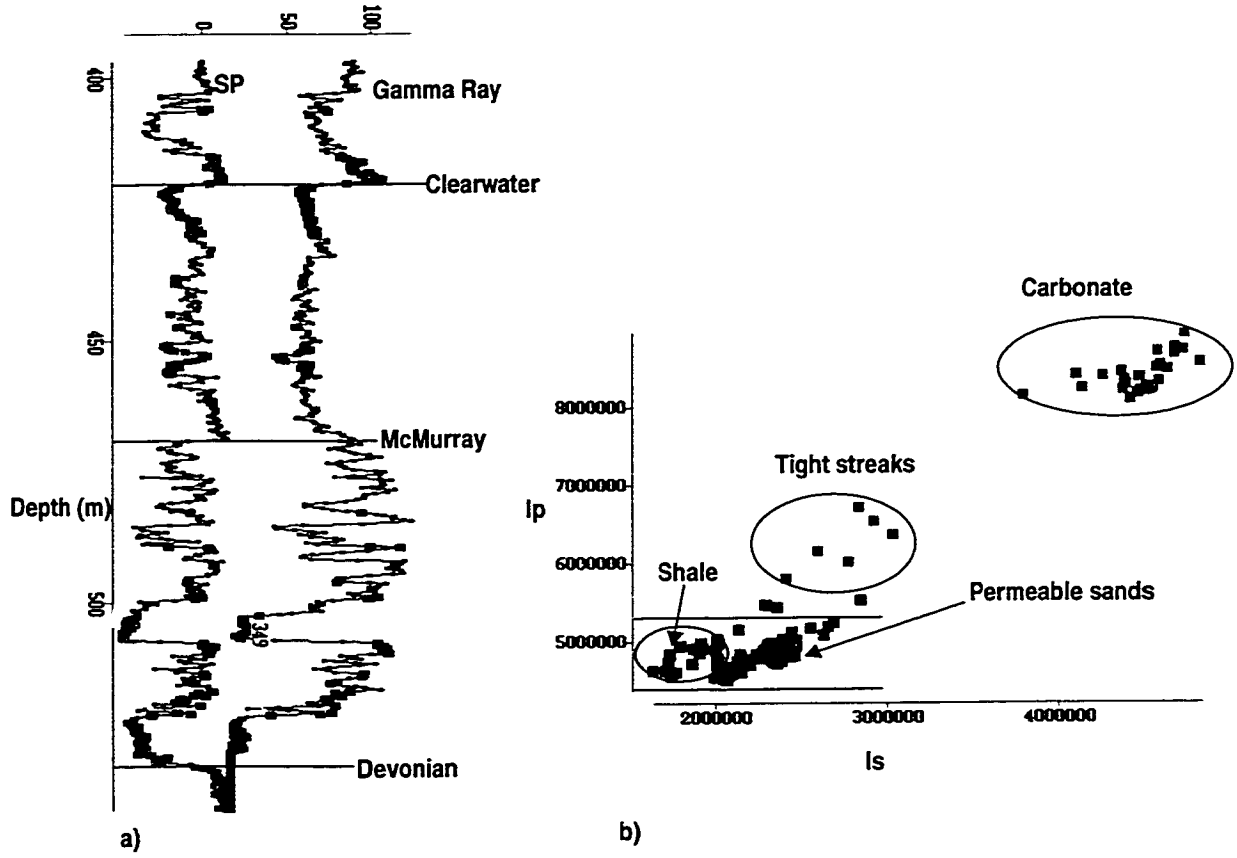

FIG. 2.15. OV11-17 cross-plot of *P*-wave impedance (Ip) against *S*-wave impedance (Is) for different lithologies; (a) SP and Gamma Ray logs, (b) the cross-plot of Ip-versus-Is.

ratio of V_p/V_s and related seismic attributes could provide a more reliable measure of areas of the reservoir which have undergone changes than just attributes derived from *P*-wave data volumes. In the early cycles of steam, changes in rock matrix are significant such as fracturing and dilation; additional shear-wave information should prove valuable in discriminating areas where fluid properties have changed and where rock properties have also changed. Thirdly, the *S*-wave travels slower through the earth which in turn provides better resolution of the reservoir interval. This also depends on the near surface effects such as frequency absorption. Usually the *S*-waves lose more high frequencies than *P*-wave due to near surface effects.

The Cold Lake production project (CLPP) is extending from original high quality reservoir to its surrounding areas where variable reservoir qualities are encountered. A seismic challenge is to map the reservoir lithology such as shale filled channels to optimize the production drilling.

Three-component acquisition made the converted-shear (*P-S*) wave data available and allows joint interpretation of *P*-wave and *S*-wave.

2.5.1 Data acquisition

In the winter of 1997 high effort 2-D seismic lines and VSP surveys were acquired in Cold Lake (see Figure 2.16). Three-component geophones (single geophone for each station) were attached to the conventional 2-D seismic acquisition (array of geophones for each station), measuring motions in the vertical, radial (inline horizontal), and transverse (cross-line horizontal) directions. All three components were recorded on the same system, resulting in data collection from 140 receiver stations (420 channels) for each source-point. No data was recorded at source-to-receiver offsets more than 695 m. The nominal CMP stacking fold was 25. Dynamite was used as source with charge size of 0.3 kg. Sources were buried 12 m below the surface to overcome near-surface effects. The group interval was 10 m which gives very dense CMP spacing of 5 m. The field acquisition parameters are listed in Table 2.2.

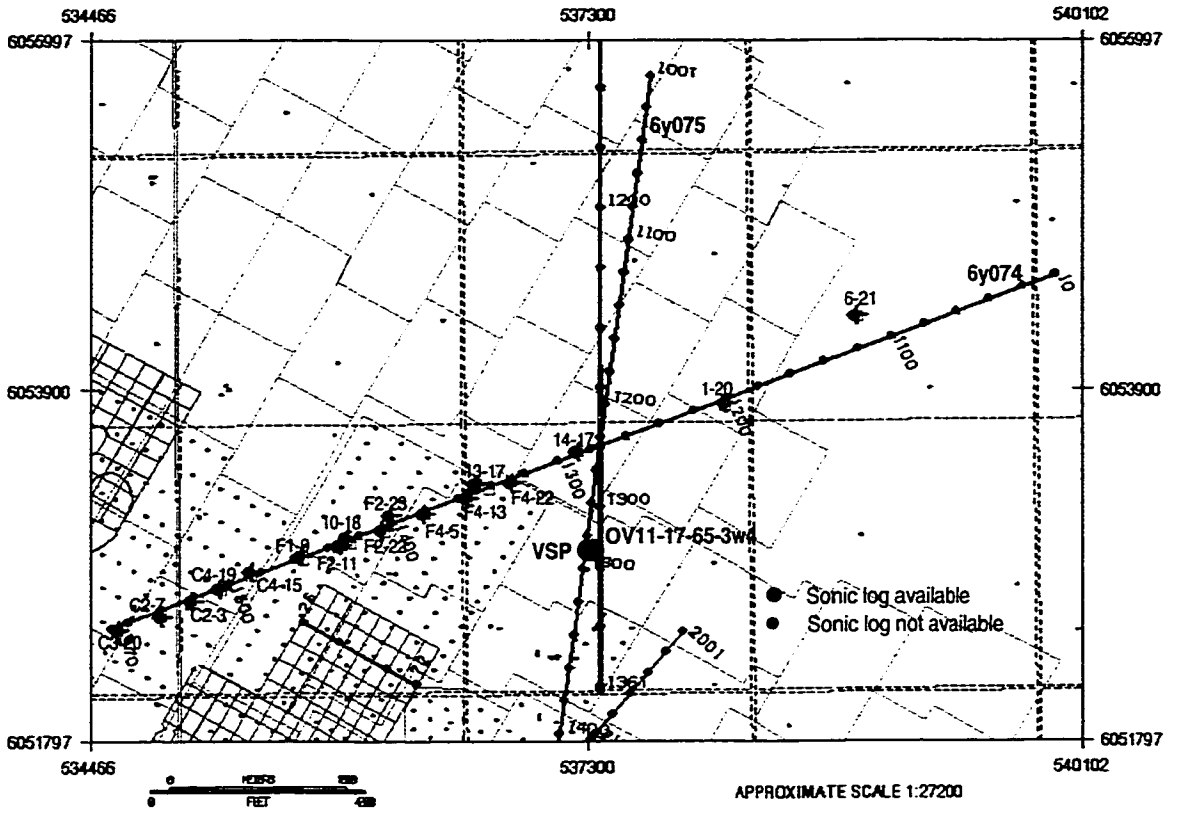

FIG. 2.16. 3-component seismic acquisition location (6y074 and 6y075) and VSP well.

Table 2.2. Field acquisition parameters for surface 3-C 2-D data.

Recorded by	Veritas Geophysical Ltd., Party 2
	March, 1997
Amplifier	I/O system II, 420 channels
	SEG-D format, IFP gain
	OUT-413(293) Hz(dB/oct) Notch OUT
Record Length	2.0 seconds, 1 ms sample rate
Source	Dynamite, 1hole per shotpoint
	0.3 kg at 12 m depth
Geophones	LRS 3-component geophone for 3-C data
	OYO 10 Hz geophone for conventional data
Source interval	20 m
Group interval	10 m
Nominal fold	2500%
Spread	695 - 5 - SP - 5 - 695 m

Vertical-, radial-, and transverse-component gathers are shown in Figure 2.17a, b, c respectively for shotpoint 1121 of line 6y075 (see Figure 2.16). A time-squared gain function followed by individual trace-balance scaling has been applied to these field

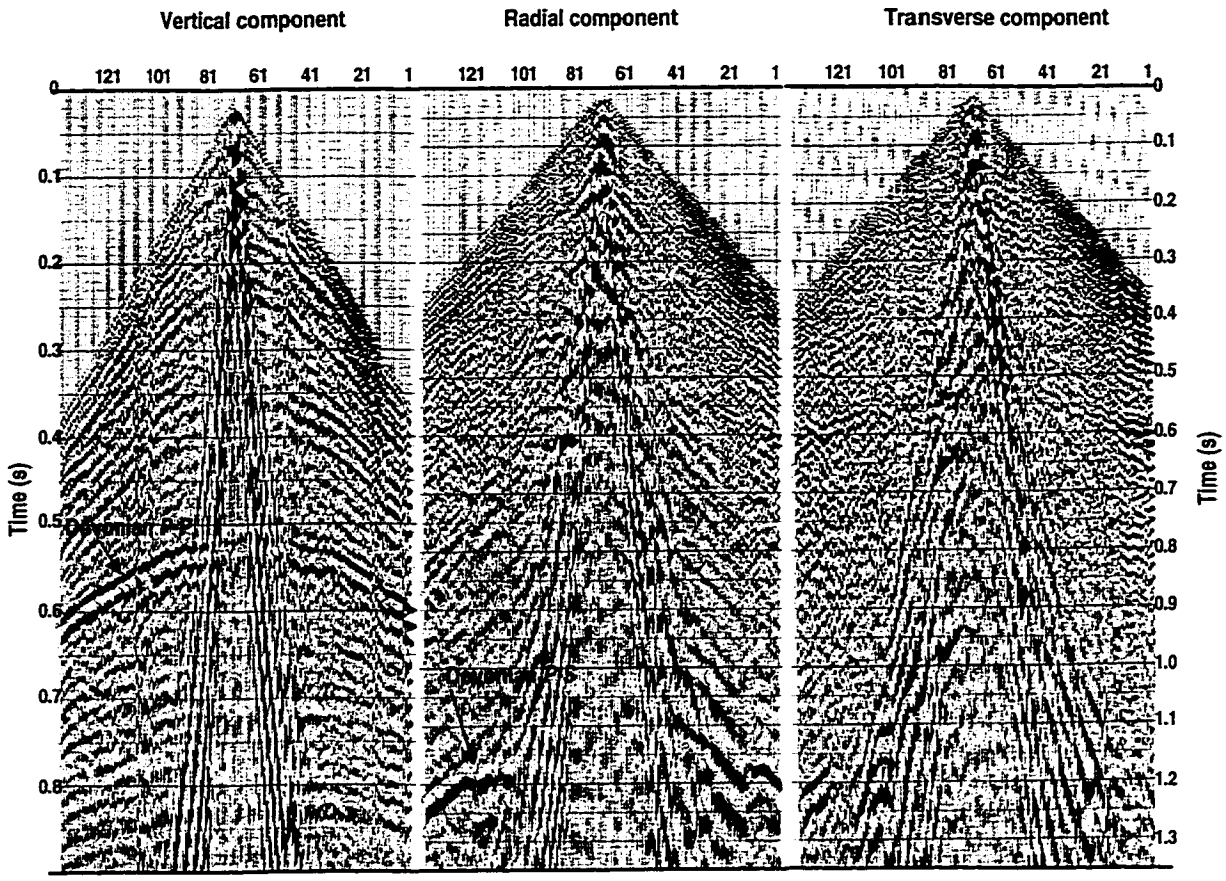

a) b) c)

FIG. 2.17. Three-component records for line 6y075 (shotpoint 1121); amplitudes of each component (panel) are normalized individually.

records. The vertical time scale on plots of two horizontal components is different from that of vertical component. The Devonian reflector is about 0.5 s for *P-P* wave (see vertical component) and 1.1 s for *P-S* wave (see radial component). To facilitate visual correlation between *P-P* and *P-S* data sets a V_p/V_s ratio should be used. For most sedimentary rocks V_p/V_s is in the neighborhood of 2.0 (e.g., Tatham, 1985). However, the Clearwater reservoir in Cold Lake is fairly shallow; the V_p/V_s from surface to Devonian can vary from 5.0 to 1.7. A quick estimation of average V_p/V_s ratio from surface to a certain reflector can be made by following formula:

$$\frac{V_P}{V_S} = \frac{2t_{P-S}}{t_P} - 1, \qquad (2.9)$$

where t_{P-S} is the converted wave (*P-S*) two-way travel time, e.g., t_{P-S} for Devonian is about 1.1 s (see Figure 2.17b); t_P is the two-way travel time for *P-P* wave, e.g., t_P is about 0.5 s (see Figure 2.17b). The average V_P/V_S ratio, therefore, from surface to Devonian is about 3.4, which is significantly higher than 2.0.

2.5.2 Data processing

Three-component surface seismic processing is well documented by Harrison (1992). These 3-C data were processed by Matrix Geoservices Ltd. The vertical channel data were processed using the conventional *P*-wave processing flow outlined in Figure 2.18. The final *P-P* wave stack sections for line 6y074 and 6y075 are displayed in Figures 2.19 and 2.20 respectively. The data have good overall signal strength with very high frequency. The dominant frequency band can be as high as 150 Hz. Noise is present in the shallow glacial till (above 220 ms) as the fold coverage is low. The poor S/N on the SW end of 6y074 and near to CDPs around 610 of line 6y075 (see Figure 2.20) are due to the drop in fold (acquisition gaps). The minor noise around CDP 310 of line 6y074 is due to the poor surface condition where geophones were planted on a swamp. The S/N improves in the Clearwater (reservoir) and McMurray intervals (between 400 ms and 520 ms).

The radial (*P-SV*) component was processed using the sequence shown in Figure 2.21. No rotation of the two horizontal components was performed as no significant reflection energy was seen on transverse component data. Also, no processing was performed on the transverse component. Shown in Figure 2.22 and 2.23 are the final migrated *P-SV* wave sections for 6y074 and 6y075 with converted-wave DMO performed. In the swamp the horizontal components are affected even more adversely than vertical component; so converted-wave data quality is very poor around CCP 310 of line 6y074 (Figure 2.22).

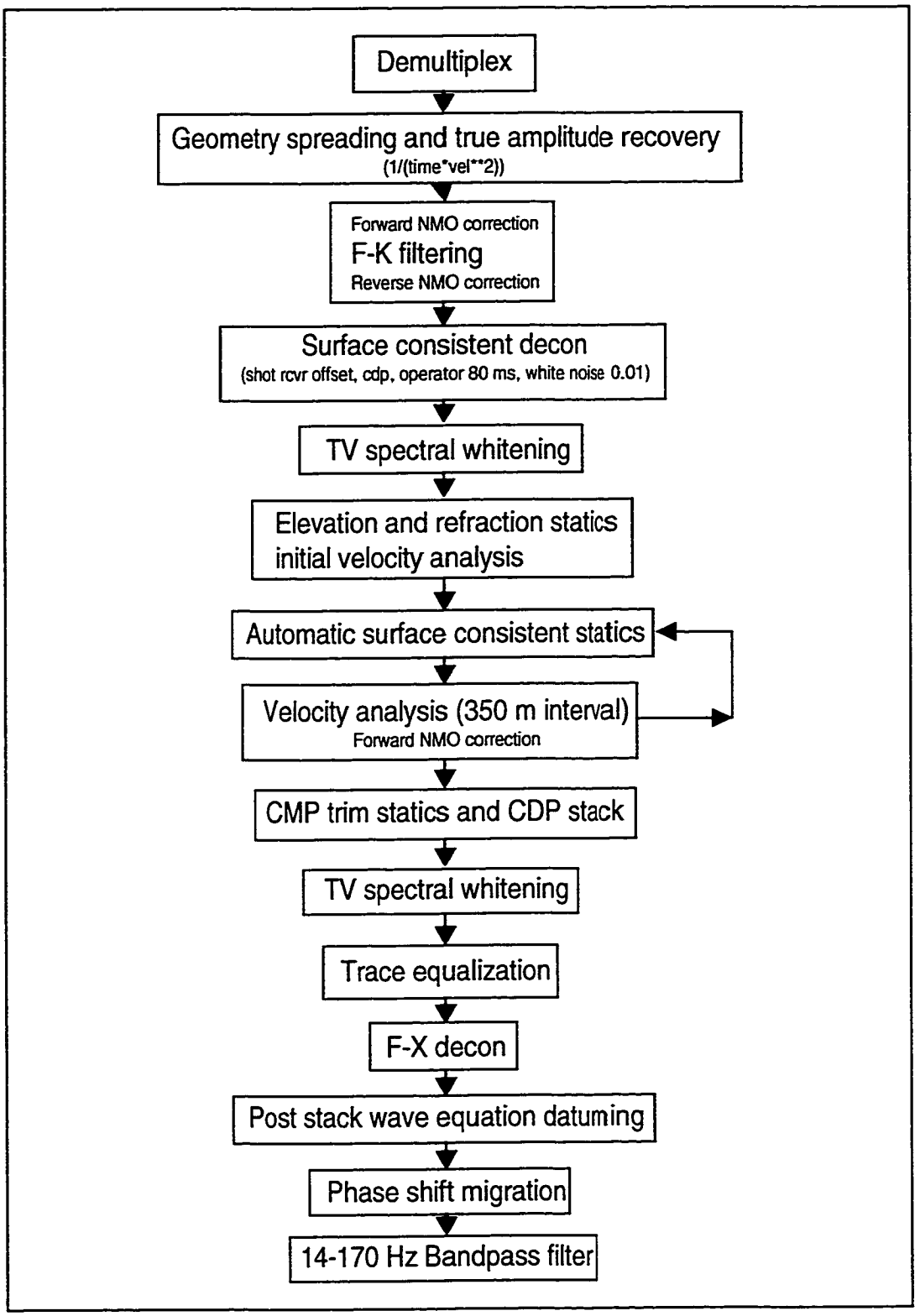

FIG. 2.18. *P-P* wave processing flowchart.

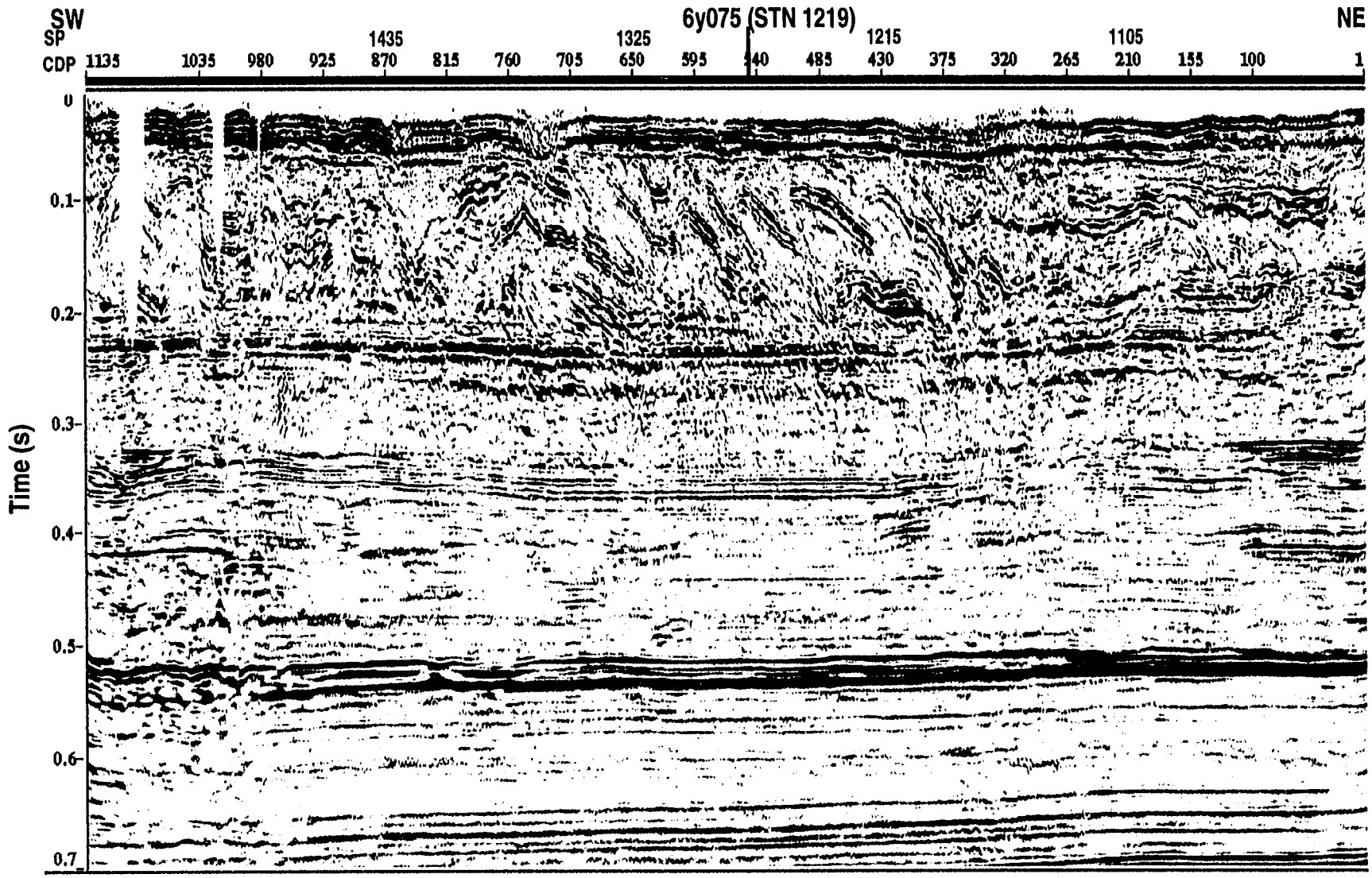

FIG. 2.19. Migrated stack section of vertical component data for 6y074.

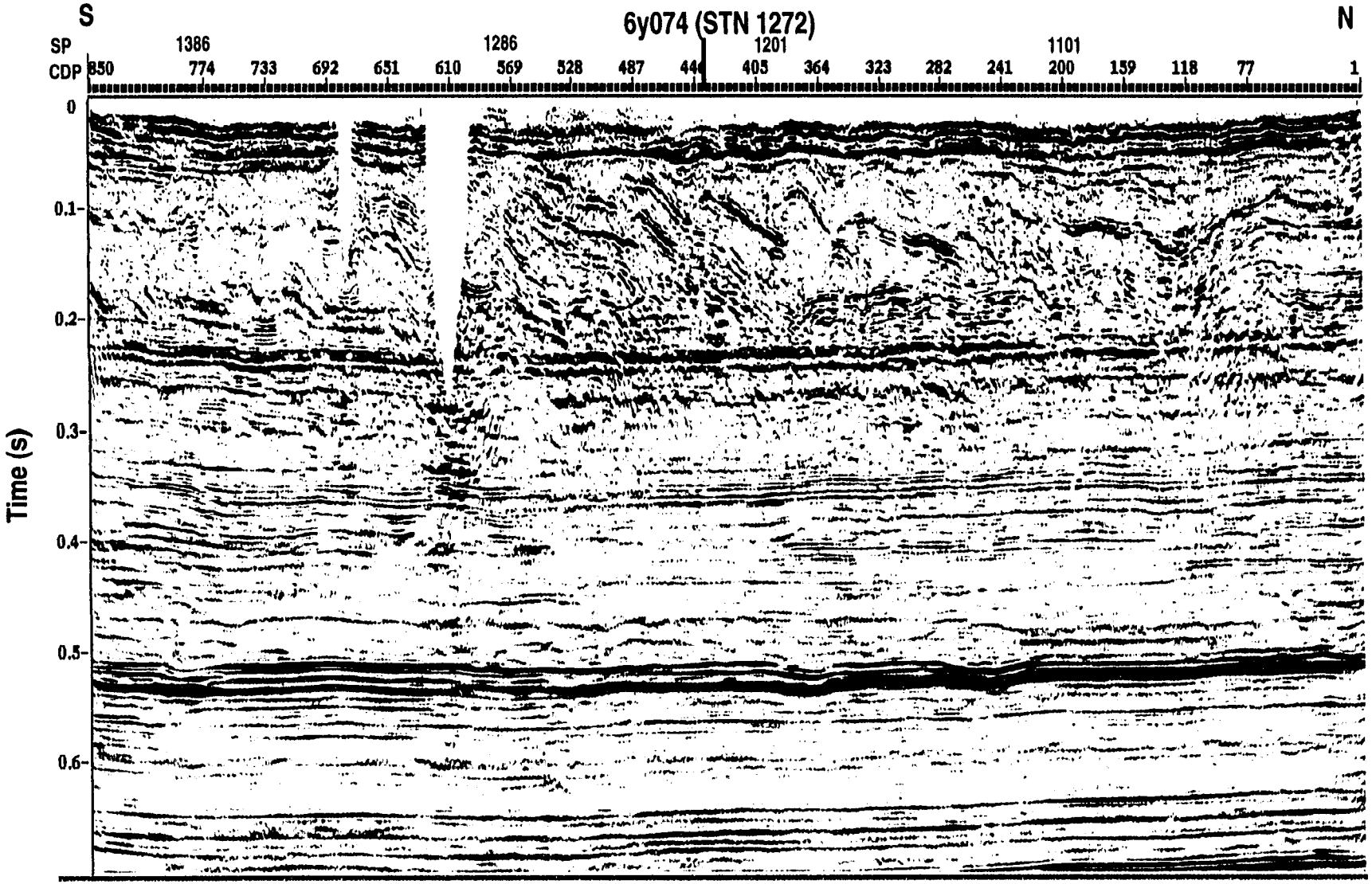

FIG. 2.20. Migrated stack section of vertical component data for 6y075.

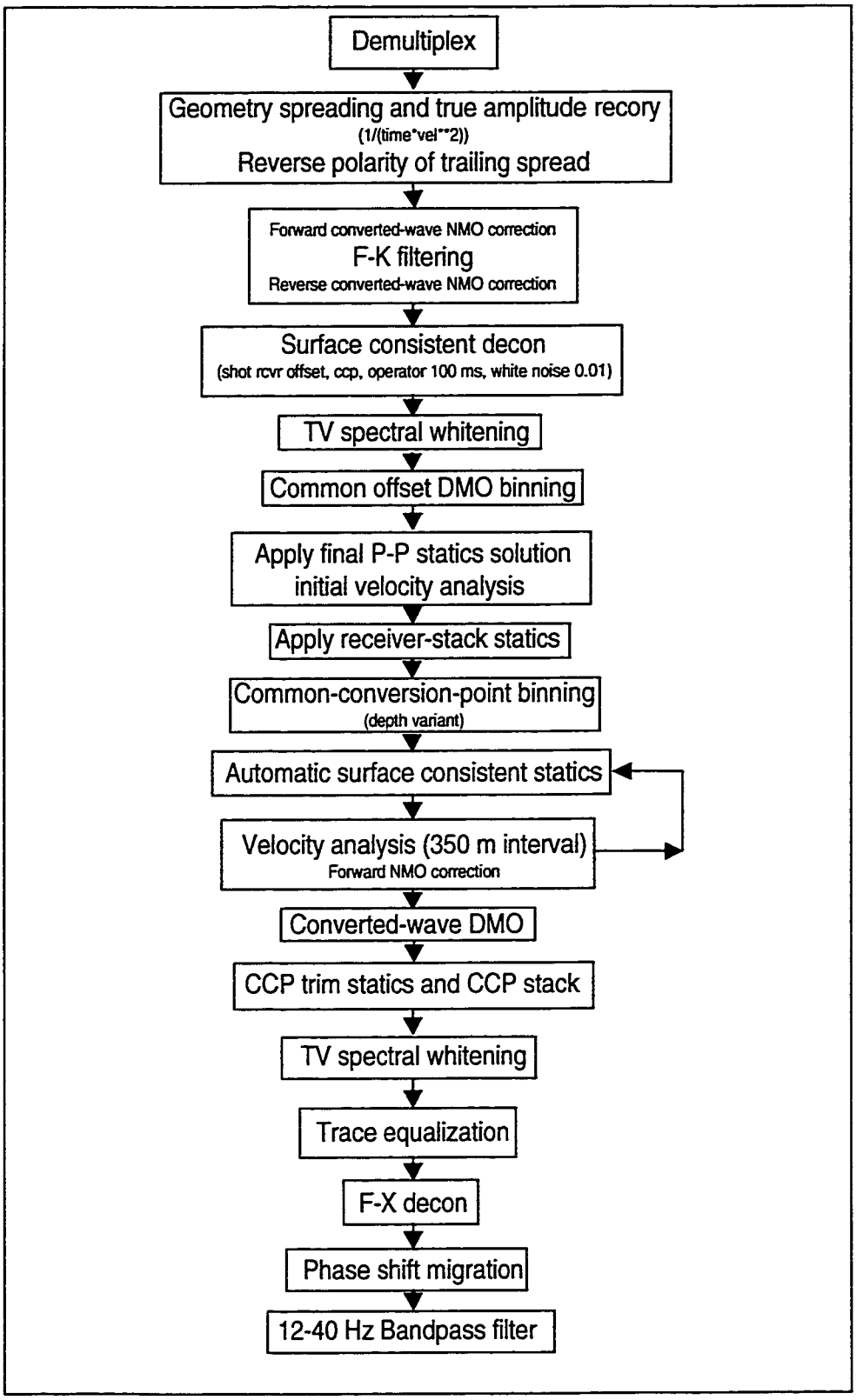

FIG. 2.21. Processing flowchart for the radial-component (P-SV) data.

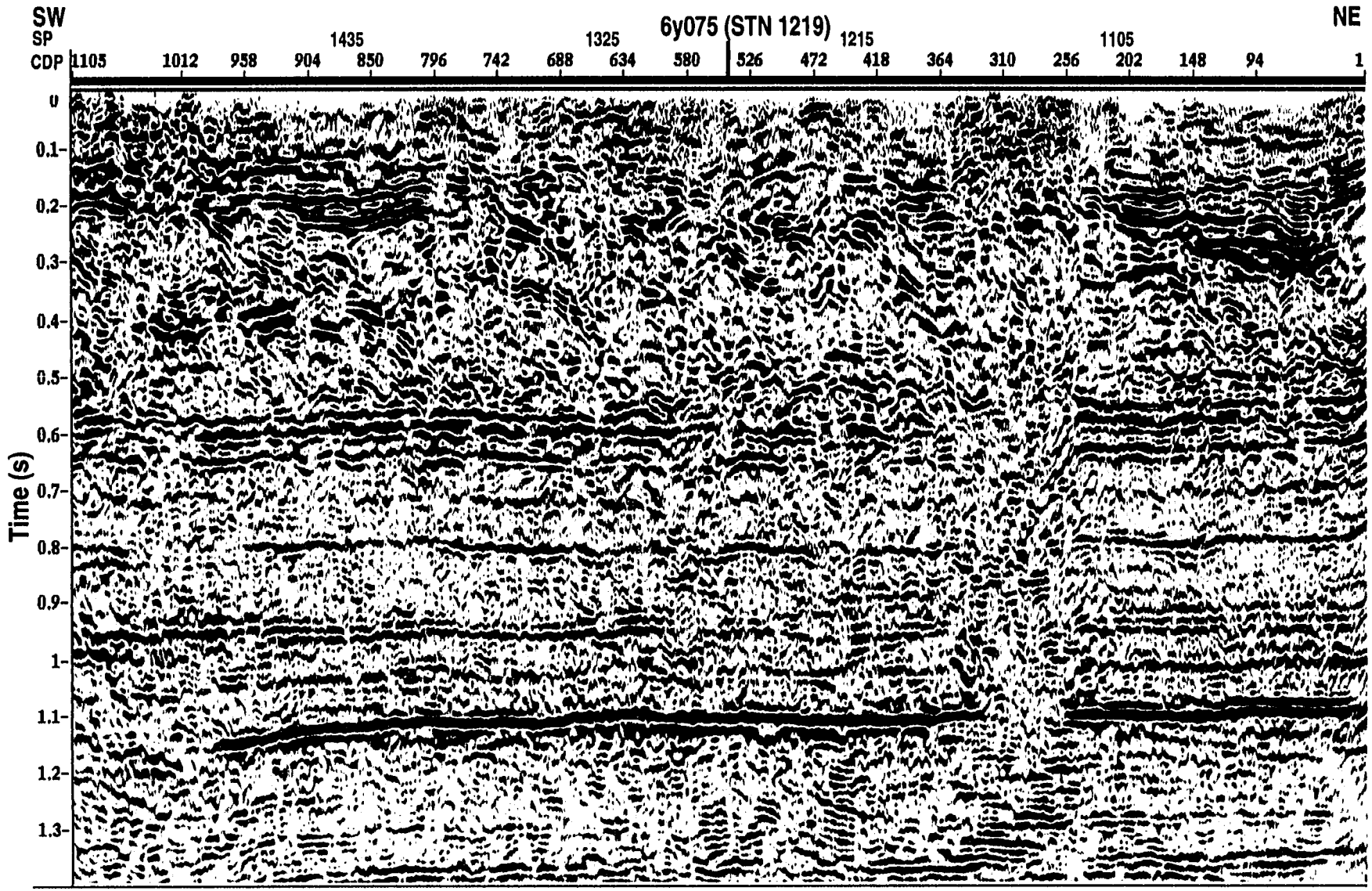

FIG. 2.22. Migrated section of radial component data for 6y074.

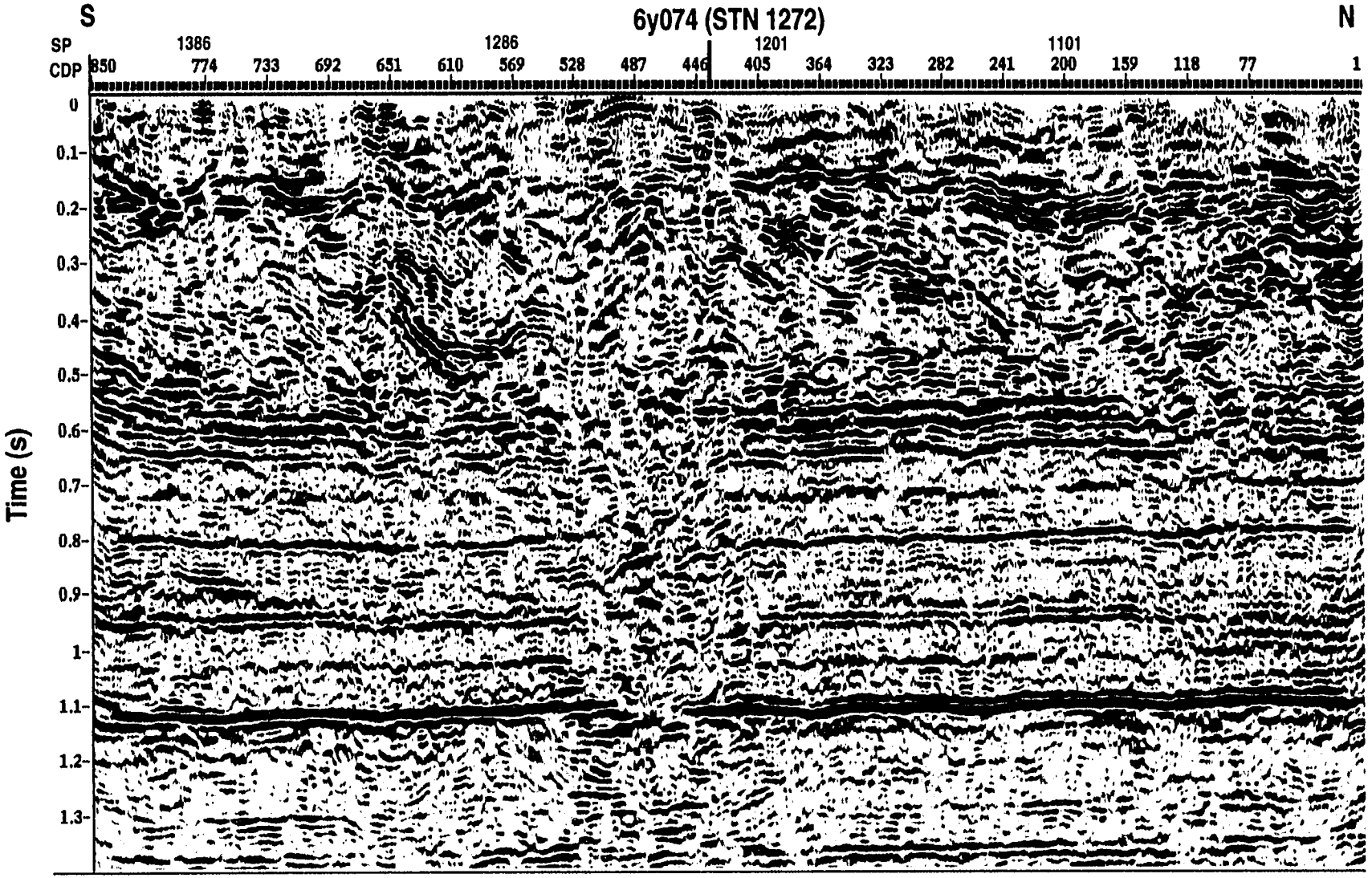

FIG. 2.23. Migrated section of radial component data for 6y075.

2.5.3 Joint *P-P* and *P-S* interpretation

The amplitude spectra of *P-P* and *P-S* wave data shows that the frequency bandwidth is much wider for *P-P* wave data than *P-S* wave data (see Figure 2.24). The frequency content of *P-P* wave is three times higher than *P-S* wave. However, the V_p/V_s of Grand Rapids to McMurray formations is about 2 (see Figure 2.13 for details); which indicates that the resolution of *P-S* wave data is lower than *P-P* wave data. At the reservoir level the P-wave velocity is about 2300 m/s, and S-wave velocity is about 1100 m/s. Assuming that the resolution is one quarter of seismic wavelength, with *P-P* wave frequency of 150 Hz and *P-S* wave frequency of 45 Hz the *P-P* wave resolution is about 4 m; while *P-S* wave resolution is about 6 m.

Sonic logs are available from 4 wells for line 6y074 and 5 wells for line 6y075 (see Figure 2.16 for details). The synthetic seismogram was made using a Butterworth wavelet with frequency bandwidth of 10-110 Hz. The ties of well synthetic to surface seismic are shown in Figure 2.25. Figure 2.25b indicates a better tie than Figure 2.25a as there are phase changes along the vertical axis. It is very common that a mistie is present between McMurray top and Devonian top. The Clearwater top is not a strong reflector and is usually manifested by a weak trough (see Figure 2.25). The sequence boundaries of C70 and C50 are characterized as in Figure 2.25 and can be tied to surface seismic data. Seismic interpretation was carried out using wells with sonic logs available as control points and integrating the thickness of each sequence at most well locations (see Figure 2.16 for reference of other wells). The final interpreted *P-P* wave sections are shown in Figures 2.26 and 2.27. With dense well control and high frequency content in seismic data sequence boundaries were interpreted with reasonable accuracy. In general, sequence C70 is mostly low energy muddy incised valley fills; but the upper part of C70 is saturated with good oil sands at well 1-20-65-3w4 (see Figure 2.30b). Sequence C50 is usually reservoir with good quality but it is very muddy to the east side of the section (compare Figure 2.30 a & b). Shown in Figure 2.27 is similar interpretation on 6y075.

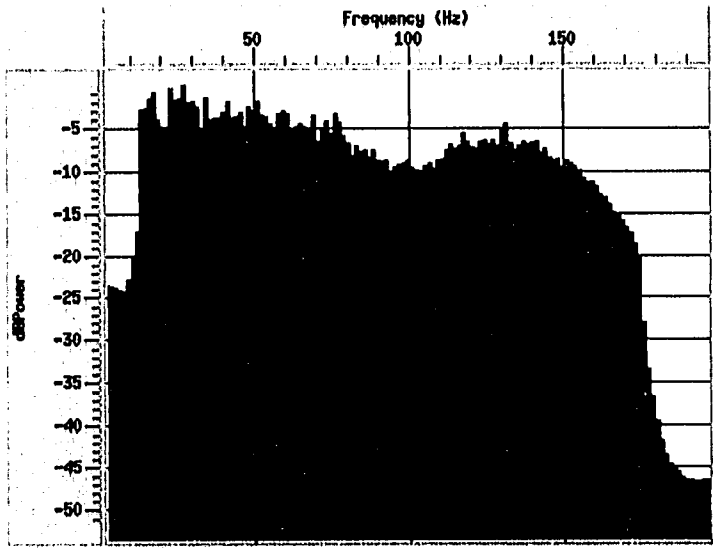

a) P-P wave of 6y074

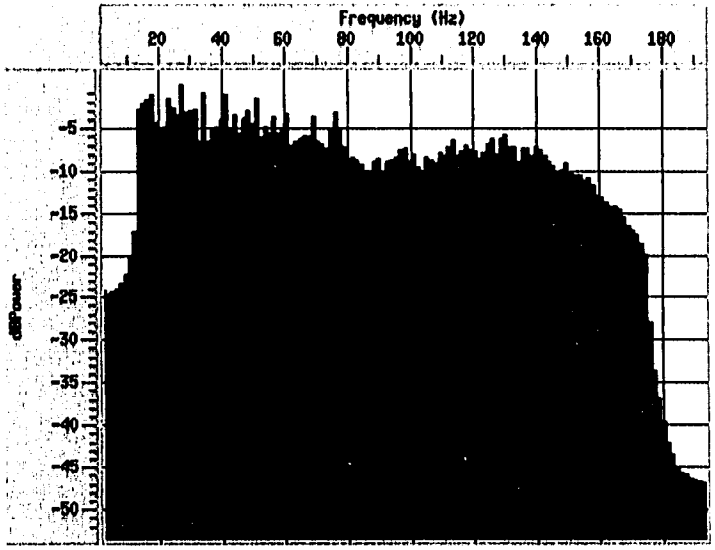

b) P-P wave of 6y075

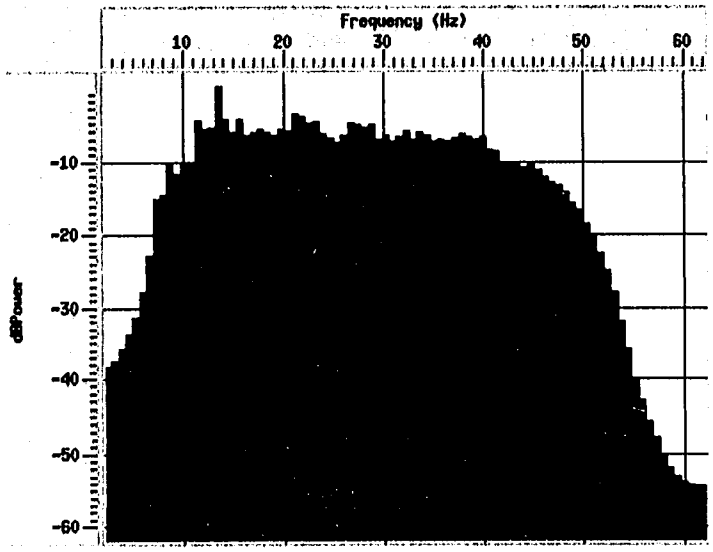

c) P-SV wave of 6y074

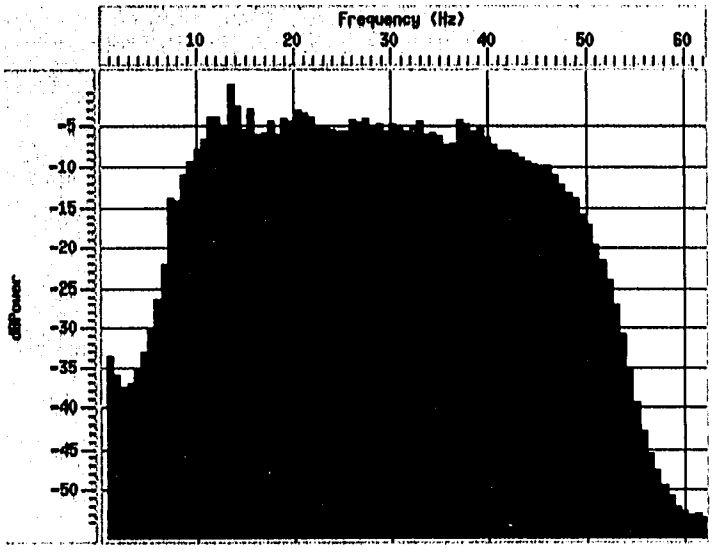

d) P-SV wave of 6y075

FIG. 2.24. Amplitude spectra of *P-P* and *P-SV* wave data.

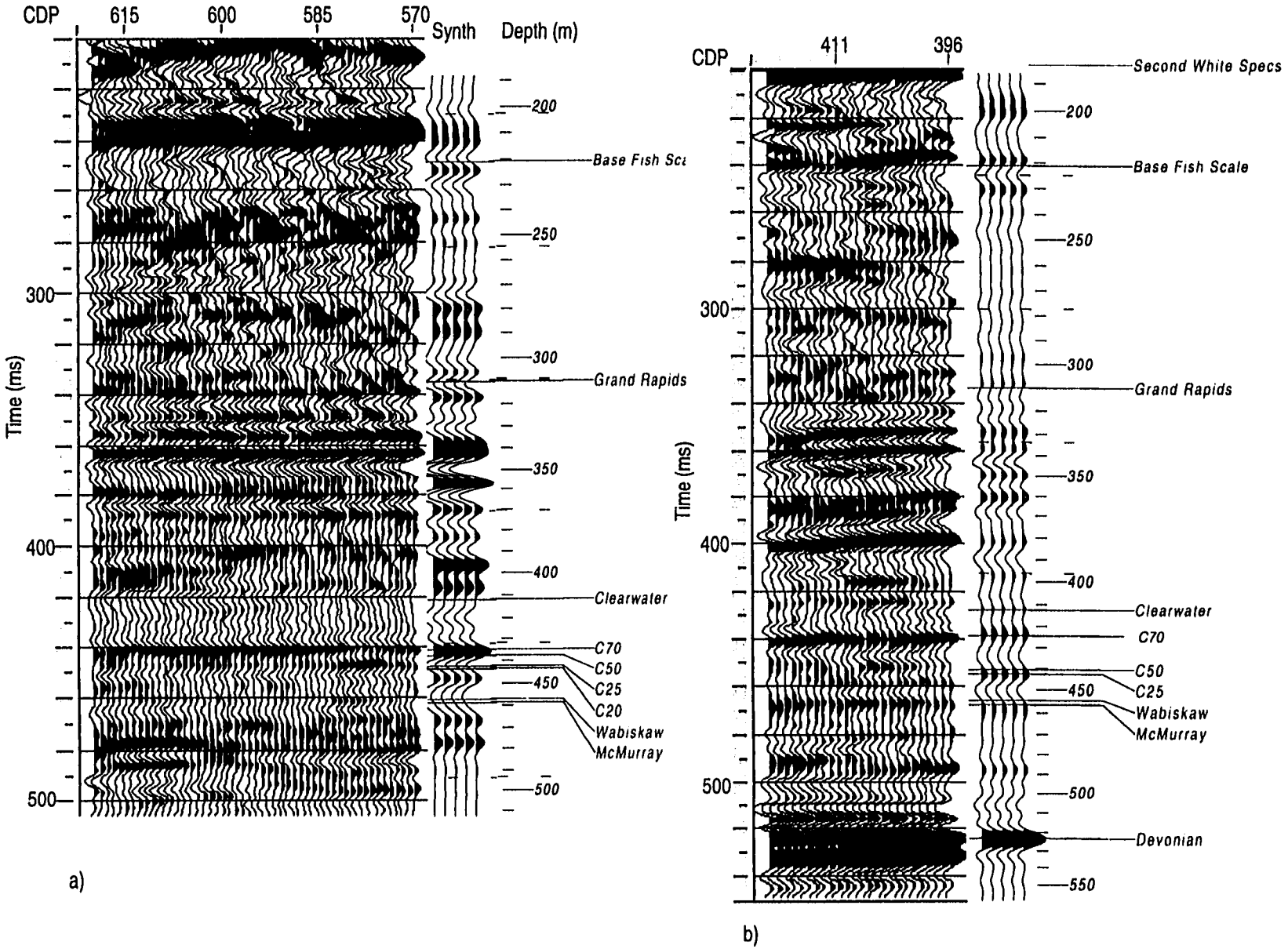

FIG. 2.25. Seismic to well synthetics tie for line 6y075: a) well 14-17-65-3w4, b) well 1-20-65-3w4.

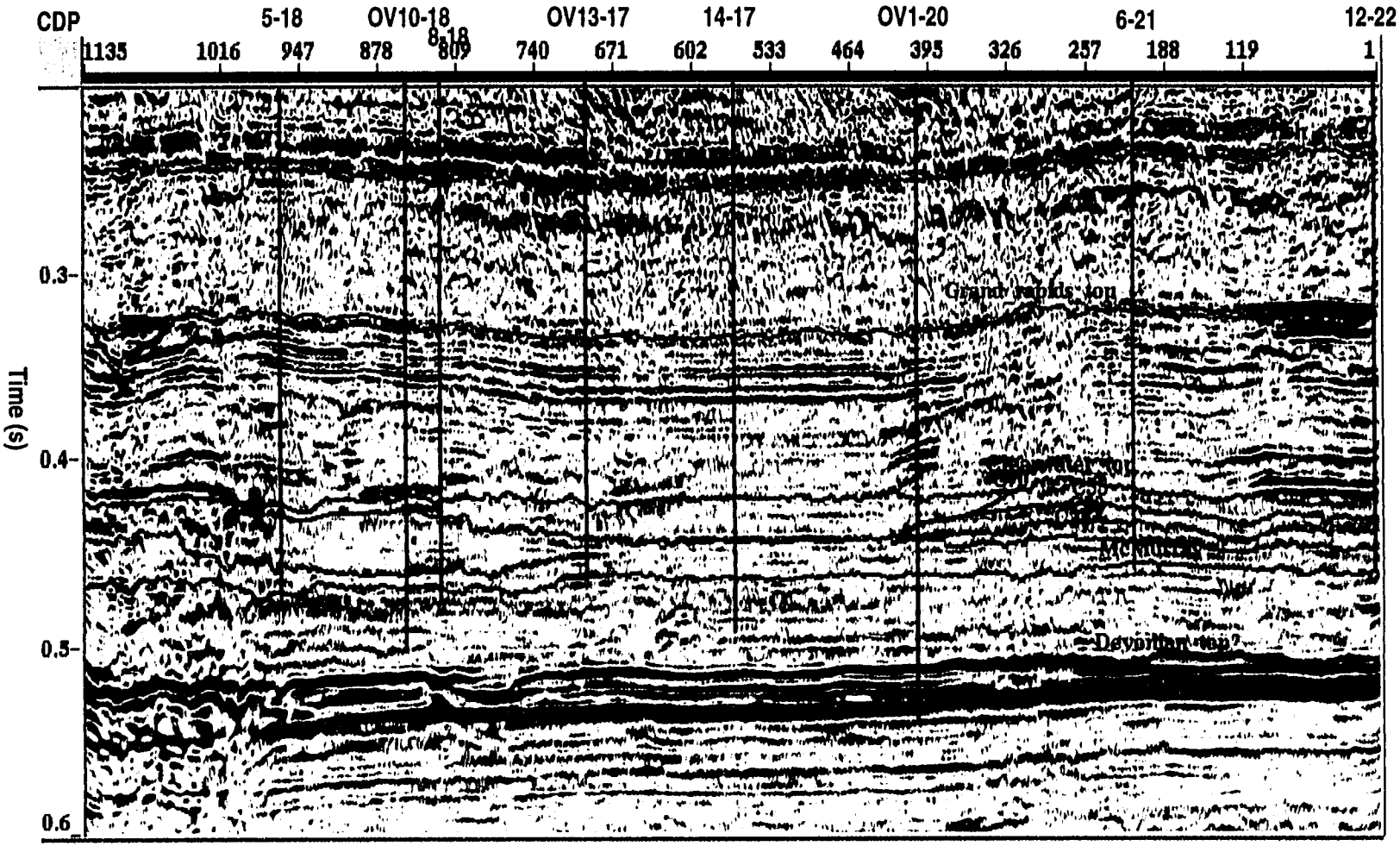

FIG. 2.26. Interpreted *P-P* wave section of line 6y074, sonic log available in wells colored with red.

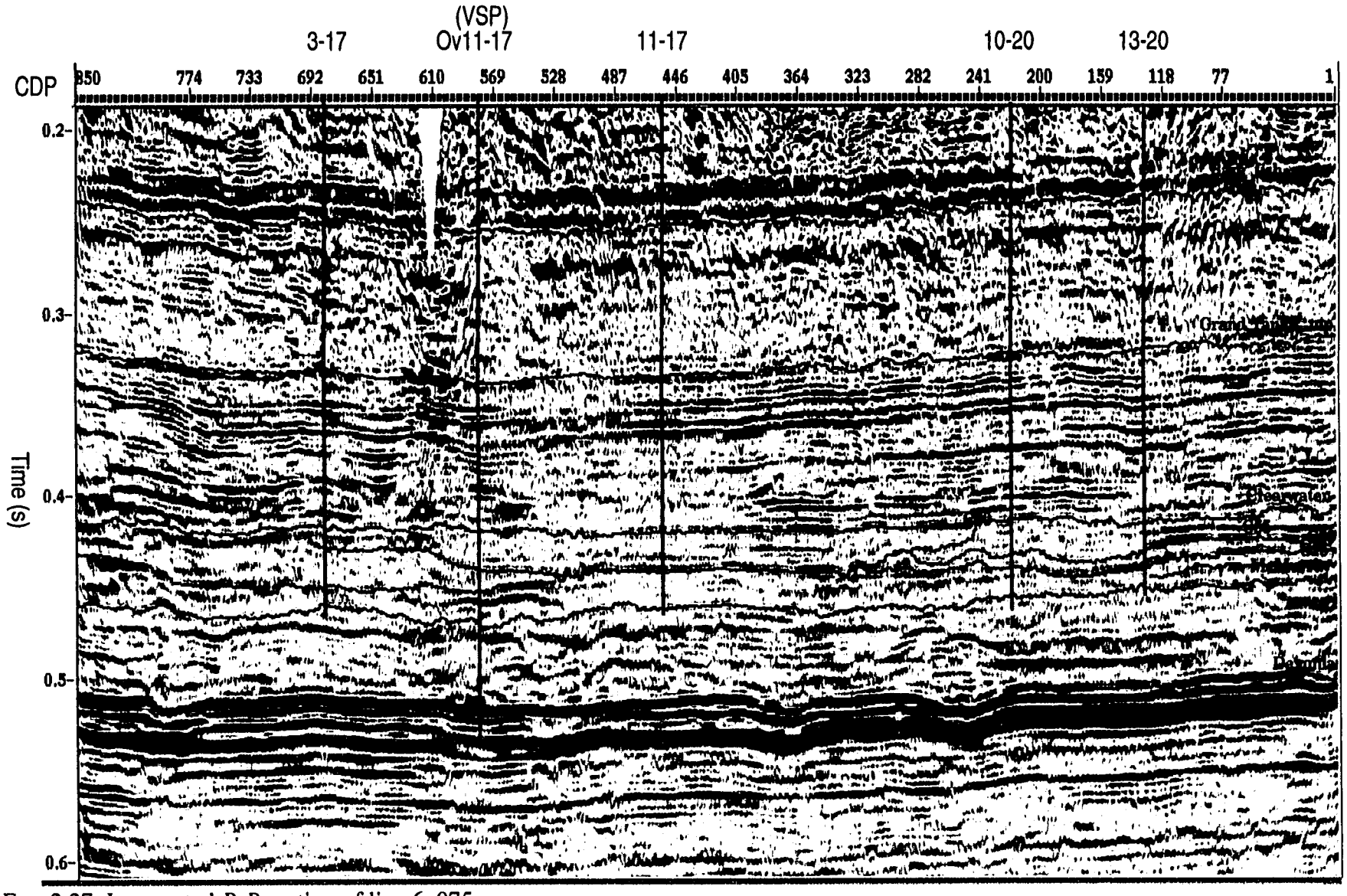

FIG. 2.27. Interpreted *P-P* section of line 6y075.

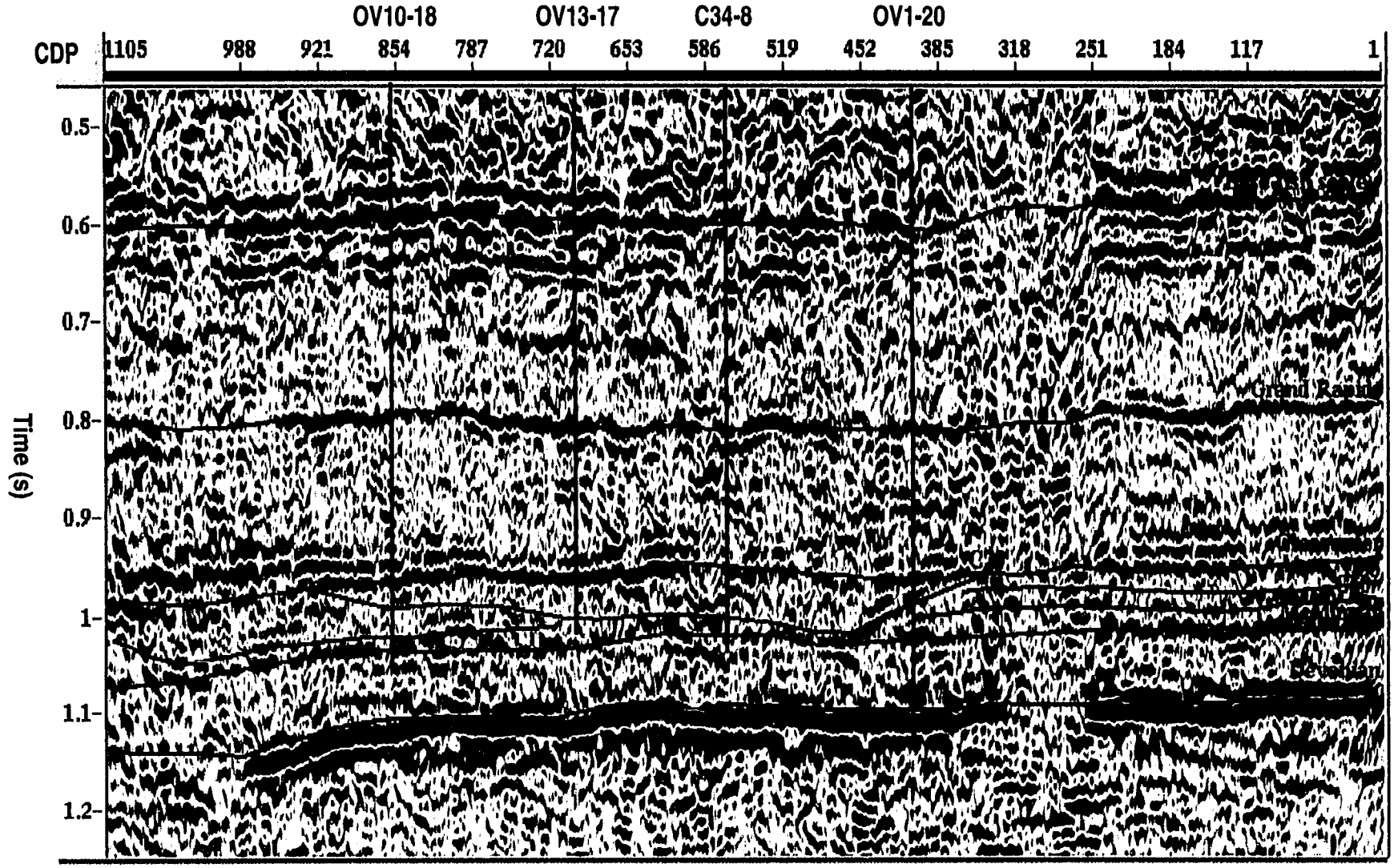

FIG. 2.28. Interpreted *P-S* section of line 6y074.

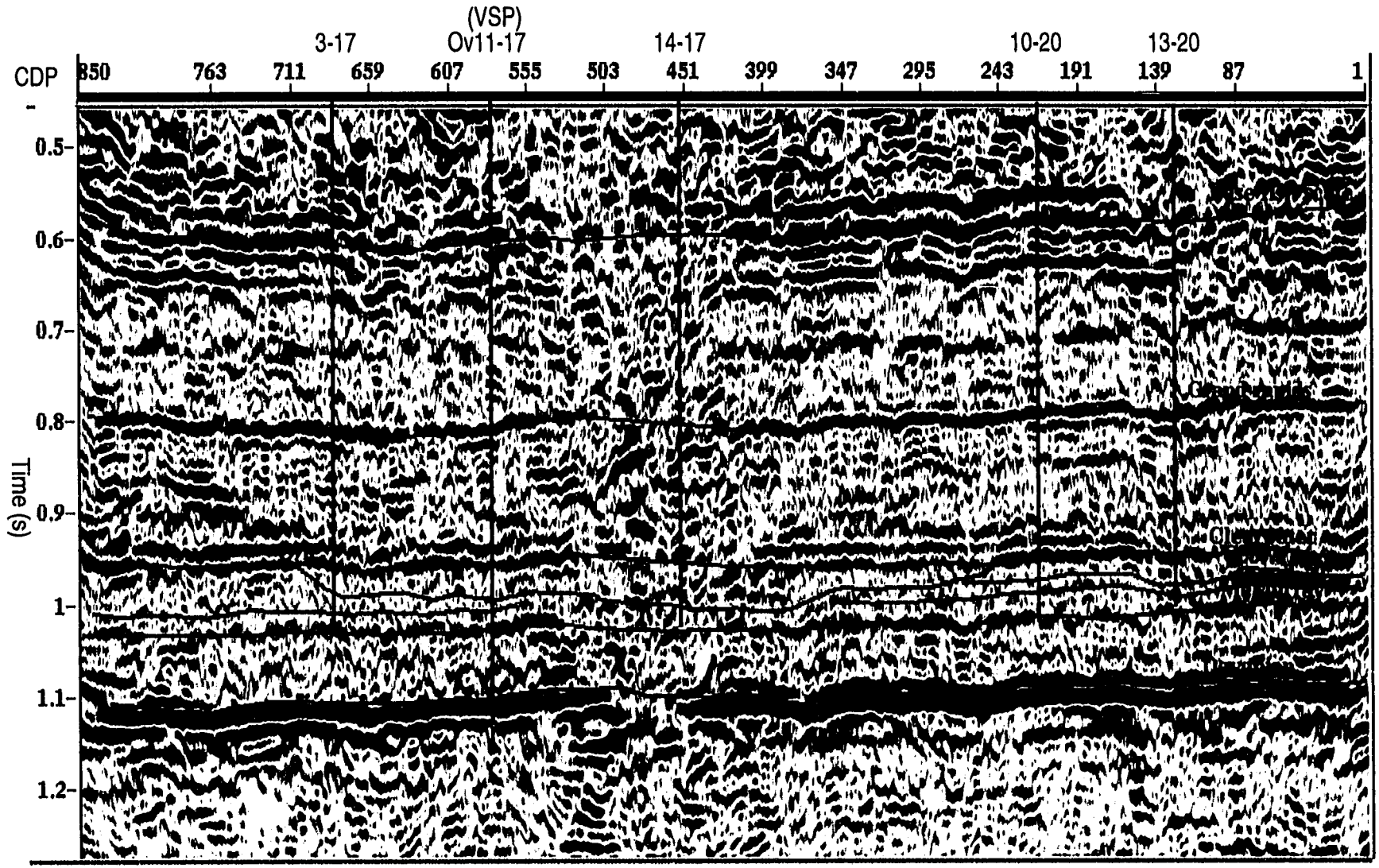

FIG. 2.29. Interpreted *P-S* section of line 6y075.

Converted-wave interpretation was carried out by integrating *P-P* and *P-S* sections with multi-component VSP that is to be discussed in the next section of this chapter.

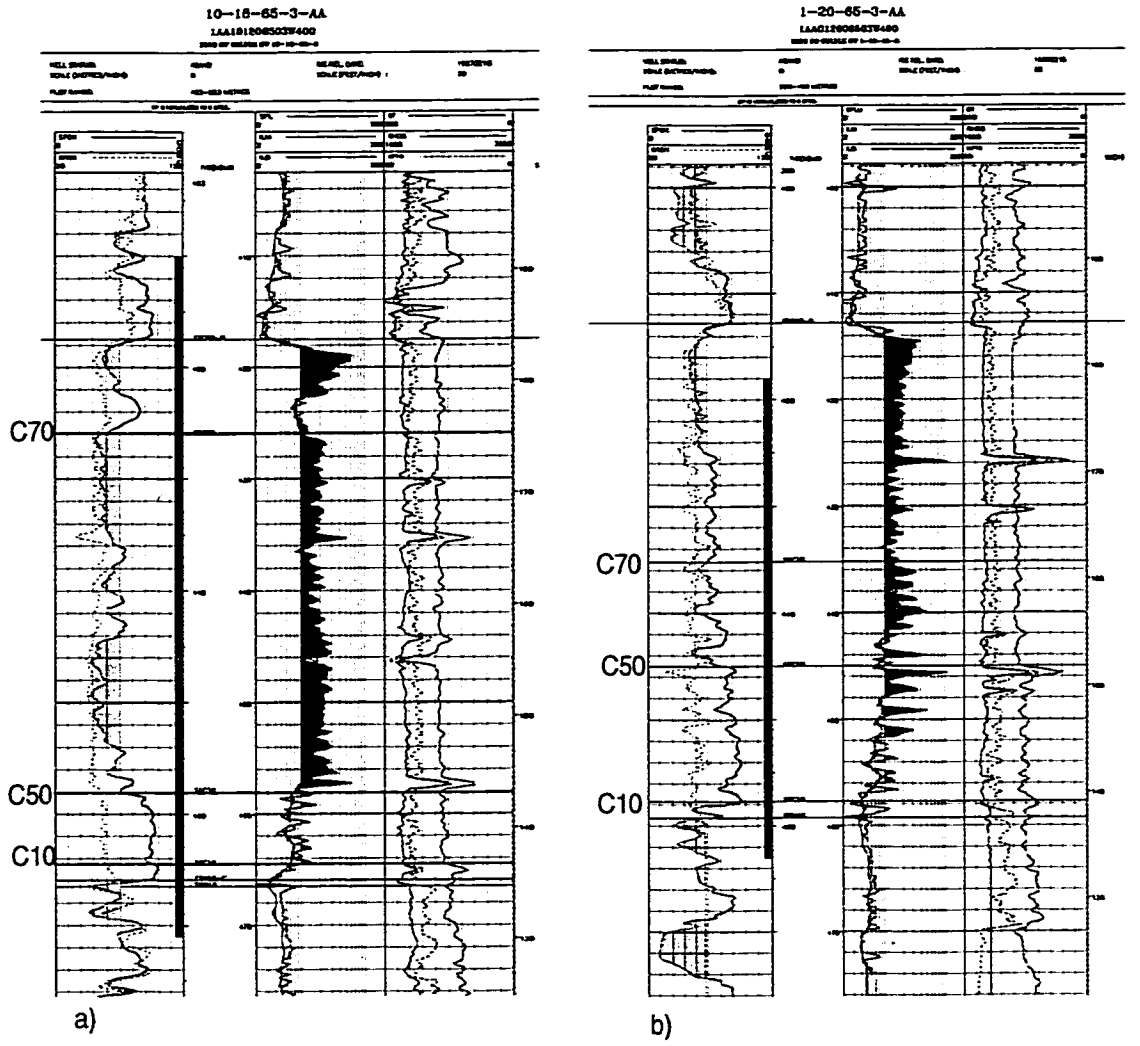

FIG. 2.30. The Clearwater sequences and reservoir quality: a) well 10-18 showing C50 good quality reservoir, b) well 1-20 showing C50 poor quality reservoir.

The most prominent feature on *P-S* wave data is that the top shale that covers the Clearwater reservoir is a strong coherent reflector as the shear impedance contrast is much higher across this interface. As discussed earlier, surface *P-S* wave resolution is lower than *P-P* wave due to near surface effects. Sequence boundaries on *P-S* data can not be seen as clearly as on *P-P* and VSP data (Figures 2.31 and 2.32). The C70 muddy

channel edge (see Figure 2.28 around well 1-20) is better defined on *P-S* wave than on *P-P* wave. Parasequence boundary C55 is traced along a small peak (red-white color). Sequence C50 is traced along the zero-crossing from black to red. Shown in Figure 2.29 is the similar interpretation for line 6y075.

2.6 Three-component near-offset and far-offset VSP studies

2.6.1 acquisition

Both near-offset and far-offset Vertical Seismic Profiles (VSP) were acquired in well OV11-17-65-3w4 on the south side of line 6y075 (see Figure 2.16). The VSP source was a high frequency vibrator (the vibrator was loaned to Schlumberger from Veritas). Both near-offset and far-offset VSP data were acquired by using 3-component geophones. An offset of 125 m was used for far-offset VSP as the target (reservoir) depth is only about 400 m. Table 2.3 shows the acquisition parameters for both near-offset and far-offset VSP.

Table 2.3. 3-C 2-D near- and far-offset VSP acquisition parameters.

Kelly Bushing (KB)	602.07 m
Seismic Reference (SRD)	602.07 m
Ground Level (GL)	597.72 m
Source Type	one Veritas M18 Buggy vibrator, 10-240 Hz sweep for 10 second
Source Offset	5 m for near-offset VSP 125 m for far-offset VSP
Source Azimuth	70 Deg from Magnetic North - near-offset 90 Deg from Magnetic North - far-offset
Receivers	Schlumberger 5-level 3-C geophones
receiver interval	5 m
acquisition software	Maxis
Date	02-Apr-97

2.6.2 Integrated interpretation

The near-offset VSP was processed to obtain a *P*-wave corridor stack or VET (VSP Extracted Trace). The frequency content of VET is up to 200 Hz, which has slightly

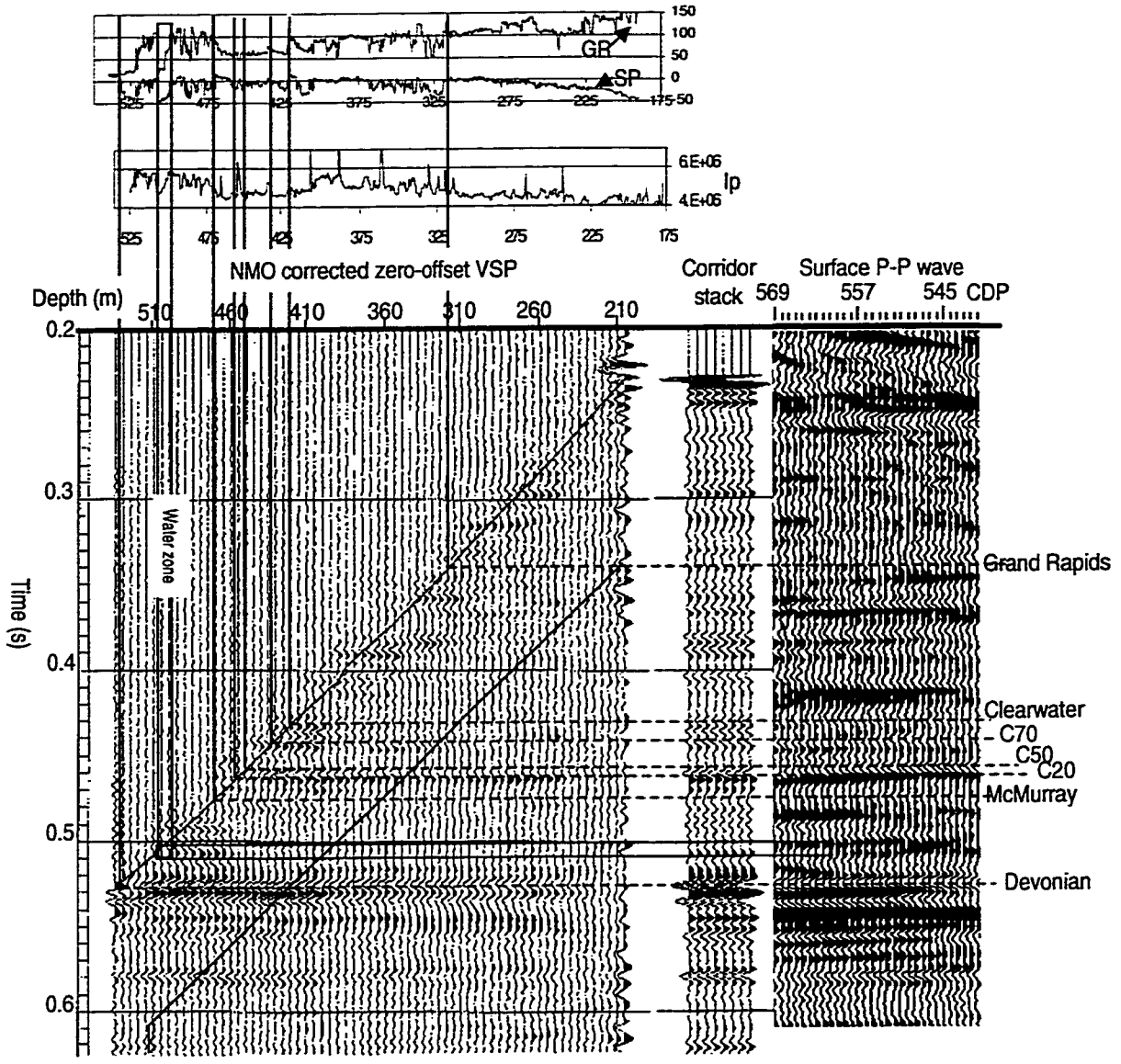

FIG. 2.31. Near-offset VSP "*L*" plot, Ip - impedance of *P*-wave.

higher resolution than surface seismic data. Figure 2.31 shows the *L* plot of near-offset VSP integrated with surface *P-P* wave data. The VET ties to surface seismic data very well. The sequence boundaries of Clearwater formation are tied from logs to seismic response via VSP. As discussed earlier, change of *P*-wave impedance at Clearwater top is small (see Figure 2.31), which indicates that Clearwater top is not a good reflector on *P*-wave data. Neither VSP nor surface *P*-wave data shows good reflection at the Clearwater top. The boundary between C70 and C50 sequences is featured with an impedance

increase which corresponds to a small white trough on both VSP and surface seismic data. There is a tight streak within sequence C20 that causes major reflection within Clearwater reservoir. The boundary between C50 and C20 can be defined as zero-crossing amplitude from positive to negative; while the boundary between C20 and C10 can be defined as zero-crossing amplitude from negative to positive. There is a significant overall impedance increase from Clearwater formation to McMurray formation. The lower McMurray water sand is also a good reflector, which is shown on both VSP and surface seismic data.

The converted shear-wave data (Figure 2.32) is illustrated by the *P-S* wave *L* plot of far-offset VSP integrated with surface converted shear-wave data. It is seen that the frequency content of VSP converted *S*-wave data is significantly higher than surface data. It has similar frequency content as the *P*-wave VSP data. As the V_p/V_s ratio is about 2 at the reservoir level, converted *S*-wave VSP data has twice the resolution of *P*-wave data, which brings the resolution to 2 m. Comparing the *P-S* synthetic seismogram to the VSP and surface seismic, misties are evident within the McMurray Formation. This is similar to all the *P*-wave data.

The *P-S* wave shows strong coherent reflections at the tops of Grand Rapids, Clearwater, and McMurray. This is because at these tops *S*-wave impedance contrast is higher than *P*-wave. Also, sequence boundaries are better defined as the resolution is higher. Sequence C70 boundary is defined as zero-crossing amplitude between small peak and a following trough (see Figure 2.32). Sequence boundaries C50 and C20 are defined as peaks (see Figure 2.32). McMurray top is defined as zero-crossing amplitude from positive to negative. The reflection of lower McMurray water zone has disappeared on *P-S* wave data because shear wave does not respond to the pore fluid.

To summarize the study, as illustrated shear-wave data enables the identification of reflections that compressional-wave does not reveal. The task of differentiating lithology and separating shale from sand is feasible with converted wave information. Also, integrating *P-P* and *P-S* wave data can help us identify fluid zone. However, the resolution of surface *P-S* wave data is not high enough to resolve the detail required due

to near surface absorption of the shear wave. Converted borehole shear wave data meets the requirement as VSP *P-S* wave data has even higher resolution than *P-P* wave data.

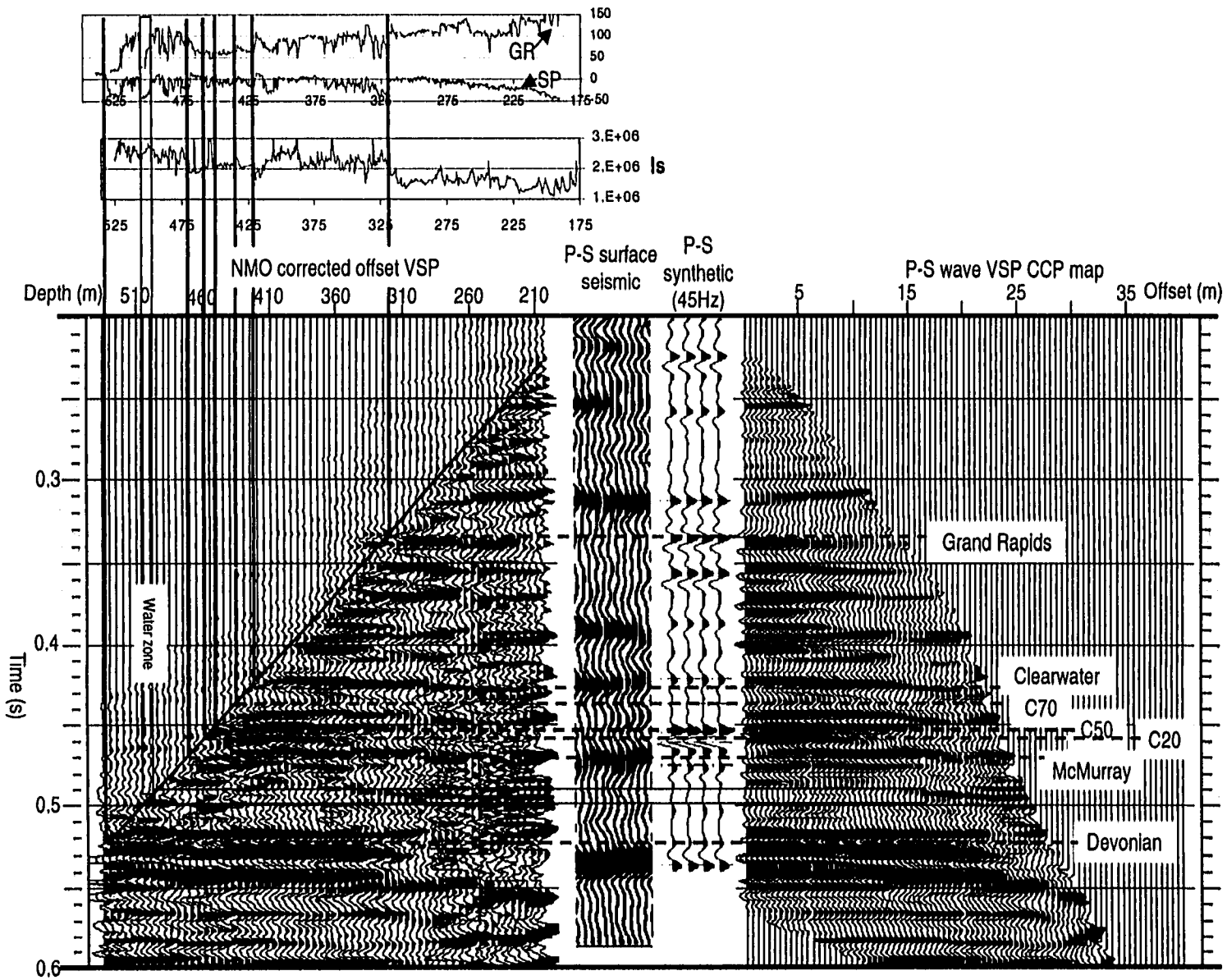

FIG. 2.32. Far-offset VSP converted-wave "*L*" plot, Is - impedance of *S*-wave.

2.7 Surface 3-D seismic acquisition and processing

2.7.1 Time-lapse 3-D seismic surveys

The research of seismic monitoring for Cold Lake production can be traced back to the late 1970's when 2-D seismic data were acquired. The initial 3-D experiments were carried out at EE pad and H pad in the mid 1980's. Both experiments were not successful due to many factors. The relationship between reservoir status and seismic survey timing was not well understood. The geophones were planted on surface instead of being buried, therefore, the frequency content was much lower. Also the group spacing was too large. In April 1990 a wide variety of seismic experiments were conducted at D3 pad (red in

Table 2.4. Time-lapse seismic surveys of Cold Lake Production Project.

Survey Pads	Time Lapse Order	Survey Date	CSS Cycle & phase	Survey Purpose
D3	1	April, 1990	6th Production	Early pilot study for time-lapse seismic monitoring, successful, seismic was surveyed in right reservoir pressure window.
D3	2	January, 1992	8th Injection	Early pilot study for time-lapse seismic monitoring, purpose was to see steam conformance during injection phase, used as a reference of earlier successful survey.
AA	1	March, 1991	8th Production	Early experiment for time-lapse seismic monitoring, results were inaccurate due to low pressure
AABBW	2	November, 1993	9th Injection	Compare steam conformance between regular pad (AA) and pads (BBW) with infill wells, due to pressure too high.
AABBWC21	3	April, 1994	10th Production	Compare steam conformance between regular pad (AA) and pads (BBW) with infill wells, a non-steam pad (C21) included, understanding of right pressure window for seismic became mature.
B2456	1	April, June, 1995	10th Production	Determine injector-only-infill (IOI) well locations. The survey was split into two different times due to unbalanced reservoir pressure in the region.
B2456	2	December, 1997	11th Production	IOI well steam performance evaluation
A2A4	1	August, 1996	10th Production	Place horizontal-injector-producer (HIP) wells
J1J8	1	January, 1997	8th Production	Reconfigured CSS wells
BBW	1	December, 1996	1st Injection	Horizontal injector base line survey
BBW	2	February, 1998	1st Production	Horizontal injector steam performance evaluation
D36 (Leming Lake)	1	March, 1997	0	Base line survey for horizontal CSS wells
D36 (Leming Lake)	2	February, 1998	1st Production	First cycle steam evaluation for horizontal CSS
D36 (Leming Lake)	3	February, 1999	2nd Production	Second cycle steam evaluation for horizontal CSS

color) during the 6th CSS production cycle - surface 3-D, cross-well tomography, and 3-D reverse vertical seismic profiling (RVSP). It was found that in steam injected reservoir the seismic data are disturbed with amplitude increase and frequency drop (seismic attenuation). Then a repeated surface 3-D survey was conducted in the same area in January 1992 during the 8th CSS cycle steam injection phase. The purpose of 1992 survey was to see steam distribution during injection phase and compare to earlier survey. The results turned out to be a good reference for the earlier survey. Further experiments were conducted at AABBW pads survey area (see Table 2.4). After three time-lapse surveys in this area combining with previous work at D3 pad a complete understanding of best reservoir pressure window (2-3 MPa) for the seismic survey was obtained. The 1992 survey at D3 pad was then treated as a psuedo-baseline reference for the 1990 survey. The learnings of D3 pad study were published by Eastwood et al (1994) and Isaac (1996). Since then 3-D seismic data have been widely used at Cold Lake for monitoring the thermal recovery of bitumen. Numerous seismic surveys have been acquired (see Figure 2.1 and Table 2.4). The areas outlined in green color and red in Figure 2.1 show the pads with the 3-D seismic survey conducted.

2.7.2 Acquisition

The seismic data acquisition is featured with geophones are buried to a depth of 10 m or deeper to improve the frequency bandwidth, experimental repeatability, seasonal vibration (winter vs summer), and to reduce surface noise, therefore one phone per station is used. The dynamite sources (from 0.1kg to 1.5kg) are also buried around 10 m below surface. The field layout can be divided into two groups. The first group has configuration of receiver interval of 16 m with receiver line separation of 96 m. and the source interval is also 16 m with source line separation of 128 m. This acquisition geometry provides grid bin size of 8-by-8 meters. The early seismic surveys such as D3 AABBW and BBW were acquired using this configuration. The second group of geometry layout is the improved one in terms of cost (25% cheaper). Both source and receiver intervals are 20 m, and both source and receiver line spacing are 120 m. Surveys conducted after 1994 were acquired using this new layout. This new acquisition configuration provides a grid

bin size of 10 m. Both of them provide an average fold of 20 at the target level. Detailed acquisition parameters for all surveyed pads are listed in Table 2.5.

With these acquisition parameters high quality (high signal-to-noise ratio, high frequency

Table 2.5. Seismic acquisition parameters for Cold Lake 3-D surveys.

Recorded by	Western Geophysical Co.
	D3 (1990)
	Sonics Exploration Ltd.
	D3 (1992)
	Veritas Geophysical Ltd.
	AABBW (1991, 1993, 1994), B2456 (1995, 1997)
	BBW (1996, 1998), A2A4 (1996), J1J8 (1997)
	D36 (1997, 1998, 1999)
Amplifier	I/O system II (B2456, A2A4, BBW, D36), Sercel 368 (D3, 1990)
	I/O system I (D3, 1992)
	SEG-D format, FP gain
	B2456: 3(12) - 413(293) Hz(db/oct), Notch OUT
	D3(1990): OUT - 356(70) Hz(db/oct), Notch OUT
	D3(1992): 3(12) - 360(75) Hz(db/oct), Notch OUT
	BBW(1996): 3(12) - 270(188) Hz(db/oct), Notch OUT
	A2A4(1996): 3(12) - 413(293) Hz(db/oct), Notch OUT
	D36(1997, 1998): 3(12) - 413(293) Hz(db/oct), Notch OUT
	D36(1999): 3(12) - 270(188) Hz(db/oct), Notch OUT
Record Length	3.0 seconds
	1 ms sample rate
Source	Dynamite, 1 hole per shotpoint (shot depth 10 m)
	charge size: 0.15 kg for B2456, D36, BBW(1998), J1J8
	0.1 kg for D3 (shot depth at 18 meters)
	0.125 kg for BBW(1996), A2A4
Geophones	1 phone per station buried at 10 m depth
	OYO 30 CT, 10 Hz - B2456, J1J8
	Sensor SM-4, 10 Hz - BBW, A2A4, D36, AABBW
	Marsh phones, 10 Hz - D3
Source interval	20 meters - B2456, J1J8, A2A4, D36
	16 meters - BBW, D3, AABBW
source line separation	120 meters - B2456, J1J8, A2A4, D36
	128 meters - BBW, D3, AABBW
group interval	20 meters - B2456, J1J8, A2A4, D36
	16 meters - BBW, D3, AABBW
receiver line separation	120 meters - B2456, J1J8, A2A4, D36
	96 meters - D3, BBW, AABBW
Grid Bin size	10 x 10 meters - B2456, A2A4, J1J8, D36
	8 x 8 meters - D3, BBW, AABBW

content) data were acquired. All the data have broad frequency bandwidth of 10 to 250 Hz or higher. The dominant frequency is around 100 to 130 Hz. Weather and seasonal changes have minimum impact on seismic data quality with the exception of water covered lakes where the best acquisition time is winter. The buried geophones are sometimes lost due to leads missing on swampy muskeg as some animals such as muskrats destroy the leads.

2.7.3 Processing and quality control

Processing of Cold Lake *P-P* wave data can be challenging due to low impedance contrast among most of clastic interfaces above Devonian. Also, as the reservoir is relatively shallow high fold is very expensive to achieve, most 3-D data is around 20 fold at the reservoir level. To find the best processing routine one dataset was processed by four processors. Each processor carried out extensive tests in their processing sequence to reach the final results. The four processing sequences are listed in Table 2.6. In general, they are similar. They all follow the flow of geometry installation, deconvolution, statics and velocity analysis, cdp stack, and migration. However, in detail, each one is somewhat different. Figure 2.33 shows one of the inline (27) sections of the survey from four processors. As it is seen the processing results can be very different. The quality of the processing changes dramatically (compare a and b with c and d in Figure 2.33). The results from processor A and B are similar (Figure 2.33a and b) except that the frequency content of B is higher than A; also, the Devonian structure (green horizon) is slightly different due to different statics solution. The structure presented by B follows the well data mapped geological trend better. Comparing two processing sequences, processor B used 4-component surface consistent deconvolution instead of 3-component surface consistent deconvolution used by A. The key reason for broader bandwidth from processor B is probably due to wider band TV spectral whitening (2/8-200/220 Hz). The denser velocity analysis performed by processor B resulted in better statics solution than processor A. A special routine called 'shallow data scaling' was performed in the processing which is quite suitable for Cold Lake Clearwater reservoir.

Table 2.6. 3-D seismic data processing sequences.

Processor A	Processor B	Processor C	Processor D
Demultiplex	Demultiplex	Demultiplex	Demultiplex
Trace edits	Trace edits	Trace edits	Trace edits
geometry installation cdp bin size: 10 x 10 m	geometry installation cdp bin size: 10 x 10 m	geometry installation cdp bin size: 10 x 10 m	geometry installation cdp bin size: 10 x 10 m
Amplitude recovery method: spherical divergence additional gain: 3 dB/second	True amplitude recovery 1/(time*vel^2)	True amplitude recovery Exponential gain	True amplitude recovery Decibel decay function from decay analysis of raw data
3-C surface consistent decon component: shot, rcvr, offset used: shot, rcvr operator length: 80 ms, prewhitening 0.01%	4-C surface consistent decon component: shot, rcvr, offset, cdp used: shot, rcvr, cdp operator length: 80 ms, prewhitening 0.1%	2-C surface consistent decon component: shot, rcvr used: shot, rcvr operator length: 60 ms, prewhitening 0.1%	4-C surface consistent decon component: shot, rcvr, offset, cdp amplitude prewhitening 0.1% phase spectr prewhitening: 0.01%
TV spectral whitening Scalar length: 300 ms Frequency panels: 12 Frequency: 2-8-140-160	TV spectral whitening Scalar length: 400 ms Frequency panels: 19 Frequency: 2-8-200-220	scaling	
elevation statics datum: 600 m replacement vel: 1800/s	elevation & refraction statics datum: 600 m replacement vel: 1800/s	elevation & refraction statics datum: 600 m replacement vel: 1800/s	elevation & refraction statics datum: 600 m replacement vel: 1800/s
	shallow data scaling		
Preliminary Velocity analysis NMO correction	Preliminary velocity analysis NMO correction	Preliminary velocity analysis NMO correction	Preliminary velocity analysis NMO correction
surface consistent statics	surface consistent statics	surface consistent statics	surface consistent statics
Final velocity analysis final NMO correction	Final velocity analysis Super bin: 5 x 5 cdps Spacing: 250 m on both directions final NMO correction	Final velocity analysis final NMO correction	Final velocity analysis Super bin: 10 x 10 cdps Spacing: 500 m on both directions final NMO correction
			Spectral balance Zerophase, frequency domain Gate: offset: 1 m: 150-1100 ms 861 m: 400-1100 ms
			Prewhitening Bandwidth: 4/8-200/250
Mute	Mute	Mute	Mute
	Time-variant scaling Base for scaling: mean Base for application: centre		
CDP trim statics	CDP trim statics	CDP trim statics	CDP trim statics
CDP stack	CDP stack	CDP stack	CDP stack
	TV spectral whitening trace equalization		
f-xy noise reduction	f-xy decon	f-xy noise reduction	
Phase shift 3-D migration	Phase shift 3-D migration	Migration (one pass omega-x finite difference)	migration
bandpass filter	zero-phase bandpass filter (6/10-160/180)	zero-phase bandpass filter (10/14-130/150)	zero-phase bandpass filter (4/8-200/250)
	Trace equalization	trace equalization	Scaling

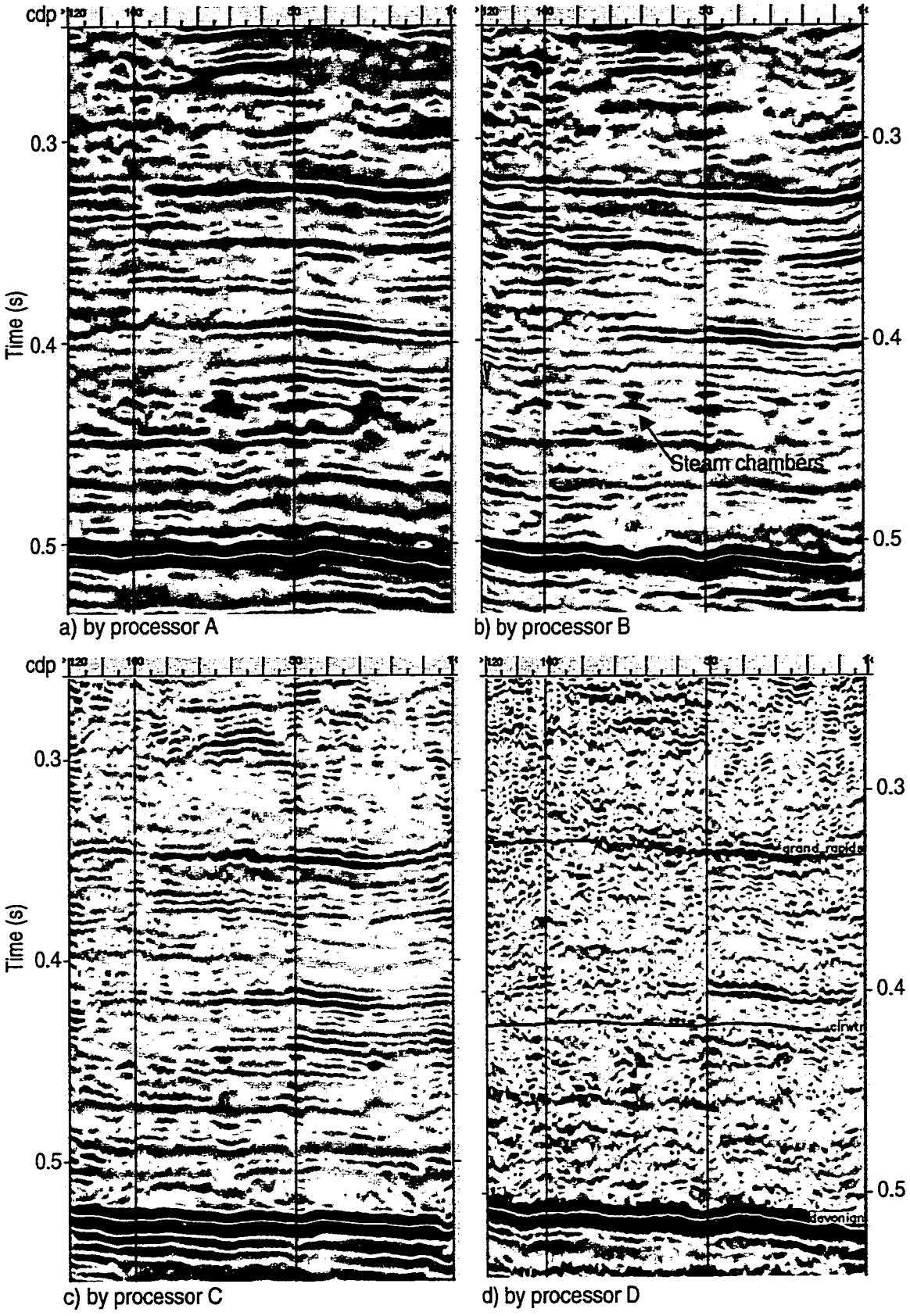

FIG. 2.33. Processed sections of inline 27 of A2A4 survey by different processors.

The output from processor C is relatively lower quality (Figure 2.33c). First, the data was not scaled properly. Due to either improper amplitude recovery or too short of an AGC window applied the amplitude character in shallow Colorado shale are lost (0.3 s on Figure 2.33a, compare a, b with c). Secondly, no TV spectral whitening was applied to the data, the frequency bandwidth is not as broad as result from processor B. Giving the same datum and replacement velocity Figure 2.33c presented a significant statics shift, which is unusual. Finally, Two-component surface consistent deconvolution was performed instead of four-component.

Figure 2.33d shows the worst processing. Reflectors are barely seen except Devonian top, an interface with strong impedance change between clastic and carbonate rocks. All factors such as poor velocity analysis, poor statics solution, and no TV spectral whitening were contributing to this final output. Regardless of the processing quality which varies dramatically, steam chambers can be seen on all the sections.

Shown in Figure 2.34 are the correspondent zero-phase wavelets estimated from three sections in Figure 2.33. It is clear that wavelet in Figure 2.34b is the best one as the side

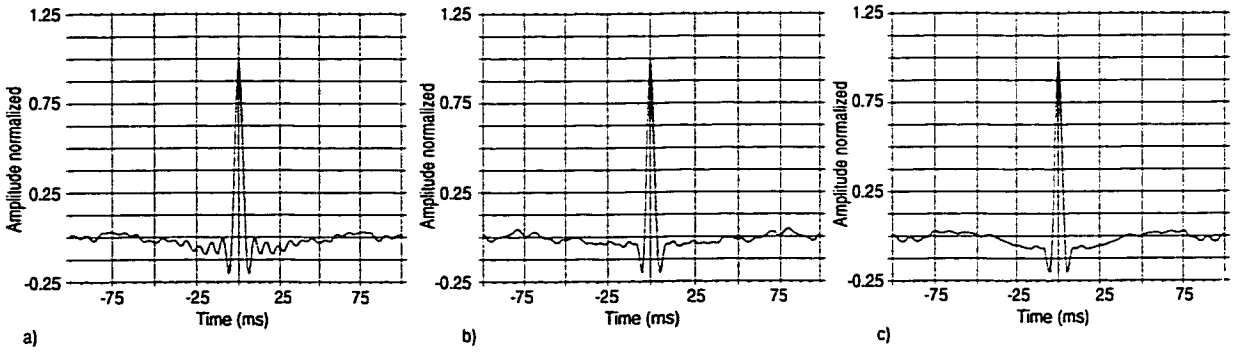

FIG. 2.34. Zero-phase wavelets extracted from sections a, b, and c in Figure 2.33.

lobes are minimized.

Reservoir monitoring and characterization are the ultimate goals of these seismic surveys. A better processing should enable us better tie seismic data to well data. Using principal

component attribute, (see Chapter 5 for details) discriminant analyses (see Chapter 4 for details) were carried out on each of the four processed volumes for steam conformance.

Table 2.7. Seismic-to-well tie statistics by different processing sequences.

Reservoir class	Processing sequence A	Processing sequence B	Processing sequence C	Processing sequence D
hot	93%	95%	94%	89%
cold	86%	90%	90%	84%

There were about 80 wells (46 hot wells) used in the statistics calibration process. The statistics of seismic-to-well tie is listed in Table 2.7. The number indicates that after classification with well calibration the percentage of seismic observations at well locations which were classified into the right class.

Processing is the very important first step for successful and accurate reservoir monitoring and characterization. This analysis which include signal-to-noise, frequency bandwidth, geological structure, pulse (wavelet) estimation, and well calibration support that processing sequence B is the best.

2.8 Field 3-D reverse VSP

The D3 pad seismic program includes surface 3-D seismic, borehole crosswell tomography, and 3-D reverse VSP. In Figure 2.35, surface 3-D seismic array is denoted by green lines. Receiver lines are oriented southeast-northwest direction, while source lines are oriented northeast-southwest direction. Six vertical observation wells were used for both crosswell tomography and 3-D reverse VSP surveys. 3-D reverse VSP survey was conducted (April 2-3, 1990) by utilizing one of crosswell tomography source wells (D3-OB4, see red solid cycle in Figure 2.35) and surface receiver array (southeast-northwest oriented receiver lines). Black solid lines are well traces of CSS (Cyclic Steam Stimulation) wells; and solid green dots are bottom hole locations. Six vertical observation wells surrounding D3-8 were drilled for crosswell tomography, and they are denoted by red cycles. The 3-D reverse VSP was recorded by utilizing surface geophones and source well D3-OB4. The acquisition parameters are listed as follow (Table 2.8).

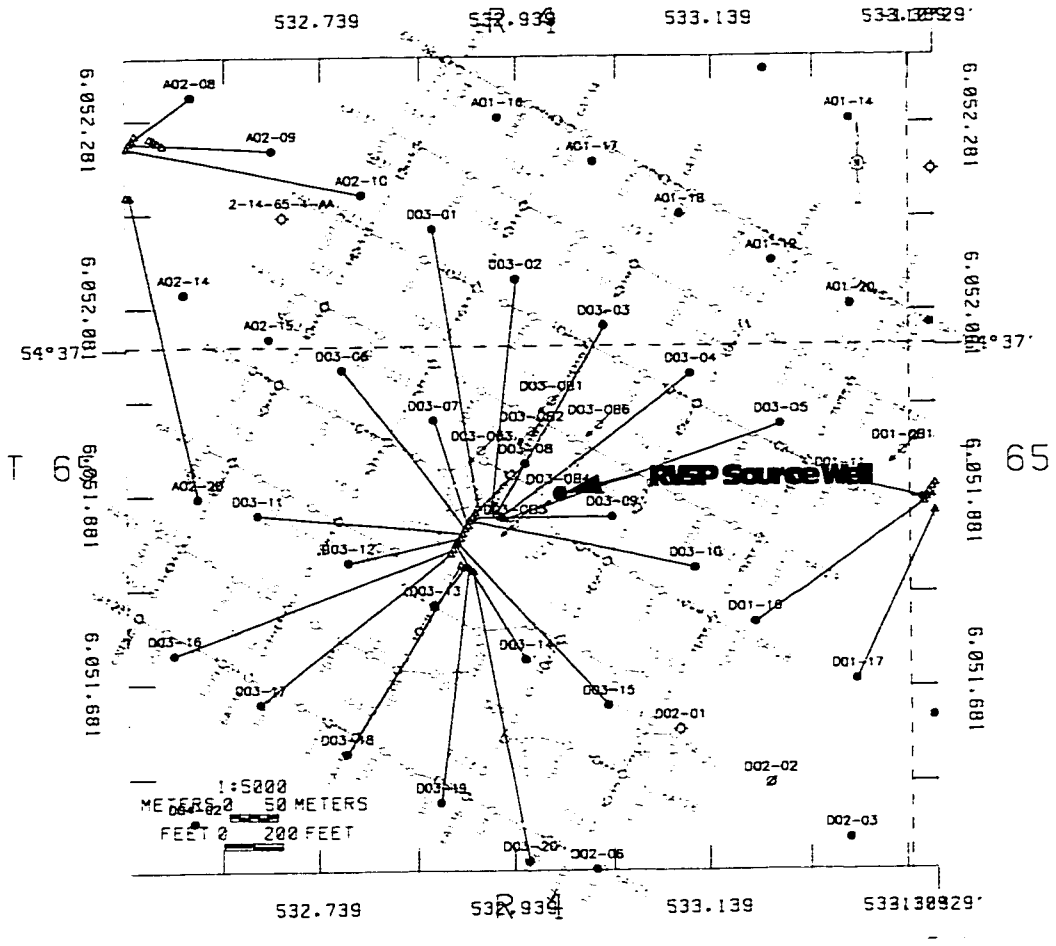

FIG. 2.35. Cold Lake D3 pad 3-D seismic layout and borehole seismic observation wells showing RVSP source well location and surface receiver lines (southeast-northwest).

The charge size of 20 grams was enough for cross-well survey but was small for VSP (the receivers were located near surface). Shown in Figure 2.36a is a common receiver gather of channel 4. Due to the weak source energy the raw record has poor signal-to-noise ratio. Also, low frequency noise is present in the data due to the operation of distant oil pump jacks. The background noise can be removed using f-x deconvolution. Figure 2.36b shows the same gather with true amplitude recovery and f-x deconvolution applied. It appears that there is a significantly amount (about 15% for *P*-wave) anisotropy around Colorado shale at shot depth of approximate 200 m. It takes longer time for direct *P*-wave to travel from shallow source location to the same receiver than deeper source location.

Table 2.8. D3 pad 3-D reverse VSP acquisition parameters.

Surface receiver interval	16 m
Surface receiver line separation	96 m
Geophone make	Sensor, SM-7, 14 Hz, 70% damping, buried 10 m
Recording instrument	SERCEL SN368/LKU
Data format	SEG-D (6250 bpi)
Sample rate	1 millisecond
Recording length	3 second
Channels per record	296
High cut	355.6
Low cut	out
Preamp gain	2.7/42 Db
Shot depth interval	3.048 m (10 ft)
Shot depth range	121.92m to 634m
Source type	dynamite
Charge size	20 grams

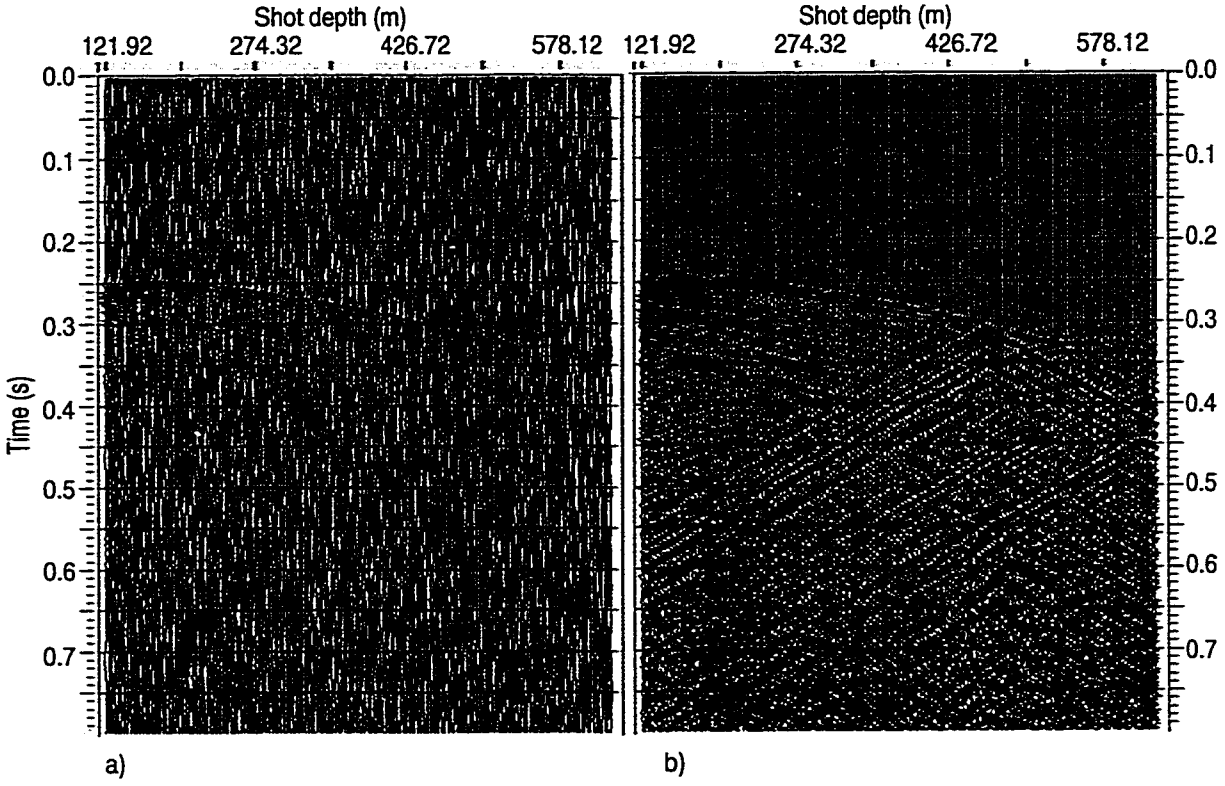

FIG. 2.36. D3 pad 3-D RVSP common-receiver gather of channel 4: (a) raw data, (b) true amplitude recovery and f-x deconvolution applied.

2.9 Conclusions and discussions

This chapter, as a general study, covers *P*- and *S*-wave analysis from three aspects and introductory study of 3-D seismic and 3-D VSP.

The mud-rock line established from *in-situ P*- and *S*-wave velocity measurement is the optimized for Cold Lake clastic rocks. It is an exponential relationship between *P*- and *S*-wave velocity. This study provided insights on the feasibility of using AVO inversion to differentiate shale from sandstone and reservoir fluid monitoring. It is predicted that AVO inversion can provide accurate steam conformance mapping in 3-D space. Lame's parameters are more sensitive to rock lithology change and formation fluids than V_p, V_s. With careful *P*- and *S*-wave impedance inversion Lame's parameters are very useful in reservoir characterization and monitoring.

Integrated surface 2-D seismic and borehole VSP *P*- and *S*-wave studies have illustrated that the task of differentiating lithology and identifying fluid can be fulfilled by integrating *P*- and *S*-wave information. However, the resolution of surface *P*-*S* wave data is not high enough to resolve the detail required. 3-D 3-component VSP is the tool that will meet this need. The 3-D VSP technique will be discussed in the next chapter.

Cold Lake surface 3-D seismic data were acquired with buried geophones with broad frequency bandwidth. The best processing will ensure successful and accurate reservoir monitoring and characterization.

The 3-D VSP data from D3 pad is quite promising after noise removal.

Chapter 3 – 3-D VSP modeling, acquisition design, and processing

3.1 Introduction

In situ seismic measurements (VSP and crosswell) have proven useful for imaging and estimating rock properties near or between wells. The advantages and importance to have VSP data in an operation area are: (1) data is in depth rather than in time, (2) wavelet is known so the phase of surface data can be understood, (3) greater vertical resolution. Because the Earth is spatially heterogeneous and our regions of interest are usually volumetric, 3-D images are critical. However, it is generally expensive or impractical to extend either measurement into three-dimensions (3-D). In recent years, vertical cable seismic (VCS) systems have been employed for marine data acquisition ('Vertical cable seismic survey makes its debut', *First Break*, **13**, 12, p. 460, 1995; Havig and Krail, 1996) as in the marine case it is easy to place a vertical receiver array (seismic cable) in the ocean. When surface 3-D seismic acquisition is taking place, the potential arises for full 3-D data recorded from downhole shots. To the best of my knowledge Imperial Oil Ltd. first acquired 3-D reverse VSP data in April 1990 at Cold Lake Production Project (CLPP). Borehole receiver tools have improved from the original 5 levels (Schlumberger VSP tools) to 48-channel VSP tools that were recently announced by CGG (The Leading Edge, 1998, **17**, No. 8, p. 1032). 3-D VSP acquisition becomes much cheaper when combined with surface 3-D acquisition (Zhang et al., 1996). The other option for land 3-D VSP is to take advantage of passive seismic monitoring in which wells and geophones are available. Therefore, the cost can be minimized. In Cold Lake, it is advantageous to acquire 3C-3D VSP data by using passive seismic monitoring wells. Passive seismic monitoring is a technique which is being developed at Cold Lake for the purpose of early detection of in-situ shear movement associated with primary casing failure. The advantages of 3C-3D VSP in Cold Lake are: (1) better shear wave data, (2) combined *P*-wave and *S*-wave data may evaluate reservoir heterogeneity and differentiate fluids. It is believed that 3C-3D VSP in Cold Lake will significantly improve passive seismic monitoring and markedly improve the analysis of vertical conformance.

With 3-D data available, migration of VSP is much more accurate. Chen and McMechan (1992) considered the 3-D case and used synthetic data from a salt structure model to perform a 3-D pre-stack depth migration. They showed that 2-D analysis produced artifacts while the 3-D algorithms provided a much more accurate picture.

In this chapter, the issues of 3-D VSP or reverse VSP acquisition survey design and processing will be addressed through ray-tracing a numerical model by comparing compressional-wave (*P*-wave) and converted-wave (*P-S* wave).

3.2 Ray-tracing and numerical modeling

3.2.1 Model description and receiver array

A plan view of the model, 3500 m by 3000 m, is shown in Figure 3.1. There are 61 receiver lines oriented East-West (E-W) - the inline direction - with a 50 meter line spacing from 0 to 3000 meters along North-South (N-S) direction (the crossline direction). The coordinate system is defined in the convention of (N-S, E-W) on the 2-D horizontal plane. There are 61 receivers per line with 50 meters receiver spacing. The array in Figure 3.1 shows every other receiver on every other receiver line.

The model consists of three layers (Figure 3.2) which were built using the SIERRA MIMIC software package. The thicknesses of the three layers from top to bottom are 800 m, 400 m, and 800 m respectively. A dome centered at (1500, 1500) is located on the top of the second layer with a radius of 630 m and a height of 210 m, which possesses dip angles that vary from 0° to 36.9° (after some math operation). The physical properties of these three

Table 3.1. Physical parameters of RVSP numerical model.

Layer	Velocity (m/s)		V_p/V_s	Poisson's Ratio	Density	Q factor	
	V_p	V_s				Q_p	Q_s
1	4000	2000	2.0	0.33	2.60	309	137
2	5200	2600	2.0	0.33	2.96	546	243
3	6400	3695	1.73	0.25	3.50	864	384
half space	7620	4399	1.73	0.25	2.89	1273	365

layers are listed in Table 3.1.

3.2.2 Ray-tracing and results

P-P and *P-S* ray-tracing through the model was implemented using the SIERRA 3-D QUIKVSP package. *P-P* reflections and *P-S* reflections from the top of the second and third layer, and direct arrivals are defined in the ray instruction. The model was shot at source depths from 1200 m to 0 m with a total of 31 shots from two different surface well locations (A) (1500,1500) and (B) (2200,1500); one well that intersected the target and one that missed the target. An array of surface receivers with 3721 channels (61 by 61) per shot record are set to record simultaneously.

Raypath plots to be shown were sampled on every other receiver in both the inline and crossline directions. Raypath view angles are defined by two parameters ϕ and β. The angle ϕ is defined as the angle between the dip plane and a horizontal plane. The angle ϕ is positive when dipped downward and negative when dipped upward (e.g. ϕ equals to zero for a horizontal plane). The angle β is defined as the angle between model N-S axis and true north direction. The angle β is positive when clockwise (β equals to zero for true north direction). The expression (ϕ,β) is used for viewing angles. Figure 3.3 shows the *P-P* reflection raypath (the front ray set is taken away for better visualization) and *P-P* coverage at viewing angles (0°, 0°) when the model is shot at depth of 0.0 m (source located on surface). In this case the plot shows the most *P-P* coverage on both dome and flat interface. The dip angle of the dome varies from 0° at the top of the dome to 36.9° where the edge of the dome intersects the flat interface. Overall, half distances of the maximum source receiver offsets are covered from all azimuths. However, only 30% to 40% of the dome area is covered. As the source moves down the borehole, the *P-P* coverage becomes smaller on both the dome and flat interface. Figure 3.4 shows the *P-P* wave areal coverage when the model is shot at this source location (depth of 0 m).

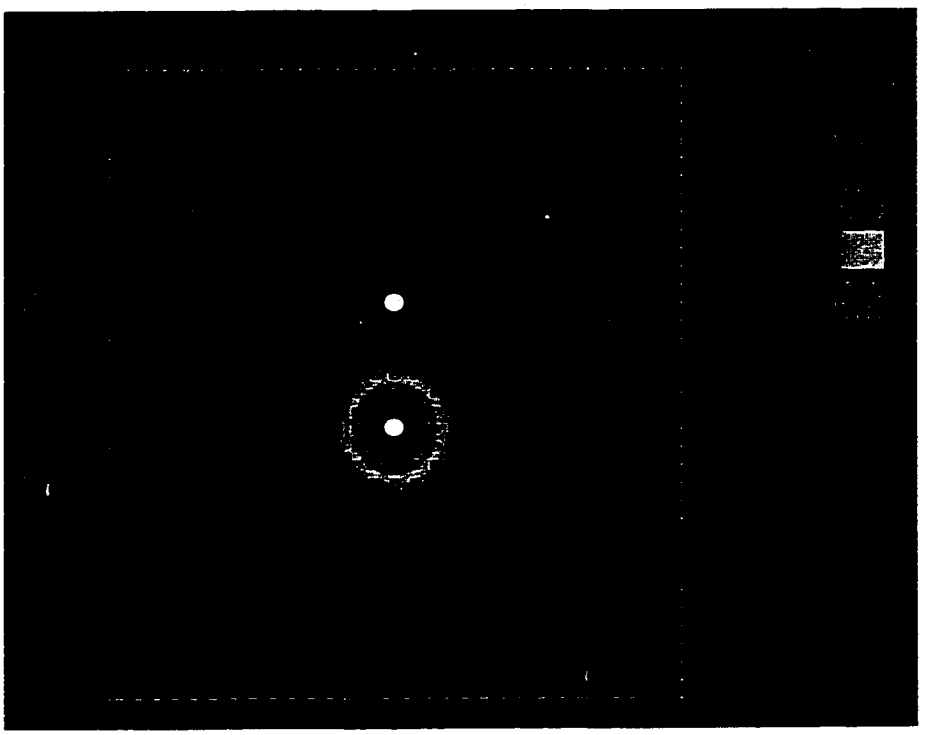

FIG. 3.1. Plan view of 3-D RVSP numerical model, receiver array is plotted on the 100 m spacing and the depth of the top of second layer. Well "**A**" is located at North-South 1500 m and East-West 1500 m, well "**B**" is located North-South 2200 m and East-West

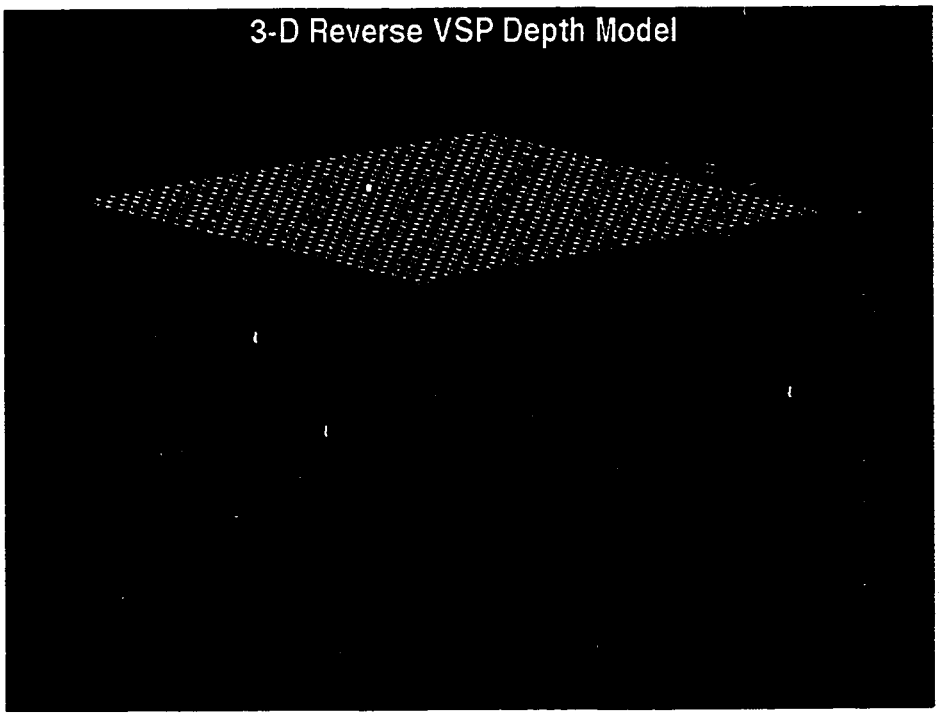

FIG. 3.2. 3-D prospective plot of the 3-D RVSP model.

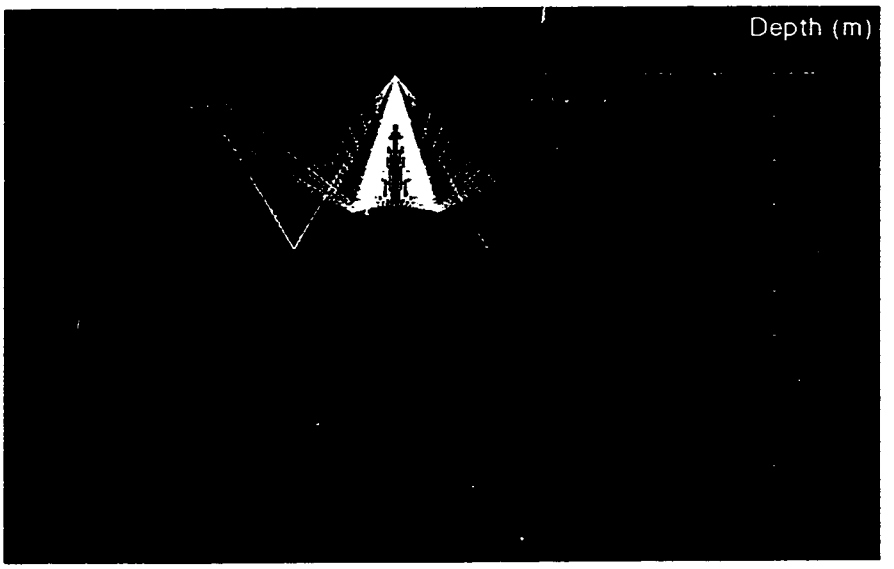

FIG. 3.3. Raytracing plot of *P-P* wave for the case of the reflector dipping away from bore hole showing *P-P* reflection raypath (the front ray set turned off for better visualization) and *P-P* coverage at viewing angles (0°, 0°) with the source depth of 0.0 m (source located on the surface) in well "A". The first viewing angle is defined as the angle between the dip plane and a horizontal plane e.g. 0° presents horizontal plane. The second viewing is defined as the angle between the model N-S axis and

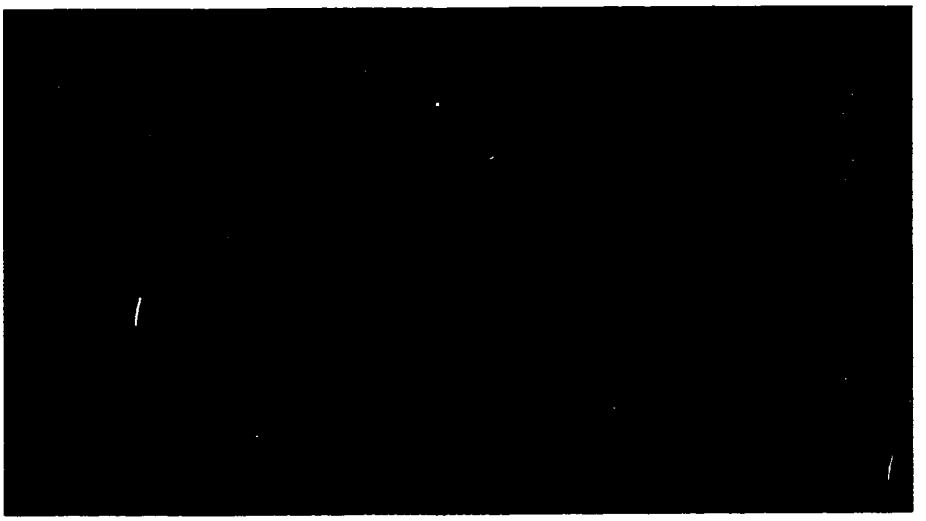

FIG. 3.4. Common reflection point of *P-P* wave areal coverage for the source positioned at surface of well "A".

The *P-S* raypath plot for a source depth of 0.0 m (source located at surface) is shown in Figure 3.5. Apparently, converted-wave events have much wider coverage on both the dome and flat interface with the same receiver array (both 2-D and 3-D space, see Figure 3.5 and Figure 3.6). In this case 60% to 70% of the dome is covered. A flat interface can be covered as much as 75% distance of maximum source-receiver offset on all azimuth directions. At this stage, two conclusions can be drawn: (1) 3-D reverse VSP *P-S* wave has wider coverage than the *P-P* wave, and it allows more dipping reflector to be imaged than *P-P* wave does; (2) unlike the normal VSP where *P-S* coverage is narrower than *P-P* wave in the 3-D reverse VSP, the converted-wave coverage is larger.

The other well location (B) (2200,1500) was used to determine the raypath (coverage) if the well misses the target (dome). Again, the model was shot through various source depths. Ray-tracing plots described above shows the case in which the reflector dips away from borehole in all azimuth directions. Two cases are considered: the reflector first dips towards the borehole and then dips away from the borehole. The *P-P* raypath plot for the source located at the top (surface) of well B is shown in Figure 3.7, viewed at a view angle (0°, 90°), which shows the maximum *P-P* coverage of 3-D RVSP at such well location. Half the distance of the source-receiver offset is covered for a flat interface, and the dome coverage is about 50-60%. One side of dome edge (close to well) can be imaged. Figure 3.8 shows the *P-S* raypath plot (one ray set taken away for visualizing outline of the dome), viewed at a angle (0°, 90°), for a source located at a depth of 200 m in the well B. Not only does it have wider coverage than previous plot in which the case source was located on surface, but 70-80% of dome surface is also covered! Figure 3.9 shows the areal coverage of *P-P* wave with the source positioned at the surface of well "B". One should be reminded that all the raytracing plots shown above are viewed in 3-D space. Many different reflection locations are recorded on one receiver (especially on Figure 3.5 and 3.9). Each surface location shown on a raypath plot is a receiver line: crossline direction when viewed at angle (0°, 0°) and inline direction when viewed at angle (0°, 90°).

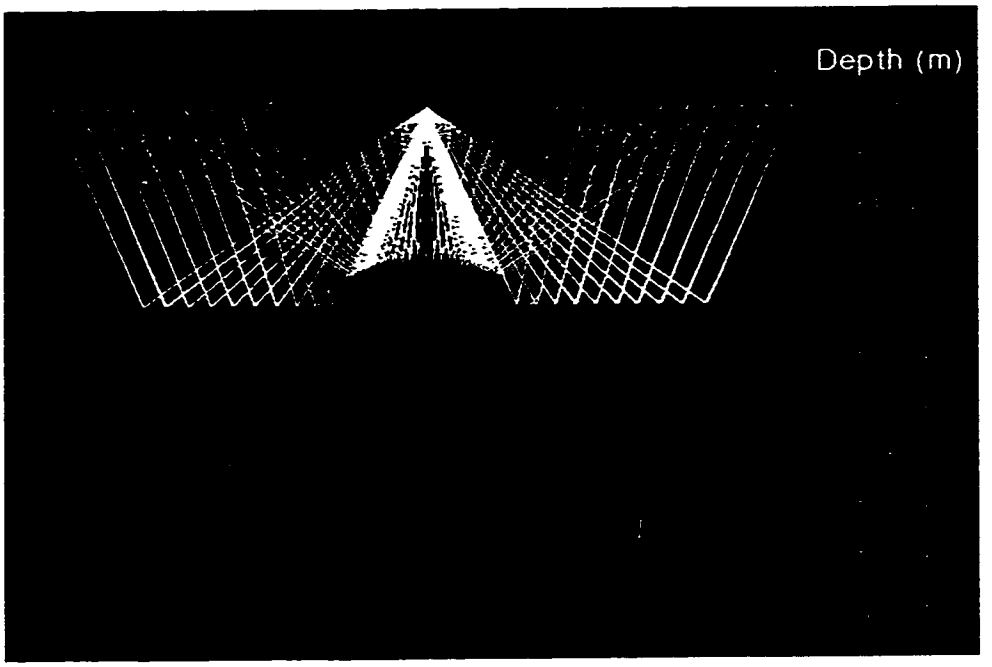

FIG. 3.5. Raytracing plot of *P-SV* wave for the reflector dipping away from borehole viewing to the north of the model, showing bigger coverage compared with *P-P* wave (FIG. 3.3).

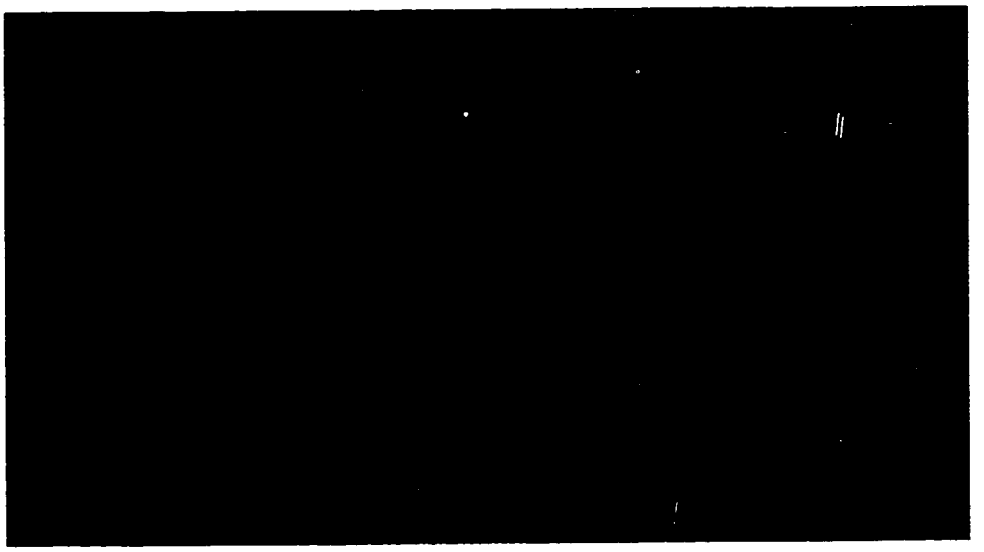

FIG. 3.6. Common reflection point of *P-SV* wave areal coverage for source positioned at surface of well "A".

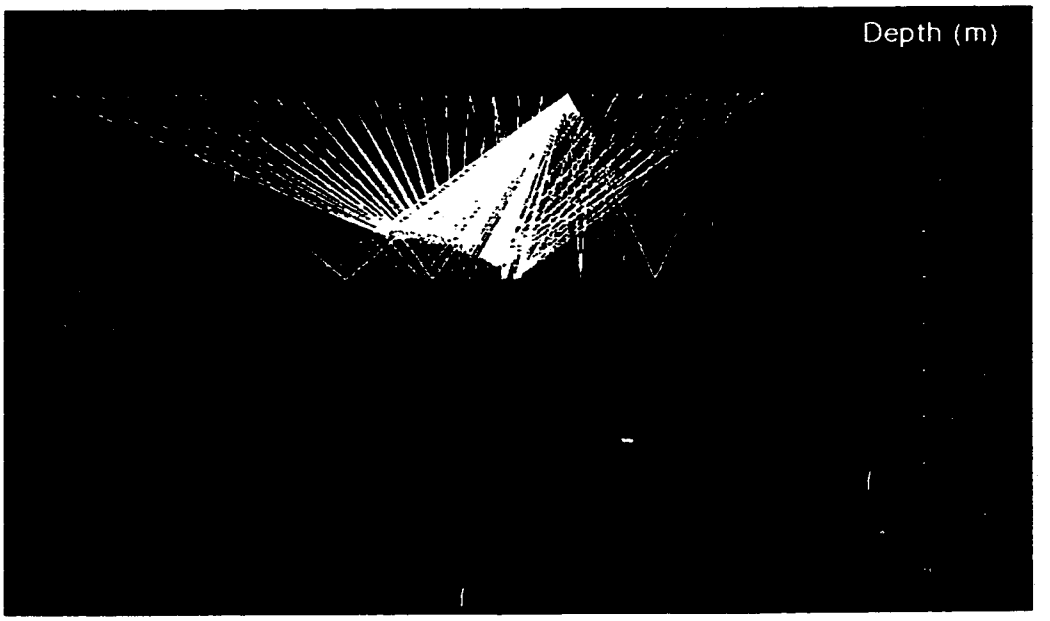

FIG. 3.7. Raytracing plot of the *P-P* wave for the reflector dipping towards the borehole viewing to the east of the model, showing raypath and coverage.

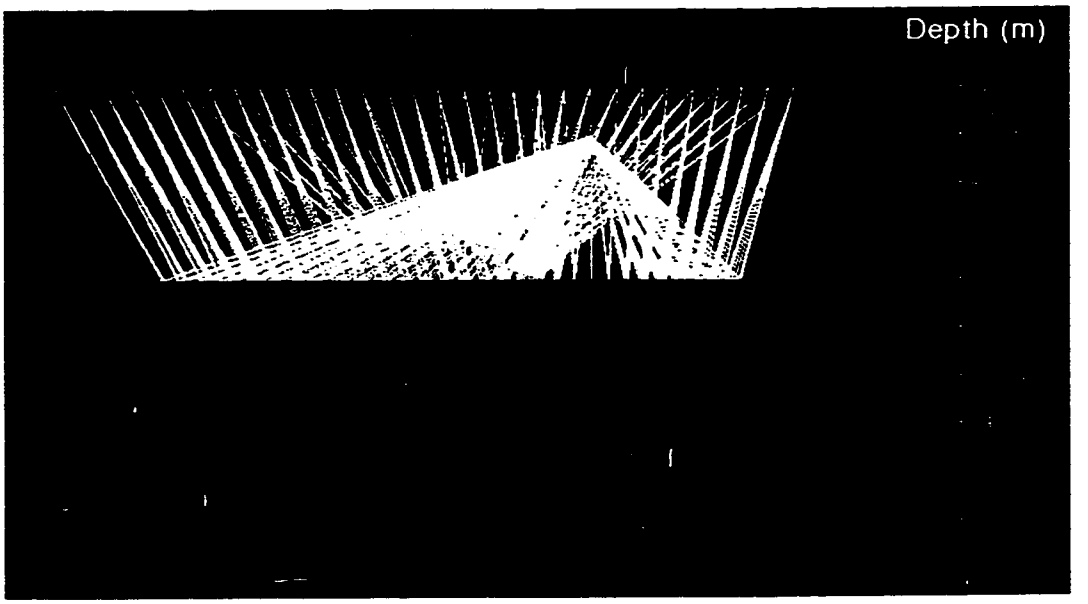

FIG. 3.8. Raytracing plot of the *P-SV* wave for the reflector dipping towards the borehole viewing to the east of model (source positioned 200 m below surface), showing bigger coverage compared with the *P-P* wave (source positioned at the surface, FIG. 3.7).

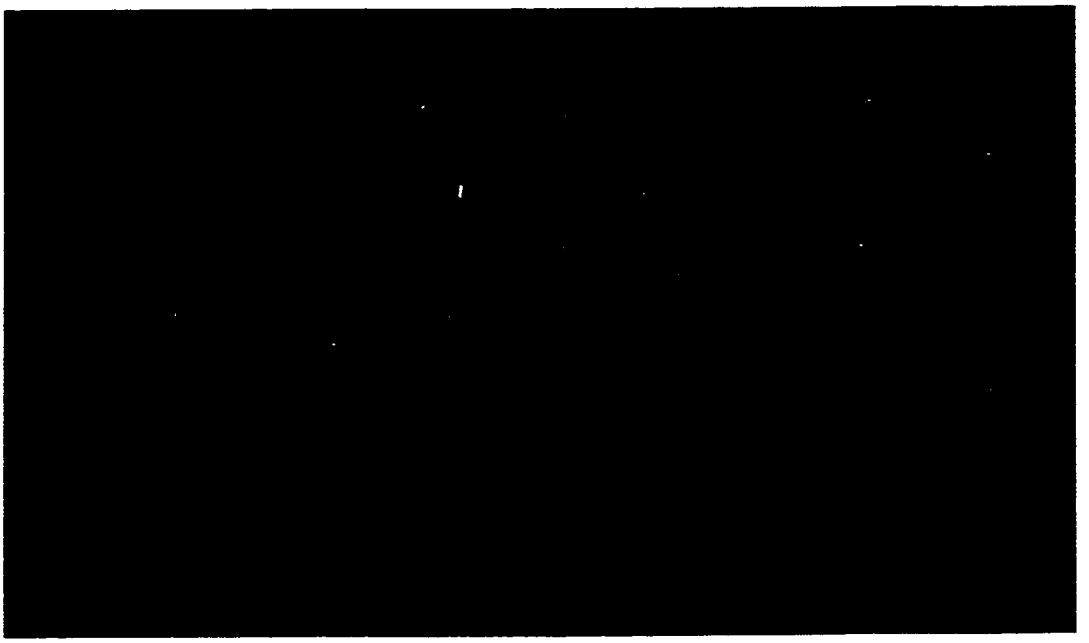

FIG. 3.9. Common reflection points of the *P-P* wave areal coverage for the source positioned at surface of well "B".

3.3 Acquisition survey design

Acquisition survey design for 3-D (R)VSP attempts to address issues of fold coverage, migration aperture, and to deduce the required acquisition parameters. The objectives of the survey must be clearly specified. There are many important input parameters, but the target depth and size may be the most influential. Offset range, source type and power, sample rate, geophones and subsurface coverage are all directly related to the target depth and size. Resolution parameters, such as the frequency required to image the target, are the starting design factors.

3.3.1 Migration aperture

The migration aperture can be estimated from the calculation of the minimum greatest offset required and the Fresnel zone of the target horizon since 70% of the diffraction energy is in the Fresnel zone.

3.3.1.1 Minimum greatest offset and dip angle for *P-P* and *P-S* waves

The source-receiver offset and the reflector dip angle for 3-D reverse VSP is considered next. The formula for the minimum greatest offset requirement is developed when certain coverage of a target is required in the case of reflector dip away from the borehole. This consideration does not include the Fresnel zone. The Fresnel zone for both the *P-P* and *P-S* waves in either surface or the VSP case can be calculated following the work by Eaton et al. (1991). The Fresnel zone for RVSP is developed in this work.

The *P-S* wave is first considered. Usually the depth of the target is known through drilling and the source depth is always known (S_d); therefore, the distance from the source to the target (K) is known. The dip angle (θ) can be estimated from migrated surface seismic section. As shown in Figure 3.10, the horizontal distance between the wellbore and the far side edge of the target is L, and the minimum source-receiver offset is X_{min}. According to Snell's law, the P-wave incident angle i and S-wave converted angle j are related as:

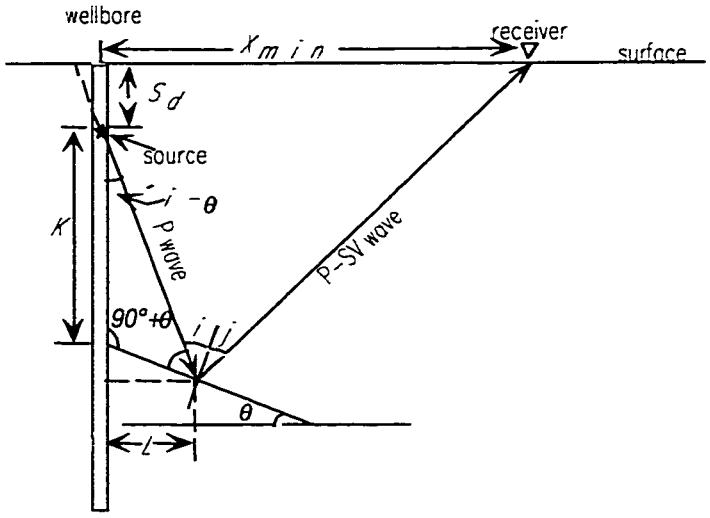

FIG. 3.10. Geometry and symbols used for the calculation of the minimum greatest offset.

$$\sin j = \frac{V_S}{V_P} \sin i \tag{3.1}$$

where V_S and V_P are the average velocities (or approximately *RMS* velocities) for the S-wave and P-wave at target depth. Using the triangle relationship in Figure 3.10,

$$X_{min} = \frac{\left(\frac{K\cos\theta}{\sin(\pi/2 - i)} + \frac{Sd}{\cos(\theta - i)}\right)\sin(i+j)}{\cos(\theta + j)} - \frac{K\cos\theta}{\sin(\pi/2 - i)} \quad . \tag{3.2}$$

which can be simplified using delta functions to:

$$X_{min} = K\frac{\gamma\cos\theta}{\cos i} + S_d\frac{\gamma + \sin(\theta - i)}{\cos(\theta - i)} \tag{3.3}$$

where γ is a function of the incident angle (i), conversion angle (j), and reflector dip angle (θ) defined by equation (3.4):

$$\gamma = \frac{\sin(i+j)}{\cos(\theta + j)} \tag{3.4}$$

The incident angle can be defined by the distance from the source to the target (K), the horizontal distance between the wellbore and the far side edge of the target (L), and the dip angle (θ) as follows:

$$\cos i = \frac{K\cos^2\theta\sqrt{K^2\cos^2\theta + L^2 + KL\sin(2\theta)}}{K^2\cos^2\theta + L^2 + KL\sin(2\theta)} \tag{3.5}$$

A similar expression for the P-P wave can be obtained when the conversion angle j is replaced by i, in which case the γ is expressed as follows:

$$\gamma = \frac{\sin(2i)}{\cos(\theta + i)} \tag{3.6}$$

As discussed in raytracing, for 3-D reverse VSP the coverage reaches maximum when the source is located at the top of a well. Assuming a target depth (K) of 2000 m, a source at the top of a well (S_d equals to 0 m), and a V_P/V_S =2.0, crossplots of minimum source-receiver offset with a horizontal distance of a subsurface image at various reflector dip angle (dip away from borehole) for both P-P and P-S waves (Figure 3.11 and 3.12) can be calculated (The Fresnel zone is not included). The downhole source energy has to be high

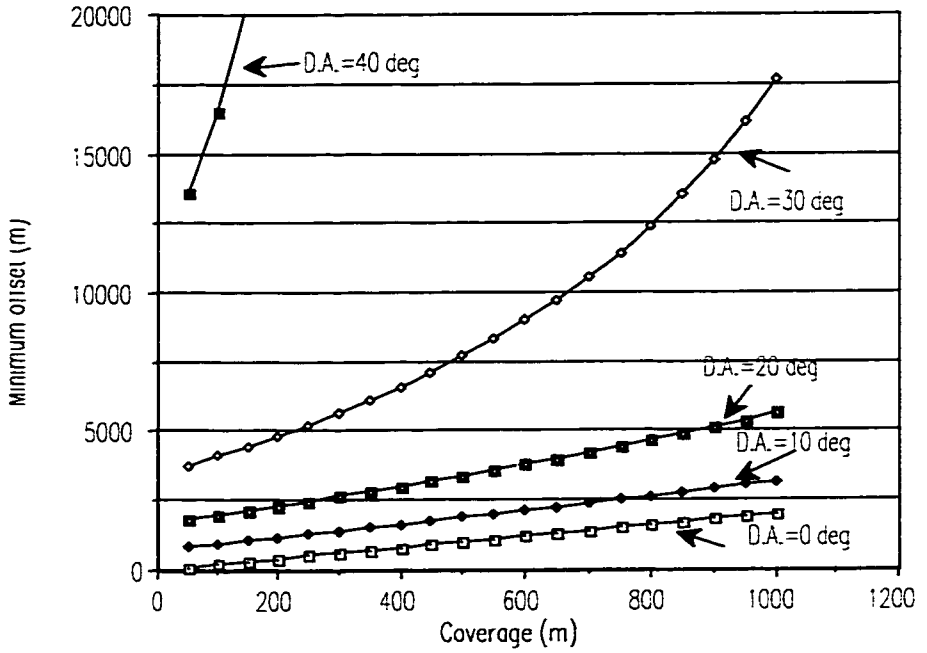

FIG. 3.11. Crossplot of the *P-P* wave coverage and the minimum greatest offset required with various reflector dip angles.

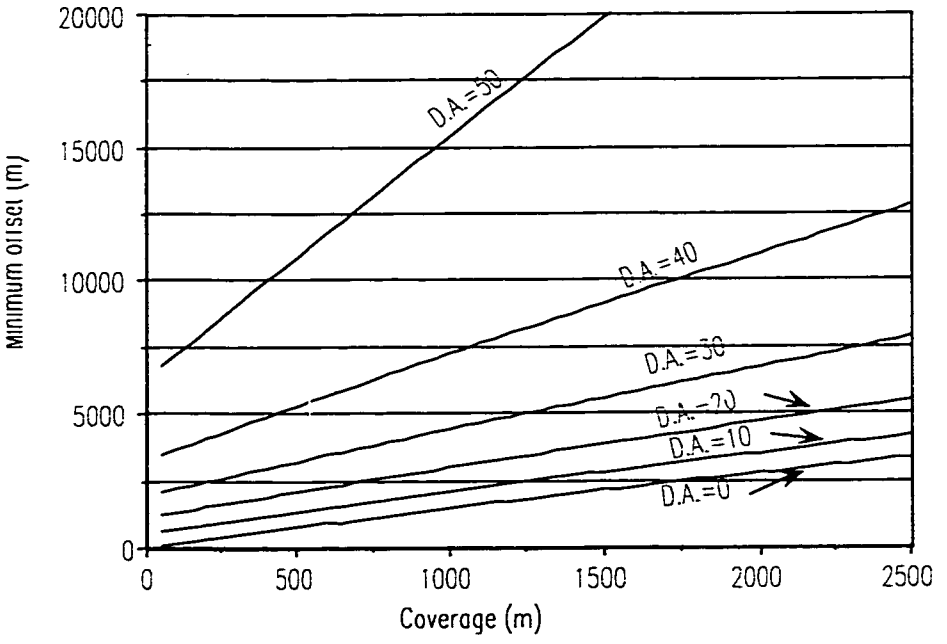

FIG. 3.12. Crossplot of the P-SV wave coverage and the minimum greatest offset required with various reflector dip angles.

enough if the offset is 2500 m. For a surface receiver array with a maximum offset of 2500 m (5000 m accross the receiver line) the *P-P* wave can probably image 2350 meters (The Fresnel zone roughly considered) if the reflector is flat (dip angle equals 0°); 1350 m if the reflector dip angle is 10°; and 450 m if the reflector dip angle is 20°. However, the *P-S* wave has much better coverage. For the same surface receiver array, *P-S* can probably image 3450 m if the reflector is flat, 2400 m if the reflector dip angle is 10°, 1400 m if the reflector dip angle is 20°, 330 m if the reflector dip angle is 30°. Again, the Fresnel zone is roughly considered. The reflector with a dip angle of 40° can not be imaged. The reflector dipping towards the borehole can be better imaged. For the RVSP, the migration aperture has its new characteristics. The source locations are restricted along the well, so the surface 3-D migration aperture concept can not be extended to 3-D RVSP.

3.3.1.2 Fresnel zone consideration

The Fresnel zone effect is another factor to be considered for migration aperture. The work by Eaton et al., (1991) on the converted-wave Fresnel zone shows that the relative changes in size and shape of the *P-S* Fresnel zone as a function of offset are not large and are comparable to the *P-P* case. For the given depth and frequency the *P-S* Fresnel radius of normal VSP is smaller than the corresponding *P-P* Fresnel radius. The Fresnel zone of RVSP will be discussed for both *P-P* wave and *P-S* wave cases. The Fresnel radii of RVSP for both zero-offset and offset are the same as normal VSP for *P-P* wave because the raypaths are the same. This can be expressed in a similar way as Stewart et al., (1984):

$$R_{F_{p\text{-}p}} \approx \left(\frac{Tzk}{(z+k)} V_p\right)^{1/2} \tag{3.7}$$

where $R_{F_{p\text{-}p}}$ is the Fresnel radius; T is the dominant period of the wavelet; V_p is the average velocity to the target horizon; z is the depth from the surface to the base of the target layer; and k is the distance from the source to the base of the target layer.

The Sheriff criterion for the RVSP *P-S* Fresnel radius (Figure 3.13) is obtained by setting the difference between the nonvertical raypath traveltime and the vertical traveltime equal to half the dominant period, as shown below.

$$R_{F_{p\text{-}sv}} \approx \left(\frac{V_p T z k}{(z + k V_p / V_s)} \right)^{1/2} \tag{3.8}$$

Figure 3.14 show the *P-P* wave and *P-S* wave Fresnel zone calculated using equation (3.7) and (3.8) for sources located at surface, Colorado shale top(180 m), Grand Rapids top (320 m), and Clearwater top (425 m, depth of target horizon) below the surface. The important points can be made from these two figures:

1) Fresnel radius decreases when the source depth increases relative to target (positive downwards);

2) Fresnel radius of RVSP *P-S* wave is bigger than that of VSP *P-S* wave; the difference increases as the source depth increase; the Fresnel radii of RVSP and VSP are equal only when the source and the receiver are on the surface at the same time;

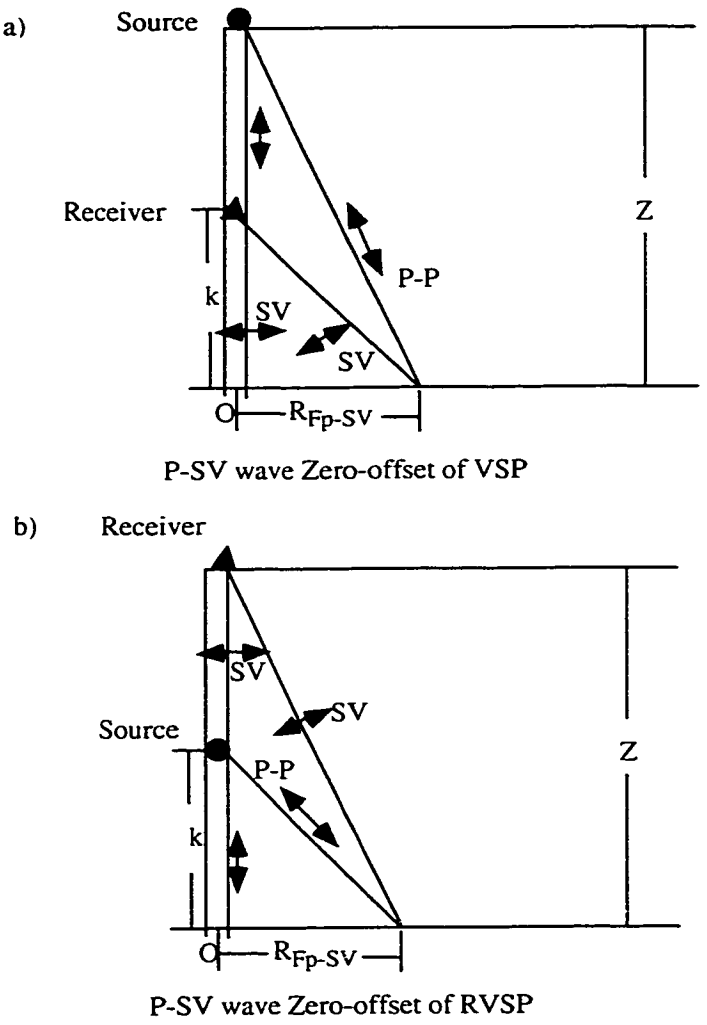

FIG. 3.13. Geometry and symbols used for the calculation of Fresnel radii of (a) VSP and (b) RVSP.

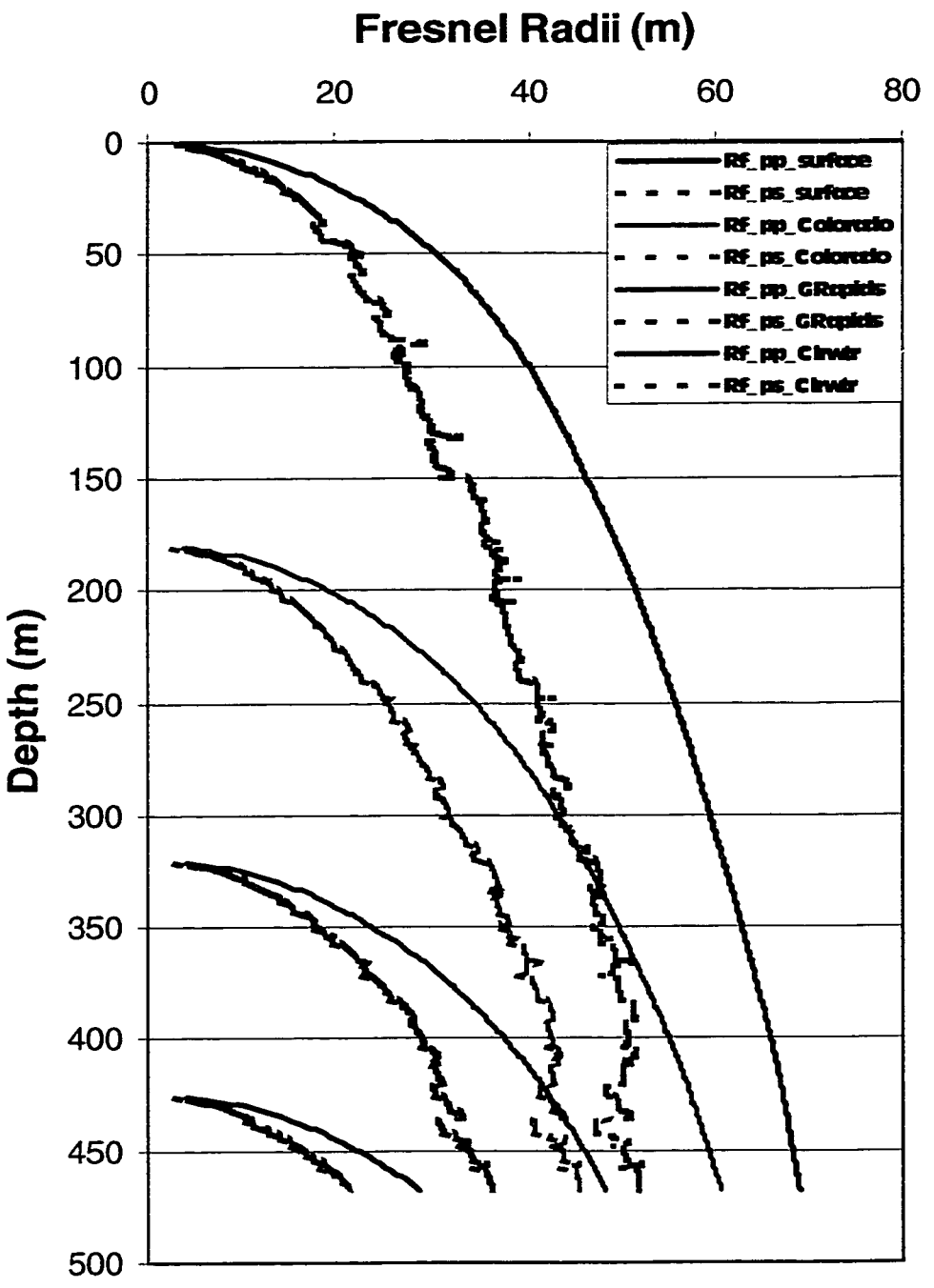

FIG. 3.14. Cold Lake Fresnel radii for *P-P* and *P-S* wave RVSP with source located at different depth (formation tops).

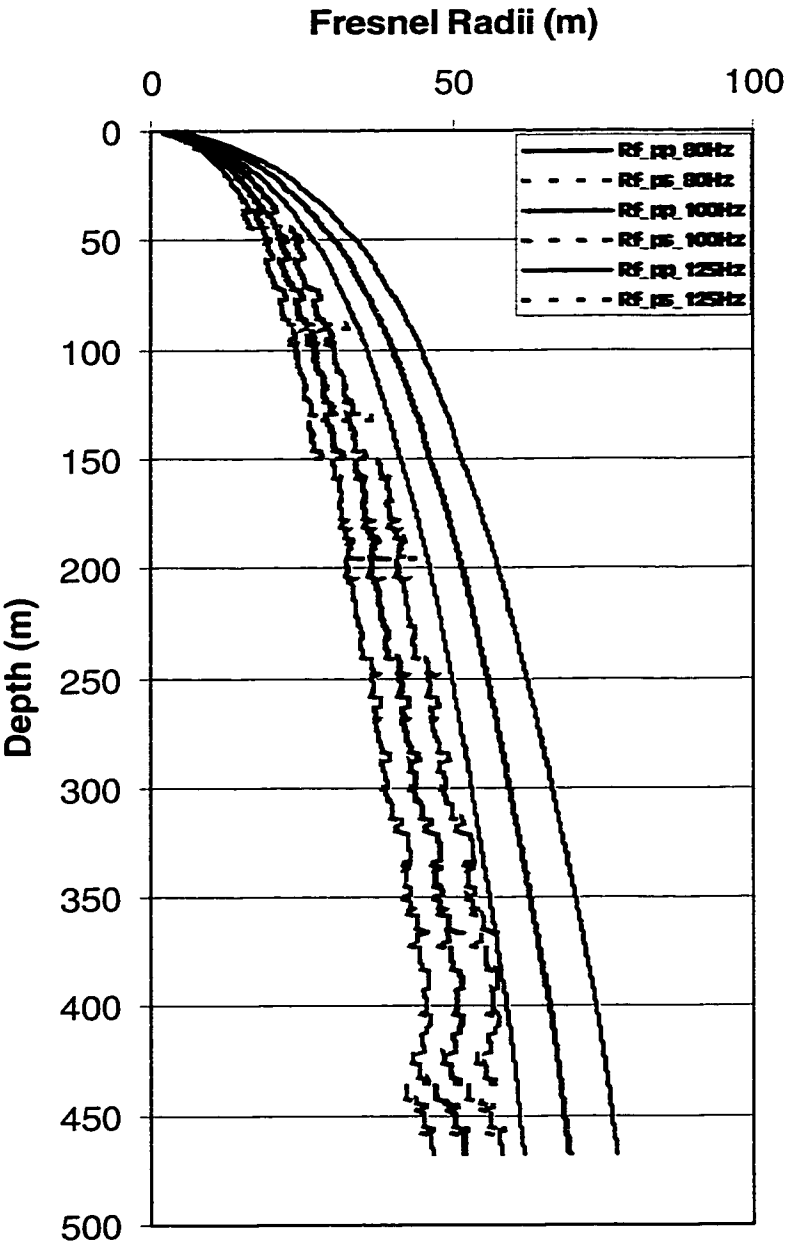

FIG. 3.15. Cold Lake Fresnel radii for *P-P* and *P-S* wave when source is located on surface with different frequencies.

3) Similar to VSP, the Fresnel radius of the RVSP *P-S* wave is smaller than that of the RVSP *P-P* wave. Higher frequency corresponds to smaller Fresnel zone.

The Fresnel radius of offset VSP *P-S* wave is found to be greater than that of zero-offset Fresnel radius; but the relative change in size of the Fresnel zone with offset is not large and is similar in magnitude to the *P-P* case (Eaton et. al., 1991).

For the case of the RVSP, relative to the borehole sources each receiver channel can be considered as an inline receiver; therefore, only inline *P-S* wave Fresnel radii need to be considered (Figure 3.15). This satisfies the equality in equation (3.9),

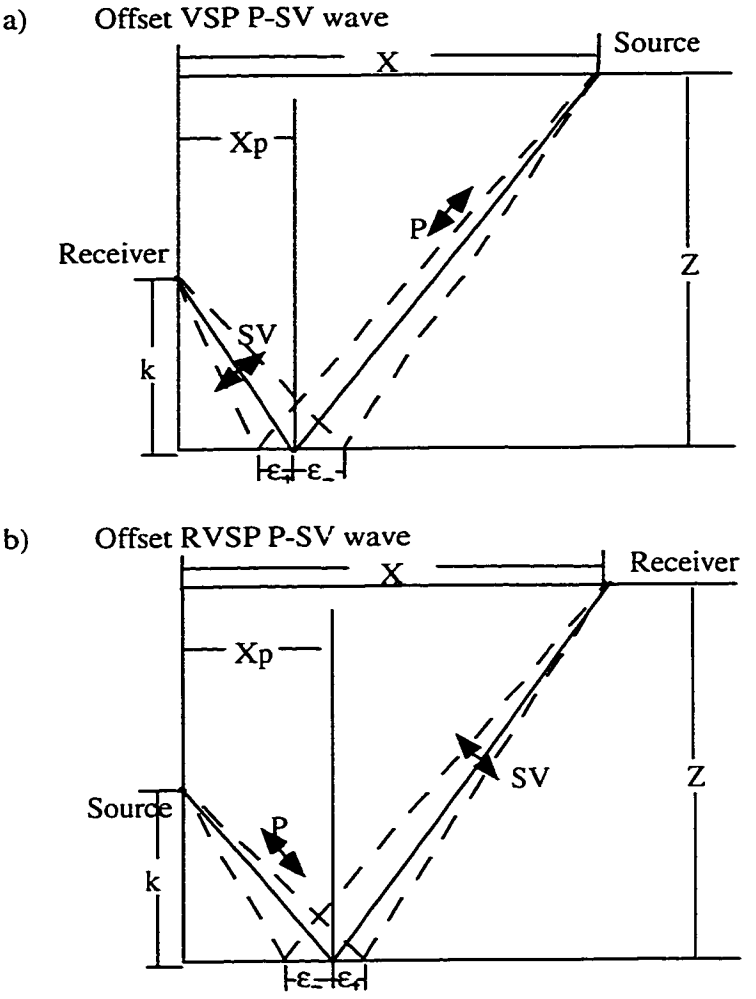

FIG. 3.16. Geometry and symbols used for the calculation of Fresnel radii of offset VSP (a) and offset the RVSP (b).

$$\frac{T}{2}=\frac{\left[(x_p \pm \varepsilon_{+/-})^2 + k^2\right]^{1/2} - (x_p^2 + k^2)^{1/2}}{v_p} + \frac{\left[(x - x_p \mp \varepsilon_{+/-})^2\right]^{1/2} - \left[(x - x_p)^2 + z^2\right]^{1/2}}{v_s} \qquad (3.9)$$

Equation (3.9) can be solved numerically. Similarly, it is believed that *P-S* wave Fresnel radius of offset RVSP is greater than that of zero-offset RVSP; but the relative change in size of the Fresnel zone with offset is not large and is similar in magnitude to the *P-P*

case. The Fresnel zone of *P-P* wave will be used in the survey design because it is the biggest one.

The Fresnel zone is sensitive to the size and shape of the targets (Lindsey, 1991, Stone, 1994). In 3-D surveys with the many valued directions of the reflection and ranges, allowance can be made for the form of the target. The behavior of the Fresnel zone is not the same on anticlines and synclines. The radius of curvature (r) is a factor. The Fresnel radius is modified by a function (ζ) defined as follow:

$$\zeta = \frac{h}{r} \tag{3.10}$$

where h is the height or depth (for the concave structure) of the target, r is the radius of the curvature of the target.

For anticline (convex form) structures, the Fresnel radius (R_{atc}) is smaller than that (R) of the flat interface:

$$R_{atc} = R\frac{1}{1+\zeta} \tag{3.11}$$

For syncline (concave form) structures, the Fresnel radius (R_{syc}) is larger than that (R) of the flat interface:

$$R_{syc} = R\frac{1}{1-\zeta} \tag{3.12}$$

The dominant frequencies for both the *P-P* wave and the *P-S* wave are similar for VSP data which indicates P-S wave data has much higher resolution, the spectra calculated from reservoir interval indicates dominant frequency of 100 Hz at the target. Similar or higher frequencies are expected for the RVSP data. The Fresnel radii is about 68 m for the *P-P* wave and 50 m for the *P-S* wave when the source is located on surface, in which case the Fresnel radii are the biggest for *P-P* and *P-S* respectively.

The Clearwater formation is planar in structure (ζ=0.0). There is no need to modify Fresnel radii using equations (3.10), (3.11), and (3.12). The calculated *P-P* wave Fresnel radius (68 m) will be used for migration aperture consideration, and the *P-S* wave Fresnel radius (50 m) will be taken into account for spatial sampling.

3.4 Processing

There are a number of steps required to process VSP data including statics removal, velocity analysis, wavefield separation, mapping, stacking, and migration. We could estimate receiver statics from deep shots or perhaps use the surface-seismic estimated values. We also need to remove the direct arriving waves to allow better imaging using the reflected events. Separation of the direct and reflected events might be assisted by using data grouped in ways other than by common shot(s) or receiver(s). However, conventional median or f-k filters on common receiver gathers are likely to be adequate. Useful possible gathers include constant s-r groups or s+r groups. A fast method is developed to remove NMO and stack the data. There are two possible methods to accomplish this: i) a VSPCDP map type of process or, ii) a CRP-type gather with stacking velocity analysis, NMO removal, and stack. Using this approximate stack structure and prior velocity values, the full pre-stack migration is possible.

Pre-stack migration could be accomplished using a reverse-time algorithm, Kirchhoff implementation, or other procedure that allows source and receiver to be at different elevations. The shot data could be upward continued to make the raw RVSP look like 3-D surface seismic data, and then the whole continued RVSP could be processed as a standard 3-D survey. Similarly, the surface recordings could be downward continued to their shot depths, then each shot is handled as a layer stripped surface seismic data set. After migrating each shot, the images could be stacked. The downward continuation methods may be the most effective. The processing flow is shown in Table 3.2.

Table 3.2. 3-D VSP processing flow

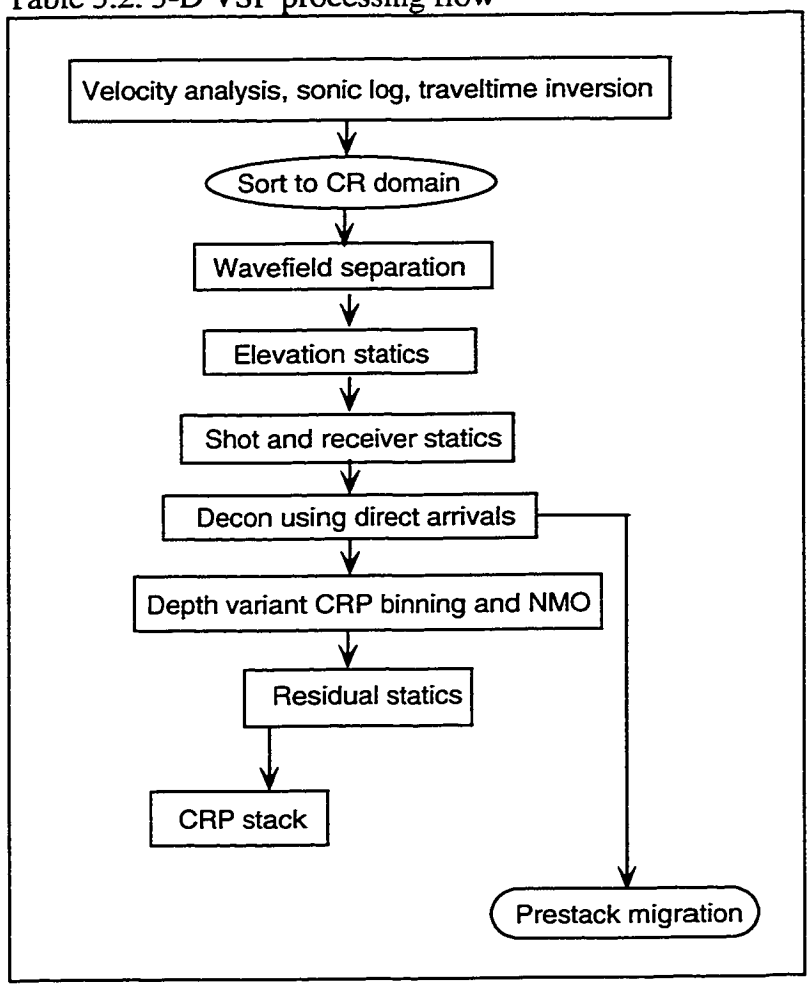

3.4.1 Normal moveout (NMO) correction, binning and stacking

The offset VSP survey is used to create reflection points that are laterally offset from the borehole. Using a ray parameter approach, Stewart (1991) developed an algorithm for 2-D *P-P* and P-S offset VSP mapping. These mapping techniques are extended to the 3-D case. The mapping technique for 3-D RVSP data can be used for 3-D VSP data by exchanging source-receiver geometry information. The examples of raw shot and receiver records are shown in Figure 3.17

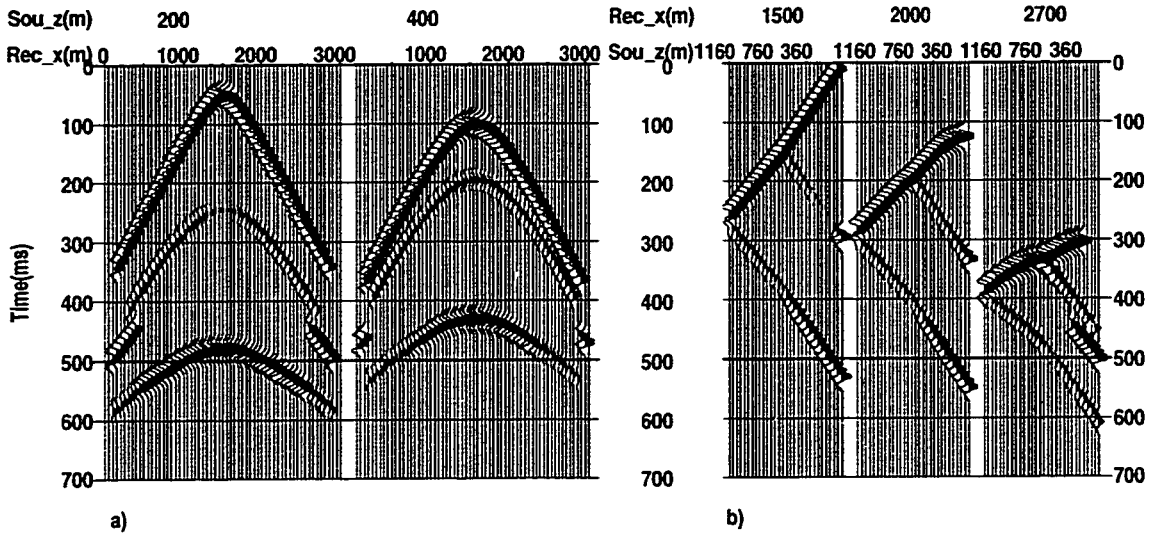

FIG. 3.17. Raw RVSP modeling records: a) shot gathers (from shot depth of 200 m and 400 m) at crossline (rec_y) 1500 m; b) receiver gathers at crossline (rec_y) 1500 m intersect with inline (rex_x) 1500 m, 2000 m, 2700 m from shots at depths (sou_z) of 1160 m to the surface.

In the 2-D case, the lateral offset of the reflection point X_r (in Figure 3.18) is given by:

$$X_r = \frac{X}{1 + \frac{\widetilde{V}_R^2 T_R}{\widetilde{V}_{RB}^2 T_{RB}}}, \tag{3.13}$$

where $\widetilde{V}_R$ is the RMS velocity of upgoing raypath or downgoing raypath , $\widetilde{V}_{RB}$ is the RMS velocity for downgoing raypath or upgoing raypath, T_R is the zero-offset traveltime (one way) from surface to reflection point; and T_{RB} is the zero-offset traveltime (one way) from

reflection point to borehole which is either a source (for RVSP) or a receiver (for VSP). X is the source-receiver offset.

The concept used to calculate the reflection point of a 3-D VSP is diagrammed in Figure 3.19. The reflection point, denoted by C in Figure 3.19, is in the xy plane instead of in the x direction only. The reflection point is located in the propagation plane of the P wave. The azimuth of the reflection point can be defined by calculating the source-receiver line azimuth angle θ with the X or Y axis; then θ is written as

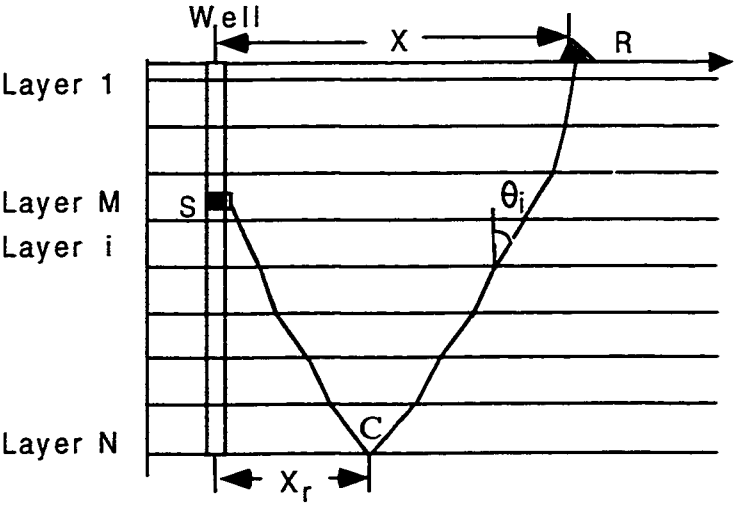

FIG. 3.18. 2-D VSP ray geometry for flat layered medium.

$$\theta = \tan^{-1}\left(\frac{\Delta y}{\Delta x}\right) \tag{3.14}$$

where ΔX and ΔY are the horizontal offsets from the well top in the x and y direction.

Extending equation (3.13) to the 3-D domain gives:

$$R_{offset} = \frac{\sqrt{\Delta X^2 + \Delta Y^2}}{1 + \frac{\tilde{V}_R^2 T_R}{\tilde{V}_{RB}^2 T_{RB}}}, \tag{3.15}$$

where ΔX and ΔY are the horizontal offset from the surface location to the well top in the x and y direction. The horizontal distance covered by the reflected wave in the x direction is given by

$$X_r = R_{offset} \sin\theta \tag{3.16}$$

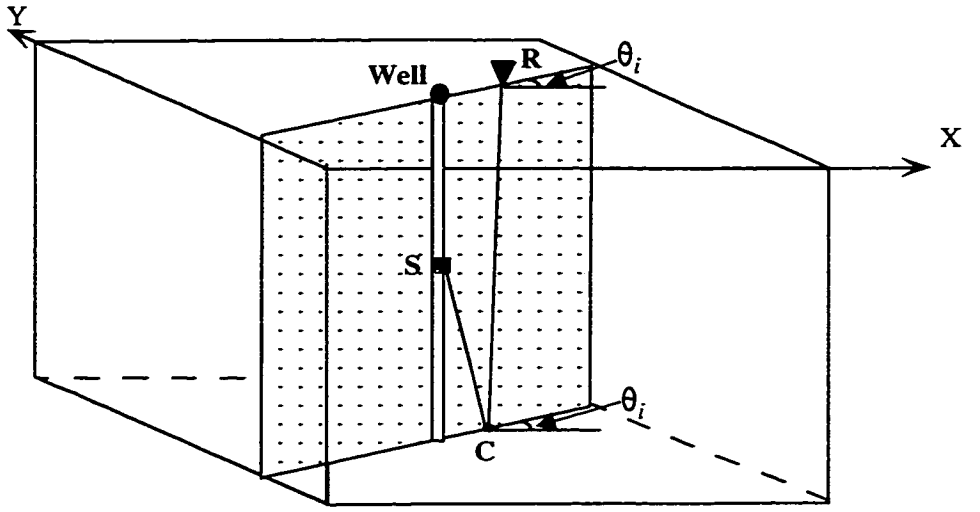

FIG. 3.19. 3-D VSP ray geometry for flat horizontally layered medium.

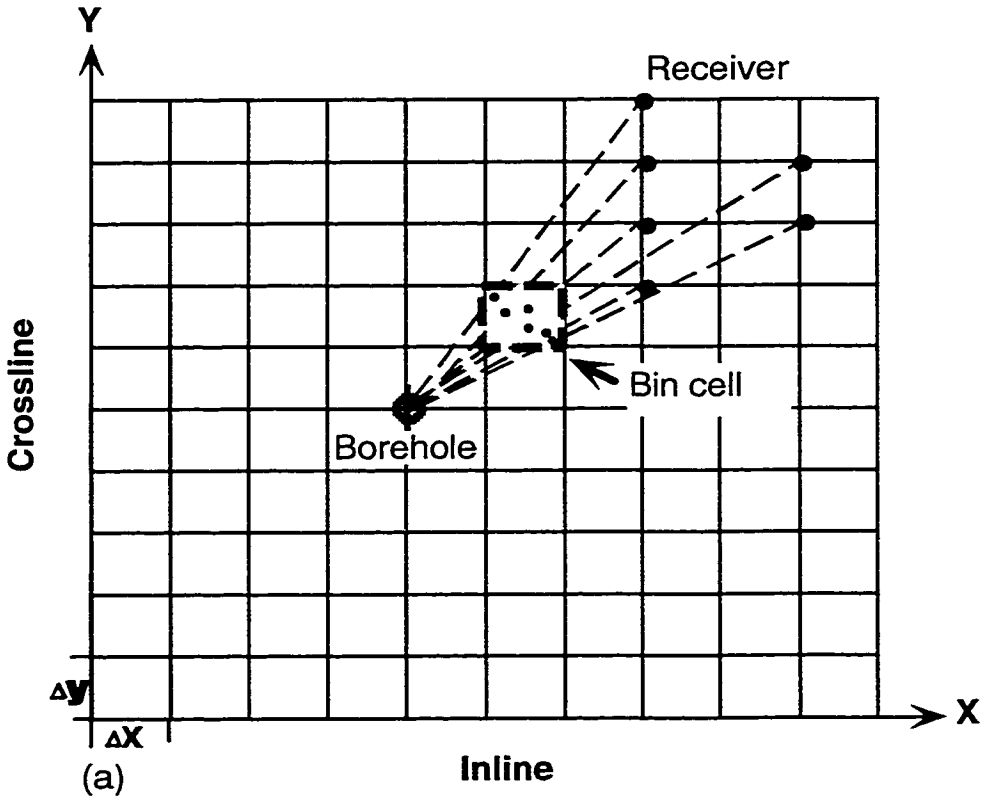

FIG. 3.20. Schematic surface diagram showing binning algorithm.

The horizontal distance covered by the reflected wave in the y direction is given by

$$X_r = R_{offset}\cos\theta \tag{3.17}$$

Equation (3.15) shows the binning method. Once the coverage of the reflection point is calculated by using equation (3.15), it can be split into the x and y axes by using equations (3.16) and (3.17).

Since the shots are in a two-dimensional plane, the 3-D VSP has the character of surface 3-D seismic data; therefore, it is necessary to define the bin grid in two dimensions as in surface 3-D data binning. This is shown in Figure 3.20. On the other hand, the receivers in the well borehole, the 3-D VSP also has the character of VSP seismic in which the reflection points for each recorded trace are variant in the depth domain as shown in Figure 3.21. If the same bin origin and grids are defined in a 2-D plane for all depth layers of interests, for the same trace at different depth points, the reflection points will be located in different bin cells.

By combining the two characteristics of 3-D VSP, the bin grids are defined in a two dimensional plane. The reflection points are calculated in 2-D plane at each depth point by using equations (3.15) to (3.17) and the reflection points of the 3-D VSP are mapped in 3-D position.

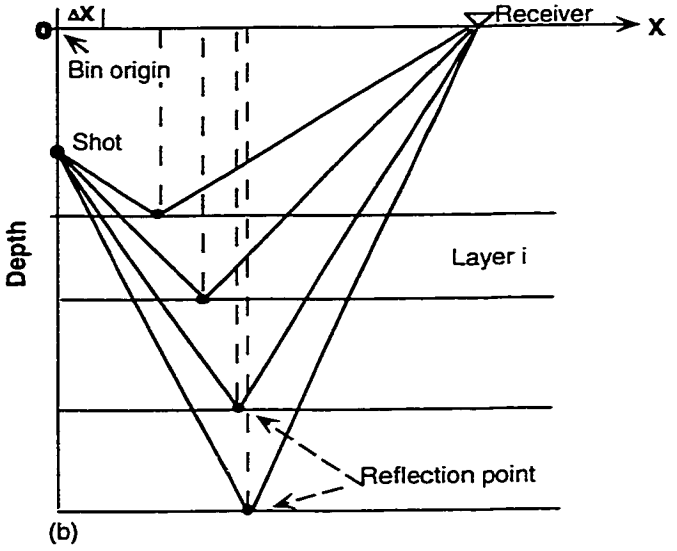

FIG. 3.21. Schematic depth domain binning algorithm.

3.4.2 3-D VSP fold distribution

For reflection imaging, the stacking fold or multiplicity is a critical parameter. In this study, several tests have been implemented on model A, in order to learn how the surface geometry and down hole operation influence the bin interval and the fold distribution.

Figures 3.23 and 3.24 are used to illustrate the bin fold distribution as depth (time) increases. These two results are the binning algorithm performed on the same dataset where the inline and crossline receiver coordinates are from 200 to 2800 m, the inline and crossline receiver intervals are 50 m. There are 30 shots located at the surface 1500 m in both directions, and they are located from the surface down to the well to the borehole 1200 m with a depth interval of 30 meters. All the shots are above (one is on) the second layer, which means the results in Figure 3.22 and 3.24 based on the same surface and depth geometry.

Same bin interval, azimuth, and bin origin are used on these layers. The bin origin and azimuth are the same as the surface layout coordinates origin and azimuth. The bin interval in both directions is 15 m.

Figure 3.22 shows the areal bin fold distribution (Figure 3.22 upper panel) around 600 ms (the reflection of the second layer). The bin fold statistics are shown in the histogram (Figure 3.22 lower panel). The overall fold distribution is not quite uniform. Two "blue" strips across the covered area East-West and North-South through the well with low fold coverage (from 3 fold to 40 fold) along which higher fold coverage (60 to 70 fold) are surrounded (Figure 3.22 upper panel). Two "red" strips across the covered area through the well 45° from any of the "blue" strips with high fold coverage (80 to 100 fold). The dominant coverage is about 50 to 60 fold but they are distributed in the 45° azimuth of the receiver line direction. They also have quite a big portion of the bin cell with low fold (3 to 10) coverage distributed along the first and last 10 inline and crossline. As the depth (time) increases, the bin fold distribution gets more uniform as illustrated in Figure 3.23. As in Figure 3.22, there are two "dark red" strips across the well top in receiver inline and crossline direction. The major fold distribution becomes much more uniform and this also

can be viewed in the lower panel of Figure 3.23, the histogram shows better distribution, and much higher fold. The dominant fold coverage of the third layer is around 40-75 fold, and there is almost no low fold less than 35 between 10-80 inline and crossline of the CRPs (reference numbers).

Comparing Figures 3.23 and 3.24, it is found that as the depth increases, the bin fold will distribute more uniformly and is higher than in the shallower layers.

Figure 3.24 shows the bin fold distribution of the same dataset of layer 3 by using the same parameters, except now shifting the bin origin 7.5 m towards the east and north directions. The two "dark red" strips have disappeared. Figure 3.25 shows the bin fold distribution of layer 3, the bin size of 30 m in both directions. Comparing Figure 3.25 and 3.24, we can see by increasing the bin size, the binfold will distribute more uniformly with high fold.

Figures 3.27 illustrate the fold distribution when fewer shots are used. In this Figure, we take out every second shot as shown in Figure 3.23, giving only 15 shots, They are located from the surface down to the well to 1160 m with an 80-m interval. Comparing Figure 3.26 with Figure 3.23, the binfold distribution is not much different. The dominant binfold is 22 to 27, which is half the amount as shown in Figure 3.23. This indicates that the number of shots or receivers downhole does not strongly influence the fold distributions.

Figure 3.27 illustrates the fold distribution when the surface geometry changes. In this test, the shot depth and number are kept the same as in Figure 3.23, but every second receiver on the surface are removed, giving a receiver interval 100 meters in both inline and crossline directions. The result in Figure 3.27 shows that the binfold is low and that there are many empty bins inside the offset of 700 m. This indicates that the surface station geometry heavily influences both the bin size and the bin fold.

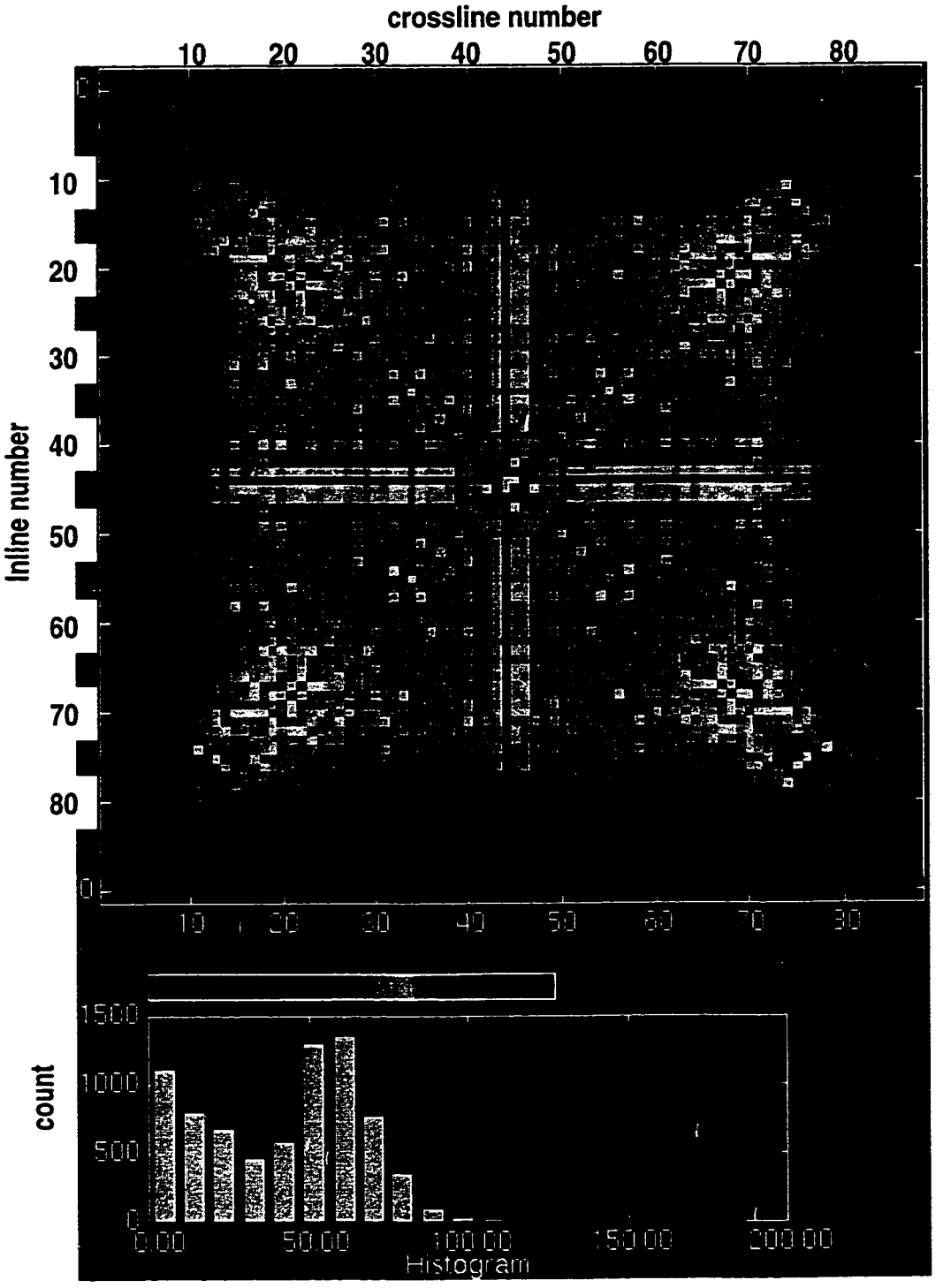

FIG. 3.22. Fold distribution at the top of the second layer with full shot and receiver (receiver interval of 50-m and shot interval of 40-m) of model A and bin size of 15x15 square m.

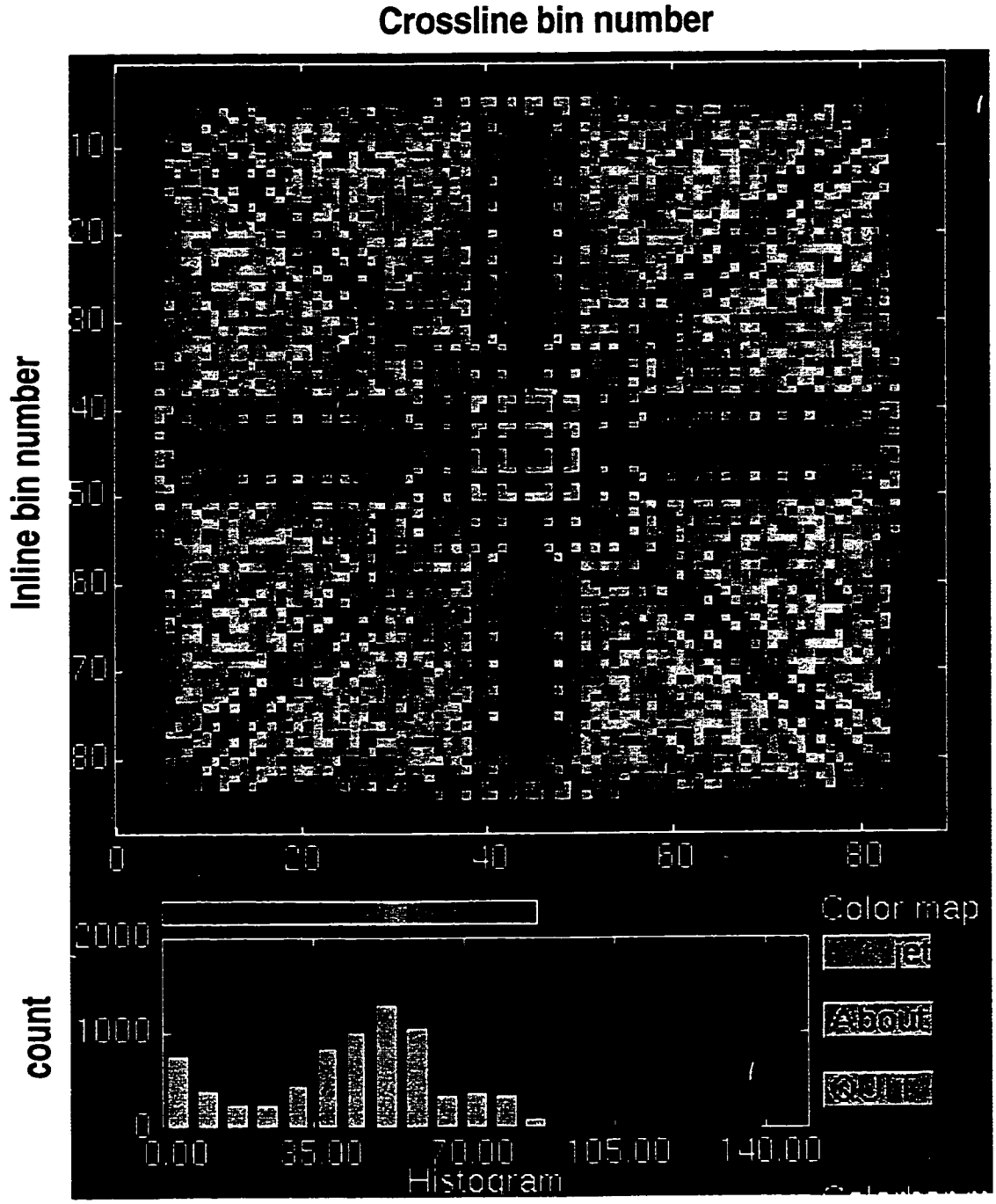

FIG. 3.23. Fold distribution at the top of the third layer with full shot and receiver (receiver interval of 50-m and shot interval of 40-m) and bin size of 15x15 square m.

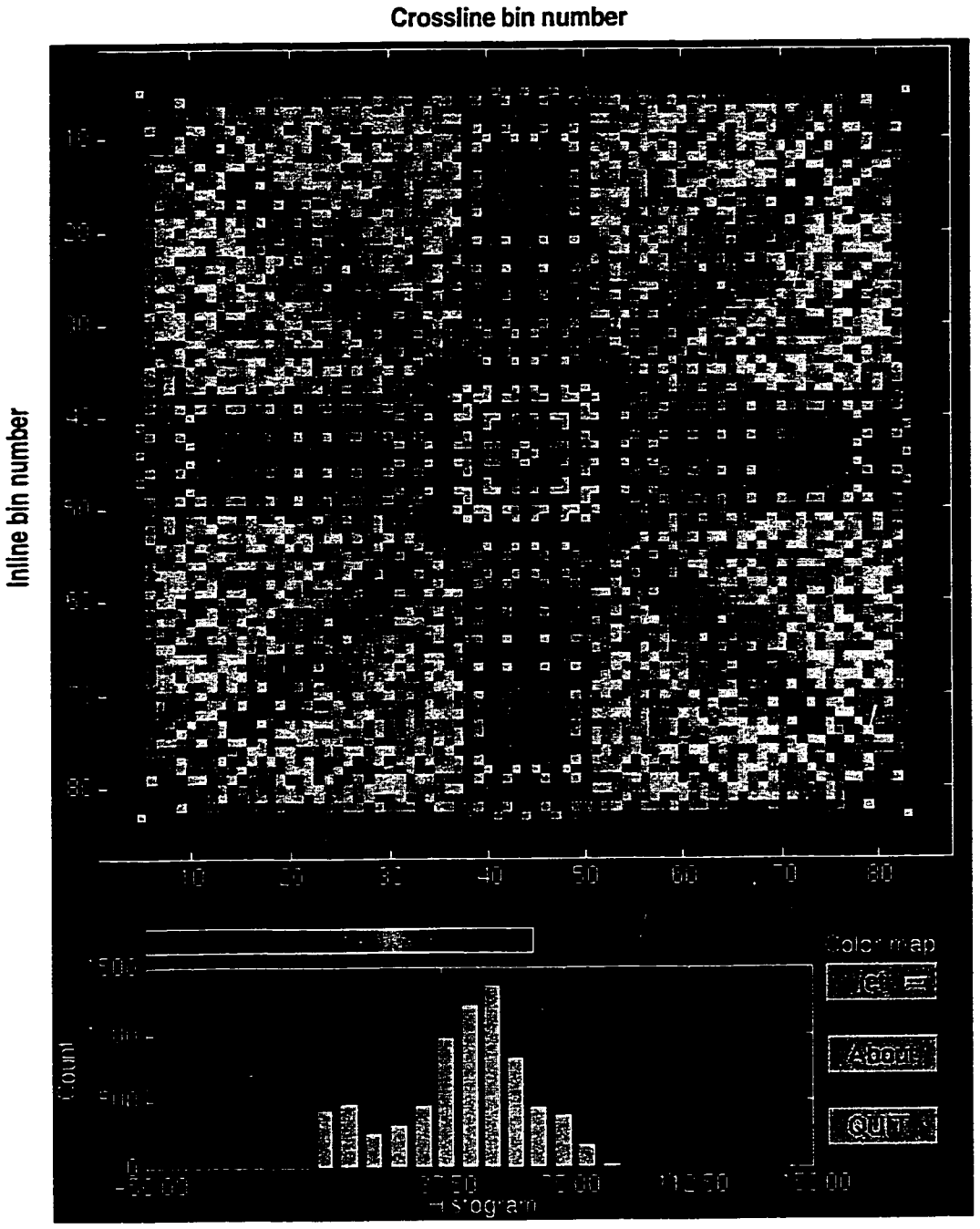

FIG. 3.24. Bin fold distribution display of the third layer of the full dataset, the receiver interval is 50 m, shot interval is 40 m, bin size 15x15 with a bin shift of 7.5 m towards the north and east direction. Upper panel is an areal distribution and the lower panel is a histogram of the fold distribution.

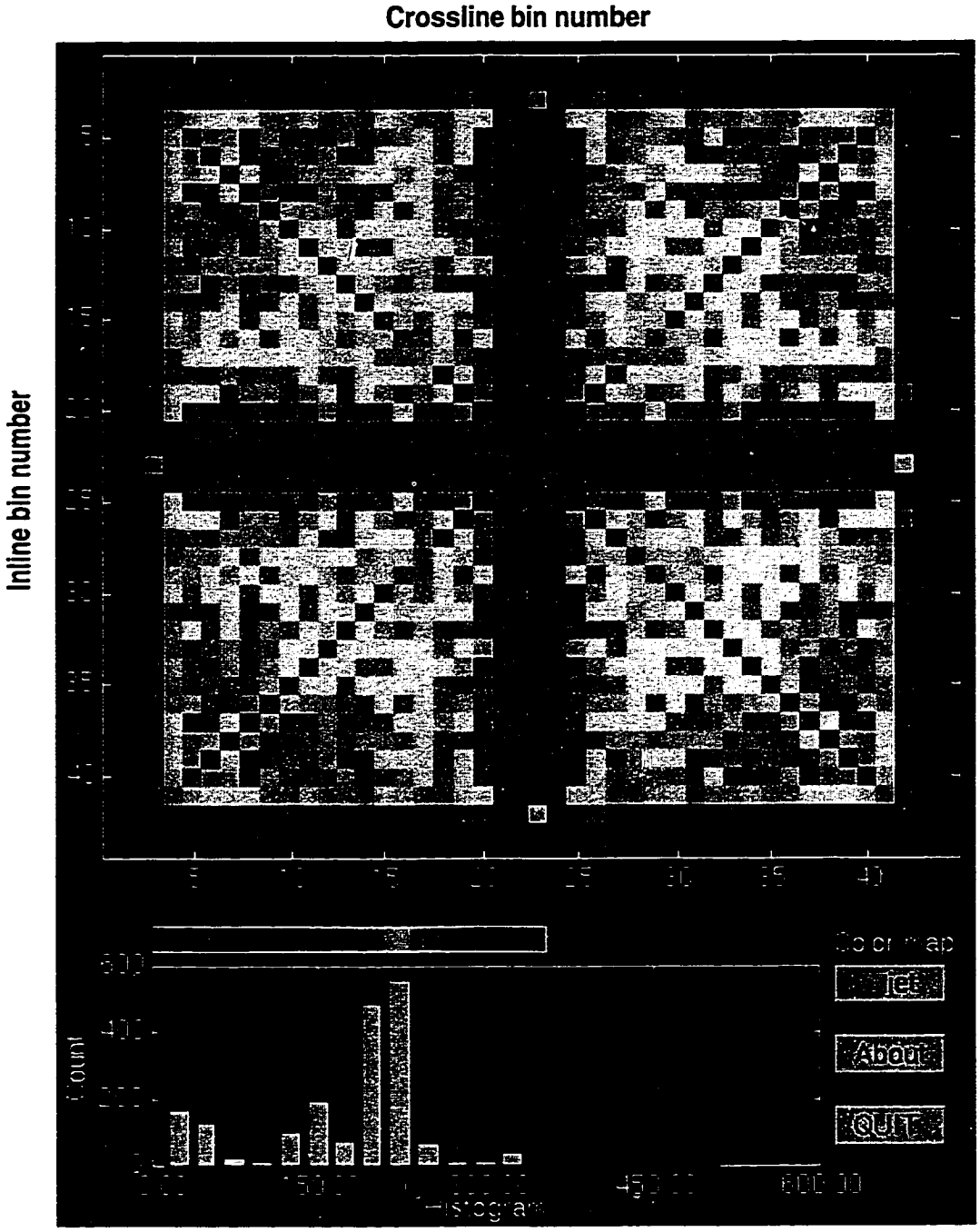

FIG. 3.25. Bin fold distribution display at the top of the third layer with the full shot and receiver and bin size of 30-by-30 m. Upper panel is an areal fold distribution, lower panel is a histogram of fold distribution. Receiver interval is 50 m, shot interval is 40 m.

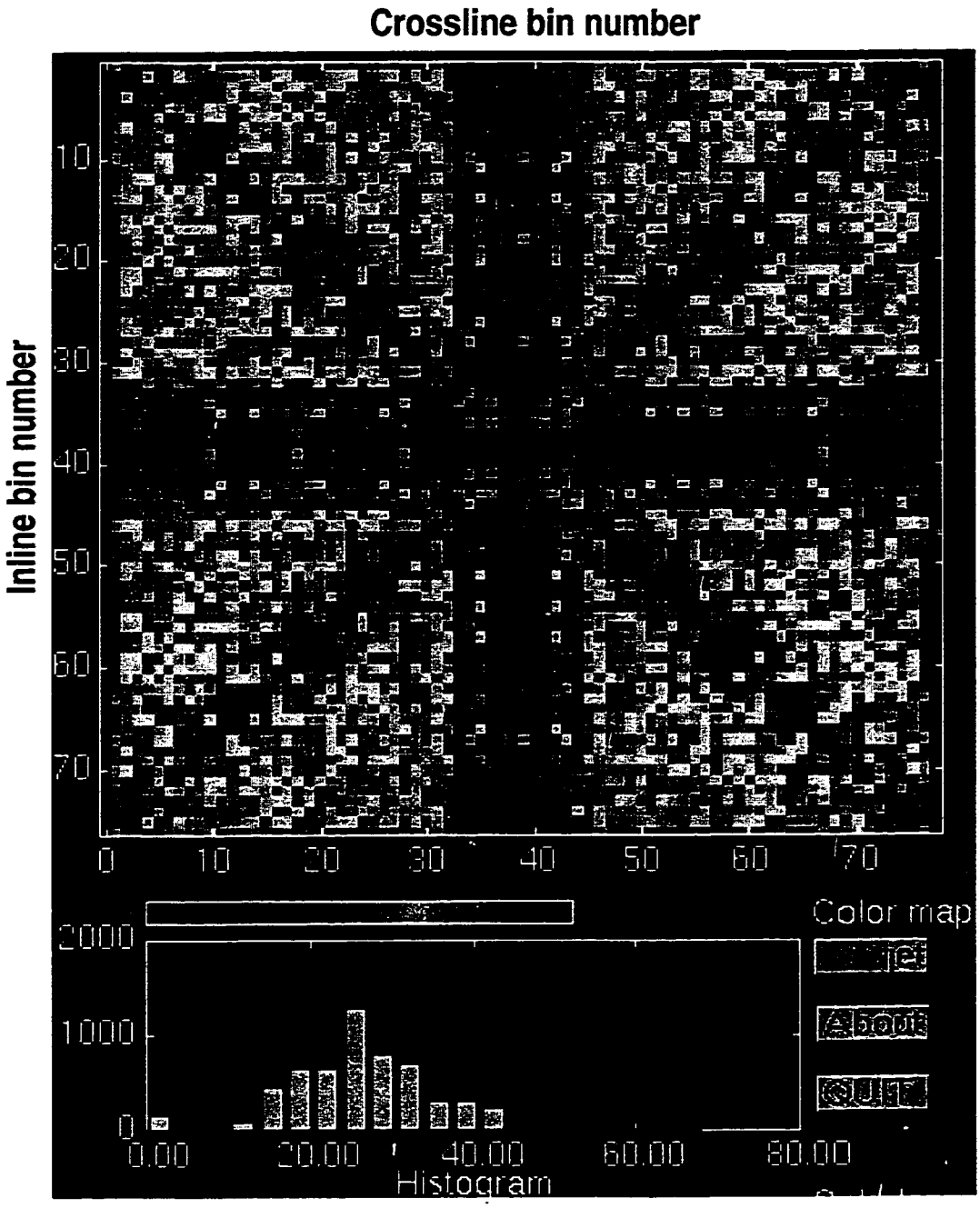

FIG. 3.26. Bin fold distribution display at the top of the third layer with all receivers (receiver interval is 50 m) and half shots (shot interval of 80 m) and bin size of 15 by 15 m. Upper panel is an areal fold distribution, and the lower panel is a histogram of fold distribution.

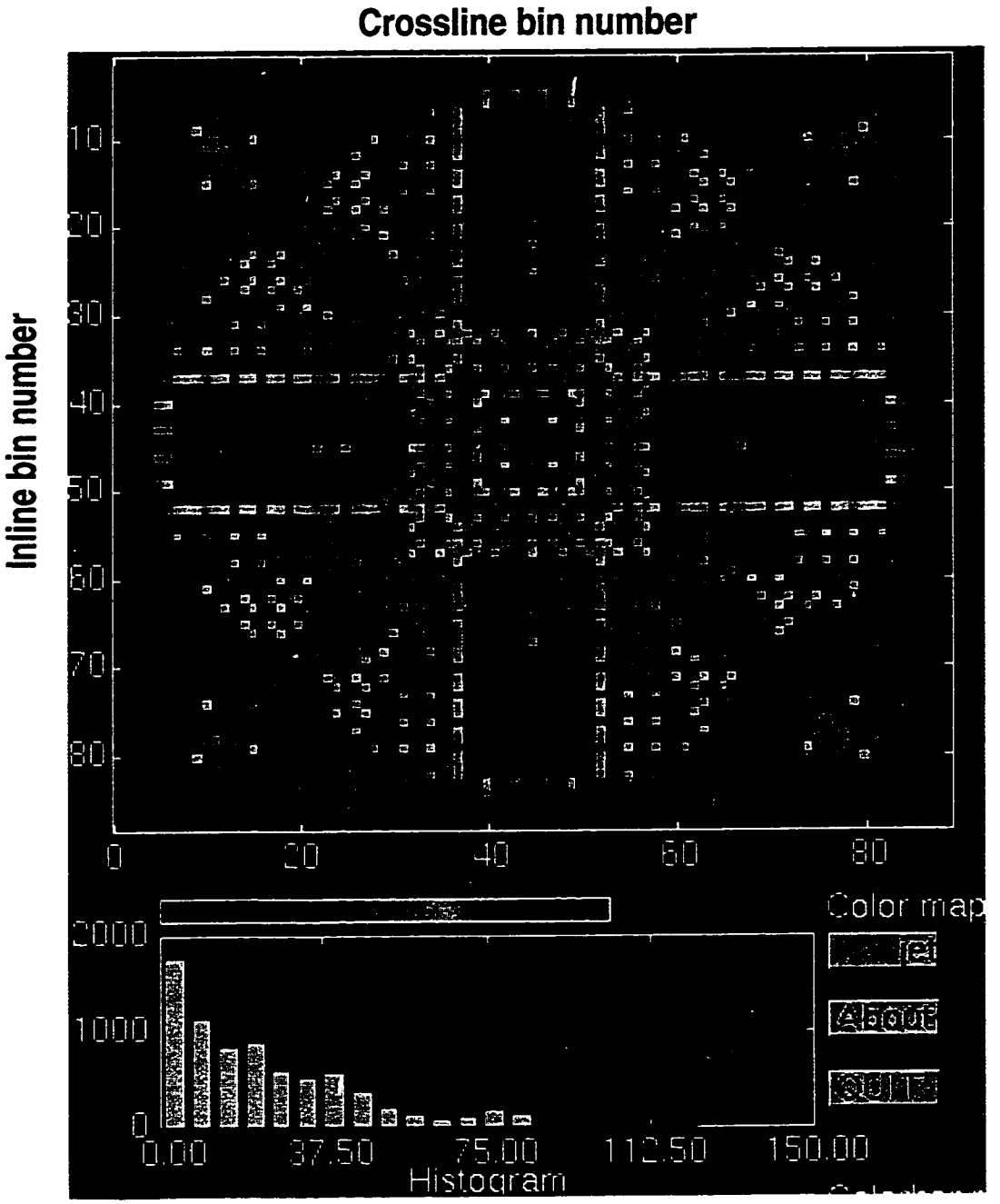

FIG. 3.27. Bin fold distribution using one quarter of the surface receivers (receiver interval of 100 m) and all shots (shot interval of 40 m) with bin size of 15-by-15 m. Upper panel is an areal distribution, the lower panel is a histogram of fold distribution.

Through these tests, it is found that the minimum bin size is 1/3 inline interval by 1/3 crossline interval.

3.4.3 Application of NMO correction

The approximate traveltime for 2-D VSP of *P-P* reflected wave (Stewart, 1991) is:

$$t = T_R + T_{RB} + \frac{X^2}{2\left[\tilde{V}_R^2 T_R + \tilde{V}_{RB}^2 T_{RB}\right]}, \tag{3.18}$$

where $\tilde{V}_R$, $\tilde{V}_{RB}$, T_R and T_{RB} are defined as in equation (3.13).

Extending equation (3.18) to the 3-D domain, the traveltime of the *P-P* reflected wave from the source to the receivers is written as

$$t = T_R + T_{RB} + \frac{\sqrt{\left(\Delta X^2 + \Delta Y^2\right)}^2}{2\left[\tilde{V}_R^2 T_R + \tilde{V}_{RB}^2 T_{RB}\right]}, \tag{3.19}$$

where ΔX and ΔY are the horizontal offset from the surface location to the well top in the x and y direction.

Equation (3.19) provides the NMO correction method for 3-D VSP wavefield. The amplitude of the seismic wavefield at time t is set to a two-way normal incidence *P-P* time (T_R) in the two-dimensional domain.

The NMO algorithm is performed on numerical 3-D VSP model datasets. The procedure is shown in Figure 3.28. The input data is the wavefield separated upgoing wave. RMS velocities and the raypath travel time are calculated by using a known interval velocity and depth information.

Figure 3.29 shows some of the results of NMO correction applied to inline (E-W direction) receivers of the numerical model. Data are sorted in common shot gathers with shot depth of 0.0 m (a and b), 120 m (c), and 320 m (d). Figure 3.29a and 3.30b are from

the same shot gather (shot depth=0 m, e.g. on surface) with the inline location of 1500 m (cross the well top, see Figure 3.1), and 2200 m (700 m away north from the well top) respectively. Comparing the two, it is clear that more stretching of the NMO correction occurs on the shallow event as the offset increases. Figure 3.29c shows the same receiver

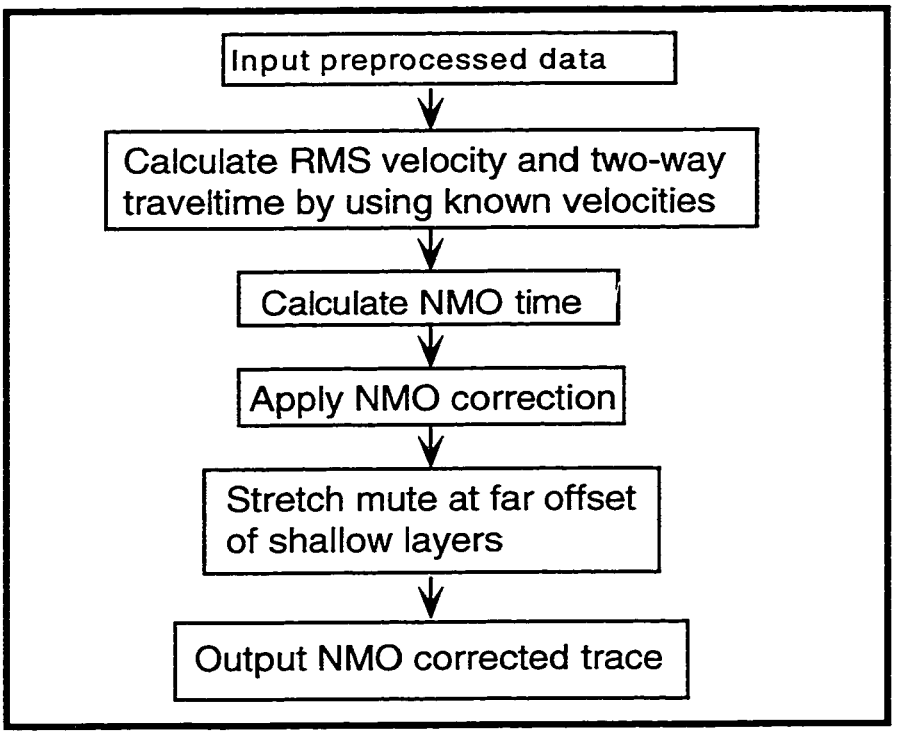

FIG. 3.28. 3-D VSP *P-P* wave NMO correction flowchart.

line as in Figure 3.29a with NMO correction applied; but the shot depth is 120 m down below surface. Comparison of Figure 3.29a and Figure 3.29c indicates that the deeper the shot depth the bigger the NMO stretch error. Figure 3.29d shows the NMO corrected shot gather inline located just 50 m away north form the well top (Figure 3.29c), but the shot depth is at 320 m down below the surface. The NMO stretching effect is even more serious, which is mostly due to the increase of shot depth.

Overall, the NMO correction performed particularly well on the deeper layers. The NMO correction error at the far offset on the shallow event can be explained by viewing equation (3.19). First, equation (3.19) is used to calculate the actual reflection traveltime

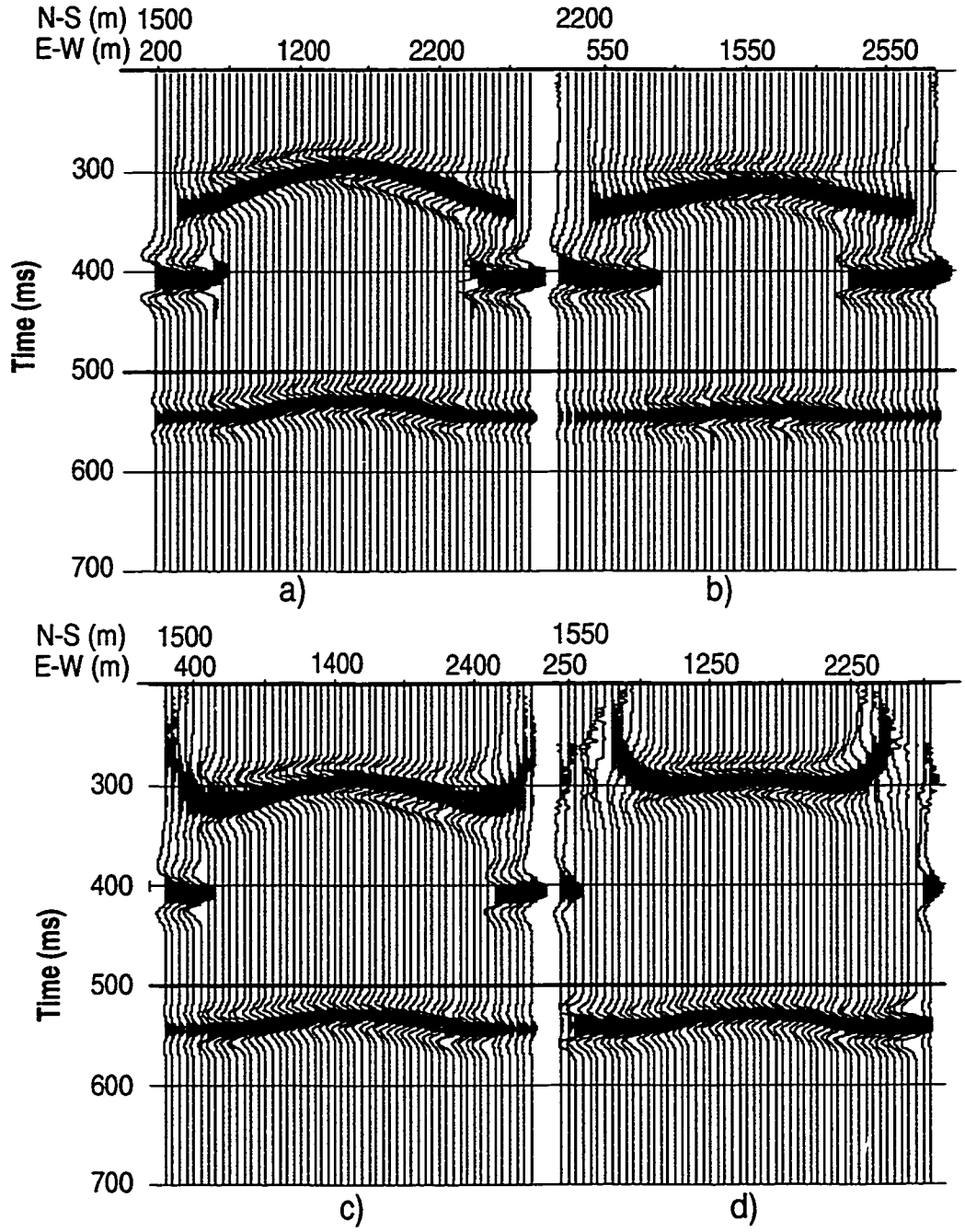

FIG. 3.29. NMO applied common shot gathers of numerical dome model with different shot depth. (a) receiver line cross the top of dome with shot on surface, (b) receiver line 700 m away north from the dome top with a shot on the surface, (c) receiver line cross the top of the dome with a shot depth 120 m, (d) receiver line cross the top of the dome with a shot depth of 320 m.

and correct it to the surface two-way traveltime. However, this equation was derived by assuming that the incident angle is small. The smaller the offset the better; for the same offset the deeper the better. Second, the depth of the tools (for VSP) or the depth of the shots (for RVSP) in the borehole contributes to the actual reflection traveltime. In equation (3.19) it is denoted as T_{RB}. When the depth is large T_{RB} is very small. The error caused by the large offset can be exaggerated in the reflection traveltime. It is found that for a horizontal offset greater than 1000 m in the model, NMO correction by using equation (3.19) will produce a large error at a layer depth of 800 m below the surface.

3.4.4 Binning and stacking applied to numerical data

The binning algorithm is applied on the modeling dataset. The flowchart of binning is shown in Figure 3.30. Due to the NMO stretch effects for far offset, the input is the NMO correction and the stretch mute applied dataset. There are four important parameters to be considered for binning: the maximum areal coverage, bin interval (size), azimuth in the bin; and fold. The maximum coverage is calculated as half of the maximum surface offset. The bin inline and crossline directions are defined the same as the surface inline and crossline directions. The bin interval (usually 1/3 of surface receiver interval) and the fold will be discussed next.

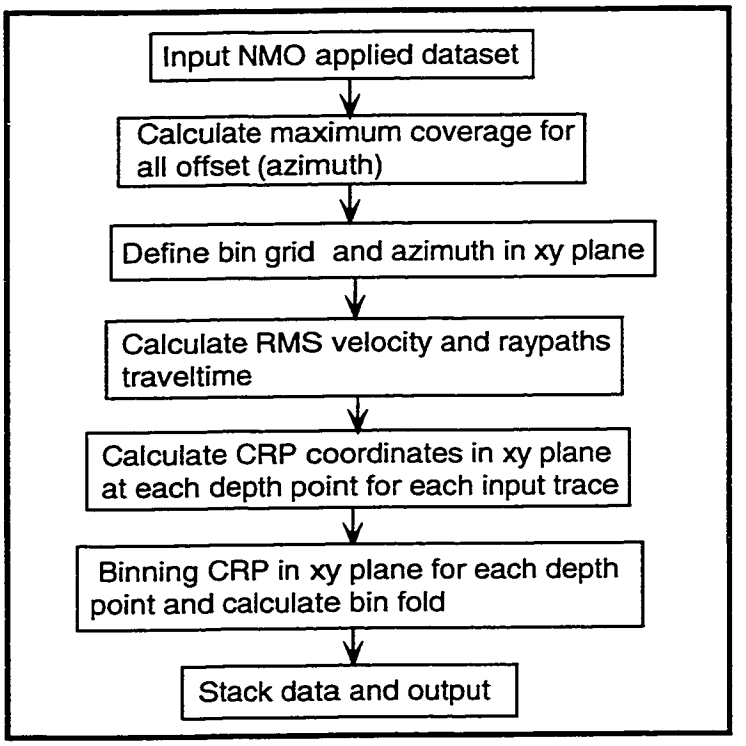

FIG. 3.30. 3-D VSP *P-P* wave binning and stacking flowchart.

As discussed above the 3-D VSP binning is depth variant; therefore, the RMS velocity and the raypath traveltime have to be calculated as the input parameters of equation (3.19). In practice, it is found that the bin interval of 15 m (approximately 1/3 of surface group interval) for both inline and crossline gives good results. Figure 3.31 shows the results of binning and stacking. Figure 3.31a is the N-S (crossline) stack section cross the top of the dome (cdp_x = 1515 m). Figure 3.31b is N-S (crossline) stack section 270 m away west from the dome top (cdp_x = 1230 m, close to the edge of the dome). It is clear that on the shallow events the NMO stretch and mute cause damage and distortion to the final stack section. The distortion is even more serious as the fold drops (Figure 3.31b shows the section location is moved to the edge of the dome, and the fold is low around the edge). The other important reason for the shallow events distortion is that the analytical binning algorithm is derived under assumption of a small incident angle and flat reflectors. This assumption certainly has a strong impact on the shallow events, especially to the shallow structure events.

Figure 3.32 shows stack sections of a simple numerical model with flat layers and a simple dip layer in the middle. Only minor distortion can be seen (see Figure 3.29a). The events are well imaged, however, a section from the lower fold area shows a clearer shallow event distortion (see Figure 3.32b).

3.5 Conclusions and discussions

A 3-D RVSP numerical modeling experiment with three-component (3-C) receivers is implemented here by raytracing through a model consisting of three layers with a dome on the top of the second layer. It is found that the converted-wave (*P-S*) image has wider coverage than the *P-P* wave. Compared with the *P-P* wave, deeper reflectors can be imaged by the P-S wave. The dome in the model has a reflector dip angle variation of 0° to 36.9° (dipping away from the borehole) and can be 60-70% imaged by the *P-S* wave, but can only be imaged 30-40% by the *P-P* wave. For a flat interface, 75% of the source-receiver offset from the borehole can be imaged by the *P-S* (V_P/V_S ratio dependent) wave, while the *P-P* wave can only image 50%. This is opposite to the normal VSP. Practically, for a source-receiver offset of 2500 meters, the *P-S* wave can image a reflector of a dip

angle of 30° while the *P-P* wave can only image 20° in both cases that reflector dips away from borehole.

A Fresnel zone of 68 m for *P-P* wave and 50 m for P-S wave should be taken into account for migration aperture in RVSP acquisition. The Fresnel zone of P-S for VSP is only 45 m.

3-D VSP binning has both characteristics of VSP and surface 3-D seismic. Surface geometry is used to determine the bin size and bin azimuth. The surface receiver interval (for RVSP) or shot interval (for VSP) is the key factor of influencing the bin fold. The number of downhole positions (either source or receiver) is the major parameter for the bin size. Changing the number of the downhole locations or the tool interval does not have much influence on the distribution of the bin fold.

The analytical NMO correction and binning algorithm works reasonably well except for the shallow events. However, for the very shallow reservoir or structure area, a ray tracing binning, and stacking algorithm is required for a proper stack section. Finally, pre-stack migration is required to position the geology properly.

Chapter 4 – Cross-calibration and normalization of time-lapse data

4.1 Introduction

In the laboratory, when oil sands are heated, the *P*-wave velocity drops significantly (Wang and Nur, 1989). This provides the basis of how seismic data can be used to understand reservoir status and monitor heavy oil production. However, interpretable field results at Cold Lake were not obtained until the early 1990's (Eastwood et al., 1994; Eastwood, 1996a and b). It is critical to understand the reservoir temperature and pressure for reservoir monitoring to be successful as they are the two important parameters controlling fluid phases (liquid or gas). Seismic data can detect gas or vapor reasonably well (bright spot). It is not as easy for seismic analysis to differentiate a water-versus-oil boundary.

In the Cold Lake B trunk production area, 46 infill wells were drilled after it was discovered that only about 50% of reservoir had been accessed after 10 cycles of steam.

In the survey area there are two types of wells: CSS and IOI wells. A CSS well is a cyclic steam stimulation well through which steam is injected into reservoir and bitumen is produced. An IOI well is an injector-only-infill well through which only steam is injected into reservoir. Figure 4.1 shows a surface view of CSS wells and IOI wells. Infill (IOI) wells were drilled in 1996 based on the steam conformance mapped by seismic data surveyed in 1995 (Eastwood, 1996b, see Figure 4.2). These wells were mostly drilled in the cold reservoir (undepleted area, blue in color) except that three (B5-

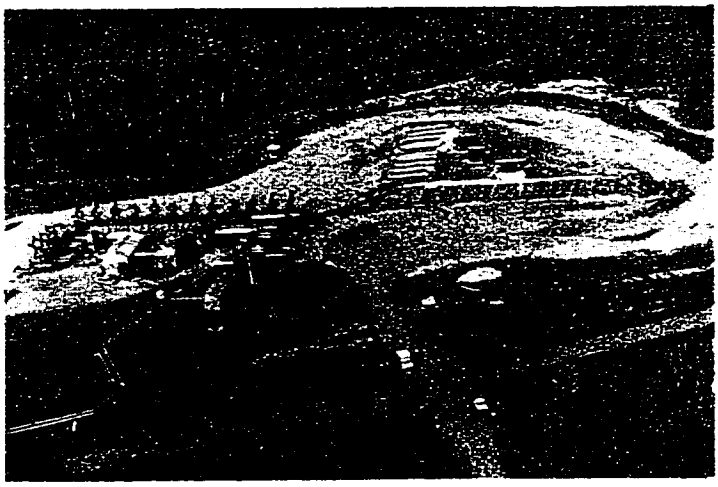

FIG. 4.1. B5 pad surface view showing CSS wells (lower left) and IOI wells (upper right).

29, B5-33, and B2-42) were drilled for the purpose of examining the steam mapping technique and data collection (cores and chips).

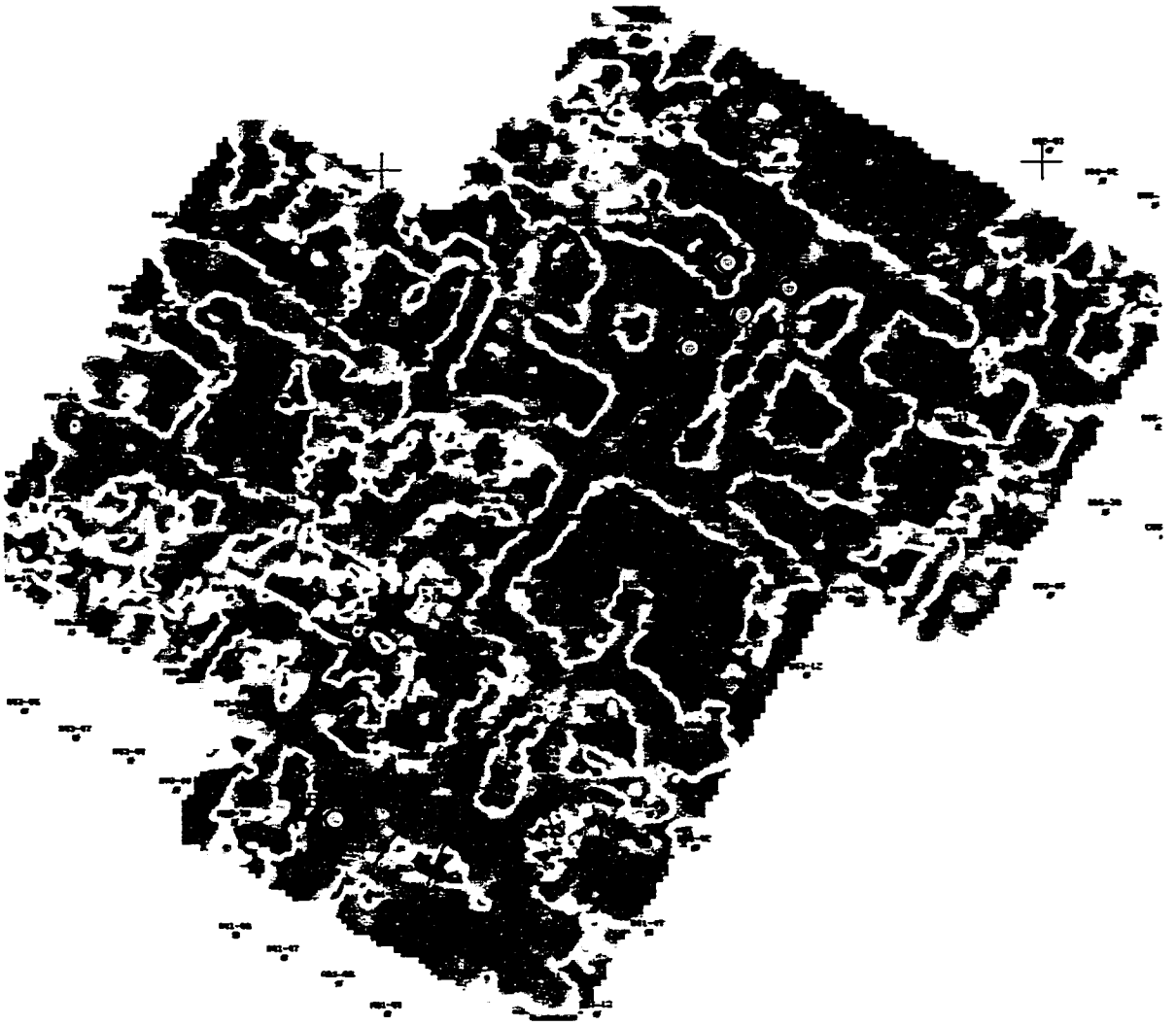

FIG. 4.2. B2B4B5B6 pads 1995 steam conformance (hot - red, cold - blue) and infill (IOI) wells trajectory (black bars) within reservoir interval.

The infill drilling results correspond well with the seismic interpretation. Figure 4.3 shows the core analysis results and formation temperature log from two infill wells (B5-33 as a hot location and B5-28 as a cold location) at B5 pad; and both wells are compared with original CSS well B5-08 that was drilled in 1985. A significant drop of oil

saturation is shown at the hot location (Figure 4.3a). The temperature can reach as high as

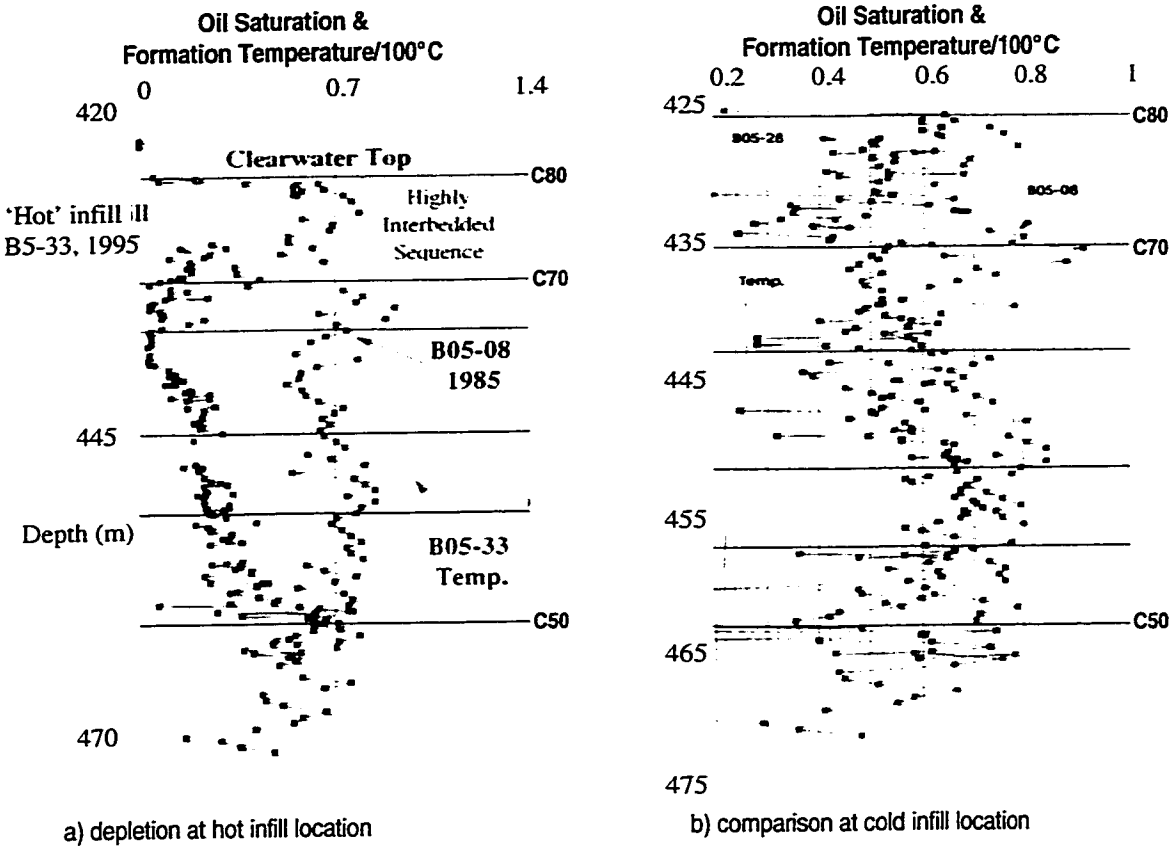

FIG. 4.3. Oil saturation and formation temperature at infill drilling locations: a) saturation difference showing depletion at hot infill location, b) saturation comparison at cold infill location.

140 °C in the production phase. However, the difference of oil saturation at cold location is small (Figure 4.3b). The temperature was about 25 °C as the highest in the formation.

The survey was repeated in late 1997 to understand steam conformance in this new phase and further evaluate IOI steam injection performance. The ultimate goal is to tie the production data with seismic by comparing pads with infill drilling and without infill drilling. In the past time-lapse seismic surveys were analyzed independently. By comparing two independent results a conclusion about reservoir dynamic change can be drawn. This approach is challenged when the questions rise: how consistent they are between the results of two surveys; and when the later reservoir status is unknown or

partially unknown can cross-calibration build up the bridge to obtain new parameters. This chapter will mainly address time-lapse seismic data normalization and calibration.

4.2 Seismic attributes and discriminant analysis

The attributes are extracted from a window encompassing the reservoir. The extraction window may be slightly broader than the reservoir interval for both amplitude-based attributes and frequency-based attributes. The extraction window usually starts 10 ms above the Clearwater reservoir top and ends 10 ms below the approximate bottom of the Clearwater. In the frequency domain, the extraction window is actually extended with an additional interpolation zone on both sides to reduce edge effects from the spectral calculations. There are 47 amplitude attributes and 35 frequency attributes. Only significant attributes are chosen for the discriminant analysis. The selection criteria for seismic attributes to map the heated reservoir zone are as follows (physical and mathematical aspects). From the rock physics stand point, seismic waves recognize steam zones for three major reasons. The most critical reason is that natural gas evolves from bitumen when the reservoir pressure is in the right range (2 to 3 MPa). In particular, for the Cold Lake data set with temperature effect the P-wave velocity drops from 2300 m/s in oil sands with 0% gas saturation to 1850 m/s with 2-5% gas saturation. Increasing the rock temperature also causes a decreasing rock velocity. In the situation with high temperature and low pressure there exists vapor in the heated zone, which causes a similar seismic response to gas. Due to the gas effects attributes associated with amplitude change (bright spot) are chosen such as peak amplitude and average absolute amplitude. Frequency-domain attributes such as central frequency are also chosen as they are related to seismic attenuation in the steam zone. The second criterion for attribute selection is to

Table 4.1 Chosen attributes for reservoir monitoring.

AP	Peak amplitude
AAB	Average of absolute amplitude
PAV	Average of positive amplitude
DMX	Maximum duration of loop
DECIL2	Low frequency
DECIL8	High frequency
CENTFREQ	Central frequency

correlate each individual attribute with wells (cyclic steam stimulation and injector-only-infill wells) in area. The ones with the best tie are chosen. Finally, the attributes chosen should be mathematically stable through the data volume. Highly redundant (highly correlated) attributes should be removed though more or less there exists redundancy between attributes. In particular, Table 4.1 shows chosen attributes for Cold Lake reservoir monitoring.

Discriminant analysis is the supervised classification through computing posterior probability. Unlike cluster analysis, discriminant analysis is implemented using a well calibration data set as supervision. There are two major different types of discriminant analysis algorithms, parametric and non-parametric. The parametric algorithm is valid if each of the variables have 'normal distributions', while the non-parametric algorithm is valid when the variables do not have normal distributions. The seismic attribute (variable) histograms are sufficiently close to the normal distribution that the parametric approach is adopted.

There are two groups of wells (hot wells and cold wells) for Cold Lake steam conformance (reservoir sweep) mapping and reservoir monitoring. The seismic data needs to be classified into two groups - hot and cold. The seismic attributes have to be trained (registered) before discriminant analysis. Figure 4.4 shows the partial seismic CDP bin grid and wells with different status (hot and cold) from a survey area. The training process is to register the well status to the certain seismic traces that satisfies a geometric condition. Usually, the training is implemented within a radius around the well. The radius is determined by the knowledge of reservoir status around the well. For example, a cyclic steam stimulation (CSS) well with many cycles of steam can heat the reservoir laterally more than 10 m in radius. Figure 4.5 shows the trained seismic traces (grid) from the original seismic grid (Figure 4.4). In this case a training radius of 12 m for hot wells and 14 m for cold wells are used. Each observation (trace) in the trained data set has a group number (n, 1 for cold and 2 for hot) assigned (see Table 4.2). Suppose that $\mathbf{x}$ is the trained data set (matrix). The covariance matrix ($\mathbf{S_n}$) within-group is expressed as follow:

$$\mathbf{S_n} = \frac{1}{F_n - 1} \sum_{j=1}^{L_n} w_j f_j (\mathbf{x_j} - \bar{\mathbf{x}}_\mathbf{n})(\mathbf{x_j} - \bar{\mathbf{x}}_\mathbf{n})^T \tag{4.1}$$

where F_n is the sum of the frequencies of the observations in group n, Table 4.2 shows the sum of the frequencies in group 1 (cold class) is 18, L_n is the total number of observations in group n, $\mathbf{x_j}$ is the j-th observation vector (e.g. obs 10 in Table 4.2), $\bar{\mathbf{x}}_\mathbf{n}$ is the mean (mean of each variable, e.g. aab in Table 4.2) vector of the observations in group n, w_j is the weight of the j-th observation in group n, f_j is the frequency of j-th observation. Both w_j and f_j are set to 1 for the seismic attribute analysis. The mean vectors ($\bar{\mathbf{x}}_\mathbf{n}$) are computed as follows:

$$\bar{\mathbf{x}}_\mathbf{n} = \frac{1}{W_n} \sum_{j=1}^{L_n} w_j f_j \mathbf{x_j} \tag{4.2}$$

where

$$W_n = \sum_{j=1}^{L_n} w_j f_j \tag{4.3}$$

W_n is actually the total number of observations for $w_j = 1$ and $f_j = 1$. These parameter values are used in seismic attribute discriminant analysis.

Let $\mathbf{V}$ denote either the pooled covariance matrix $\mathbf{S}$ or one of the within-group covariance matrices $\mathbf{S_n}$ (the pooled covariance matrix $\mathbf{S}$ will be used in linear discrimination, within-group covariance matrix $\mathbf{S_n}$ will be used in quadratic discrimination). The squared distance from observation $\mathbf{x_j}$ (for a cdp location) to group n is

$$d_n^2 = (\mathbf{x_j} - \bar{\mathbf{x}}_\mathbf{n})^T \mathbf{V}^{-1} (\mathbf{x_j} - \bar{\mathbf{x}}_\mathbf{n}) . \tag{4.4}$$

The group-specific density estimate at $\mathbf{x_j}$ from group n is then given by

$$f_n(\mathbf{x_j}) = (2\pi)^{-p/2} |\mathbf{V}|^{-1/2} \exp(-0.5 d_n^2(\mathbf{x_j})) \tag{4.5}$$

Using Bayes' theorem, the posterior probability of $\mathbf{x_j}$ belonging to group n is

$$p(n|\mathbf{x_j}) = \frac{q_n f_n(\mathbf{x_j})}{\sum_{k=1}^{K} q_k f_k(\mathbf{x_j})}, \tag{4.6}$$

where the summation is over all groups which is also called the estimated unconditional density at $\mathbf{x_j}$, K is the total number of groups, q_n is the prior probability of an observation $\mathbf{x_j}$ belonging to group n. Considering two different types of discrimination and whether the prior probabilities are equal or not, the squared distance from $\mathbf{x_j}$ to group n is generalized as

$$D_n^2(\mathbf{x_j}) = d_n^2(\mathbf{x_j}) + g_1(n) + g_2(n) \tag{4.7}$$

where

$g_1(n) = ln|\mathbf{S_n}|$ if the within-group covariance matrices are used, or

$g_1(n) = 0$ if the pooled covariance matrix is used; and

$g_2(n) = -2ln(q_n)$ if the prior probabilities are not all equal, or

$g_2(n) = 0$ if the prior probabilities are all equal.

The posterior probability of $\mathbf{x_j}$ belonging to group n is then generalized and equal to

$$p(n|\mathbf{x_j}) = \frac{\exp(-0.5\, D_n^2(\mathbf{x_j}))}{\sum_{k=1}^{K} \exp(-0.5\, D_k^2(\mathbf{x_j}))} \tag{4.8}$$

Table 4.3 shows the statistics of the extracted attributes from seismic data. To make the different seismic attributes comparable, they have to be normalized before training and discrimination. The normalization is implemented by setting the standard deviation of 1.0 and mean value of 0.0 (see Table 4.4). The prior probabilities for both group 1 (cold) and 2 (hot) are set to 0.5. The discriminant analysis is applied to the trained data set. The results are listed in Table 4.5. There are 93 out of 95 observations originally trained as

cold class (group 1) classified into cold class, which is about 97.89% well to seismic tie for cold class. Only 2 observations have been classified from cold class into hot class. Also, 87 out of 95 observations are classified from hot class into hot class (91.58% well to seismic tie), and 8 out of 95 observations are classified from hot class into cold class. Finally, the discriminant analysis is applied to the whole survey area, and 8914 out of 11455 observations (77.82%) are classified into cold class while 2541 observations are classified into hot class. Discriminant analysis applied to the training data set is a way of quality control for seismic data processing and training radius. Improvement of seismic-to-well tie could be achieved by reducing the size of training radius if the mistie was due to too large of training radius. However, for the same radius a better well-to-seismic tie reflects better quality of processing.

Some individual attributes are plotted for part of the survey in Figures 4.6 - 4.8. The attributes are normalized to have a mean of zero and a standard deviation of unity (1.0). The maps are presented with two colored positing (red and blue) which span two standard deviations in the data on either side of the mean. The average absolute amplitude (aab, Figure 4.6) is providing an estimation of the seismic energy which is reflected from the interval. This attribute correlates very well with hot and cold wells. The peak amplitude (ap, Figure 4.7) is a measure of the single largest impedance contrast in the interval and should correlate with the top or bottom of steam conformance when steam chamber is present. When steam conformance is absent, this attribute reflects the single largest amplitude in the interval (e.g. a tight streak may cause that). The low frequency (decil2, the frequency value for which 20% of the energy is contained within, see Figure 4.8) provides a measure of the low frequency content in the seismic trace. This attribute is sensitive to seismic attenuation due to the presence of steam chamber.

The output of discriminant analysis is the posterior probabilities of belonging to each of the classes with value of 0 to 1. Figure 4.9 shows the contoured color plot of discriminant analysis that is the probability of belonging to the heated class (group 2). Compared with

the overall discriminant analysis results (Figure 4.9), there is more noise present in the individual attribute plots.

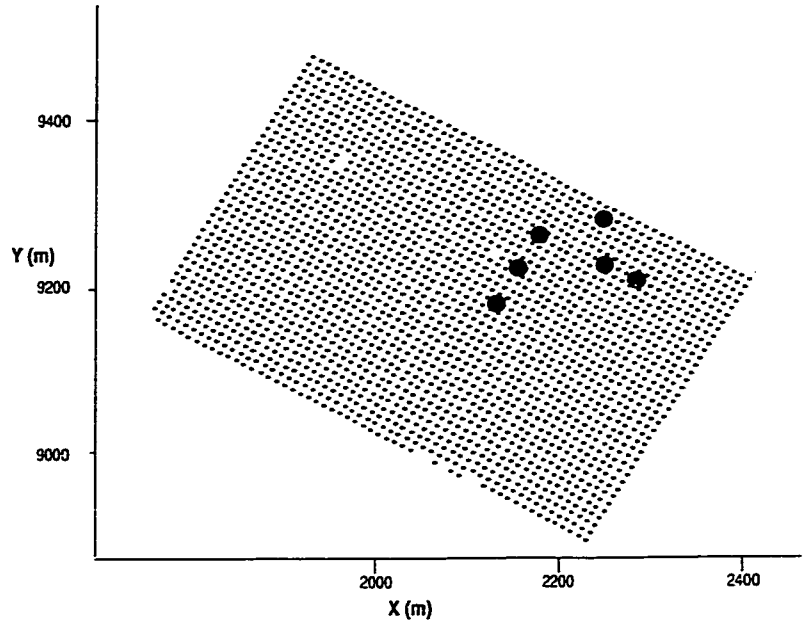

FIG. 4.4. Seismic grid and calibration wells (red circles are hot wells, blue circles are cold wells).

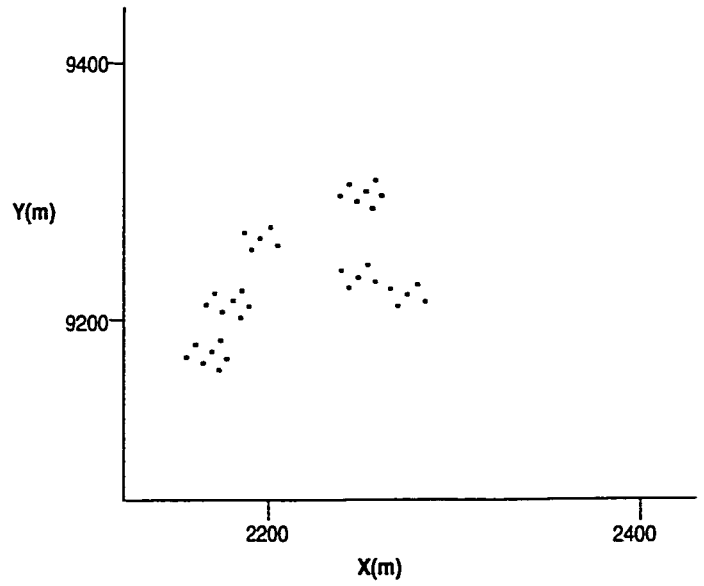

FIG. 4.5. A modification of Figure 4.4 showing seismic grid for training (red for hot, blue for cold).

Table 4.2. The training data set for 6 wells in Figure 4.1 (group 1 for cold, group 2 for hot).

obs	well	group	cdp_x	cdp_y	distance	aab	pav	ap	dmx	centfreq	decil2	decil8
1	well-1	1	2154	9170	13.34	-0.68	-0.573	-0.828	-0.843	-0.162	2.349	-0.18
2	well-1	1	2159	9179	10	-1.37	-0.879	-1.547	-0.955	0.358	2.526	0.708
3	well-1	1	2163	9165	8.94	-1.14	-0.55	-1.121	-0.71	-1.2	0.772	-0.685
4	well-1	1	2168	9174	1.41	-0.8	0.396	-0.623	-1.024	0.289	1.185	0.619
5	well-1	1	2172	9160	13.93	-0.71	-0.84	-1.305	-0.354	-1.38	0.063	-0.589
6	well-1	1	2173	9183	11.66	-1.46	-1.177	-1.288	-0.334	-0.064	0.495	-0.028
7	well-2	1	2165	9210	13.34	-1.11	-1.346	-1.26	0.093	0.232	-0.685	1.5
8	well-2	1	2170	9219	10	-1.06	-0.94	-0.947	-1.393	0.074	-0.126	1.426
9	well-2	1	2179	9214	1.41	-0.82	-0.818	-0.993	-1.403	-0.299	1.589	0.839
10	well-2	1	2183	9200	13.93	-1.1	-0.899	-1.15	-0.972	0.012	2.909	0.749
11	well-2	1	2184	9222	10.82	-1.01	-1.126	-0.791	-1.504	-0.147	4.041	1.067
12	well-2	1	2188	9209	10.77	-0.96	-1.054	-0.9	-1.201	-0.427	4.243	0.555
13	well-3	1	2246	9291	8.94	-1.15	-0.791	-1.087	-1.129	0.7	2.928	1.185
14	well-3	1	2237	9296	13.34	-1.13	-1.135	-0.672	-0.313	0.919	0.967	1.716
15	well-3	1	2242	9304	9.43	-0.87	-0.622	-0.642	-0.117	0.461	1.008	1.811
16	well-3	1	2254	9286	13.6	-1.58	-1.642	-1.558	-1.194	0.065	0.314	1.316
17	well-3	1	2256	9308	10.82	-0.7	-0.484	-0.516	0.306	-0.105	1.884	1.092
18	well-3	1	2259	9295	9.85	-1.77	-1.665	-1.556	-0.941	0.068	-0.639	0.877
19	well-4	2	2186	9267	9.43	0.669	-0.017	0.697	0.517	-0.086	-0.479	0.306
20	well-4	2	2190	92	9.85	0.199	-0.188	-0.501	0.316	-0.168	-0.643	0.023
21	well-4	2	2195	9262	1	1.884	0.896	0.555	0.012	-0.405	-0.131	-0.797
22	well-4	2	2200	9271	10.82	0.676	-0.138	0.319	0.196	0.09	-0.273	1.178
23	well-4	2	2204	9257	11.18	1.497	0.638	1.047	0.221	-0.487	0.062	-1.043
24	well-5	2	2238	9237	10.3	2.849	1.506	3.251	0.215	-0.648	-0.009	-1.182
25	well-5	2	2242	9224	9.43	1.247	0.011	0.968	-0.021	-1.787	-0.261	-1.144
26	well-5	2	2247	9232	0	2.824	0.859	2.994	-0.771	-0.642	-0.166	-0.942
27	well-5	2	2252	9241	10.3	2.365	1	1.688	0.727	-0.037	-0.407	0.266
28	well-5	2	2256	9228	9.85	2.904	1.313	2.623	-0.007	-0.726	-0.212	-1.526
29	well-6	2	2264	9223	10.82	2.506	1.279	2.461	0.403	-1.828	-0.381	-1.776
30	well-6	2	2268	9209	9.43	0.9	-0.273	1.863	0.223	-0.607	-0.335	-1.394
31	well-6	2	2273	9218	1	2.269	1.656	1.885	1.198	-0.599	-0.371	-1.725
32	well-6	2	2278	9226	10.3	1.175	0.499	0.734	0.316	0.165	-0.476	-1.077
33	well-6	2	2282	9213	9.85	3.366	3.082	2.275	-0.079	-0.56	-0.287	-1.429

Table 4.3. Basic statistics of seven seismic attributes.

NAME	MEAN	STD	N
AP	3744.073938	1214.541994	11469
DMX	9.655636	3.460257	11455
PAV	1315.561749	371.419608	11469
AAB	1238.878725	310.897530	11469
DECIL2	27.387908	14.555580	11469
DECIL8	104.925582	24.100546	11469
CENTFREQ	150.272209	33.024873	11469

Table 4.4. Basic statistics of zero-mean normalized seven seismic attributes.

Variable	N	Mean	Std Dev	Sum	Minimum	Maximum
AP	11469	0	1.0000	0	-2.1437	4.8025
DMX	11455	0	1.0000	0	-2.1162	5.5587
AAB	11469	0	1.0000	0	-2.8761	5.4308
DECIL2	11469	0	1.0000	0	-1.7746	5.3695
CENTFREQ	11469	0	1.0000	0	-2.4817	4.8708

Table 4.5. Discriminant analysis results of training data set.

From group	group 1	group 2	total
Group 1	93	2	95
percent	97.89	2.11	100
Group 2	8	87	95
percent	8.42	91.58	100
total	111	89	190
percent	53.16	46.84	100

Table 4.6. Discriminant analysis on the whole survey data set.

	group 1	group 2	total
obs	8914	2541	11455
percent	77.82	22.18	100

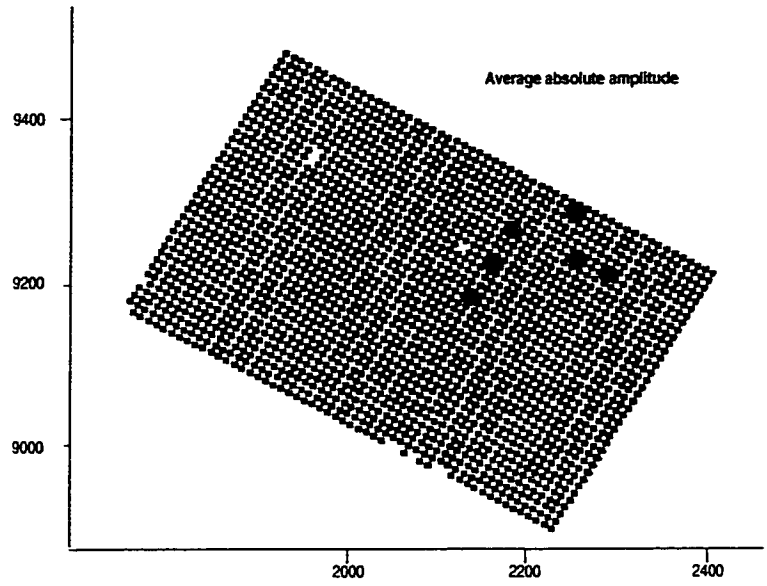

FIG. 4.6. Normalized, zero-mean attribute of the average of absolute amplitude posted as two classes, positive values are red, and negative values are blue.

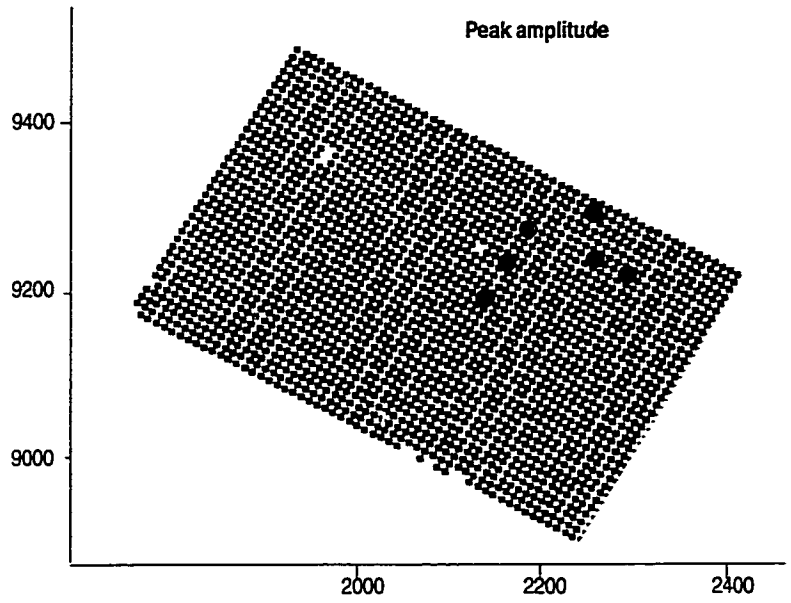

FIG. 4.7. Normalized, zero-mean attribute of peak amplitude posted as two classes, positive values are red, and negative values are blue.

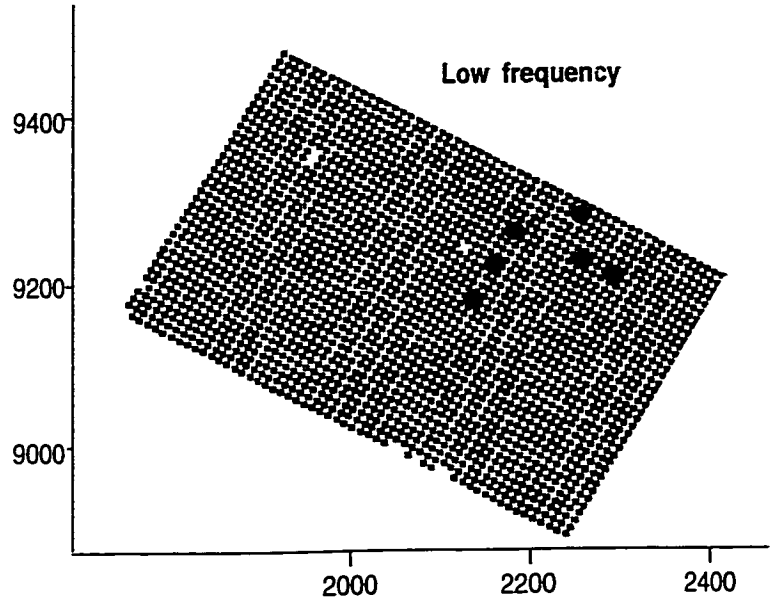

FIG. 4.8. Normalized, zero-mean attribute of low frequency posted as two classes, positive values are red, and negative values are blue.

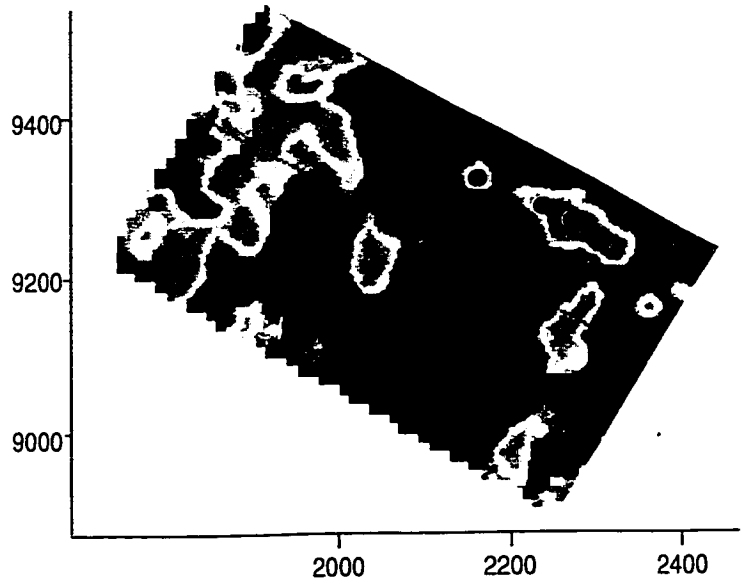

FIG. 4.9. Results of discriminant analysis contoured from 0 (blue, cold) to 1 (red, hot) with contour interval of 0.1.

4.3 Time-lapse data normalization filter

The Wiener-Levinson filter is used for time-lapse seismic data normalization (see Appendix A). A derived matching filter should be a wavelet-like pulse. The length of the filter should cover the major changes (both phase and amplitude) of the pulse. Figure 4.10 shows an example of 80 ms long shaping (normalization) filter (operator). The magnitude of the pulse indicates amplitude adjustment between two traces (surveys), and the fact that the pulse is not zero phase indicates phase change between two traces (surveys). Seismic data normalization can be applied to phase or amplitude alone, or by both. An average filter can be extracted and used to normalize seismic data between two surveys. Detailed discussions follow.

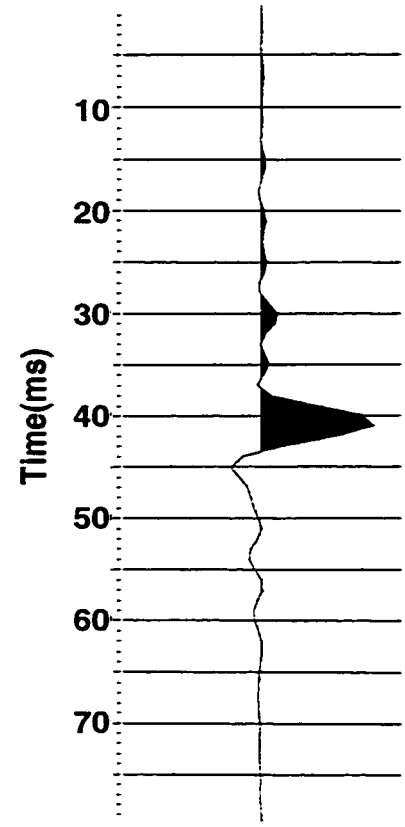

FIG. 4.10. A shaping filter for time-lapse data normalization.

4.4 Calibration sets

4.4.1 Time-lapse seismic surveys

Time-lapse seismic surveys (for example the 1995 survey versus the 1997 survey) conducted at B trunk area (also called B2B4B5B6 pads) of Cold Lake operation are analyzed to illustrate data normalization algorithm. The purpose of these surveys is to monitor the reservoir performance and to evaluate the joint well production pattern by combining cyclic steam stimulation (CSS) wells with the injector only infill (IOI), and to compare with simple CSS well production. The survey conducted in 1995 was used for defining the infill drilling locations (Eastwood, 1996a, 1996b). The 1995 survey was acquired at two separate times when reservoir pressures were similar throughout B trunk survey area. The southern part of the region was surveyed in April, 1995; the northern part was surveyed in June, 1995. To evaluate the infill well steam performance the 1997

survey was used to map the steam conformance. One line (inline 95) of repeated 3-D survey area is shown in Figure 4.11. The steam chamber is clearly seen in the reservoir portion on the seismic section (bright spot), and significant changes have occurred between surveys of '95 and '97 with amplitude increase and frequency drop especially on the left hand side of reservoir interval.

4.4.2 Well calibration sets

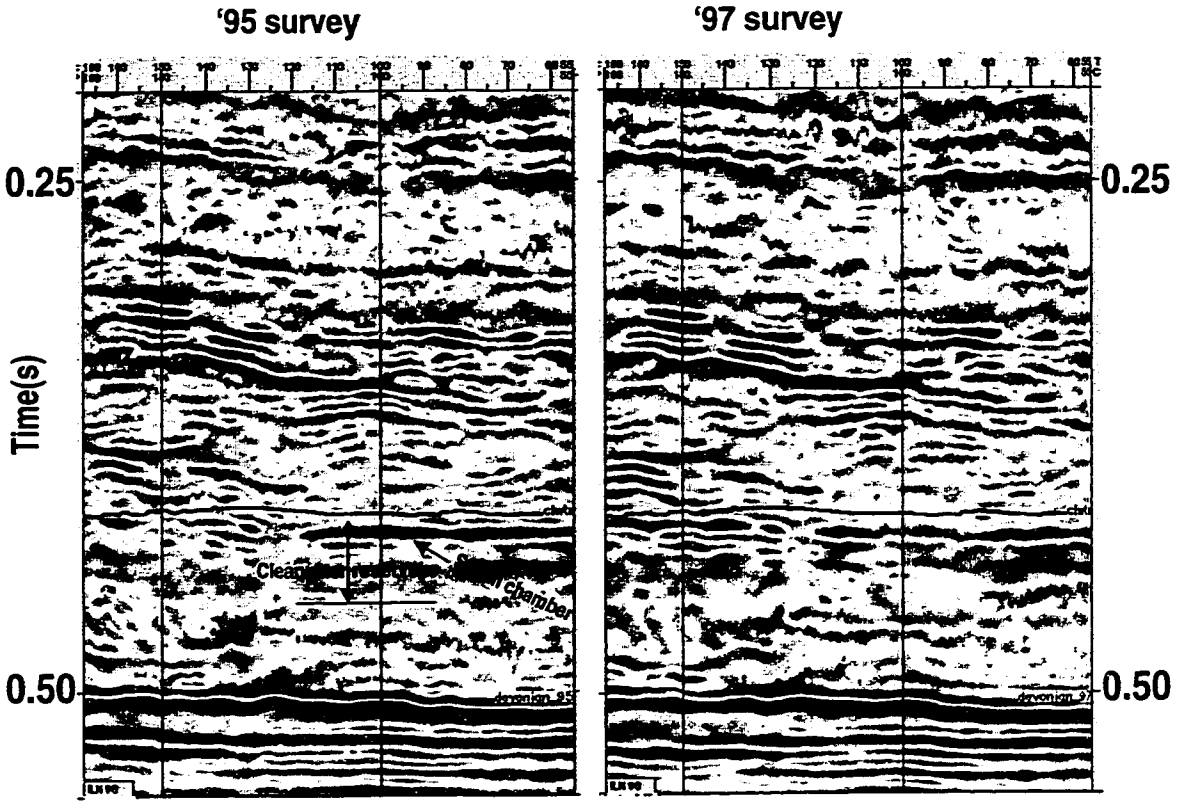

FIG. 4.11. Repeated 3-D seismic surveys (inline 95) of B trunk area, Cold Lake, Alberta. Steam chambers are developed in the reservoir interval on the left side of 1997 survey. Green horizon is Devonian top.

Based on 1995 infill drilling results and reservoir status (most CSS wells were hot except abandoned ones) **a well calibration set of '95** was developed (see Figure 4.12). Most of

CSS wells were hot (represented by red color). Cold wells at B02 and B05 pads were determined from infill drilling results. Cold calibration points (also called pseudo "wells") at B04 and B06 pads were determined through an iterative process. First, an initial steam conformance map was obtained from discriminant analysis of seismic attributes with a list of known hot and cold wells for the calibration set. Cold spots (points, pseudo "wells") were picked from this initial steam conformance map, and then vertical seismic sections were examined as a quality control to make sure that those spots are indeed "cold" (no steam disturbance, no brightness of amplitude, and no frequency drop or attenuation). Finally, cold pseudo wells are taken into account in seismic attribute calibration; crossplots of seismic attributes for such calibration lists are viewed to make sure that the selected cold pseudo wells are cold. In the B trunk time-lapse analysis, cold pseudo wells on B04 and B06 pads were consistently picked for both surveys of '95 and '97. All the CSS wells on the edge of survey area (green color) are excluded for calibration as seismic data quality goes down along the survey edge (fold drops, signal-to-noise goes higher).

The calibration set (well list) for '97 seismic survey was built differently (see Figure 4.13). The IOI wells should no longer be cold as one cycle of steam has been injected into the reservoir through these wells. Indeed, the purpose of '97 seismic survey was to monitor the IOI through mapping the updated steam conformance. Therefore, IOI wells are excluded in the '97 calibration set (represented by green color). Cold calibration points are only restricted on those cold pseudo wells on B4 and B6 pads. Pads B2 and B5 are avoided for cold calibration points for the '97 survey as these two pads are the IOI pilot study area. The well spacing on these two pads is much tighter. Most CSS wells are still hot (red) as steam was injected into them during first cycle of IOI. However, some CSS wells have significantly cooled as bitumen is produced. When used in the calibration set, these wells may be "warm". The crossplots of seismic attributes around this well may be scattering across hot-cold regions. Figure 4.14 shows seismic attributes

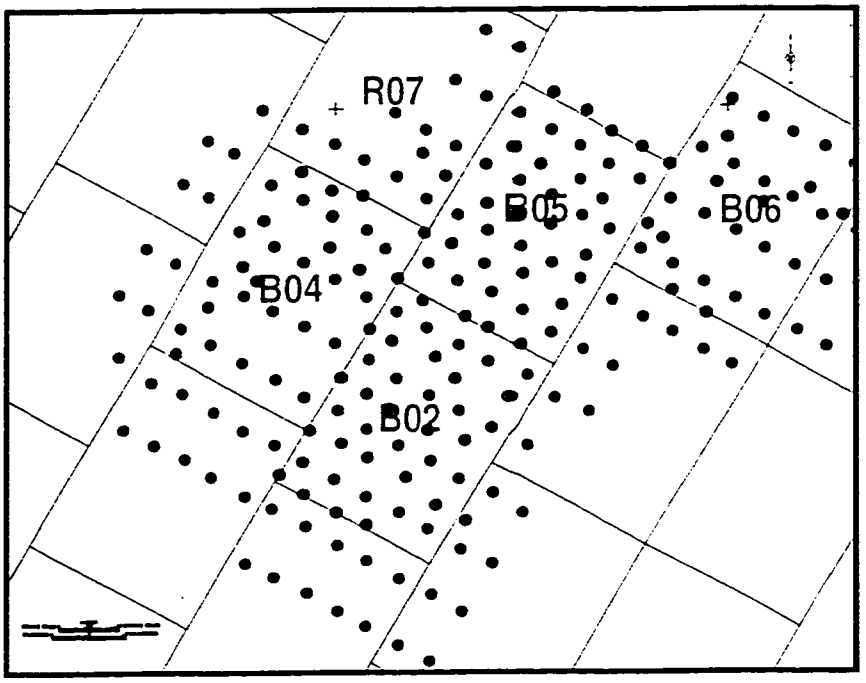

FIG. 4.12. Well calibration set based on 1995 well's status, red - hot wells, blue - cold wells, and green - wells excluded from calibration list.

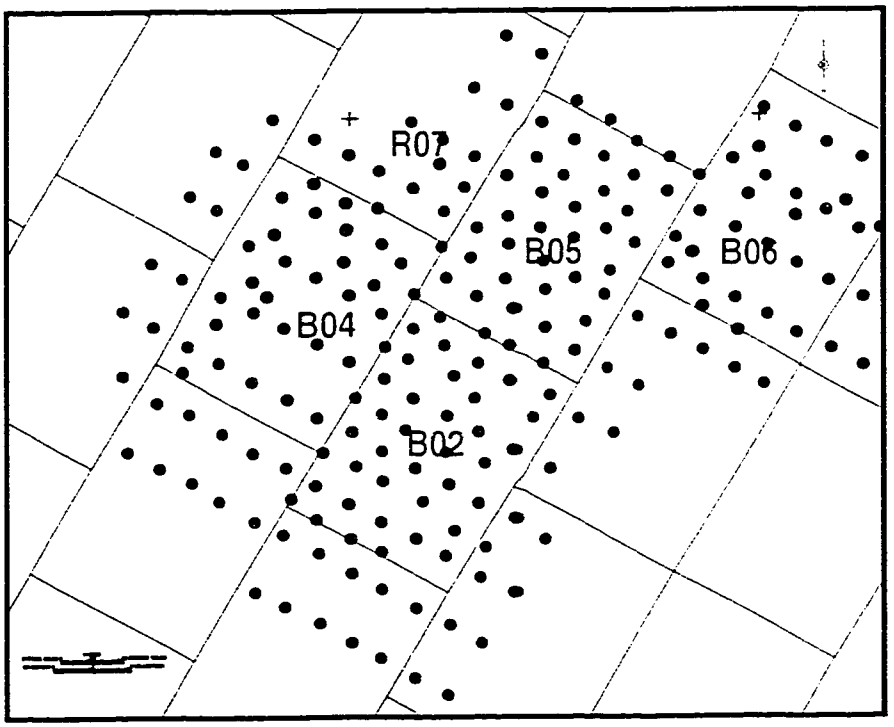

FIG. 4.13. Well calibration set based on 1997 well's status, red - hot wells, blue - cold wells, and green - wells excluded from calibration list.

crossplots of two attributes from trained data set with hot (red dots), cold (blue dots), and wells across boundaries between red and cold (green dots) within a certain training radius (red circle in Figure 4.14a). A well on the edge of steam chamber may behave like this through CSS during first cycle of IOI.

Two calibration sets discussed above have different features. Comparing the '95 calibration set with '97 calibration set, the '95 calibration set (Figure 4.12) has more robust cold calibration points as most of cold calibration points are drilling results (IOI wells). Also, statistically, it is better balanced in terms of the number of calibration points (wells) of hot versus cold (82 versus 78). The '97 calibration set, however, has an unbalanced number of hot to cold points (75:18).

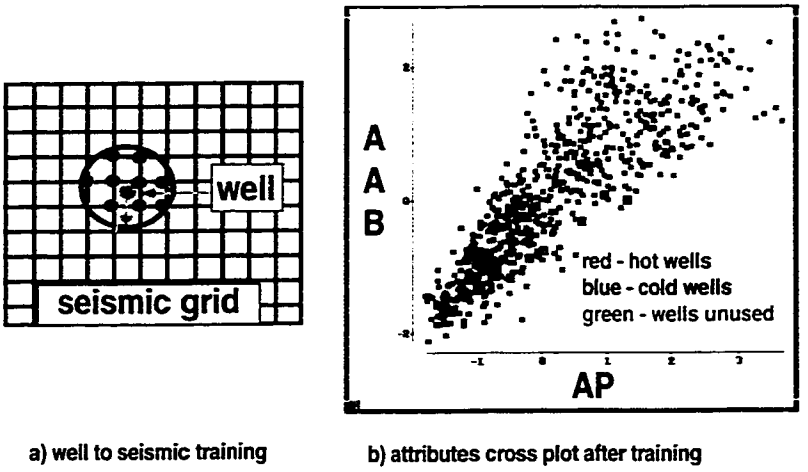

FIG. 4.14. Well to seismic attribute training within certain radius (a) and attributes crossplots (b) of average absolute amplitude (AAB) versus peak amplitude (AP) for a calibration well set.

To illustrate the importance of the calibration set, the '95 seismic survey data was analyzed using each of the two calibration sets. The correct steam conformance map of the '95 seismic survey is shown in Figure 4.15. It was obtained by using the '95 calibration set via discriminant analysis. However, the difference can be significant when a different calibration set was used. Figure 4.16 shows difference contours of pre-IOI steam conformance by using calibration sets of '95 versus '97. The difference was obtained by simply subtracting result with '95 calibration set from result with '97 calibration set. The difference ranges from -0.73 to 0.93 which are represented by different colors: green - blue - white - pink (see color legend in Figure 4.16). Most areas show a difference of -0.3 to 0.3 which can be assumed as relatively no difference in steam

conformance. Differences represented by white to pink colours indicate 0.4 or higher difference in steam conformance, which is significant. If the '97 calibration set was used, more hot reservoir is indicated. Figure 4.17 A & B show enlarged section of Figures 4.15 and 4.16. Two IOI wells (B2-29 and B2-35) were drilled based on the '95 steam distribution map (see Figure 4.16A). These two locations have been confirmed as cold

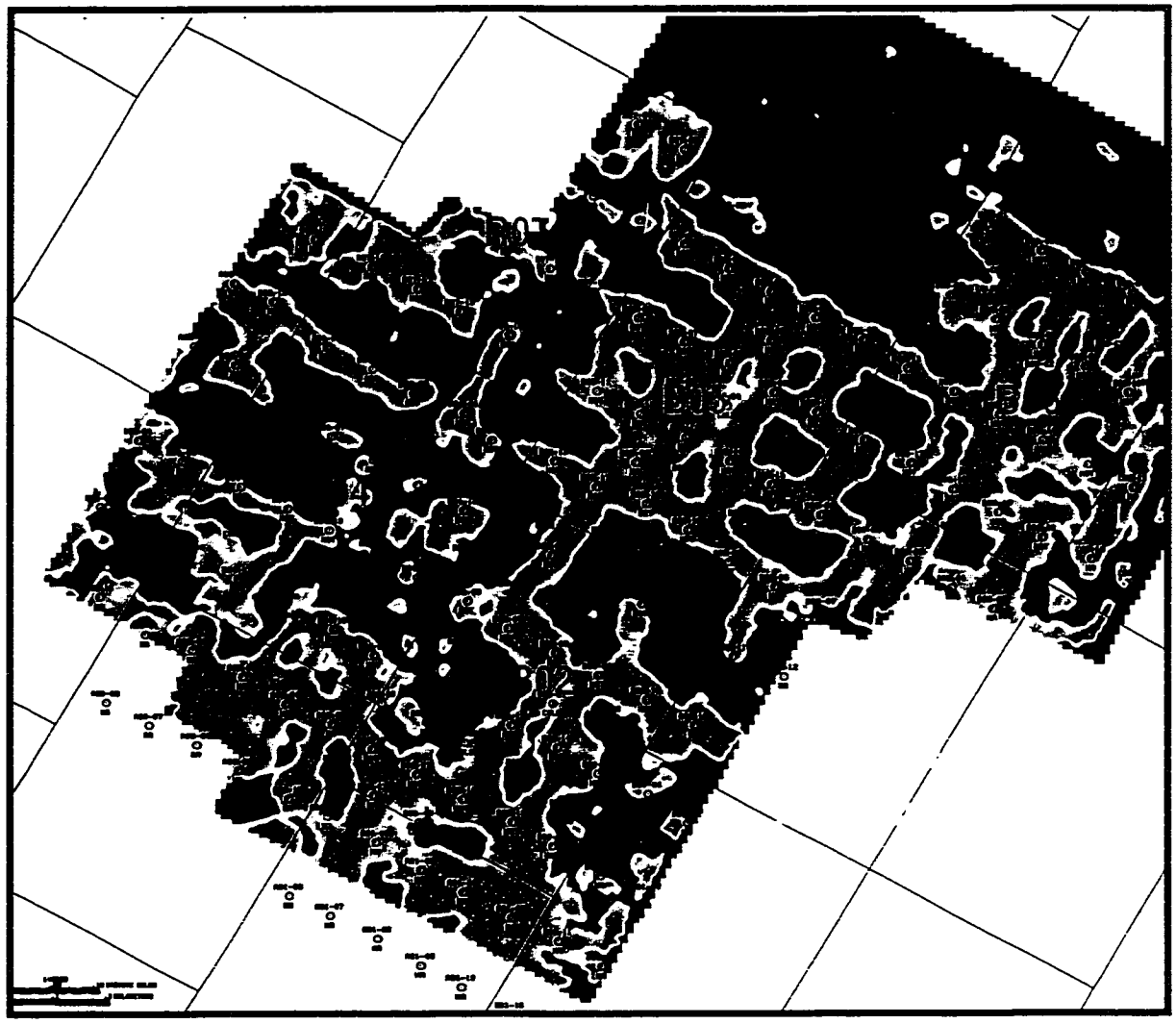

FIG. 4.15. The 1995 steam conformance map before injector-only-infill (IOI) wells. Obtained by using correct calibration set ('95 calibrations set, see Figure 4.5), pink - hot reservoir, blue - cold reservoir.

reservoir by drilling. However, with the inappropriate '97 calibration set, discriminant analysis indicates that these two locations are hot (see Figure 4.16B).

The examples above have demonstrated that calibration is a key factor for accurate analysis when a statistical method such as discriminant analysis is used in steam conformance mapping. The correct input of calibration and training set helps better classify seismic data (attributes) into the right categories. A proper calibration list requires experience and background knowledge of reservoir status including engineering, geophysics, and geology.

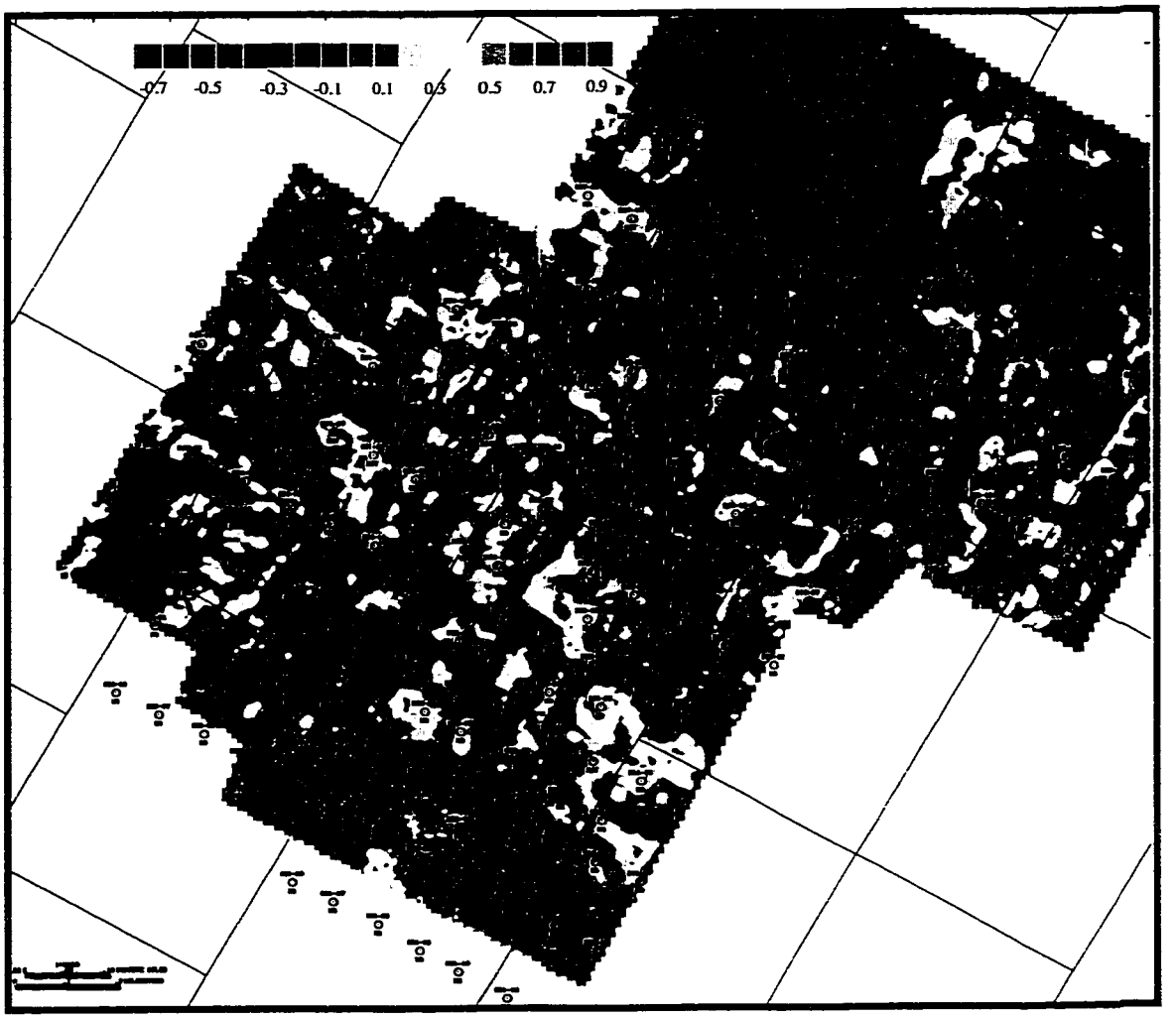

FIG. 4.16. Steam conformance difference of '95 survey when using different calibration sets (subtraction of result of '95 calibration from result of '97 calibration).

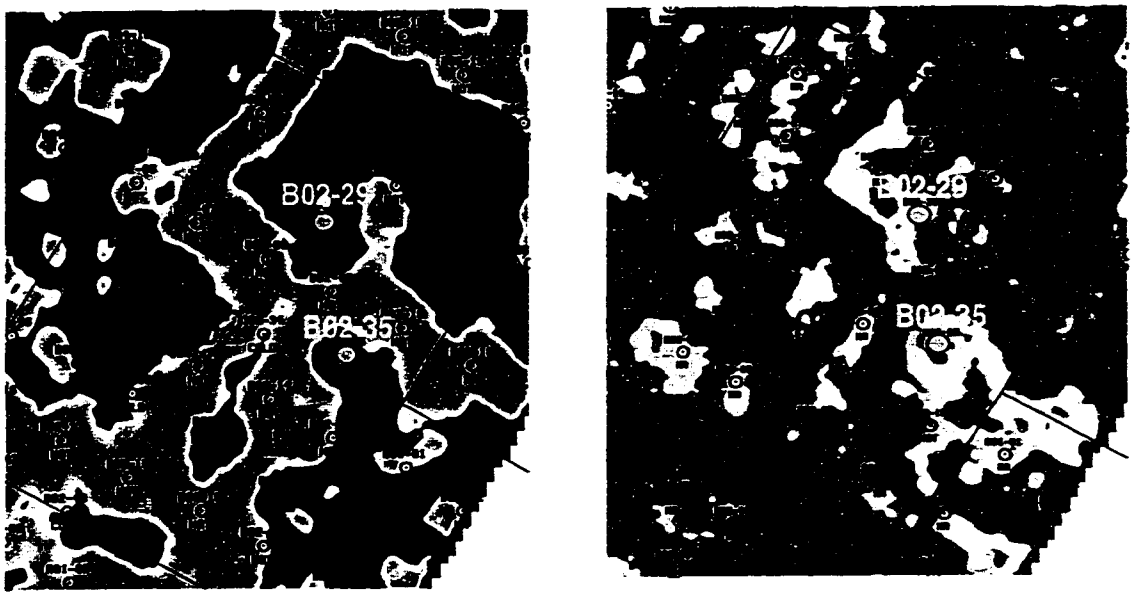

A) B02 pad '95 steam distribution

B) B02 pad '95 steam distribution difference

FIG. 4.17. B2 pad pre-IOI steam distribution (A) and steam distribution difference when using different calibration sets.

4.5 Cross-calibration and data normalization in time-lapse seismic analysis

4.5.1 Cross-calibration

For the '97 (post-IOI) steam conformance using the '97 calibration set, discriminant analysis provides the steam conformance map shown in Figure 4.18. This conformance map is not acceptable simply because there appears significant areal steam coverage on the northern pad locations where no wells have ever been drilled! It is clear that there significant artifacts in the result. Also, it is unlikely that with only one cycle that steam has almost reached everywhere in reservoir (compare Figure 4.15 and Figure 4.18). Even though the result is very discouraging the well-to-seismic tie statistics of the calibration set is quite good. This is a 99.12% tie for cold calibrations (18 wells) and 85.88% tie for hot calibrations (75 wells). Note that this calibration set has unbalanced

number of hot versus cold points (see Table 4.7). With existing calibration sets the other option we have is to use '95 calibration set. It may not be true to assume that IOI wells are still cold as we have sent one cycle of steam to the reservoir through these IOI wells.

Table 4.7 Well-to-seismic statistics for post-IOI survey with '97 calibration set.

	total calibration points	well to seismic tie
cold	113	99.12
hot	354	85.88

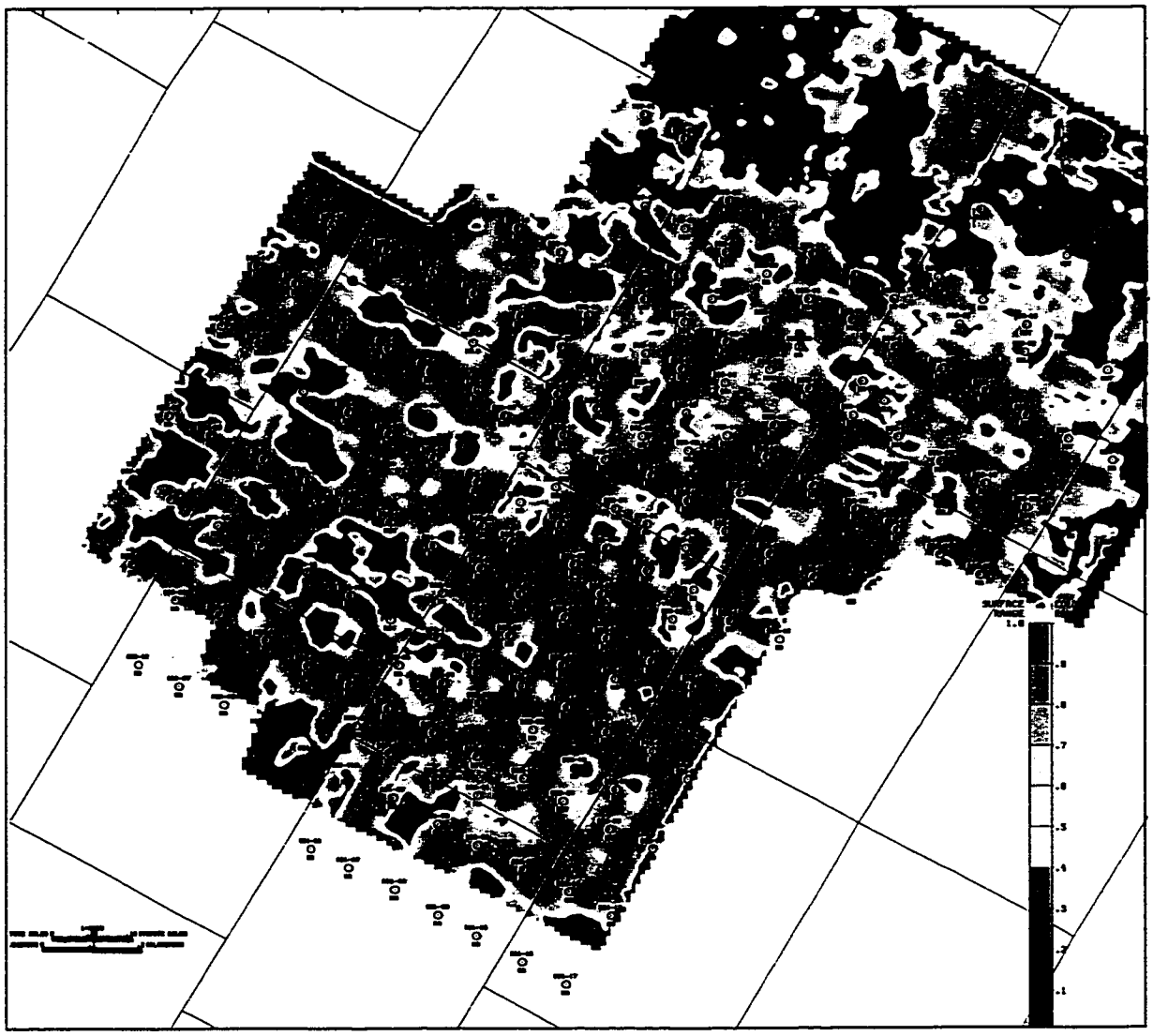

FIG. 4.18. The 1997 Steam conformance map after IOI with '97 calibration set (see Figure 4.6), red - hot reservoir, blue - cold reservoir.

Still, it is interesting to see the result with calibration. Figure 4.19 shows the post-IOI steam distribution with '95 calibration set. Comparing with Figure 4.18, steam is still present on the northern pads but with slightly less areal coverage. Even though the result is still not acceptable, the total areal conformance is less, but clearly, an improved calibration of training method is required.

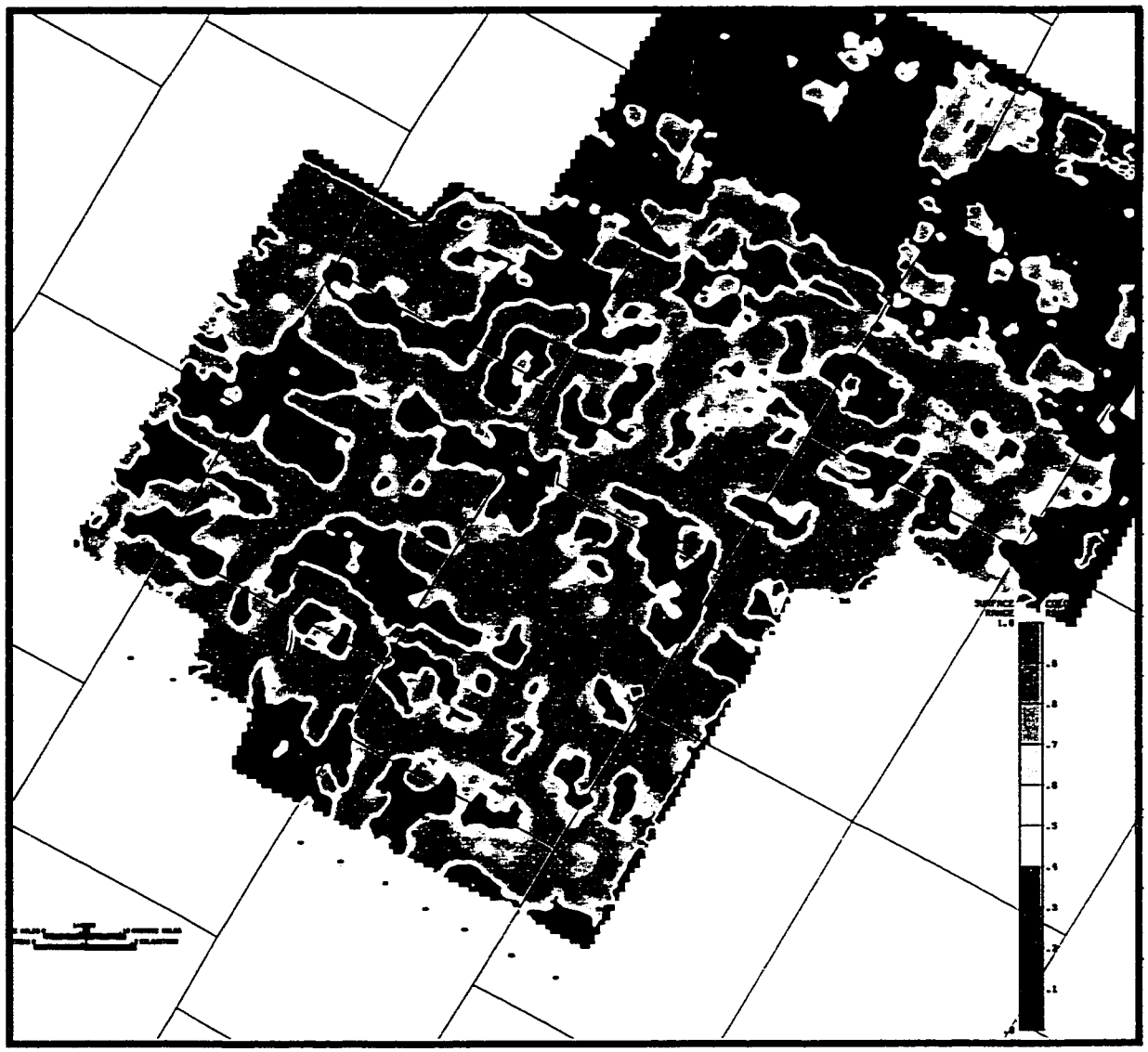

FIG. 4.19. The 1997 steam conformance map after IOI with '95 calibration set (see Figure 4.5), red - hot reservoir, blue - cold reservoir.

The schematic in Figure 4.20 is used to illustrate the concept of seismic attributes **cross-calibration**. Cross-calibration can also be called **cross-training** as the process is part of statistical analysis. This novel approach uses the '95 (pre-IOI) calibration set to train '95 seismic data (attributes) to get a new training set. This training set is then applied to the discriminant analysis of the '97 seismic data. The seismic attributes training set of survey **A** is applied to the discriminant analysis of survey **B**. This process is called cross-calibration or cross-training. This process should provide consistent analysis between time-lapse seismic surveys. Therefore, it provides consistent results in terms of reservoir status, and parameters. It provides a mean for reservoir prediction. In this case the reservoir status of '95 is known; only seismic data is available for '97. The unknown is the '97 reservoir status. To make this process work, time-lapse seismic data normalization is required. The issues of data normalization are discussed in the following section. The concept of cross-calibration is first applied to the analysis of the two survey datasets. Figure 4.21 shows post-IOI steam conformance without time-lapse seismic data normalization but with cross-calibration. Seismic attributes of '95 survey were trained with '95 calibration set, then applied to the discriminant analysis of '97 survey. The result looks quite encouraging even though no data normalization has been applied yet. There appears some steam on the northern non-steamed pad locations but on different spots. The result is still not acceptable but cross-training has made quite a difference, especially on B6 pad.

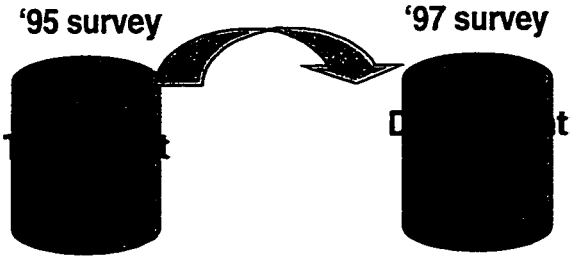

FIG. 4.20. Schematic diagram illustrating the concept of time-lapse seismic data cross-calibration or cross-training.

4.5.2 Data normalization

With the theory of shaping filtering discussed earlier in mind, the time-lapse seismic data normalization can be implemented in a number of different ways:

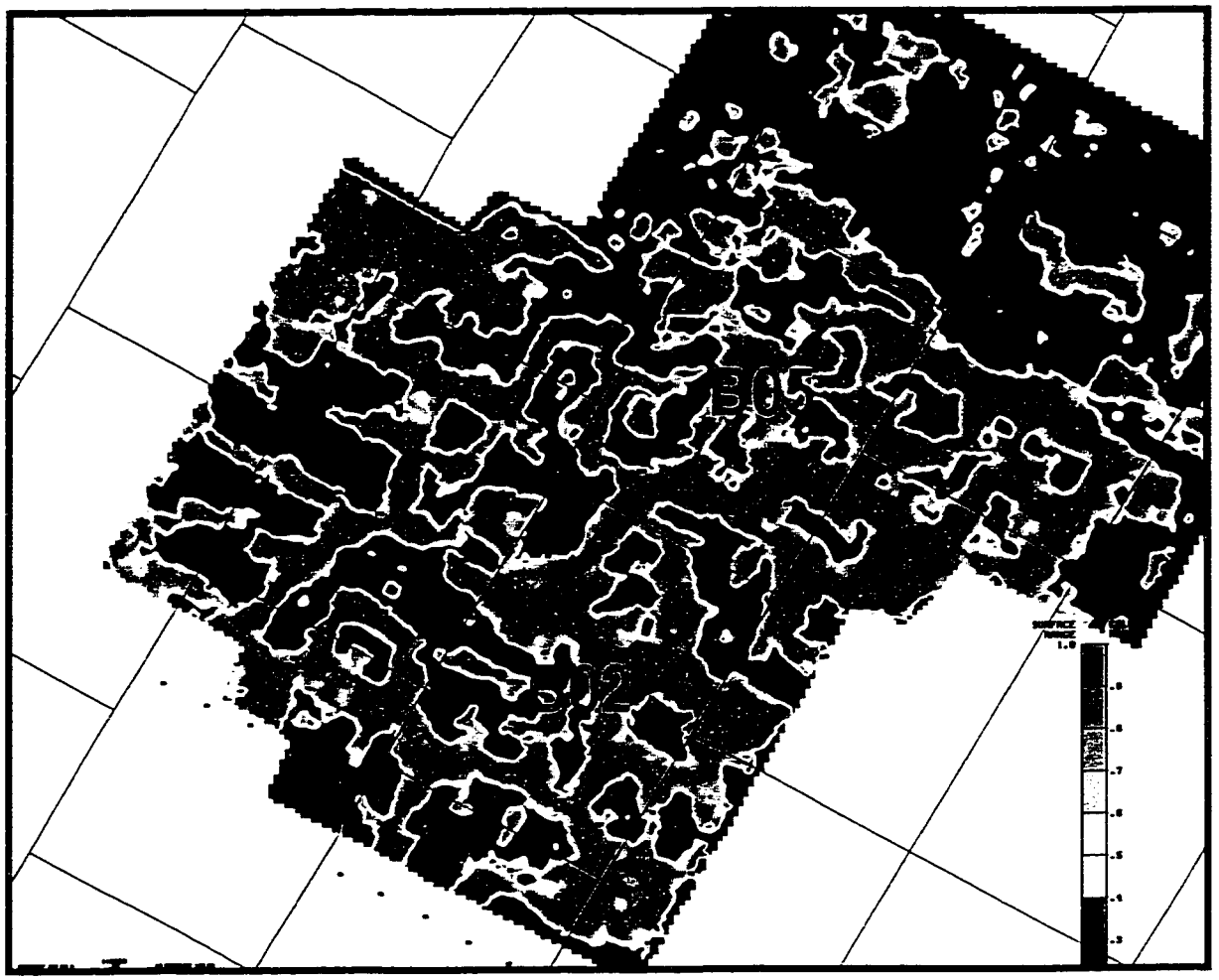

FIG. 4.21. The 1997 steam conformance obtained by applying '95 training set to '97 discriminant analysis, no seismic data normalization is applied.

1. Whole survey match operator — average filter of all filters that are derived from each post-stack CDP trace pair between surveys excluding reservoir interval, both phase and amplitude are adjusted between surveys.

2. CDP-to-CDP match operator — a single filter is extracted from each CDP pair. Data normalization is implemented on the post-stack trace base. Both phase and amplitude are normalized for each trace, which may be different.

3. Shot phase match operator — filters are derived to match the phase of each trace of a shot gather of survey A to its correspondent stack CDP of survey B. Only phase is normalized.

4. Shot phase match plus CDP-to-CDP match operator — combination of above operations 3 and 2.

5. CDP-to-CDP gain match operator — a filter is extracted for each CDP traces pair but only amplitude adjustment is applied.

6. Multi-trace operator — one filter is derived from a block of CDP traces and applied to the whole survey data normalization.

A number of rules should be followed when a filter is designed. These rules include:

(1) The section used for the filter design should have minimal or no acquisition fingerprint.

(2) Focus on the data portion where the best repeatability retains.

(3) Exclude the reservoir portion where changes occur from survey to survey.

(4) Use the information above the reservoir rather than below the reservoir as changes occurred in reservoir between surveys may affect the seismic section below it except special situation such as Cold Lake, Alberta where reservoir is very shallow (around 420 meters to 470 meters). In this case a part of seismic section (certain distance) below the reservoir is used.

(5) The operator should have reasonable length and cover at least a few wavelengths so that it does not pick up the local geology.

With current acquisition geometry, seismic artifacts (acquisition fingerprint) appears at about 200 ms (200 meters in depth) and above on the section in Cold Lake 3-D seismic data. Figure 4.22 shows the time slice of 175 ms of the coherence cube calculated from

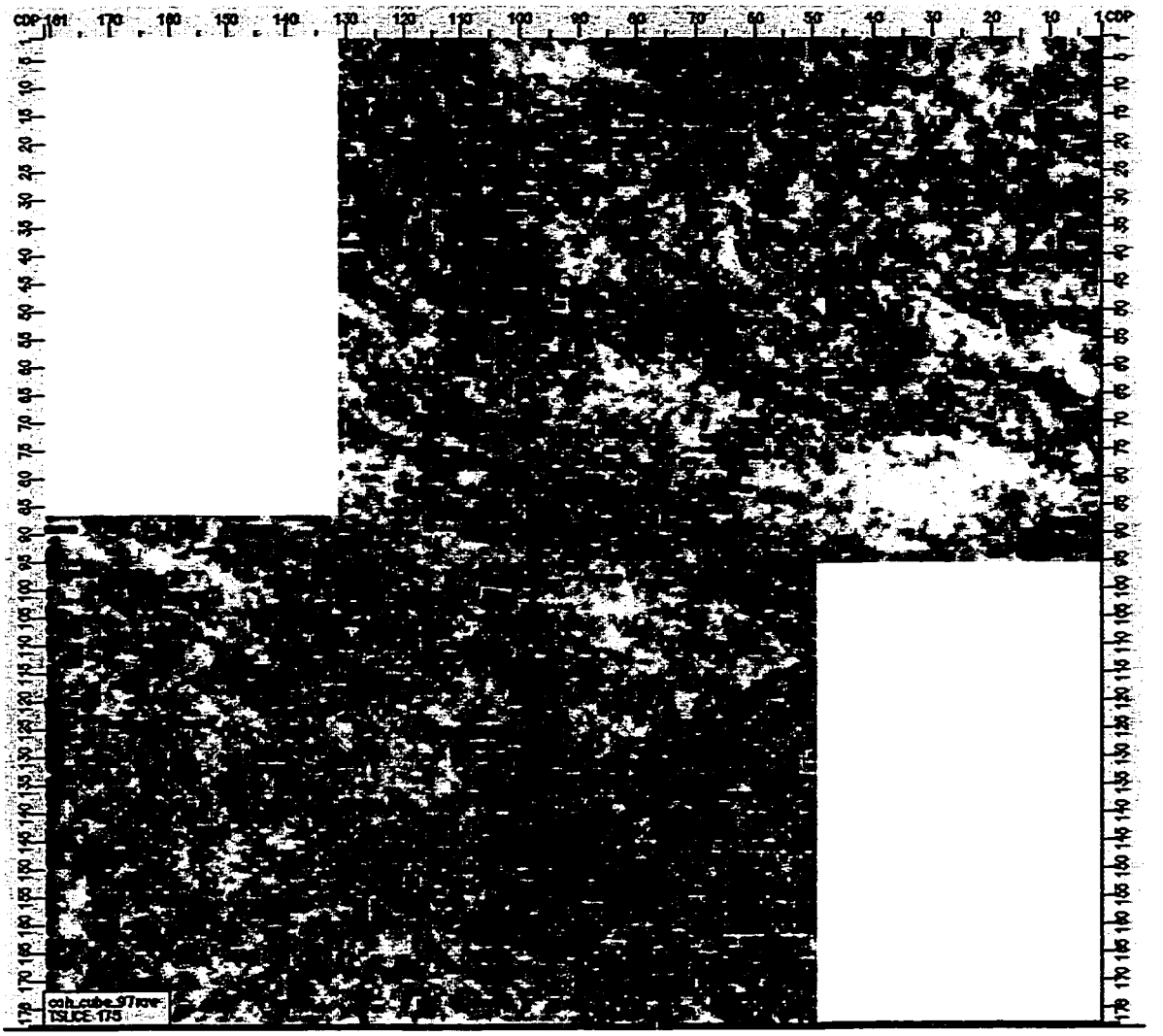

FIG. 4.22. Time slice at 175 ms from coherence cube of 1997 survey showing acquisition artifacts, white - high coherence value, black - low coherence value.

the '97 seismic survey. It is due to acquisition that strong amplitude "fabric texture" present. These artifacts disappeared as the time slice is moved down.

Figure 4.23 shows an inline seismic section (inline 91) of the '97 survey. The section can be classified into three major zones: the zone of artifacts above 200 ms (shallow zone). Due to the change of fold coverage the seismic characteristics have significant changes in this zone. Amplitude varies strongly from trace to trace. The dynamic zone is the reservoir portion and its surrounding area (see the box with black dotted line in Figure 4.23) when the steam chamber is changing from time. The time sags on the Devonian top

are associated with the presence of a steam chamber. Therefore, Devonian top is also subject to change. This zone (400 ms to 550 ms) should be excluded when designing a shaping filter. It is assumed that data in time window of 300 ms to 1000 ms excluding changing zone have good repeatability and define it as repeatable zone, which is used for filter design. After normalization filter is extracted, the data normalization is implemented in the entire time window of 0 to 1000 ms.

The subtracted difference can be used to check the repeatability between two surveys. Figure 4.24 shows the difference by subtracting the '95 migrated stack section from the '97 migrated stack section without data normalization. As expected there is significant energy in the changing zone including the steam zone and Devonian top. Also, the residual energy above and below the changing zone is very strong. Coherent energy in time window of 300 ms to 400 ms and lower part of the section (550 ms and below) can be minimized. Figure 4.25 shows the similar subtracted difference between the two surveys but with CDP-to-CDP trace normalization. It is clear that a simple CDP-to-CDP normalization has significantly reduced the difference between the two sections above and below the changing zone (compare Figure 4.24 and Figure 4.25).

Figure 4.26 shows the post-IOI steam conformance with cross-calibration and CDP-to-CDP data normalization. Obviously, improvement has been made as the picture is cleaner compared with Figure 4.21. The random noise area is much smaller on northern pad locations where there are no wells or steam. Improvement is still needed as the northern pad locations are not totally clean. Pre-stack efforts have been made for data normalization. It would be very difficult to attempt to normalize pre-stack data between surveys on the base of shot-to-shot gather or receiver-to-receiver gather as the survey patch between two surveys is different (e.g. different layout). Also, the surface conditions were different between two surveys as they were surveyed in different seasons. The Post--IOI survey was conducted in winter when ground was frozen. Finally, the fold distributions between two surveys are significantly different as described earlier.

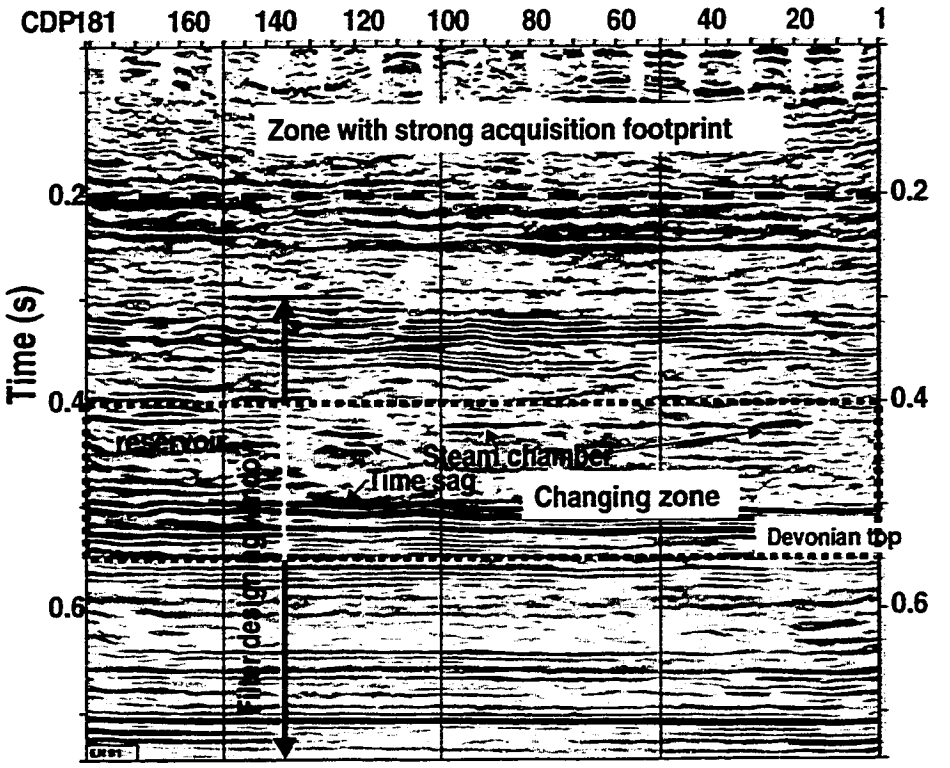

FIG. 4.23. Time-lapse seismic section showing data normalization filter design window.

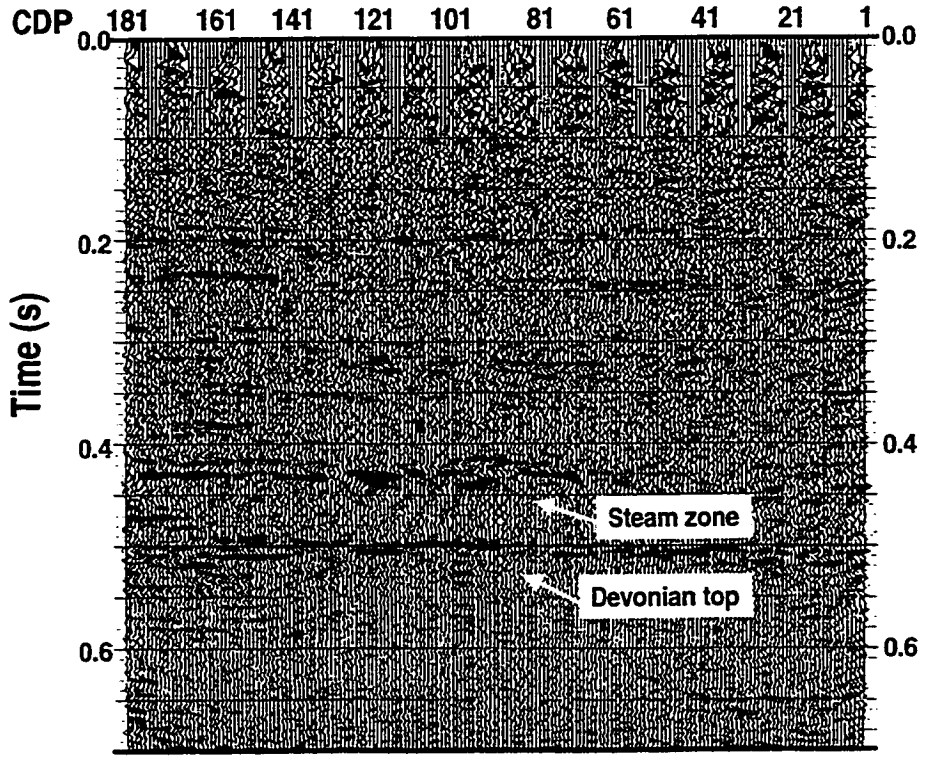

FIG. 4.24. Migrated stack difference subtracting '95 section from '97 section without normalization.

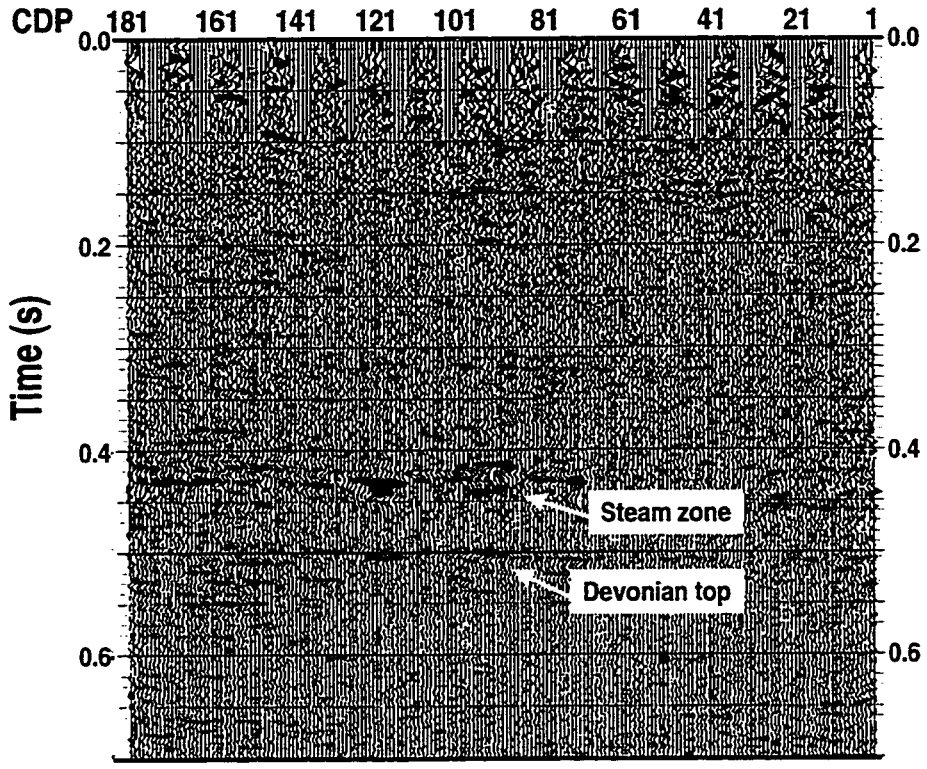

FIG. 4.25. Migrated stack difference by subtracting '95 data from '97 data with CDP-to-CDP normalization.

If seismic phase is consistent throughout processing the phase of each trace of a shot gather of post-IOI ('97) survey can be matched to its corresponding stack CDP of the pre-IOI ('95) survey. Therefore, shot phase match filtering is an operation between a pre-stack gather and a post-stack CDP trace of time-lapse surveys. In this operation, only phase is normalized. The steam conformance obtained from applying this filter is shown in Figure 4.27. Comparing Figure 4.26 and 27, it indicates that pre-stack phase matching operation did not improve the result much. A post-stack multi-trace operator is extracted from areas where reservoir has no changes between '95 and '97 surveys (yellow block areas in Figure 4.27) and applied to normalize '97 data set. The steam conformance map from this operator shows a significant improvement (Figure 4.28). The 'noises' on northern pad locations are almost all removed. Figure 4.28 is the enlarged northern part of B2 pad showing the comparison of results from different match operator. In general, all results show post-IOI steam channels are bigger (Figure 4.29 b, c, and d). According to production engineering data (pressure, temperature, and gas saturation), three wells

annotated with yellow dots show no steam. However, some kind of noise is shown around the wells on the result without data normalization (Figure 4.29b).

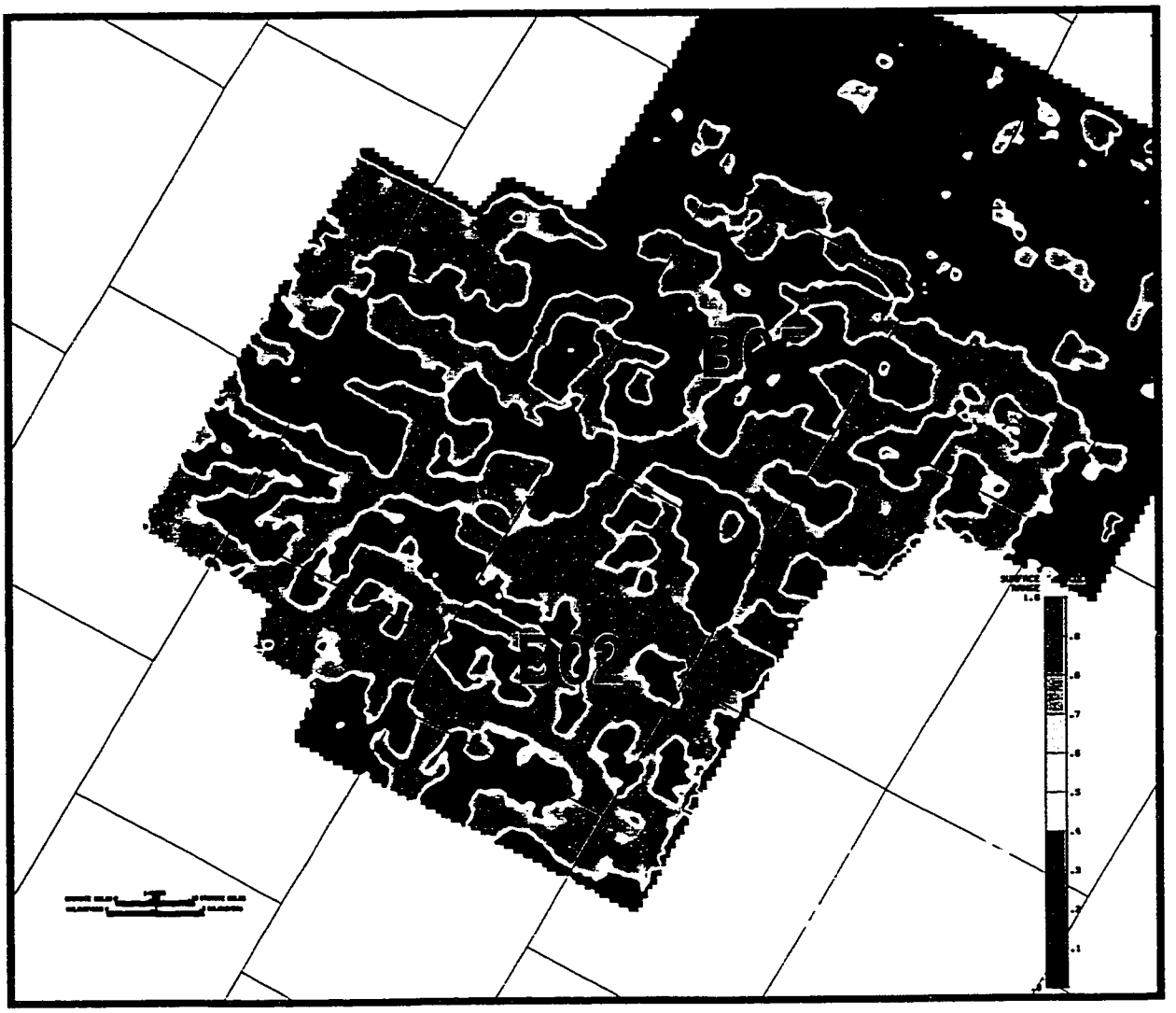

FIG. 4.26. The 1997 steam conformance by applying 1995 training set to 1997 discriminant analysis with seismic data normalization applied.

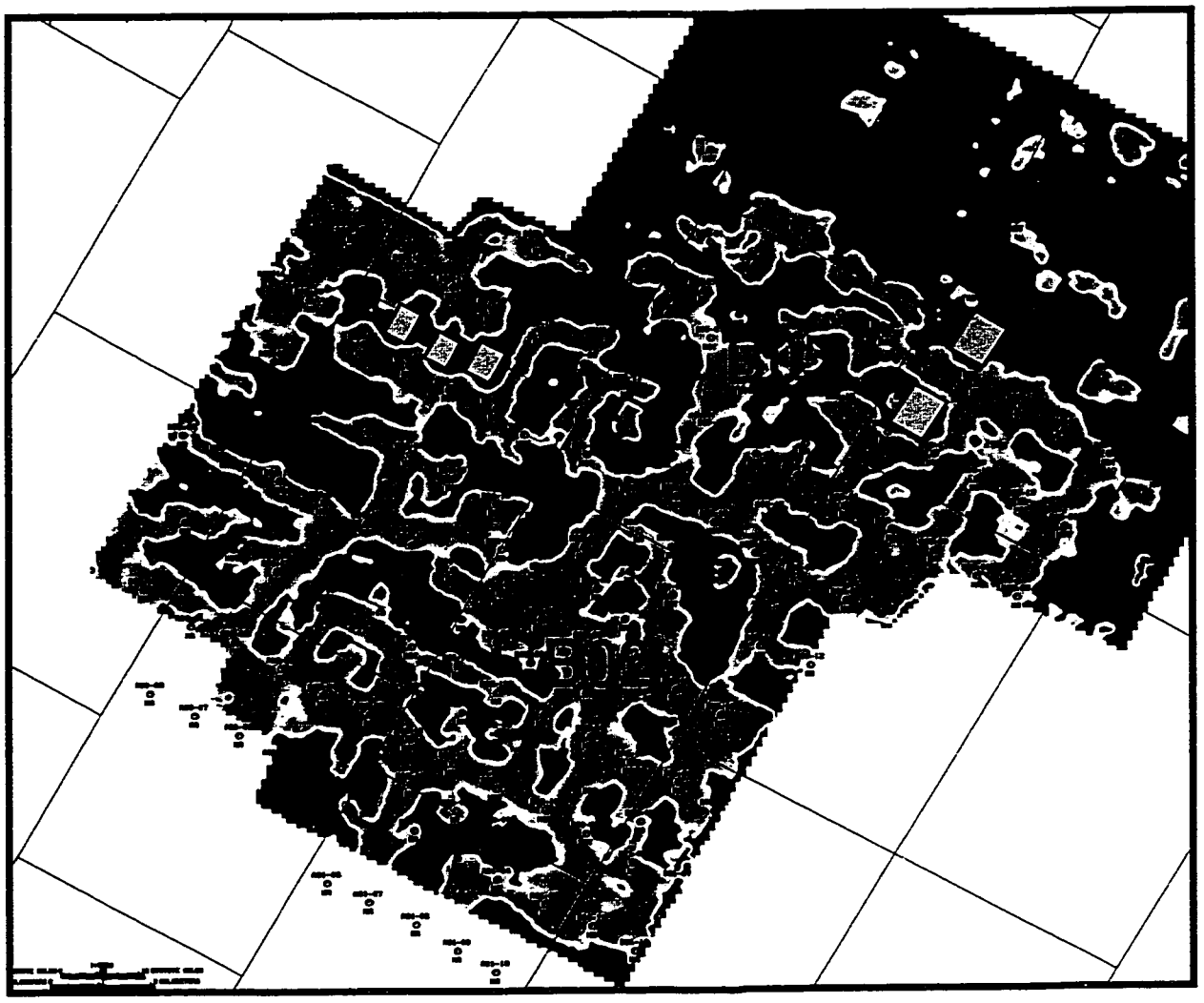

FIG. 4.27. The 1997 steam conformance by applying 1995 training set to 1997 discriminant analysis with seismic data normalization of shot phase match plus post-stack CDP-to-CDP match applied. Yellow blocks are the location for filter extraction for multi-trace normalization match filtering.

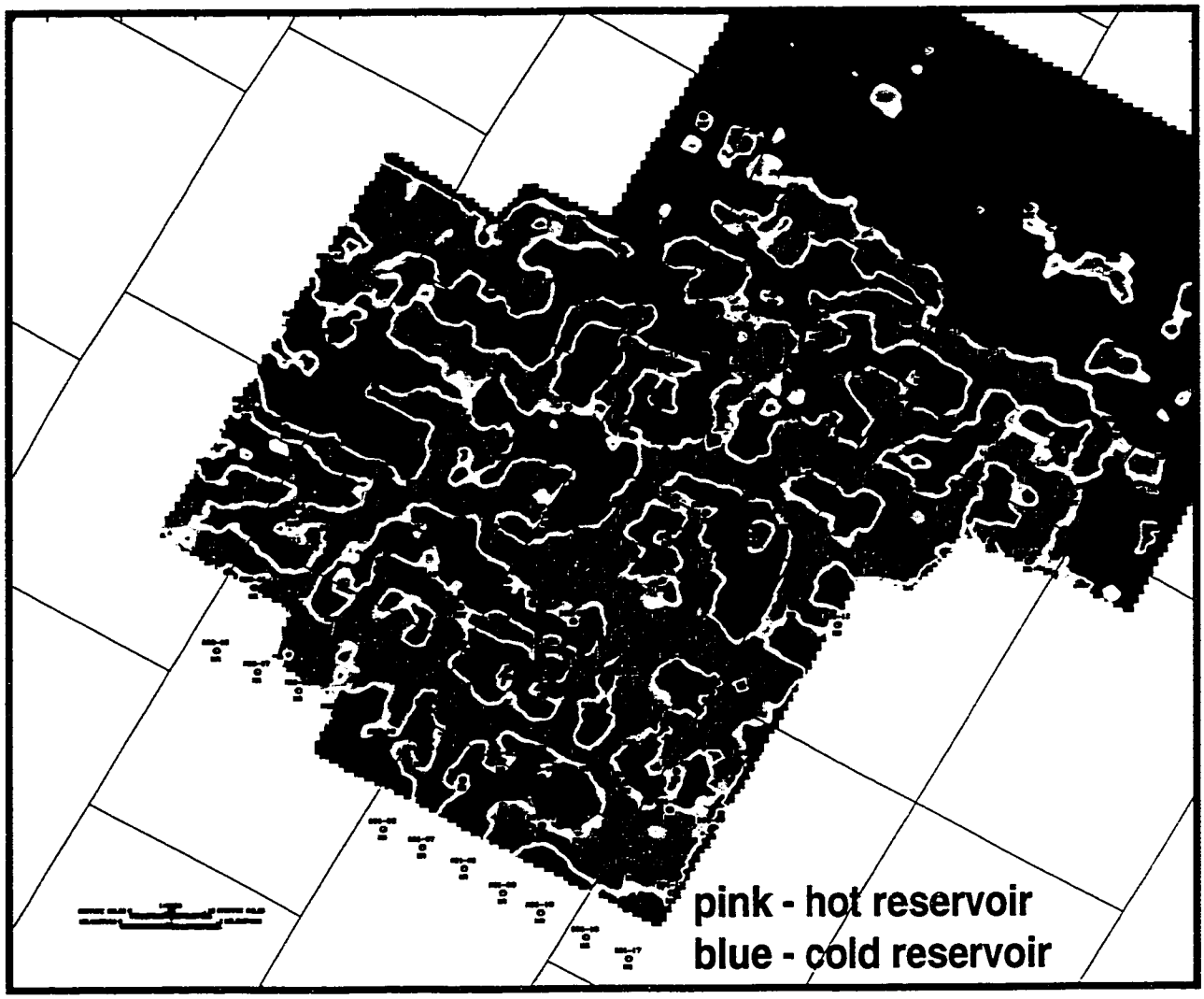

FIG. 4.28. The 1997 steam conformance by applying 1995 training set to 1997 discriminant analysis with seismic data normalization of post-stack multi-trace match operator applied.

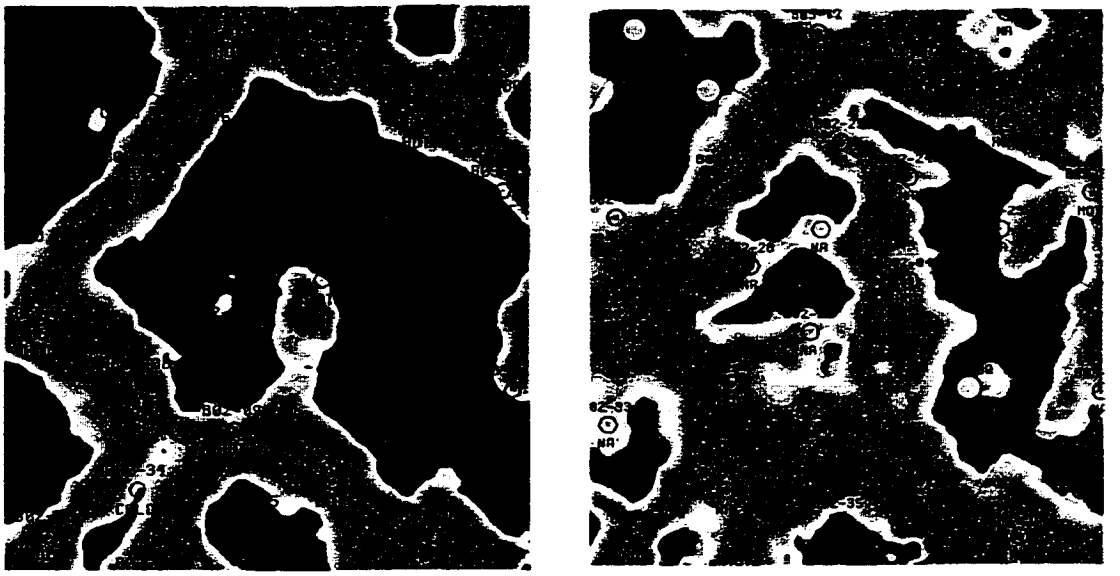

a) '95 steam distribution

b) '97 steam distribution (no operator)

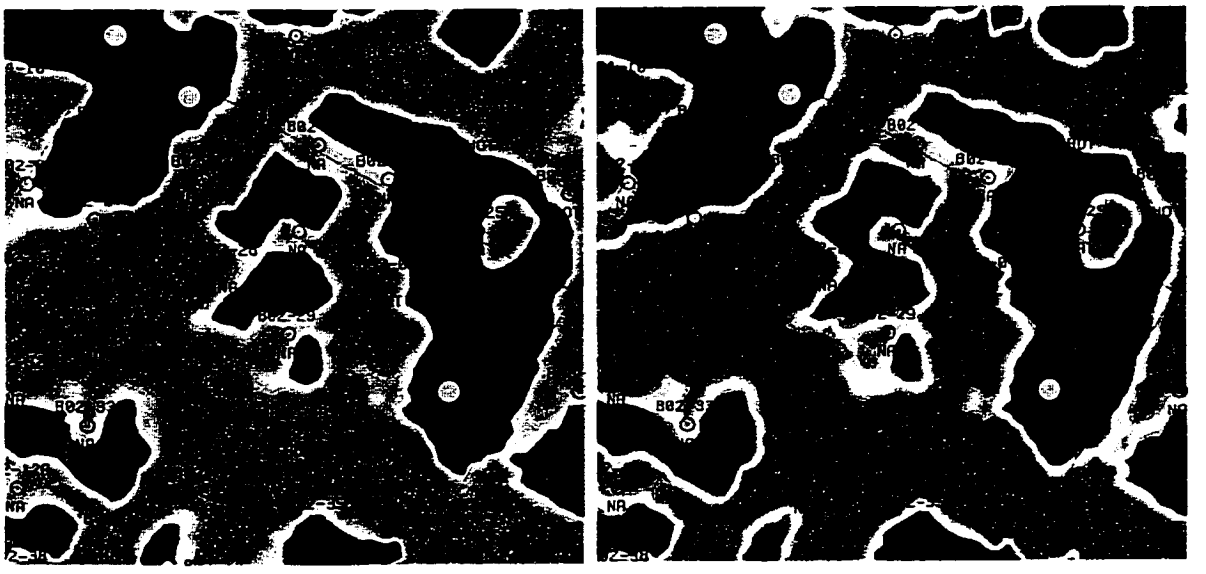

c) Shot phase match + cdp match

d) Multi-trace operator

FIG. 4.29. The steam conformance before and after injector-only-infill wells (well number 21 or higher) and comparison of different normalization operator.

4.6 Conclusions

It is clear that in the discriminant analysis use of a different calibration set provides different results of steam distribution. Significant differences result from using different calibration sets. In the training set, it is better to have a balanced number of calibration points for each class. Time-lapse cross training or cross calibration works; it gives better, more stable, and consistent results than independent calibration. However, without data normalization cross calibration was impossible. Data normalization is the key process for proper calibration. The best results were obtained from multi-trace operator derived from the unchanged reservoir. It was found that pre-stack data normalization is unnecessary. The match operator determined from the whole survey is the worst.

Chapter 5 – Non-redundant attributes: attributes from principal component decomposition

5.1 Introduction

A primary goal in reservoir characterization or monitoring is to obtain a robust and accurate relationship between the seismic data and the reservoir property of interest. Seismic attributes extracted from the data volume provide a basis for the calculation of the reservoir properties. The attributes represent a data reduction technique where a few select attributes replace the seismic trace. The attributes are chosen in an attempt to capture only the variation in the salient reservoir property and to exclude other information.

Conventional seismic attributes, such as average amplitude, isochron, peak amplitude, central frequency, etc. are readily extracted from a data volume and can be related to reservoir properties in many instances. However, these attributes do not necessarily capture the entire variance of the reservoir property of interest. As well, these attributes have some degree of correlation, and thus, analysis techniques must be able to compensate for the redundancy.

In contrast, seismic attributes calculated from principal component decomposition of the seismic data are not correlated and the full suite of principal components contain all the variance in the seismic data (Hemon and Mace, 1978; Fournier and Derain, 1995). Perceived disadvantages of principal component attributes are that they are data set dependent and are not directly related to physical properties.

Previous attribute analysis for seismic monitoring in Cold Lake used seven conventional attributes from the amplitude and frequency domain calculated over the reservoir interval (Eastwood, 1996). The suite of attributes was selected by first removing highly correlated attributes and retaining only those attributes which were correlated with well control

(Eastwood, 1996). The suite of attributes was also physically justified based on simple forward modeling with synthetic data. Well control (steam injection locations and known cold reservoir location) was used to calibrate the seismic attributes for use in discriminant analysis. The output from the discriminant analysis for every trace location is the similarity to the two classes, on a scale of 0 to 1. These attributes, however, contained some redundant information and did not capture all the variance in the seismic data for the reservoir interval.

The application of this previous technique to a new monitoring project at Cold Lake (A02/A04 pads) produced results that were not as definitive as previous applications. The new result at A02/A04 showed less spatial coherence for the mapped features, with the discriminant function providing an 80% agreement with well control compared to a previous 95% agreement with well control. In addition, the seismic map cannot be fully reconciled with engineering pressure communication data, and no anomaly is present in the northeast corner of the survey (well A02-10).

Principal component attribute analysis at the A02/A04 seismic monitoring project produced better results than the conventional attribute analysis. In particular, the discriminant function provided an 90% correlation with well control, and the areal conformance was better correlated with the engineering pressure communication data. Finally, the spatial coherence of the mapped features is higher with the principal component analysis than with the conventional attributes and an anomaly is present in the northeast corner of the survey (well A02-10). To achieve this superior result, it was necessary to include all twenty principal components (which accounted for 99% of the statistical variation in the seismic data) in the calibration procedure for the discriminant analysis. The full suite of principal component attributes is defendable, since the analysis was also performed first with a minimal set of principal components and then increased, and the results were compared to our conventional analysis technique, which has stronger deterministic foundation.

To minimize the dependence on the seismic data sets, time-lapse data sets were analyzed by merging two data sets together. The principal components were extracted from the

merged data set, and attributes were calculated separately from each individual data set by using the same principal component shapes. A significant improvement has been made by applying this technique.

5.2 Principal component attributes

Principal component attributes (PCA) are the attributes from the principal component decomposition of seismic data. Figure 5.1 illustrates the concept of principal component attributes. The idea behind PCA is that a seismic trace is composed of a finite set of waveform shapes. The concept is similar to Fourier analysis, which states that a seismic trace can be reconstructed using a weighted linear sum of shapes. These weights become the attributes. We consider N seismic traces ($x_i(t)$, $i=1, N$ and $t=1, M$) to form the covariance matrix.

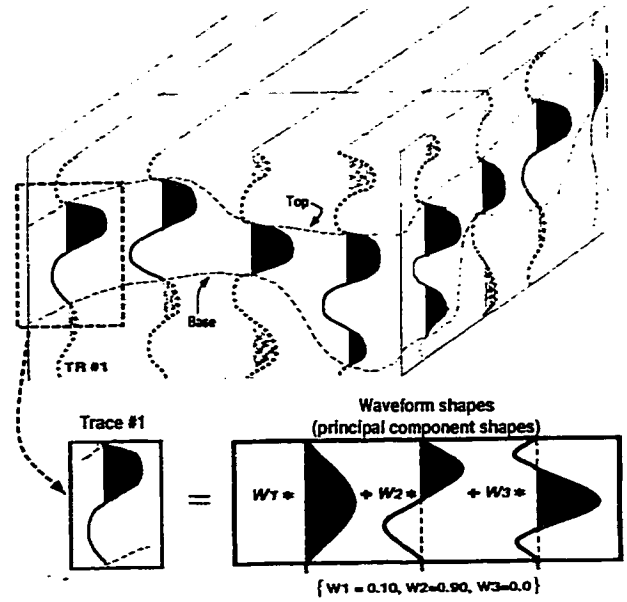

FIG. 5.1 Illustration of the concept of principal component attributes.

$$\mathbf{C} = \mathbf{X}^T \mathbf{X} \tag{5.1}$$

This matrix is square of size N and it is symmetric. The Singular Value Decomposition (***SVD***) is formed to decompose the matrix as follows:

$$\mathbf{C} = \mathbf{R}\ \mathbf{L}\ \mathbf{R}^T. \tag{5.2}$$

The matrix **L** is the diagonal matrix of the eigenvalues. The columns of matrix **R** are the eigenvectors corresponding to these eigenvalues. The ith principal component is defined as

$$p_i(t) = \sum_{j=1}^{N} r_{ij}\, x_j(t). \tag{5.3}$$

Where r is the eigenvector corresponding to the ith largest eigenvalue. Each principal component is just a certain linear combination of the input traces. The seismic trace reconstruction is the inverse transform of the above process and is given by

$$x_i(t) = \sum_{j=1}^{N} r_{ji}\, p_j(t)\,. \tag{5.4}$$

Some features are worth noting in the principal component decomposition process. First of all, the energy of each principal component is just its corresponding eigenvalue. Despite the fact the eigenvalues do not enter into the definition of the transform in the above equation, they are the keys to understanding the importance of the principal component. The eigenvalue is the indicator of the relative importance of each component contributing to the original data. Components corresponding to very small eigenvalues contribute very little to the make up of the original data and can be ignored without great loss; therefore, the total energy of the seismic traces is the sum of the eigenvalues. The most important feature in attribute analysis is that all the principal components are orthogonal. In other words, they are independent of one another and the principal component attributes (eigenvectors) are independent of one another. They are not correlated and not redundant in statistical analysis.

5.3 Analysis and comparison to conventional attributes

5.3.1 Data sets

The analysis and comparison have been carried out at A02/A04 pads (the example of poor signal-to-noise ratio data) and J01/J08 pads (the example of good signal-to-noise ratio data) surveys. To address the issue of time-lapse analysis when using principal component attributes the 95 and 97 surveys of B02 pad data (part of B2456 pads survey) were analyzed. Figure 5.2 shows a seismic section at A2/A4 pads, which illustrates where reservoir has been accessed by steam. The data were poorly processed. Due to the low reflection coefficient (almost no impedance change), picking the Clearwater formation

top is a difficult task; however, the depth data is widely available from well picks. The interpretation of the Clearwater was accomplished through depth-to-time conversion using the appropriate velocity. Both the conventional and principal component seismic attributes were extracted in a time window of 5 ms above and 50 ms below the Clearwater top horizon (see Figure 5.2). The 3-D seismic data show a bright spot and a frequency drop (attenuation) in the place where steam has accessed reservoir.

5.3.2 Areal steam conformance mapping using conventional and PCA attributes

Traditionally, attribute analysis was composed of seven conventional attributes from the amplitude and frequency domain calculated over the reservoir interval. These conventional attributes, such as average absolute amplitude, peak amplitude, central frequency, low frequency, high frequency, and maximum duration are readily extracted from a data volume and can be related to reservoir properties in many instances. The suite of attributes was selected by first removing highly correlated attributes and retaining only those attributes which were highly correlated with well control (Eastwood, 1996). The suite of attributes was also physically justified based on simple forward modeling with synthetic data. Well control (steam injection locations and known cold reservoir locations) was used to calibrate the seismic attributes for use in discriminant analysis. The output from the discriminant analysis for every trace location is the similarity (posterior probability) of the two classes, on a scale of 0 to 1.

Figure 5.3 shows the result of the discriminant analysis of A02/A04 seismic data by using seven conventional attributes. It was noted that: (1) the conformance map looks very noisy, (2) the well-to-seismic tie statistics for both hot spots (CSS wells) and cold spots are below 80%, (3) well A2-10 has been steaming for 10 cycles, but it is not shown hot enough as expected. Further analyses were carried out using nine attributes (Figure 5.4) and five attributes (Figure 5.5). Among three conformance maps (Figure 5.3-5.5) the cleanest one is from the five attributes analysis while the well-to-seismic tie statistics

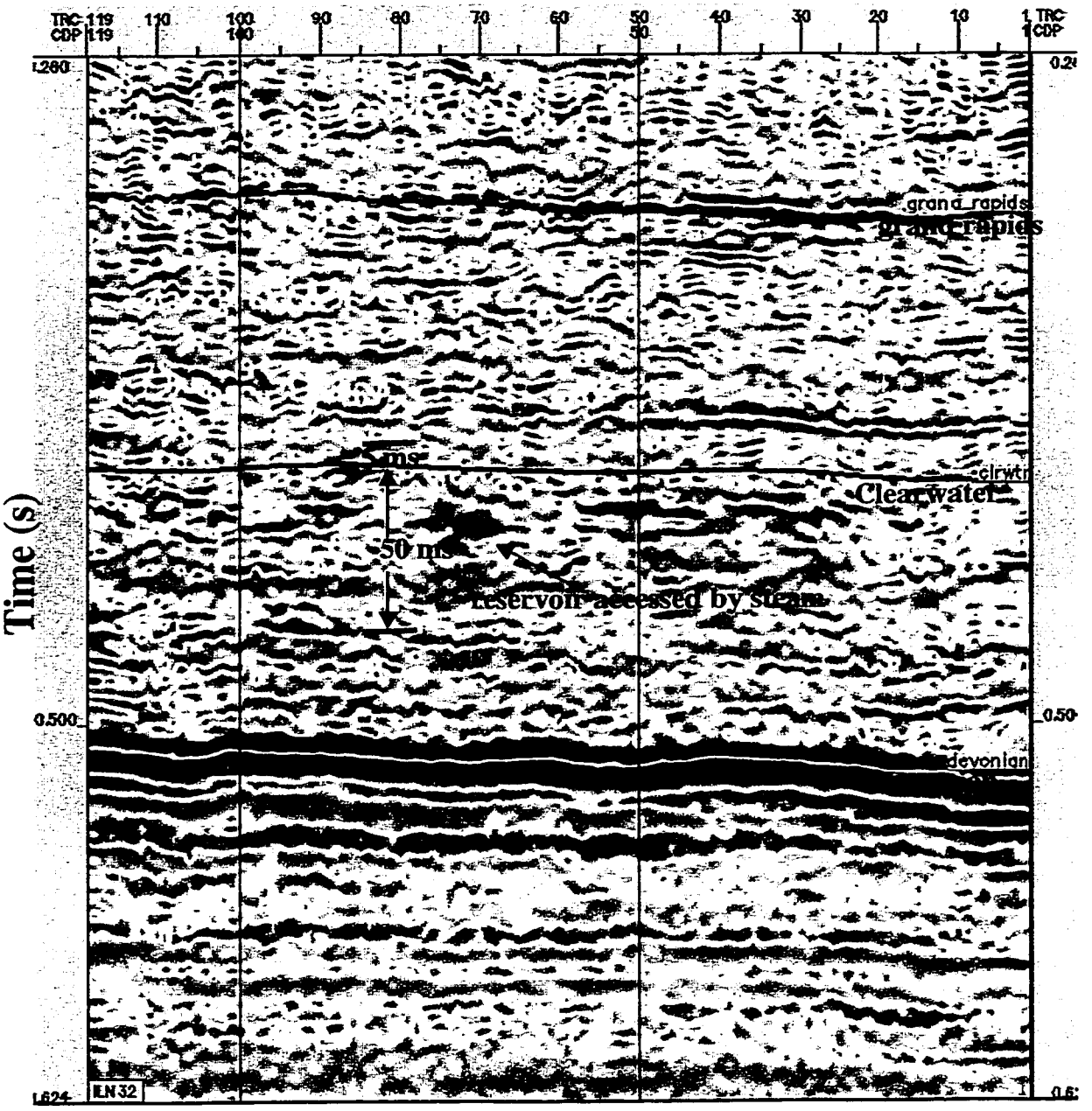

FIG. 5.2 A seismic section (inline 32) of A2A4 pads survey showing features of steam channels, seismic attribute extraction windows, and the noisy nature of the data.

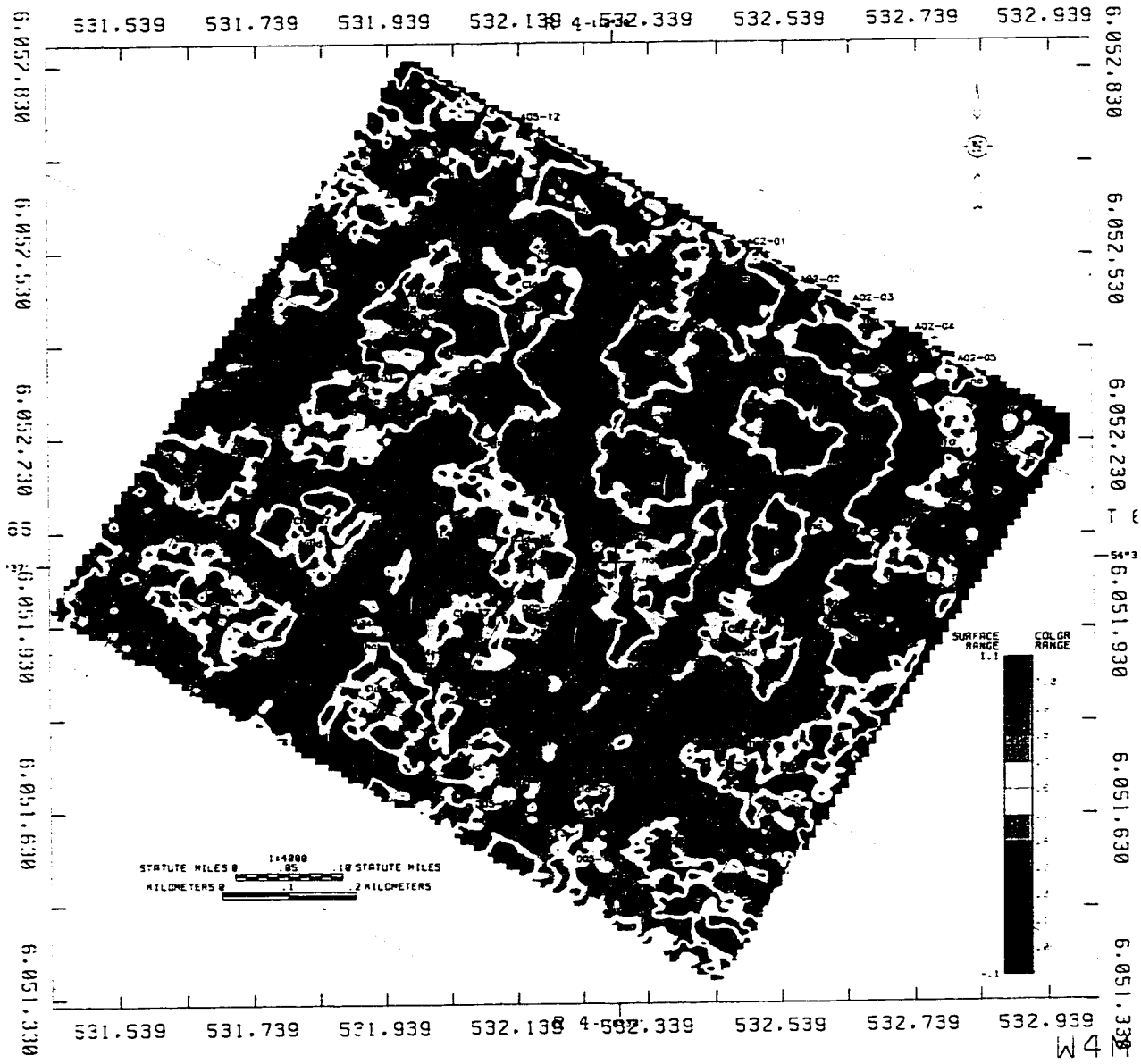

FIG. 5.3. Discriminant analysis results of hot versus cold reservoir of A2/A4 pads using conventional seven attributes (aab-average absolute amplitude, ap-peak amplitude, pav-positive average amplitude, dmx-maximum duration, centfreq-central frequency, decil2-low frequency, decil8-high frequency), global calibration.

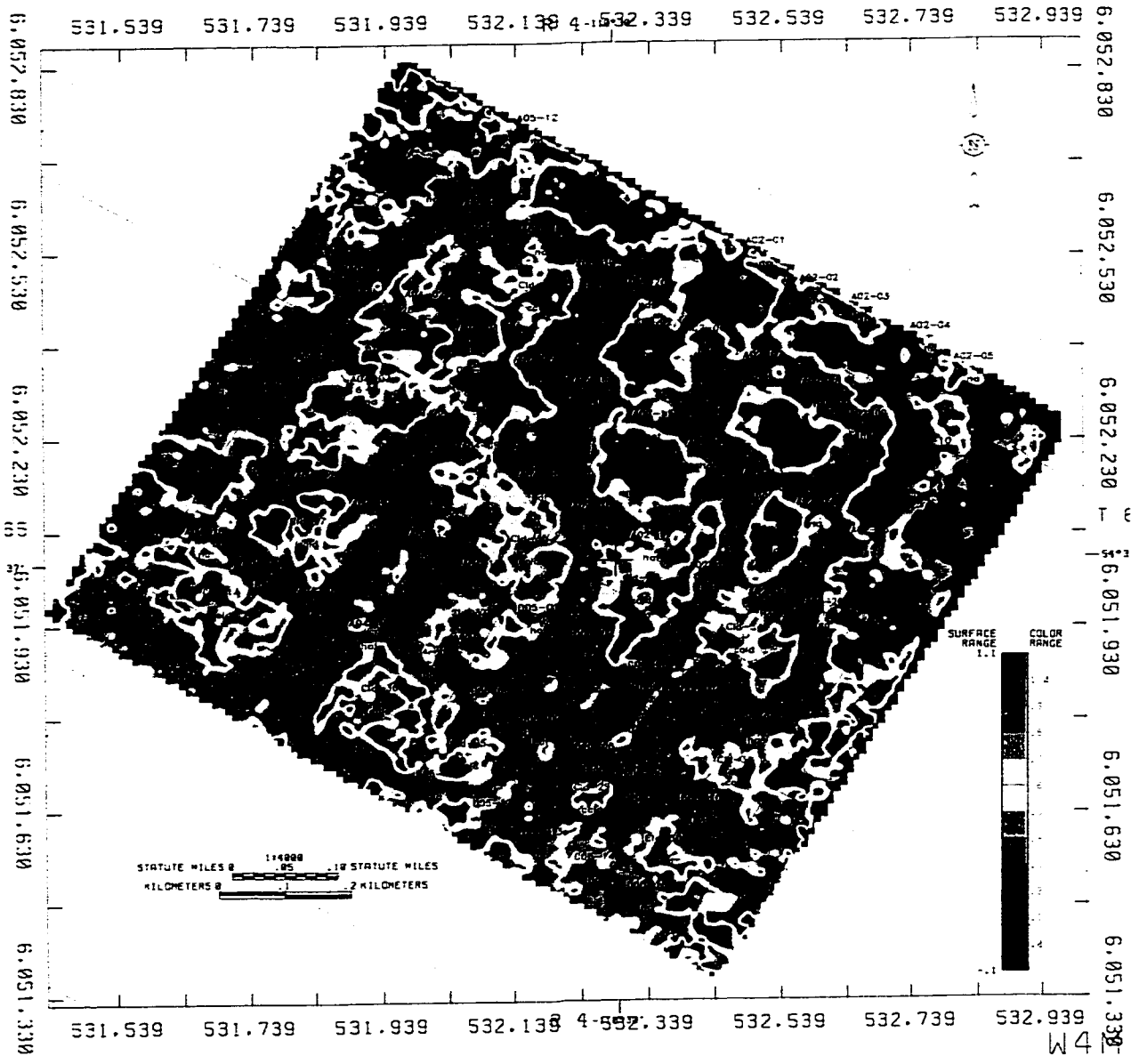

FIG. 5.4. Discriminant analysis results of hot versus cold reservoir of A2/A4 pads using conventional nine attributes (aab, ap, pav, pan, dmx, dmn, centfreq, decil2, decil8), global calibration applied.

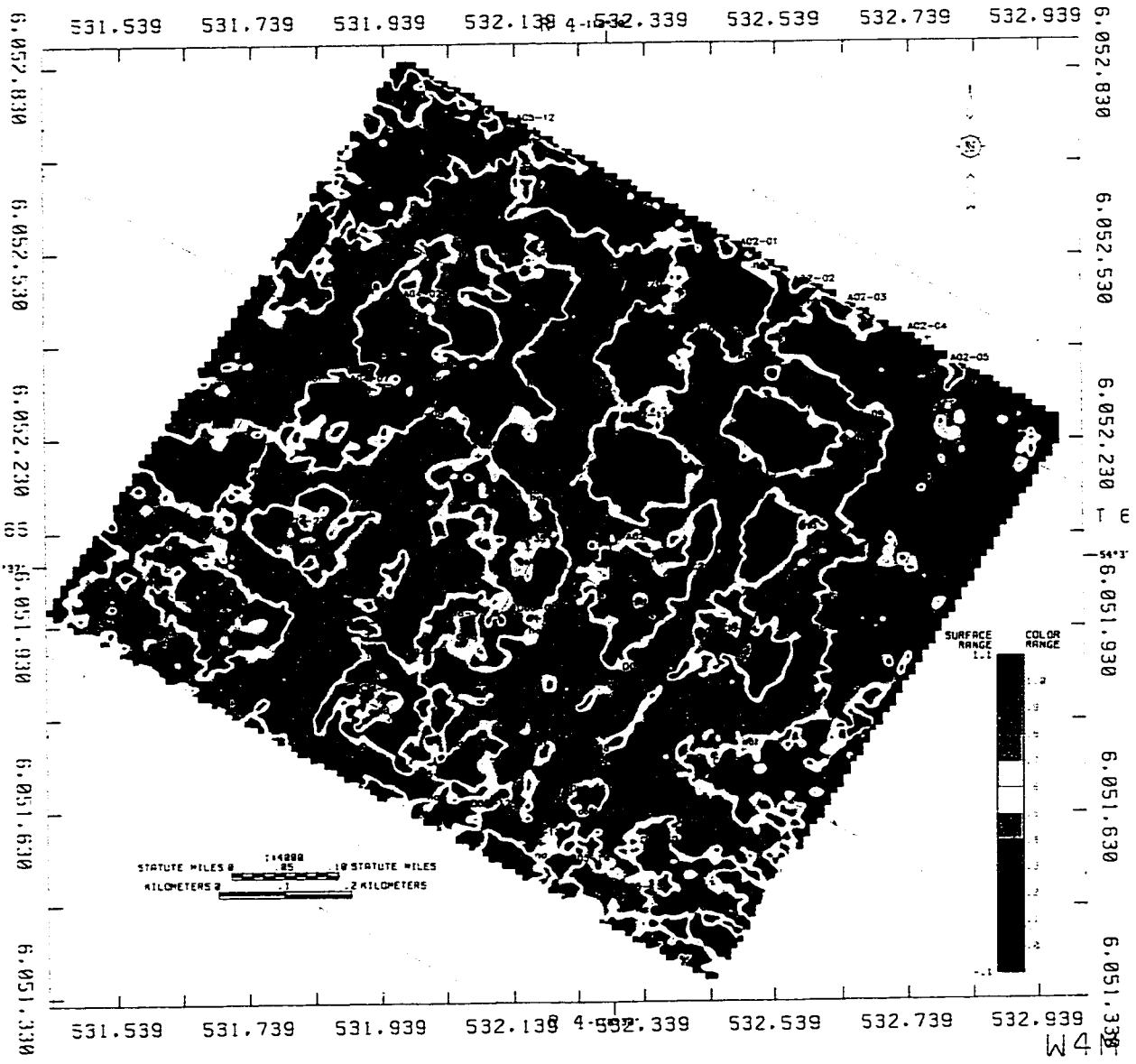

FIG. 5.5. Discriminant analysis results of hot versus cold reservoir of A2A4 pads using five conventional attributes (aab, ap, pav, centfreq, decil2, decil8), global calibration applied.

remains similar. It should be noted that global calibration was used in the discriminant analysis of above results. Global calibration means that one single scale (standard) is applied to all data traces (the whole survey area) in the statistical analysis, or the posterior probability is computed using calibration set from the whole survey area. In a large survey area the geology could change from one to another, thus local calibration is more applicable in that case. Local calibration indicates that different scales (standards) are applied to different restricted areas. The discriminant analysis routine allows local calibration by assigning a value to the parameter k, which is the number of surrounding calibration points included. Though the survey area of A2/A4 pads is small (1.1 km by 1.1 km), local calibration analysis was carried out. Figure 5.6 shows the results of the local calibration discriminant analysis with a parameter k of 20 (calibration points for each local area) which is roughly about one pad size. The result shows similar pattern, less areal conformance, and that it is noisier comparing to global calibration (Figure 5.5). By reducing the size of the local calibration of k to 15 (Figure 5.7), 10 (Figure 5.8), 5 (Figure 5.9), the results get noisier and noisier, therefore, it was concluded that local calibration is not a solution to improve the image in this case. The fundamental disadvantage with conventional attribute analysis is that attributes contain some redundant information and when a limited number of attributes are used in the discriminant analysis it does not capture all the variance in the seismic data for the reservoir interval. Table 5.1 shows correlation coefficients for nine conventional attributes for all traces of the whole survey area. Basically, almost all of the nine conventional attributes (in this table) are correlated. The average of absolute amplitude (aab_a) is strongly correlated to the peak amplitudes (pav_a) (correlation coefficient greater than 0.85). Similarly, a low frequency (decil2) is strongly correlated to the central frequency (centfreq) (correlation coefficient greater than 0.77). This is illustrated in the cross plot of the conventional attributes (Figure 5.10) in which a linear relation may be constructed between some attributes. However, principal component attributes are orthogonal to each other. It is very clear that the correlation coefficients are all zero (Table 5.2), and the cross plots of the principal component attributes are randomly

Table 5.1. Pearson correlation coefficients of nine conventional attributes (N=12708).

	AP_A	DMX_A	PAV_A	AAB_A	DECIL2	DECIL8	CENTFRQ	AMN_A	AMX_A
AP_A	1.00000 0.0	0.02653 0.0028	0.61648 0.0001	0.73767 0.0001	-0.01451 0.1019	-0.08692 0.0001	-0.05622 0.0001	-0.83186 0.0001	0.71131 0.0001
DMX_A	0.02653 0.0028	1.00000 0.0	0.13025 0.0001	0.13280 0.0001	-0.57503 0.0001	-0.35868 0.0001	-0.61942 0.0001	-0.02820 0.0015	0.01052 0.2357
PAV_A	0.61648 0.0001	0.13025 0.0001	1.00000 0.0	0.85707 0.0001	-0.04021 0.0001	-0.18817 0.0001	-0.14676 0.0001	-0.40881 0.0001	0.77302 0.0001
AAB_A	0.73767 0.0001	0.13280 0.0001	0.85707 0.0001	1.00000 0.0	-0.05701 0.0001	-0.20864 0.0001	-0.16258 0.0001	-0.67868 0.0001	0.66838 0.0001
DECIL2	-0.01451 0.1019	-0.57503 0.0001	-0.04021 0.0001	-0.05701 0.0001	1.00000 0.0	0.36367 0.0001	0.78960 0.0001	-0.00802 0.3659	0.03068 0.0005
DECIL8	-0.08692 0.0001	-0.35868 0.0001	-0.18817 0.0001	-0.20864 0.0001	0.36367 0.0001	1.00000 0.0	0.77775 0.0001	0.06546 0.0001	-0.06895 0.0001
CENTFRQ	-0.05622 0.0001	-0.61942 0.0001	-0.14676 0.0001	-0.16258 0.0001	0.78960 0.0001	0.77775 0.0001	1.00000 0.0	0.02727 0.0021	-0.02616 0.0032
AMN_A	-0.83186 0.0001	-0.02820 0.0015	-0.40881 0.0001	-0.67868 0.0001	-0.00802 0.3659	0.06546 0.0001	0.02727 0.0021	1.00000 0.0	-0.35575 0.0001
AMX_A	0.71131 0.0001	0.01052 0.2357	0.77302 0.0001	0.66838 0.0001	0.03068 0.0005	-0.06895 0.0001	-0.02616 0.0032	-0.35575 0.0001	1.00000 0.0

AP_A - peak amplitude.
DMX_A - maximum duration.
PAV_A - average of all positive amplitude.
AAB_A - average of absolute values of all amplitudes.
AMX_A - maximum amplitude.
AMN_A - minimum amplitude.
DECIL2 - low frequency content.
DECIL8 - high frequency content.

scattered, in which no linear relation may be extracted. Following the definition of the principal component attribute, seismic traces of the A2/A4 survey area are decomposed into finite sets of 32 shapes. The corresponding principal component attributes (eigenvector) were extracted. Some basic statistics of the first 10 principal component attributes for A2/A4 pads seismic data are listed in Table 5.3. In general, for Cold Lake seismic data which has a dominant frequency of 100 to 120 Hz and a fold of 12 to 20 at the level of interest (Clearwater formation, window of 400 ms to 460 ms), the first 20 shapes capture more than 99.99% of the information (variance) in original seismic data.

The typical hierarchy of the Clearwater formation, principal component shapes and the variance captured are listed in Table 5.4. If the data is filtered down to 62 Hz only 12 attributes are needed to capture more than 99.99% of the information of the filtered data

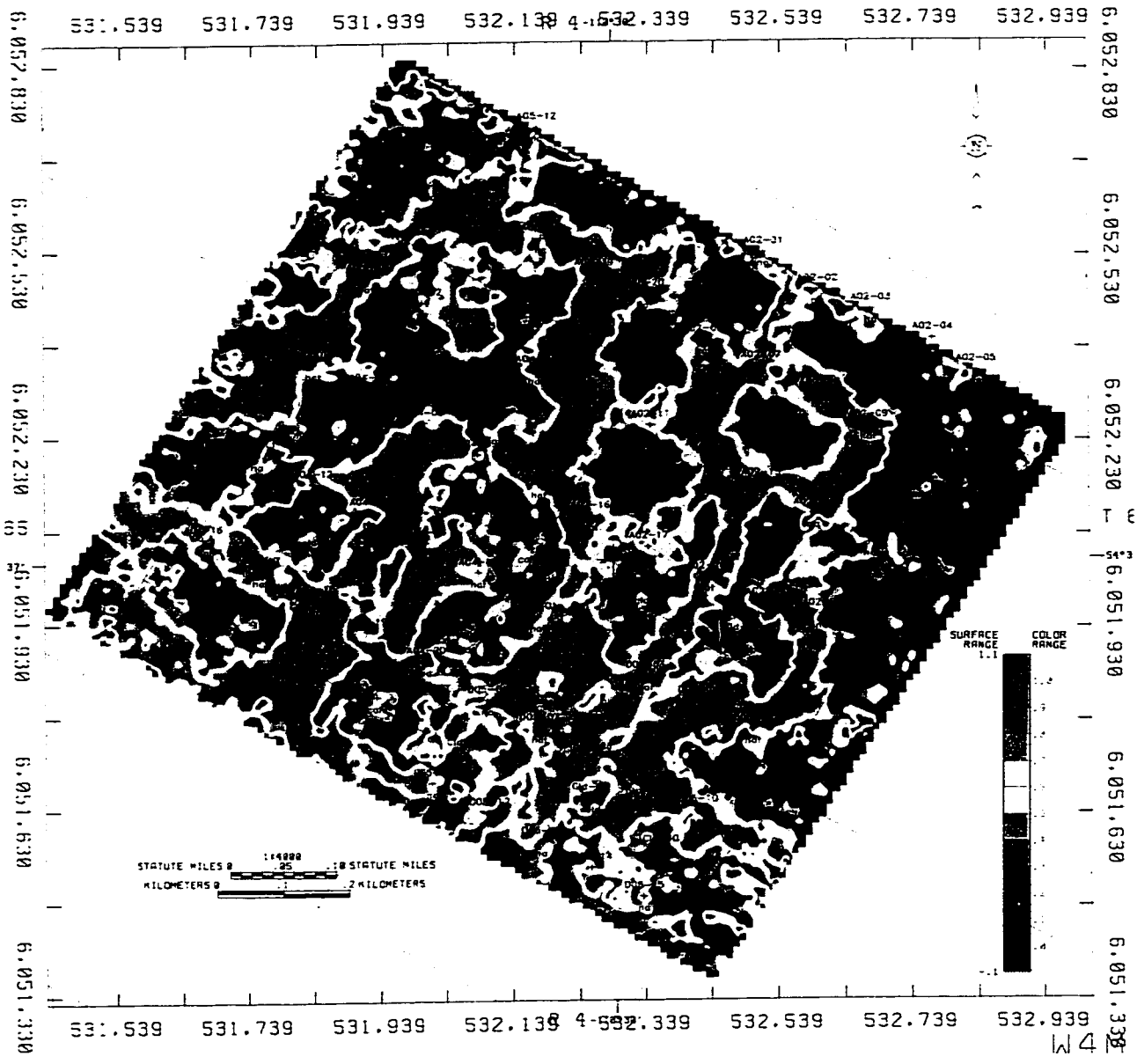

FIG. 5.6. Discriminant analysis results of hot versus cold reservoir of A2A4 pads using five conventional attributes (aab, ap, pav, centfreq, decil2, decil8) with local calibration applied (calibration parameter k=20 for surrounding calibration points).

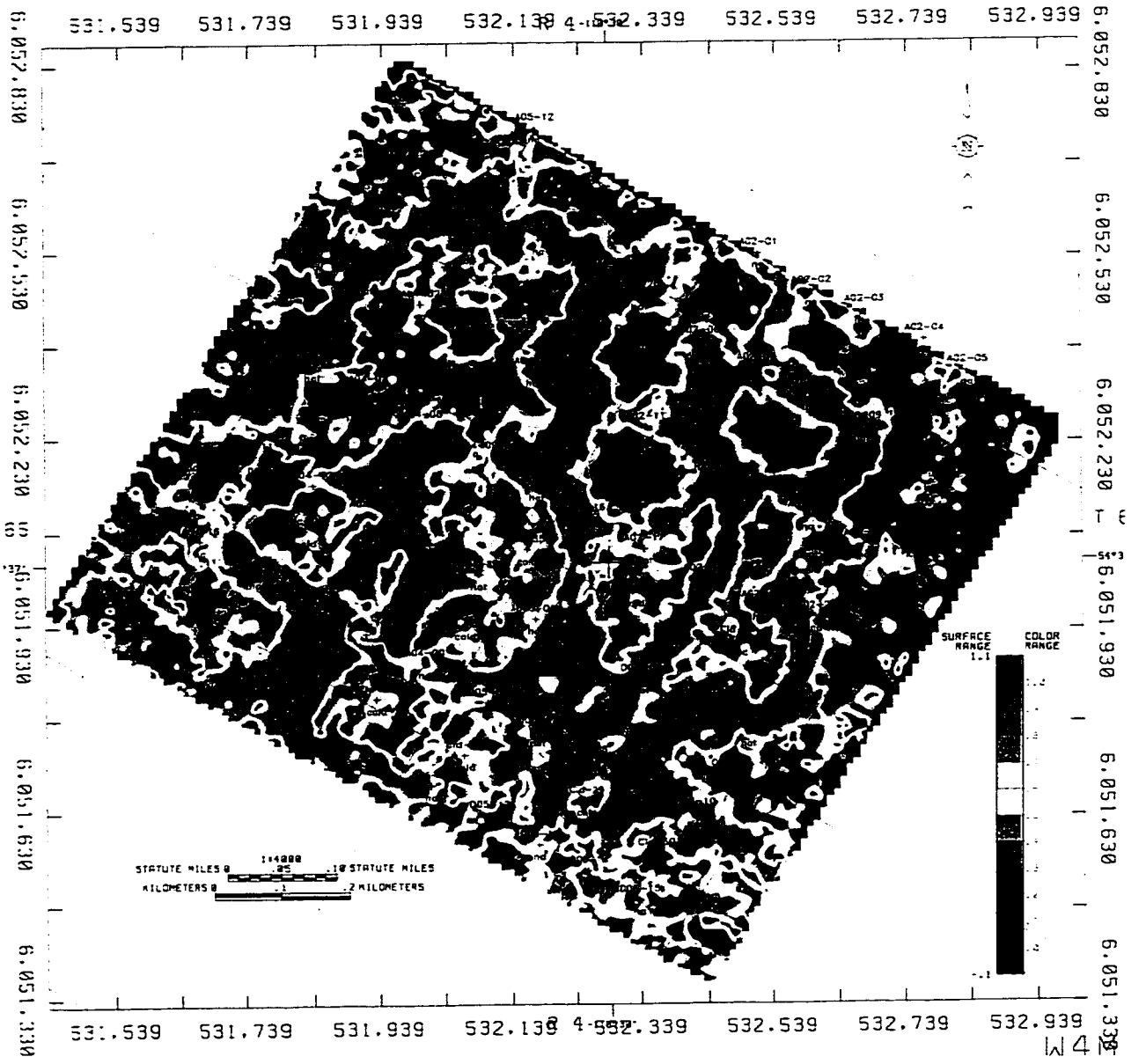

FIG. 5.7. Discriminant analysis results of hot versus cold reservoir of A2/A4 pads using conventional five attributes (aab, ap, pav, centfreq, decil2, decil8), local calibration applied (calibration parameter k=15).

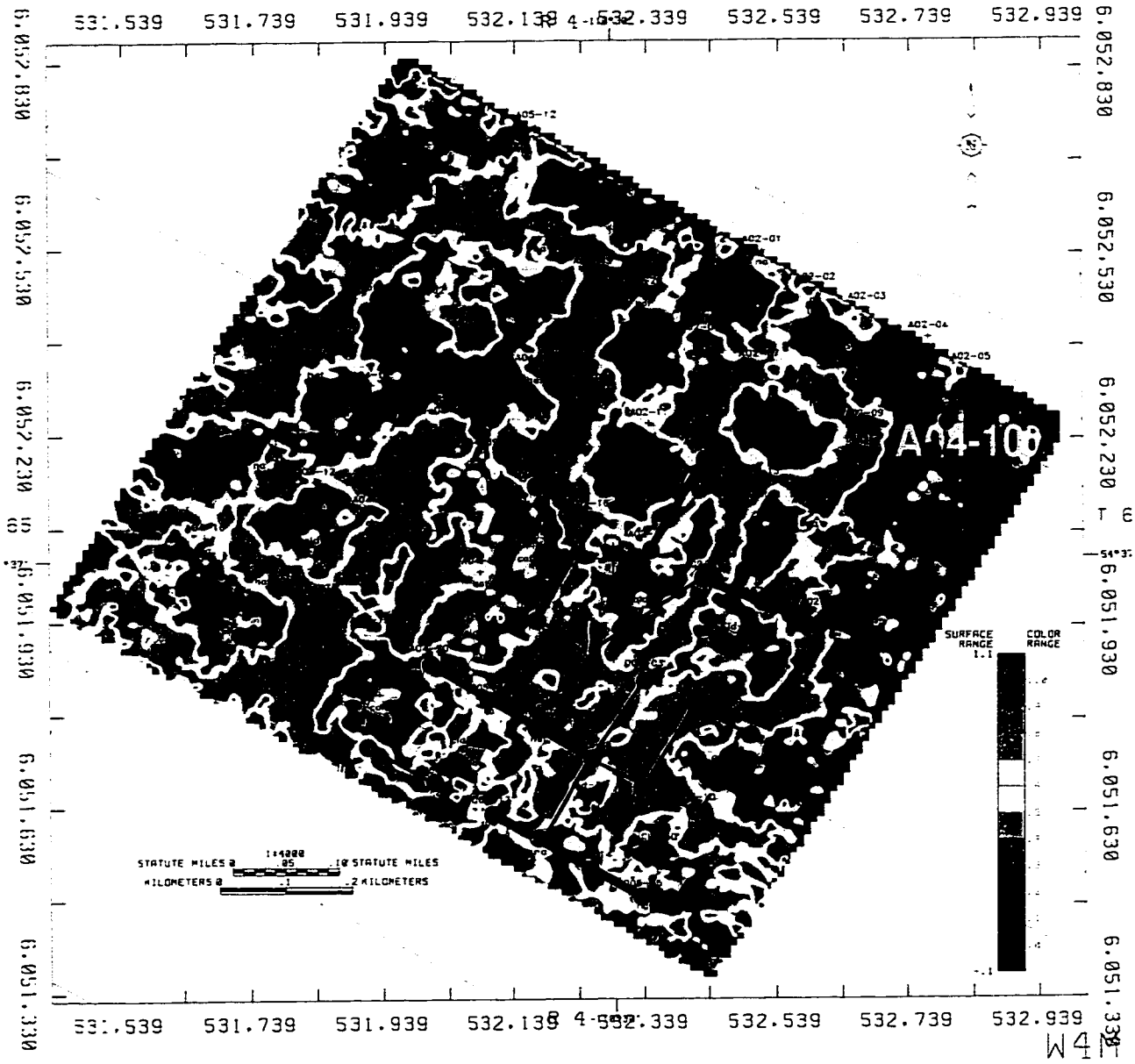

FIG. 5.8. Discriminant analysis results of hot versus cold reservoir of A2A4 pads using five conventional attributes (aab, ap, pav, centfreq, decil2, decil8), local calibration applied (calibration parameter k=10).

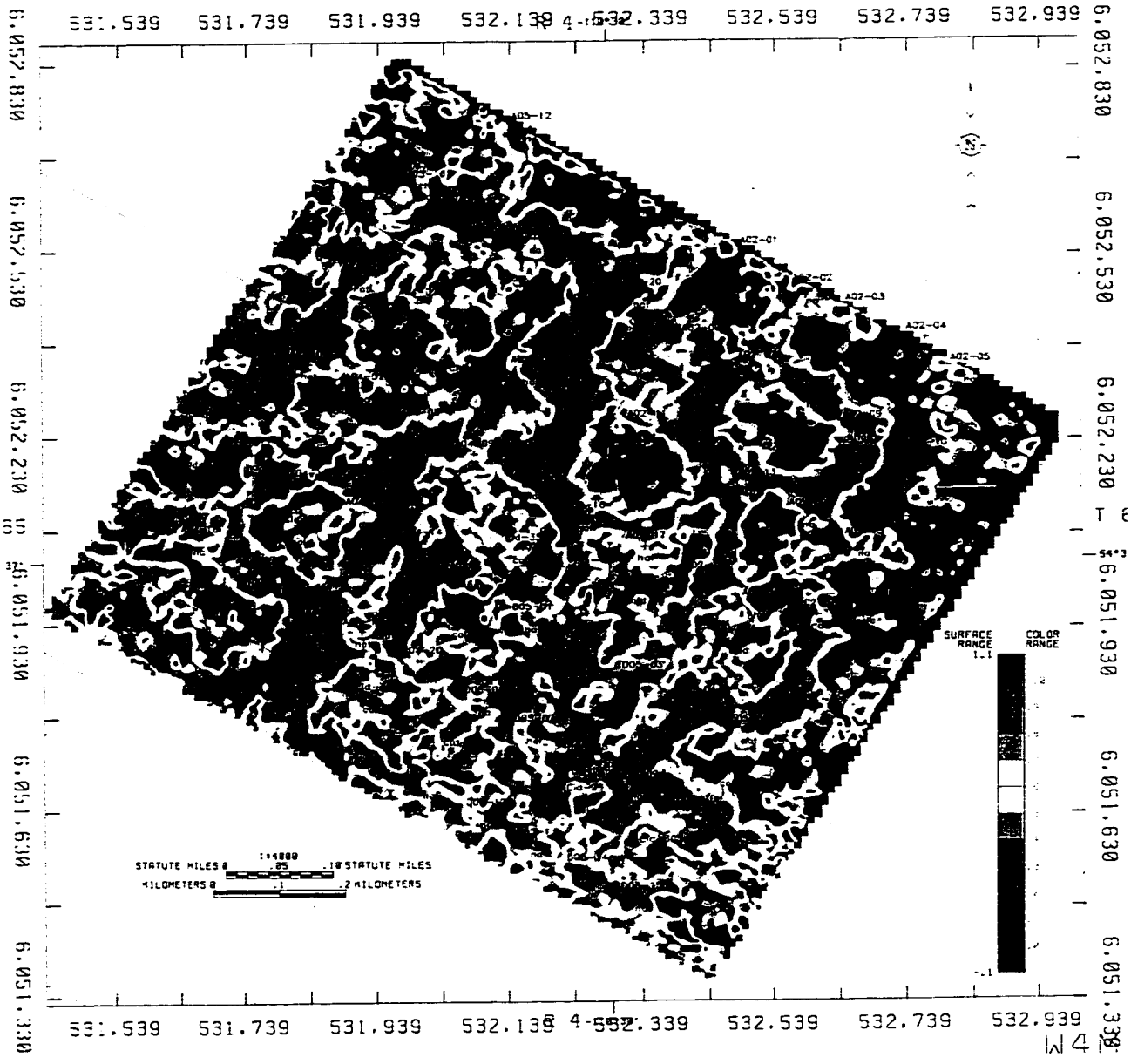

FIG. 5.9. Discriminant analysis results of hot versus cold reservoir of A2A4 pads using conventional five attributes (aab, ap, pav, centfreq, decil2, decil8), local calibration applied (calibration radius parameter k=5).

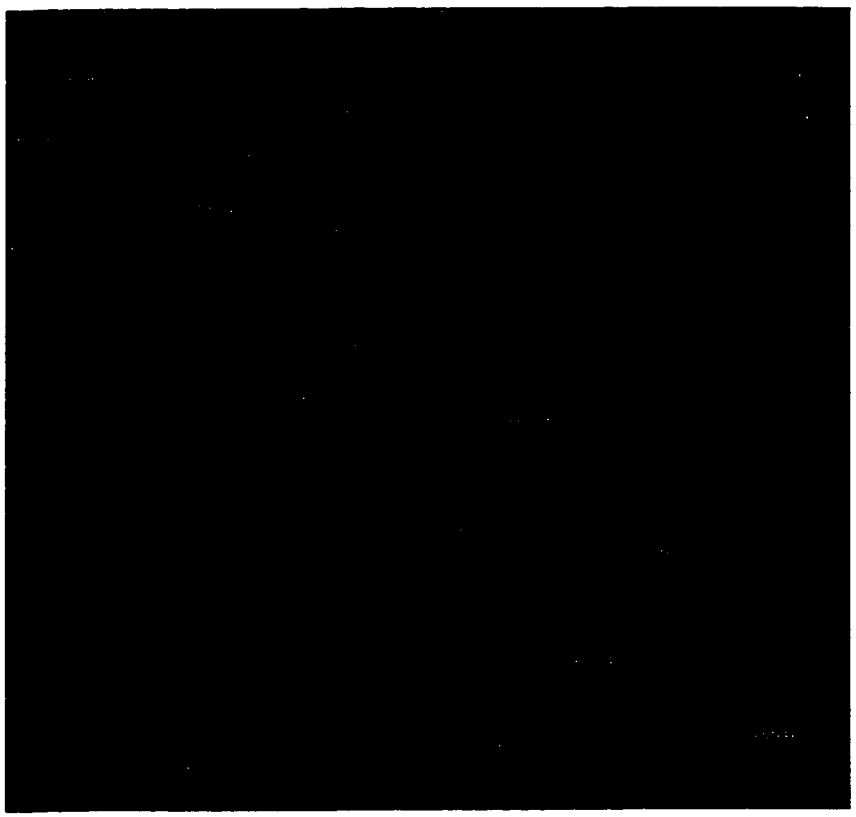

FIG. 5.10. Cross-plots of six conventional attributes showing some correlation between attributes.

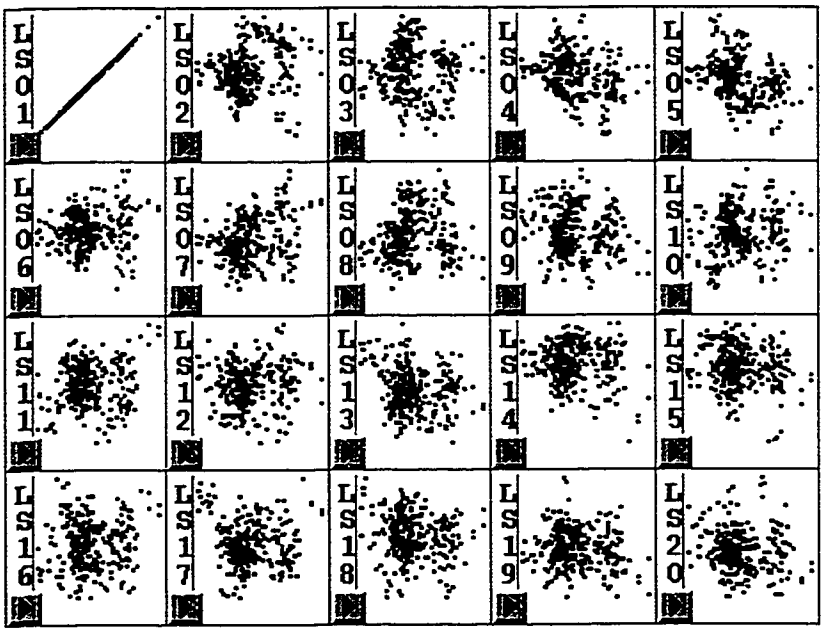

FIG. 5.11. Cross-plots of principal component attribute-1 (ls01) against 20 principal component attributes (ls01-ls20) showing no correlation between attributes.

(see Table 5.4). To capture 99.99% of the information when data is filtered down to 25 Hz only 6 attributes are needed. The lower the band of data the higher the percentage of

Table 5.2. Pearson correlation coefficients of the 10 PCA attributes (N=12709)

	PCA01	PCA02	PCA03	PCA04	PCA05	PCA06	PCA07	PCA08	PCA09	PCA10
PCA01	1.00000	-0.00000	0.00000	0.00000	-0.00001	0.00001	-0.00000	-0.00001	-0.00001	-0.00001
	0.0	0.9996	0.9998	0.9998	0.9994	0.9994	0.9997	0.9989	0.9993	0.9987
PCA02	0.00000	1.00000	0.0000	0.00000	-0.00000	0.00000	-0.00000	-0.00000	-0.00001	-0.00002
	0.9996	0.0	1.0000	0.9997	0.9996	0.9999	0.9998	1.0000	0.9990	0.9982
PCA03	0.00000	0.00000	1.00000	-0.00000	0.00000	-0.0000	0.0000	0.00001	-0.00000	0.00001
	0.9998	1.0000	0.0	0.9996	1.0000	0.9998	0.9999	0.9993	0.9999	0.9995
PCA04	0.00000	0.00000	-0.00000	1.00000	0.00000	0.00000	-0.00000	0.00000	0.00000	0.00001
	0.9998	0.9997	0.9996	0.0	0.9997	0.9996	0.9999	0.9996	0.9999	0.9994
PCA05	-0.00001	-0.00000	0.00000	0.00000	1.00000	-0.00001	-0.00000	-0.00001	0.0000	-0.00001
	0.9994	0.9996	1.0000	0.9997	0.0	0.9995	0.9996	0.9995	0.9996	0.9994
PCA06	0.00001	0.00000	-0.00000	0.00000	-0.00001	1.00000	-0.00000	0.00000	0.00001	-0.00001
	0.9994	0.9999	0.9998	0.9996	0.9995	0.0	0.9999	0.9999	0.9991	0.9993
PCA07	-0.00000	-0.00000	0.00000	-0.0000	-0.00000	-0.0000	1.00000	-0.0000	-0.00000	-0.00000
	0.9997	0.9998	0.9999	0.9999	0.9996	0.9999	0.0	0.9999	0.9996	0.9997
PCA08	-0.00001	-0.00000	0.00001	0.00000	-0.00001	0.00000	-0.00000	1.0000	0.00000	-0.00000
	0.9989	1.0000	0.9993	0.9996	0.9995	0.9999	0.9999	0.0	0.9998	0.9999
PCA09	-0.00001	-0.00001	-0.0000	0.00000	0.00000	0.00001	-0.00000	0.0000	1.00000	-0.00000
	0.9993	0.9990	0.9999	0.9999	0.9996	0.9991	0.9996	0.9998	0.0	1.0000
PCA10	-0.00001	-0.00002	0.00001	0.00001	-0.00001	-0.00001	-0.00000	-0.0000	-0.00000	1.00000
	0.9987	0.9982	0.9995	0.9994	0.9994	0.9993	0.9997	0.9999	1.0000	0.0

variance captured by the first few attributes. The high-frequency component of the data is thrown away when filtering the high end of the data. However, this provides a means to measure the influence of the frequency content to the effectiveness of reservoir monitoring (steam conformance mapping). To obtain the high frequency component geophones are buried 10 m below the surface, which significantly increases the cost of the survey (about $100 drilling cost for each geophone).

Table 5.3. Basic statistics of the first 10 principal component attributes of A2/A4 pads

Variable	N	Mean	Std Deviation	Sum	Minimum	Maximum
PCA01	12709	922.980648	2032.715089	11730161	-4827.9000	9080.000000
PCA02	12709	-1330.228787	1819.034723	-16905878	-9419.7000	5519.800000
PCA03	12709	493.728291	1471.646745	6274793	-4499.0000	7018.400000
PCA04	12709	442.033041	1307.245714	5617798	-4730.9000	5525.70000
PCA05	12709	-465.775607	1178.946397	-5919542	-5079.1000	4438.700000
PCA06	12709	-285.721995	1083.039590	-3631241	-4404.8000	4300.500000
PCA07	12709	822.010600	933.735152	10446933	-2875.6000	4487.100000
PCA08	12709	-813.715171	807.035934	-10341506	-4200.2000	2486.200000
PCA09	12709	-240.836789	558.714046	-3060795	-2332.6000	1986.500000
PCA10	12709	-11.359353	304.846091	-144366	-1319.6000	1208.200000

How many principal component attributes are needed in discriminant analysis to obtain the best steam conformance map? Is the wider frequency band (higher frequency) the better result of the analysis or is the low frequency data sufficient enough for Cold Lake reservoir monitoring? This issue will impact the data acquisition cost since we may not need to bury geophones if low frequency data is acceptable for steam conformance mapping. The following discussions will address the above two questions.

Table 5.4. Hierarchy of Clearwater formation PC shapes

shape #	100% frequency		High cut 62 Hz		High cut 25 Hz	
	var cap %	acc var %	var cap %	acc var %	var cap %	acc var %
1	11.400	11.400	26.177	26.177	48.239	48.239
2	11.050	22.450	20.952	47.129	31.084	79.323
3	10.043	32.493	13.720	60.849	11.821	91.144
4	8.758	41.251	10.818	71.667	7.596	98.740
5	7.990	49.241	8.788	80.455	1.155	99.895
6	6.434	55.675	7.391	87.864	0.100	99.995
7	5.772	61.447	5.497	93.343	0.005	100.000
8	5.335	66.782	4.111	97.454		
9	4.821	71.603	1.860	99.314		
10	4.694	76.297	0.541	99.855		
11	4.194	80.491	0.116	99.971		
12	3.806	84.297	0.024	99.995		
13	3.651	87.948	0.005	100.000		
14	3.361	91.309	0.001	100.001		
15	3.225	94.534				
16	2.438	96.972				
17	1.521	98.493				
18	1.127	99.620				
19	0.315	99.935				
20	0.058	99.993				

To find out the number of linear shape attributes needed the data with bandpass filtered down to 25 Hz was first used in the discriminant analysis. The results indicate that the statistics of well-to-seismic tie increase both hot and cold classes as the number of attributes involved increases (see Table 5.5). It should be noted that the 7th attribute in the 25 Hz data only capture 0.005% of the information or variance (see Table 5.4) which could be noise, therefore, it may not add value to the result of analysis. As a matter of fact, the statistics of well-to-seismic tie for seven attributes is even lower than six attributes (see Table 5.5).

Table 5.5. Well-to-seismic tie statistics using 25 Hz data

class	number of attributes used						
	7	6	5	4	3	2	1
hot	82.1	84.7	84.7	83.4	80.2	75.8	74.5
cold	80.1	77.6	78.1	76.8	78.1	76.0	72.7

The statistics show the same trend, that is by increasing the number of attributes in the discriminant analysis the well-to-seismic tie statistics improve when the full frequency content is used, except that the last two attributes (0.007% variance captured) improved the statistics (see Table 5.6). This table also shows that the low-variance end of the attributes is not always noise. It may contain a signal of the reservoir properties. One way to prove this is to generate some numerical modeling data that does not contain any noise and analyze the low-variance end of attributes.

Table 5.6. Well-to-seismic tie statistics using full frequency data

class	number of attributes used		
	22	20	16
hot	89.17	88.54	83.44
cold	83.88	82.64	79.75

From the above analysis and the results in Table 5.7, it is observed that the data with full frequency content gives a better tie of the well-to-seismic than the data with a high cut bandpass filtered applied. Also, a full set of attribute gives the best tie of well-to-seismic.

Table 5.7. Comparison of well-to-seismic statistics between conventional and principal component attributes.

class	conventional attributes	linear shape attributes		
	full frequency 7 attributes	full frequency 22 attributes	high cut 62 Hz 14 attributes	high cut 25 Hz 7 attributes
hot	79.75	89.17	82.80	82.17
cold	74.69	83.88	79.34	80.17

Most importantly principal component attributes have significantly improved the statistical tie between the well and the seismic for both hot and cold calibration points. Figures 5.12 to 5.14 further illustrate that increasing the number of principal component attributes in discriminant analysis improves the steam conformance mapping. Visually, it seems that the improvement is marginal by comparing the results from the 22 attributes (Figure 5.12) which capture 100% of the information (see Table 5.4) and 16 attributes

(Figure 5.13) which capture 96.97% of information (see Table 5.4). However, a significant amount of the noise is introduced to the image (see Figure 5.14) when only 8 attributes is used, which only capture 66.78% of the information (see Table 5.4). Figure 5.15 shows the result from the full set of attributes, in which the data is high cut bandpass filtered down to 62 Hz. Though the major character is the same the image is noisy and S.E. corner does not tie to pressure data as the high frequency component of the data was left out of the analysis. In Figures 5.8 and 5.12, the steam conformance maps are overlain with the well-to-well connections derived from the wellhead pressure communication data at D05 pad and surrounding area. The seismic map from conventional attributes cannot be fully reconciled with the engineering pressure communication data (Figure 5.8), i.e. the engineering pressure data suggests strong communication among wells D05-12 to D05-15 (S.E. corner) and strong communication among wells A02-18 to A02-20 (last row of A02 pad). The seismic map from conventional attributes shows that no anomaly is present in the northeast corner of the survey (well A02-10).

The principal component attribute analysis at the A02/A04 seismic monitoring project produced better results than the conventional attribute analysis (Figure 5.12). In particular, the discriminant function provided an 89% correlation with well control, and the areal conformance was better correlated with the engineering pressure communication data (compare Figure 5.12 with Figure 5.8). Finally, the spatial coherence of the mapped features is higher with the principal component attribute analysis than with the conventional attributes and an anomaly (steam chamber) is also present in the northeast corner of the survey (well A02-10).

Three horizontal wells were drilled recently as infill wells to the survey area to enhance the recovery (see Figure 5.16 for well path denoted in green lines). Temperature and resistivity logs of well D03-H3 are plotted in Figure 5.17. The high temperature locations are the steam chambers intersected by the horizontal well, where the resistivity is low as the reservoir is depleted and water saturation is high. Figure 5.18 shows the overlain plot of resistivity, seismic classification (in the scale of 0 to 1) by using traditional attributes

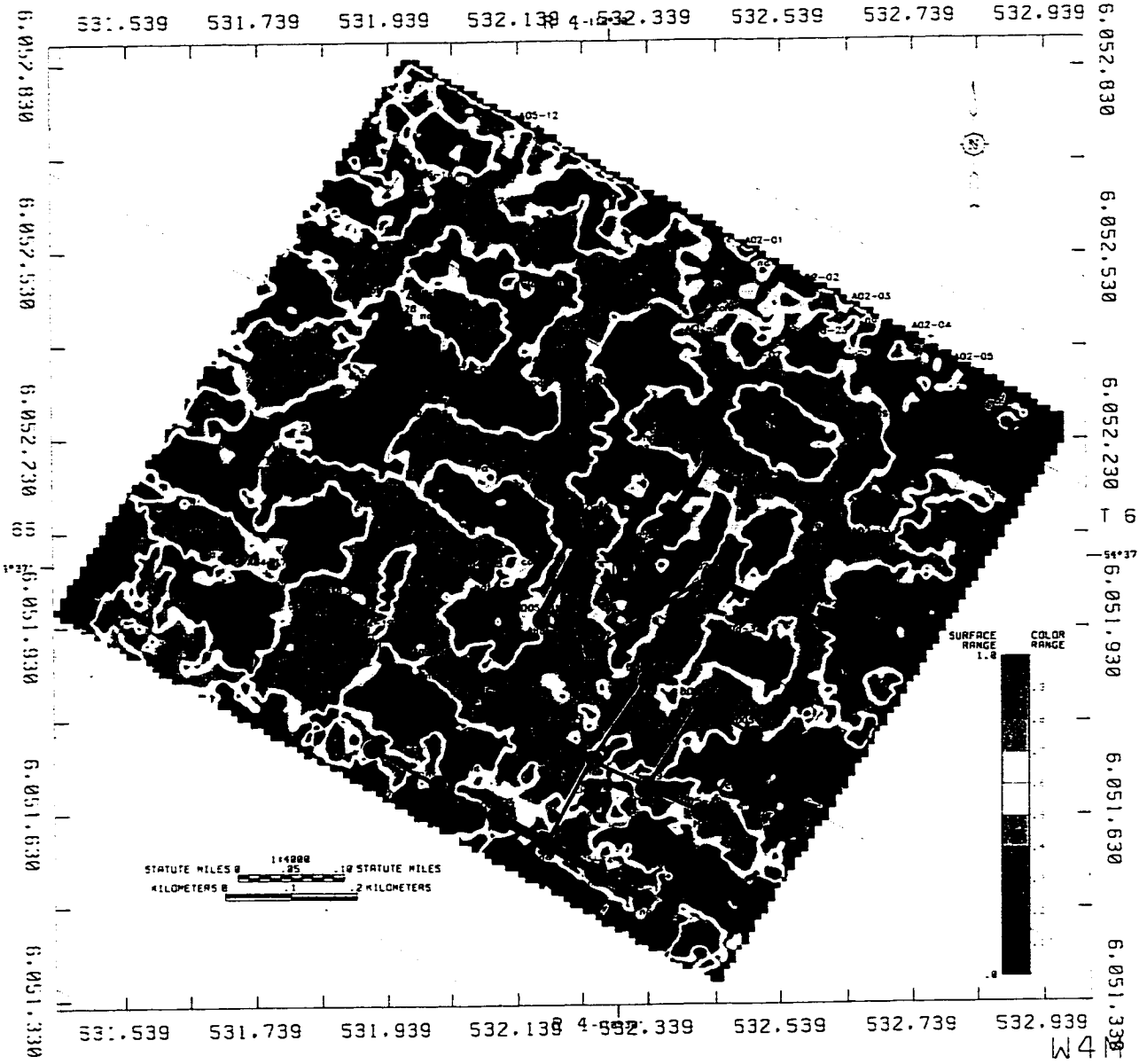

FIG. 5.12. Discriminant analysis results of hot versus cold reservoir of A2A4 pads using 22 principal component attributes for full data frequency content, global calibration applied.

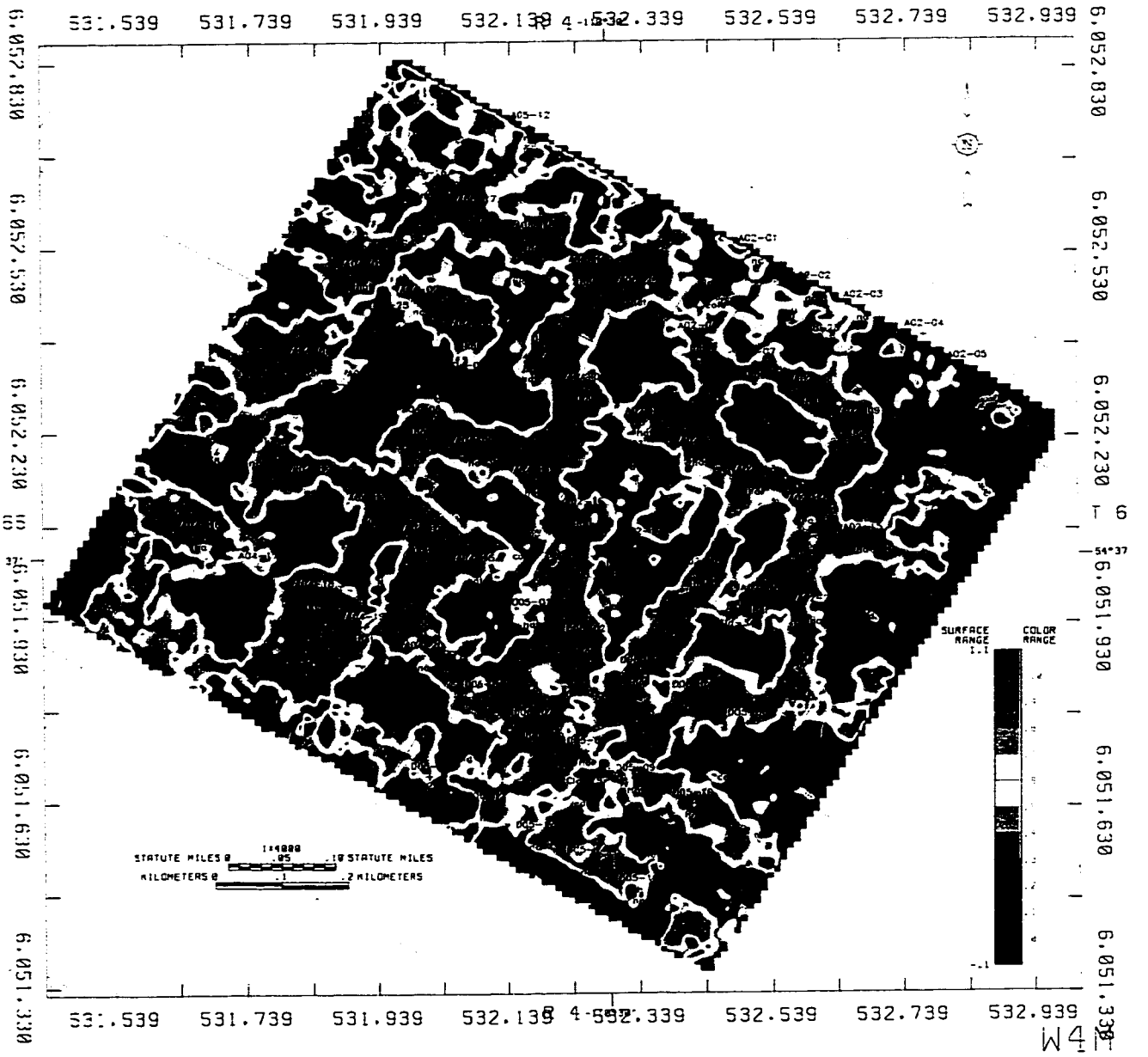

FIG. 5.13. Discriminant analysis results of hot versus cold reservoir of A2A4 pads using 16 principal component attributes for full data frequency content, global calibration applied.

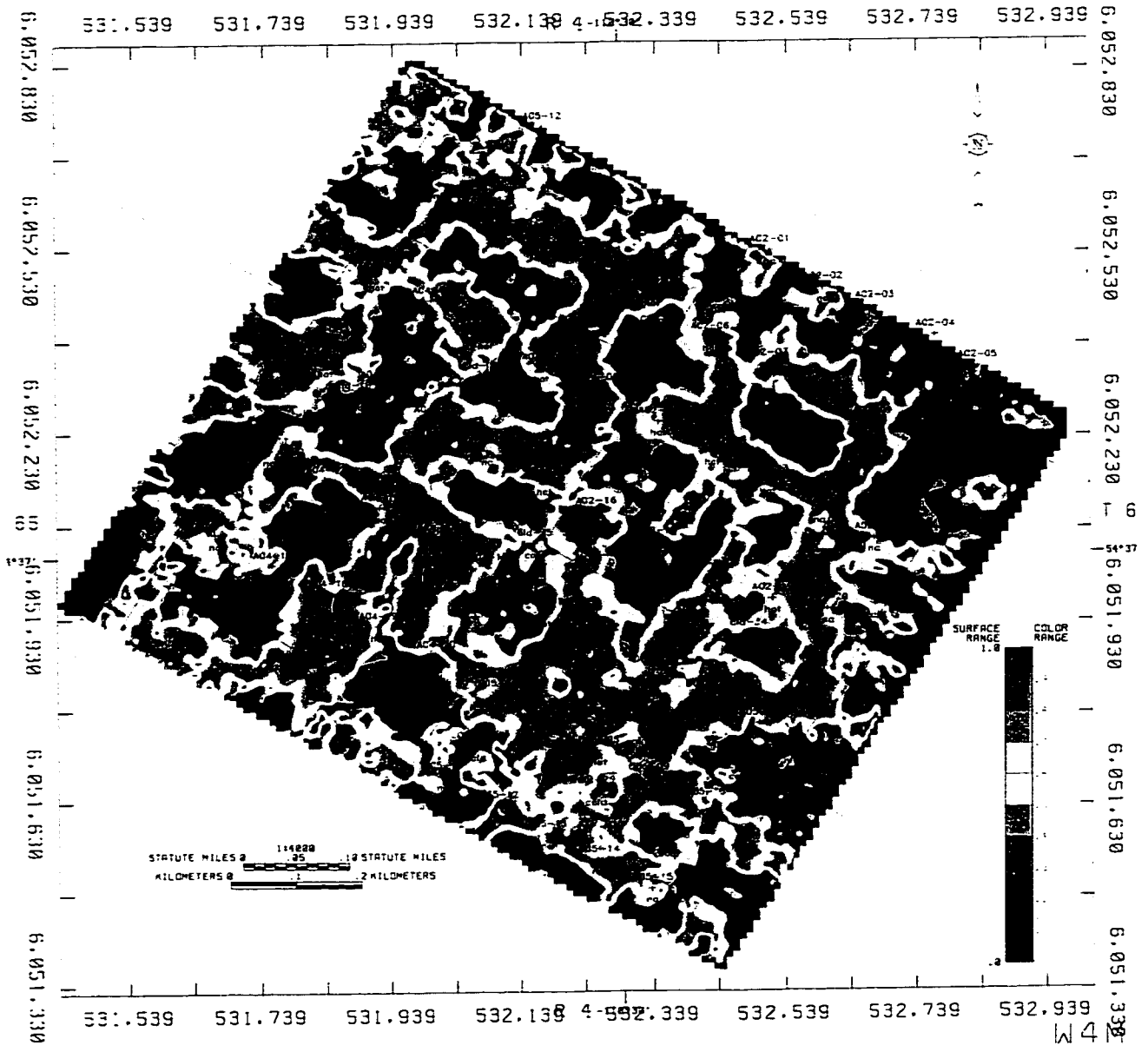

FIG. 5.14. Discriminant analysis results of hot versus cold reservoir of A2/A4 pads using 8 principal component attributes for full data frequency content, global calibration applied.

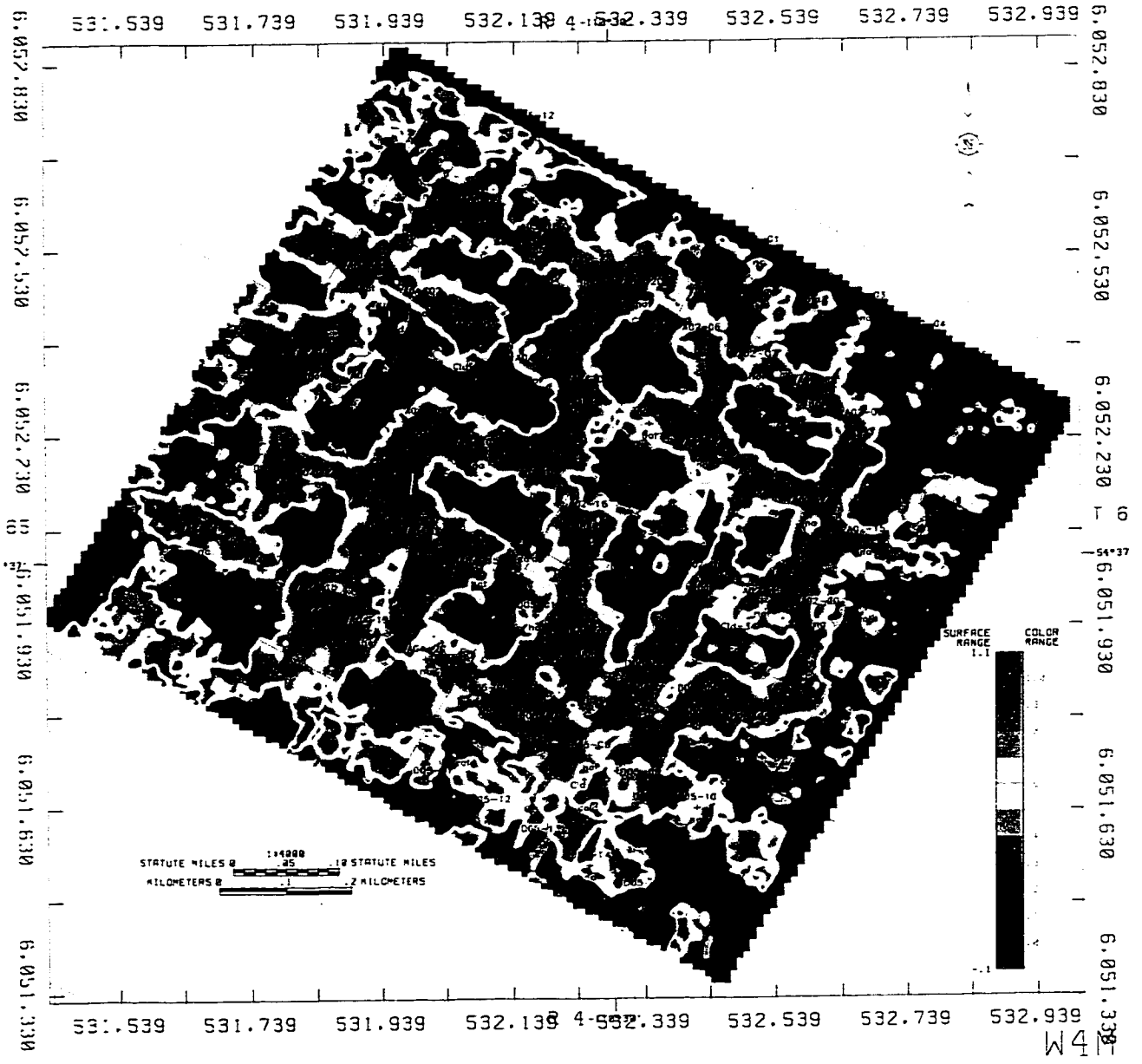

FIG. 5.15. Discriminant analysis results of hot versus cold reservoir of A2A4 pads using 13 principal component attributes for data with frequency high cut ~60 Hz, global calibration applied.

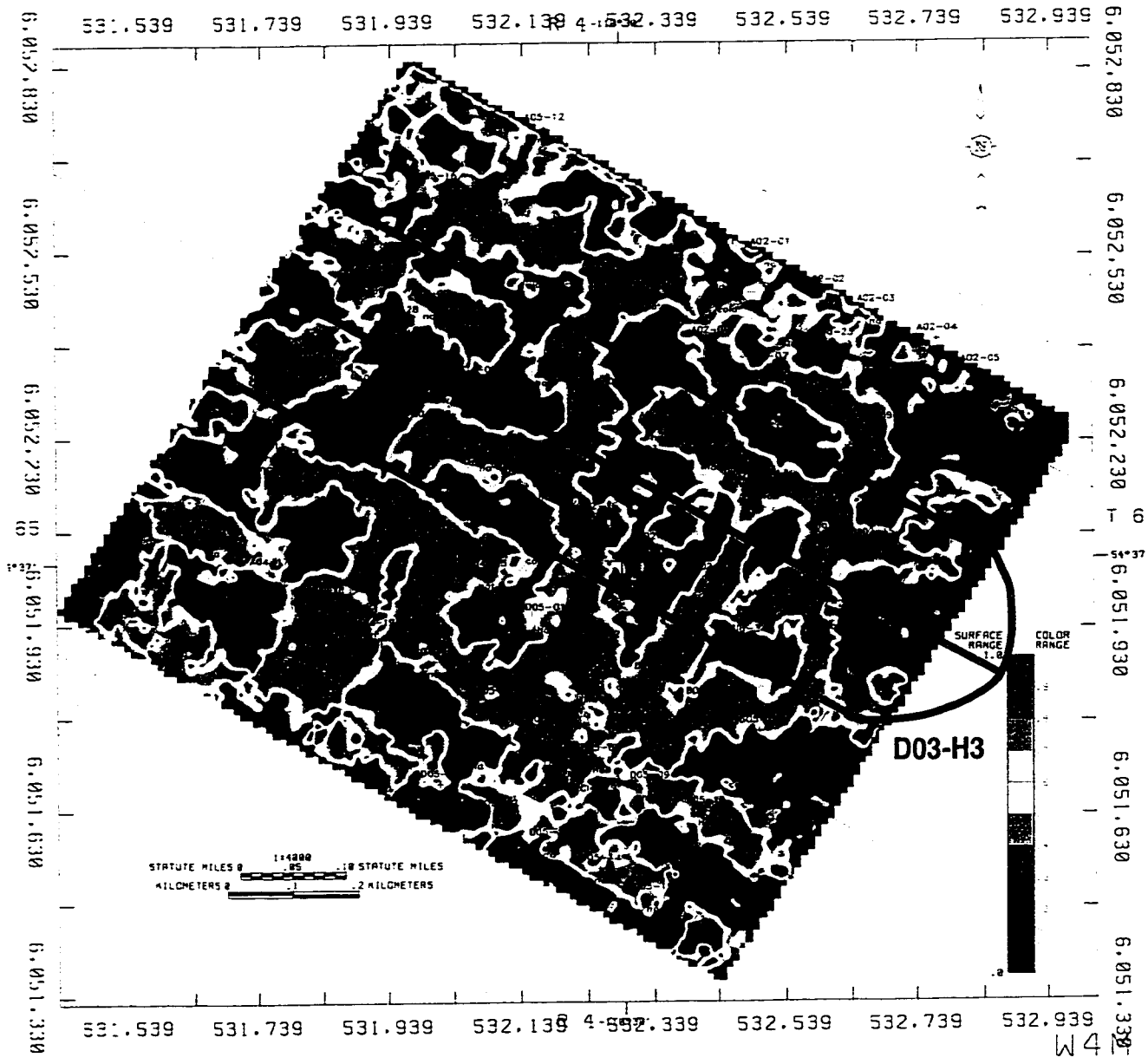

FIG. 5.16. Areal steam conformance map of A2A4 pads overlain with infill horizontal well locations.

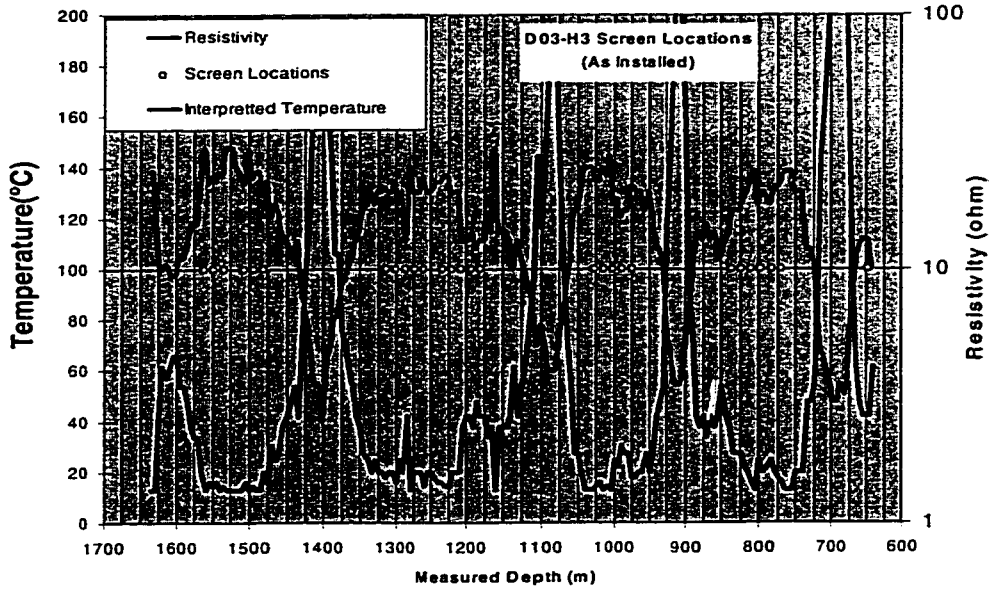

FIG. 5.17. Resistivity and temperature profile along horizontal well D03-H3.

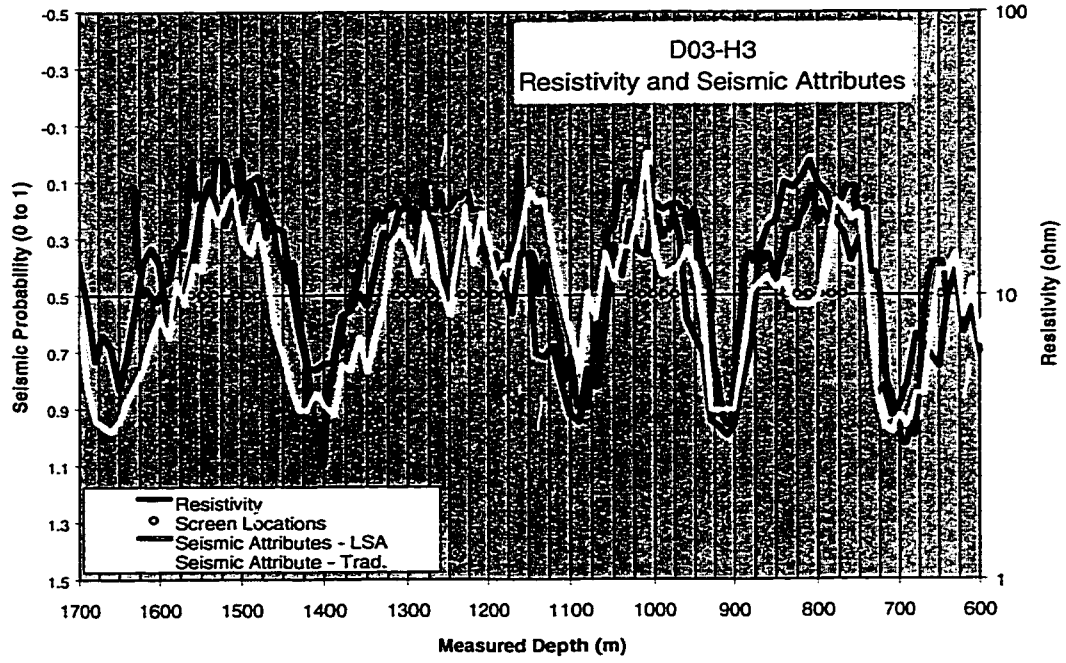

FIG. 5.18. Resistivity and seismic probability from conventional and principal component attributes of hot versus cold reservoir along horizontal well D03-H3.

and principal component attributes. It is indicated that principal component attribute results in a better fit to resistivity than conventional attributes. Similarly, the linear shape attribute analysis has made improvement over the J trunk (J1/J8 pads) area. Statistically, the well-to-seismic tie of the 23 linear shape attributes is only marginally higher than the 7 conventional attributes (see Table 5.8, 90.5% vs. 89.6% for hot and 97.2% vs. 96.3% for cold). However, the actual images look very different. Figure 5.19 shows steam conformance over the J trunk area from the seven conventional attributes analysis. The orange dots are the infill locations solely derived from engineering well-to-well pressure communication data. The number of inside dots shows the infill priorities. Comparing the result from the principal component attributes (Figure 5.20), the areal conformance from the conventional attribute analysis is significantly bigger. The result from the principal component attributes analysis fits better.

Table 5.8. Well-to-seismic tie statistics at the J trunk

class	conventional attributes 7 attributes	linear shape attributes 23 attributes
hot	89.6	92.3
cold	96.3	98.1

5.3.3 Time-lapse cross-calibration using principal component attributes

The principal component attributes are not directly related to the physical properties (no physical meaning for each attribute), yet, they fit well to the Cold Lake steam conformance mapping, as it is a multi-variant analysis. Perceived disadvantages of the principal component attributes are that they are data set dependent and they are not applicable for single attribute analysis. To illustrate the point of data set dependent time-lapse seismic surveys of the B02 pad was elected and analyzed (data range of inline is 100 to 200 and cross line is 60 to 120). The analysis was focused in a constant time window of 510 to 560 ms with an extension of one pulse width of 12 ms, making the total window length of 62 ms. Figure 5.21 shows a finite set of 32 seismic shapes that were decomposed independently from the 1995 survey and 1997 survey of the B02 pad area.

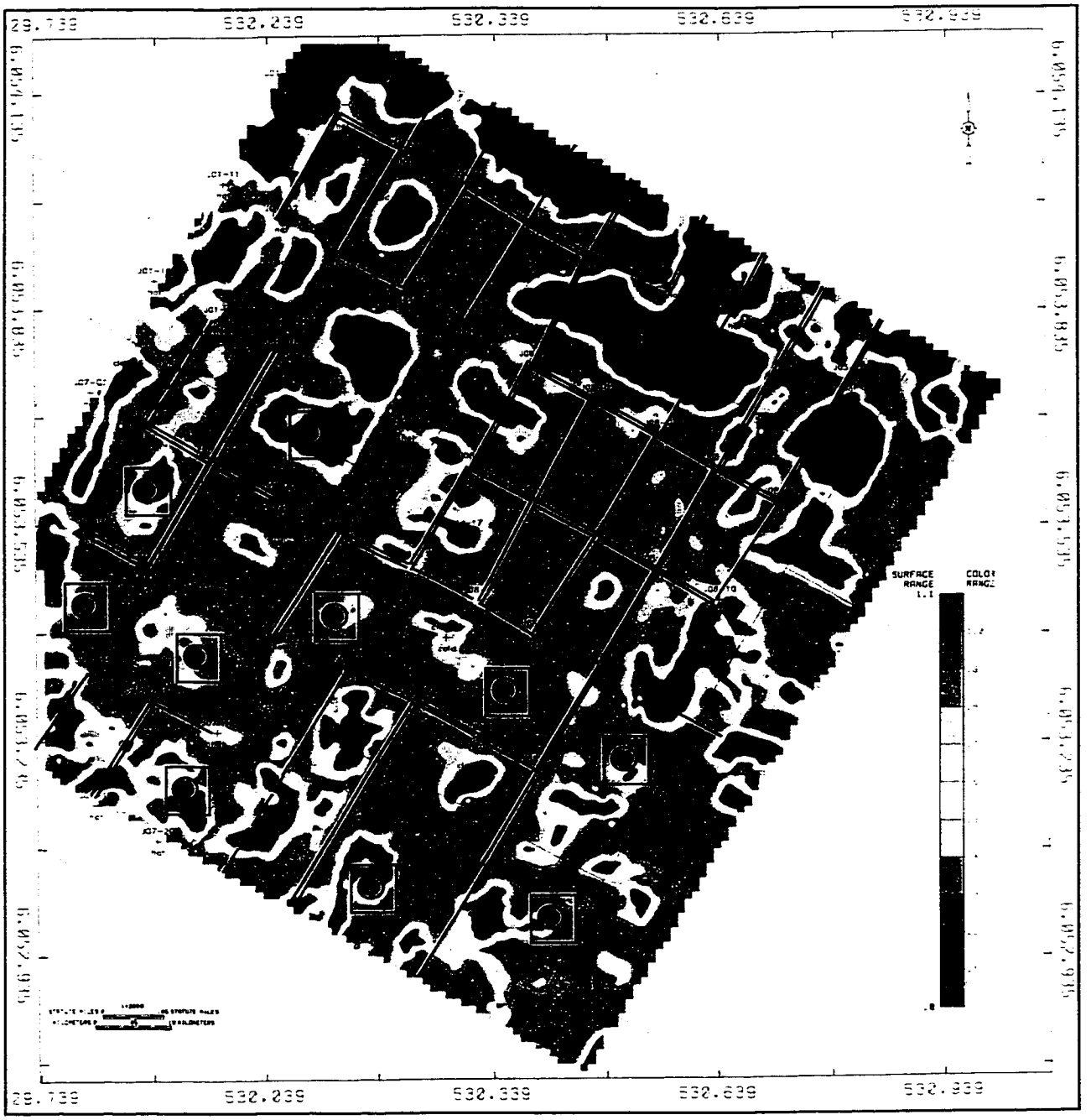

FIG. 5.19. Discriminant analysis results of hot versus cold reservoir of J1J8 pads using conventional 7 attributes for full data frequency (global calibration applied). Black lines are well-to-well connections derived from engineering pressure communication data. Double solid lines indicate strong connection, single solid line indicates moderate connection, dashed line indicates weak connection. Dots indicates proposed infill locations.

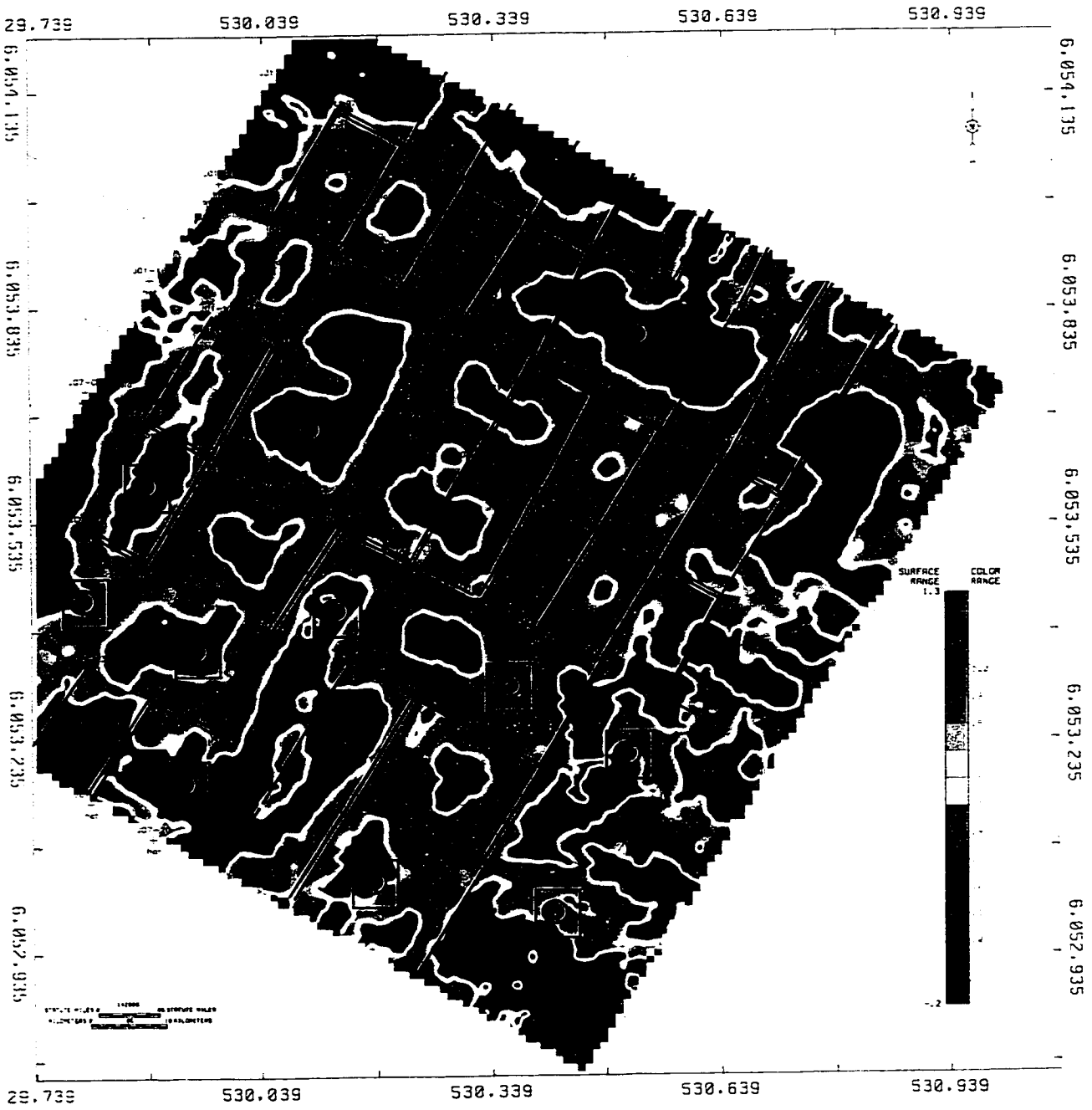

FIG. 5.20. Discriminant analysis results of hot versus cold reservoir of J1J8 pads using 23 principal component attributes for full data frequency (global calibration applied). Black lines are well-to-well connections derived from engineering pressure communication data. Double solid lines indicate strong connection, single solid line indicates moderate connection, dashed line indicates weak connection.

It was obvious that the two sets of seismic shapes were very different, that is, principal component attributes of the two surveys were not corresponding. Figures 5.22 and 5.23 show the first linear shape attributes of the 1995 survey and the 1997 survey respectively through independent decomposition. Although they are just the first attributes for each survey, Figure 5.23 (1997 survey) shows a good conformance change introduced by the injector-only-infill wells (reference Chapter 4). Unfortunately, in this case attributes from the 1995 survey can not be used to calibrate the attributes from the 1997 survey. The essence of reservoir monitoring is to use past reservoir status (known) to compute current reservoir status (unknown) via seismic data analysis. Seismic data can be used as a bridge to predict the future (within certain time frame) reservoir status, therefore, cross-calibration is required in the time-lapse analysis. As demonstrated above, the linear shape attributes are data set dependent and not corresponding. To avoid this issue, the time-lapse data sets were analyzed by merging the two data sets together. The seismic shapes were extracted from the merged data set, and the attributes were calculated separately from each individual data set using the same principal component shapes. Figure 5.24 shows the 32 seismic shapes from the decomposition of the merged data set. This set of seismic shapes was used consistently to extract the principal component attributes for both the 1995 and 1997 surveys. The variance captured in the three different decompositions shows very similar distribution (Figure 5.25). Using the same set of seismic shapes does not mean that the attributes from the two different surveys are the same. Figures 5.26 and 5.27 show the first principal component attributes of the 1995 and 1997 surveys respectively from joint shapes, in which the steam conformance looks different. The changes appear on the 1997 survey (Figure 5.27). It has made no difference in the discriminant analysis for the 1995 survey whether attributes were extracted from shapes decomposed independently or jointly. The final steam conformance maps are almost identical (Figure 5.28 *vs* Figure 5.29); however, it has made a big difference when cross-calibration is applied in discriminant analysis. Figures 5.30 and 5.31 show the current (1997) steam conformance using the discriminant analysis

of the attributes from shapes decomposed independently and jointly. Joint seismic shape decomposition has made a significant improvement.

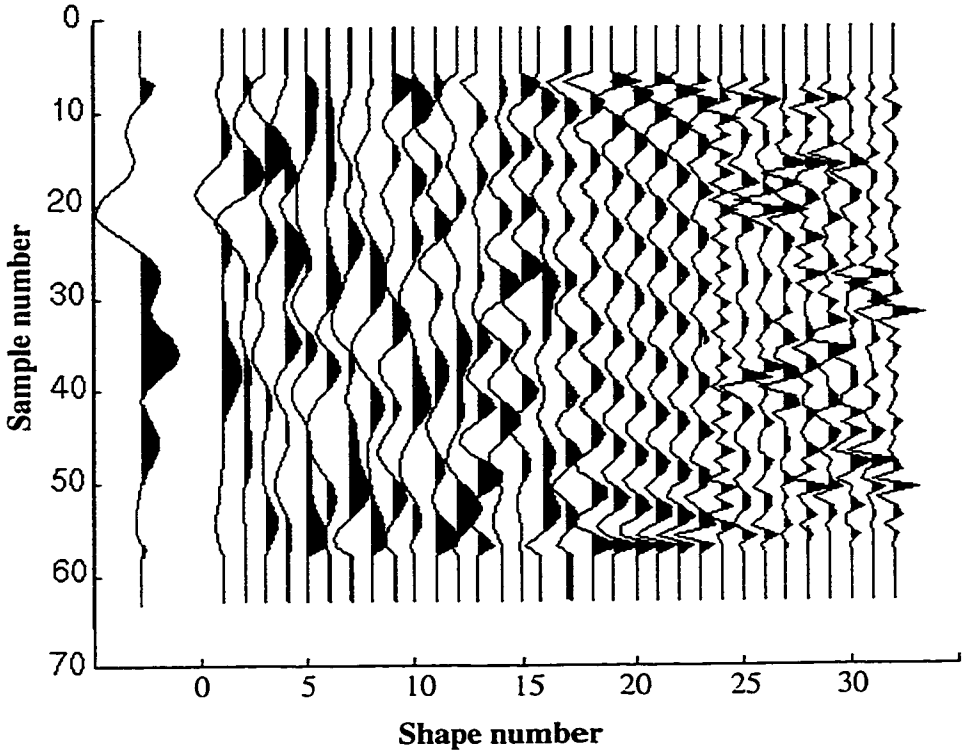

a). shape of mean (left) and seismic shapes (32) from 1995 survey

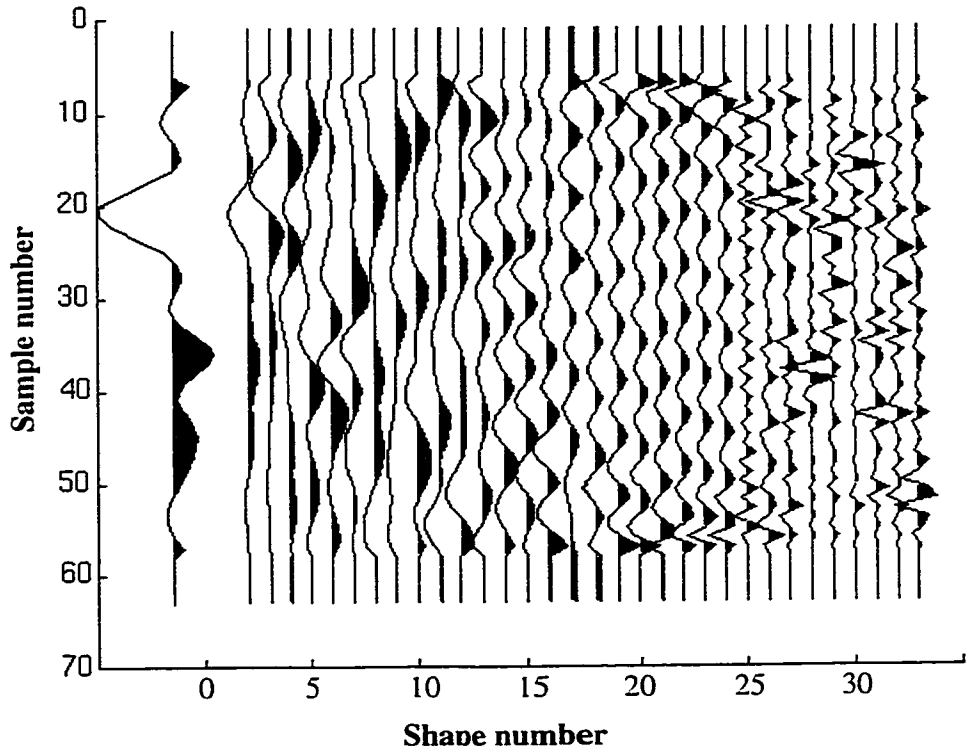

b). shape of mean (left) and seismic shapes (32) from 1997 survey

FIG. 5.21. Independently decomposed finite set of seismic shapes (32) from B2 pad of 1995 survey (a) and 1997 survey (b) showing that shapes are data set dependent. The shape of mean is obtained by taking mean of 32 attributes.

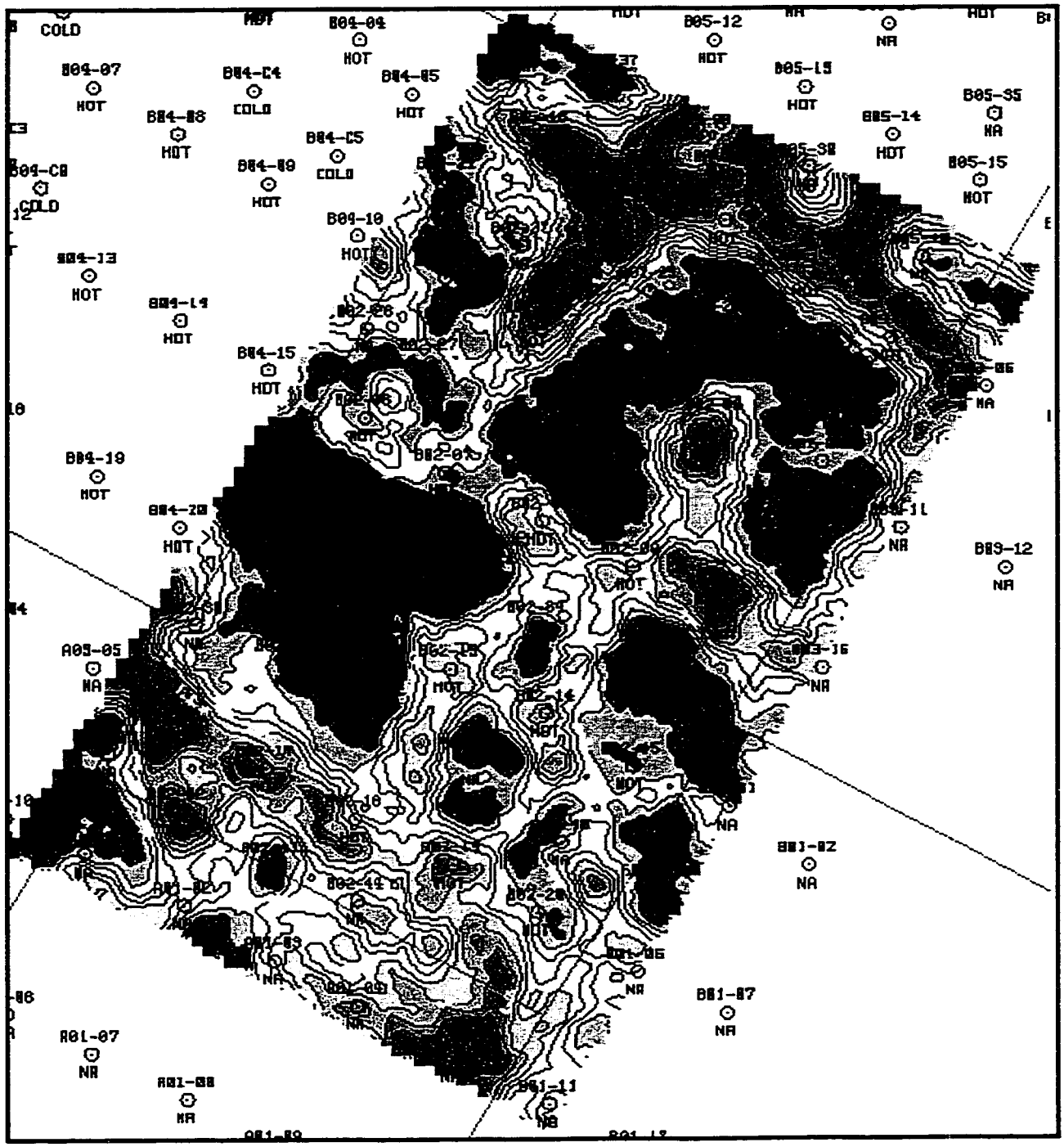

FIG. 5.22. Contour plot of the first principal component attribute of the 1995 survey from independent seismic shape decomposition.

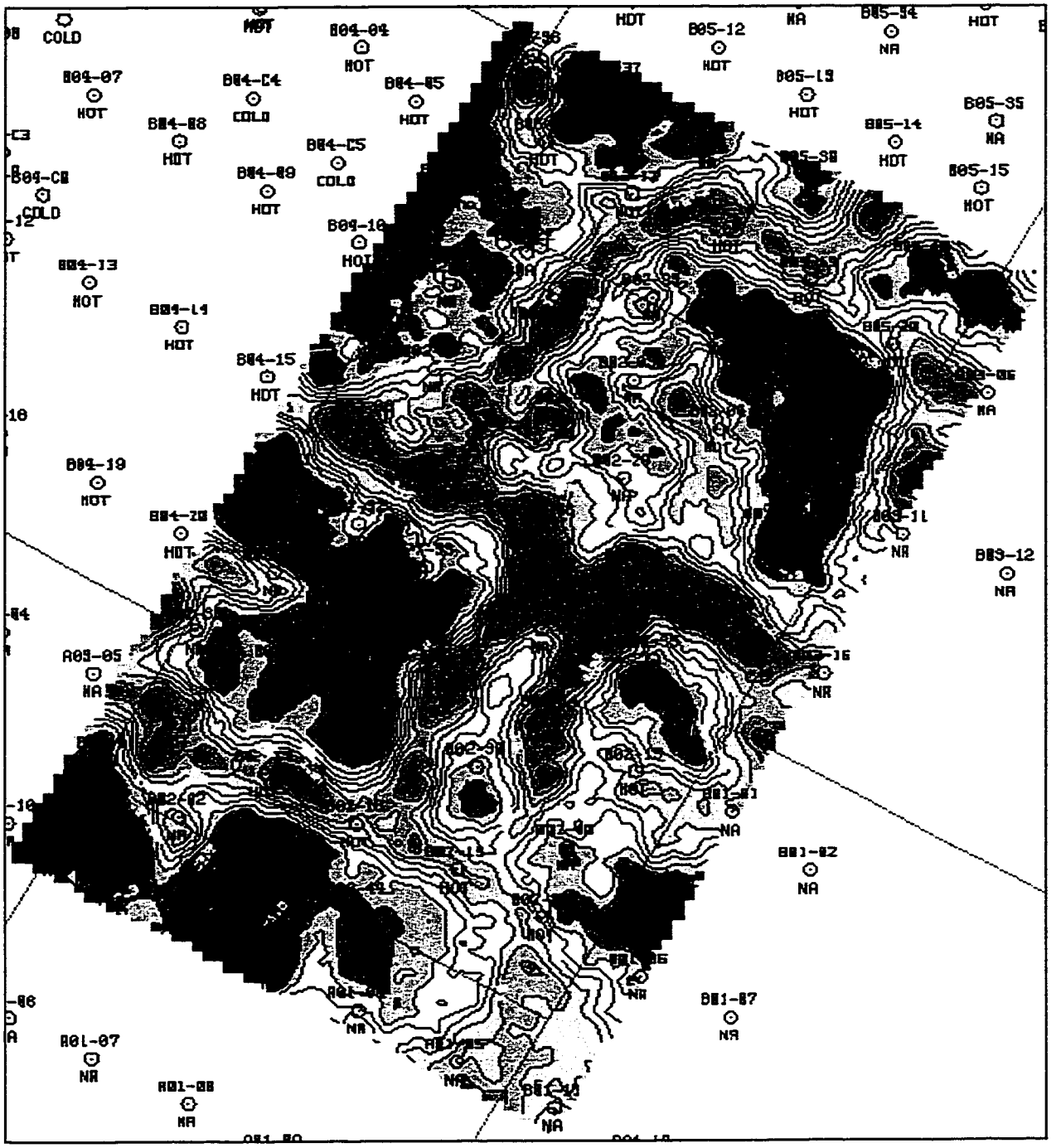

FIG. 5.23. Contour plot of the first principal component attribute of the 1997 survey from independent seismic shape decomposition.

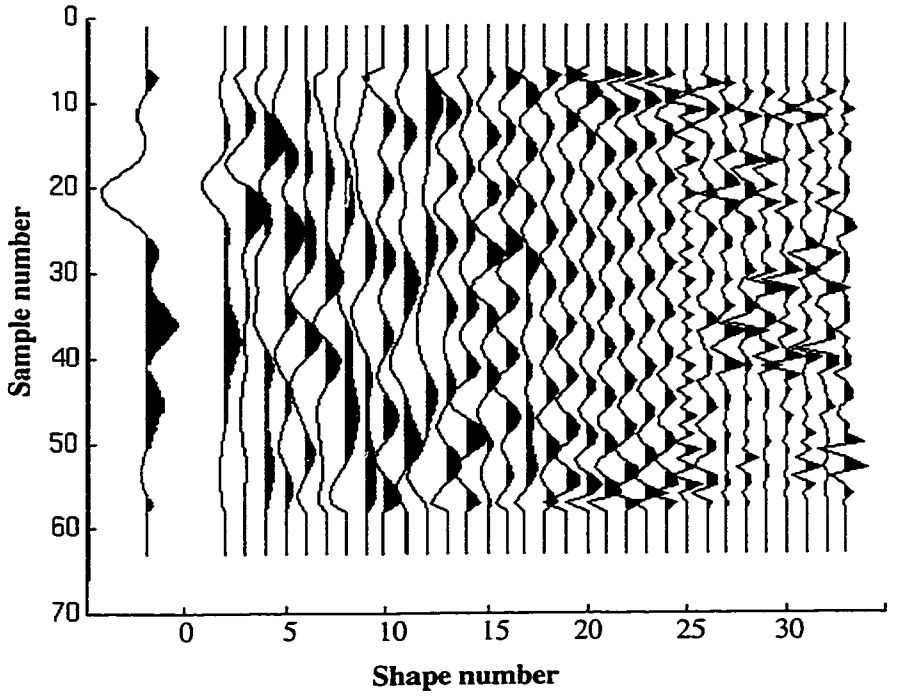

FIG. 5.24. Jointly decomposed finite set of seismic shapes (32) from B2 pad of the 1995 survey and 1997 survey. The shape of mean (left) is obtained by taking mean average of 32 shapes

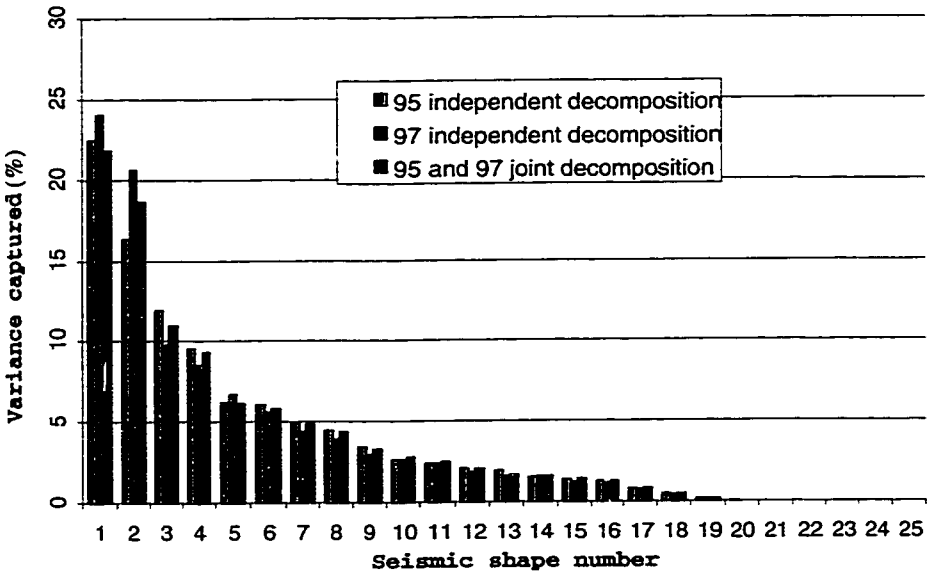

FIG. 5.25. Comparison of variance (information) captured (%) for seismic shape between joint decomposition and independent decomposition of 1995 and 1997 surveys.

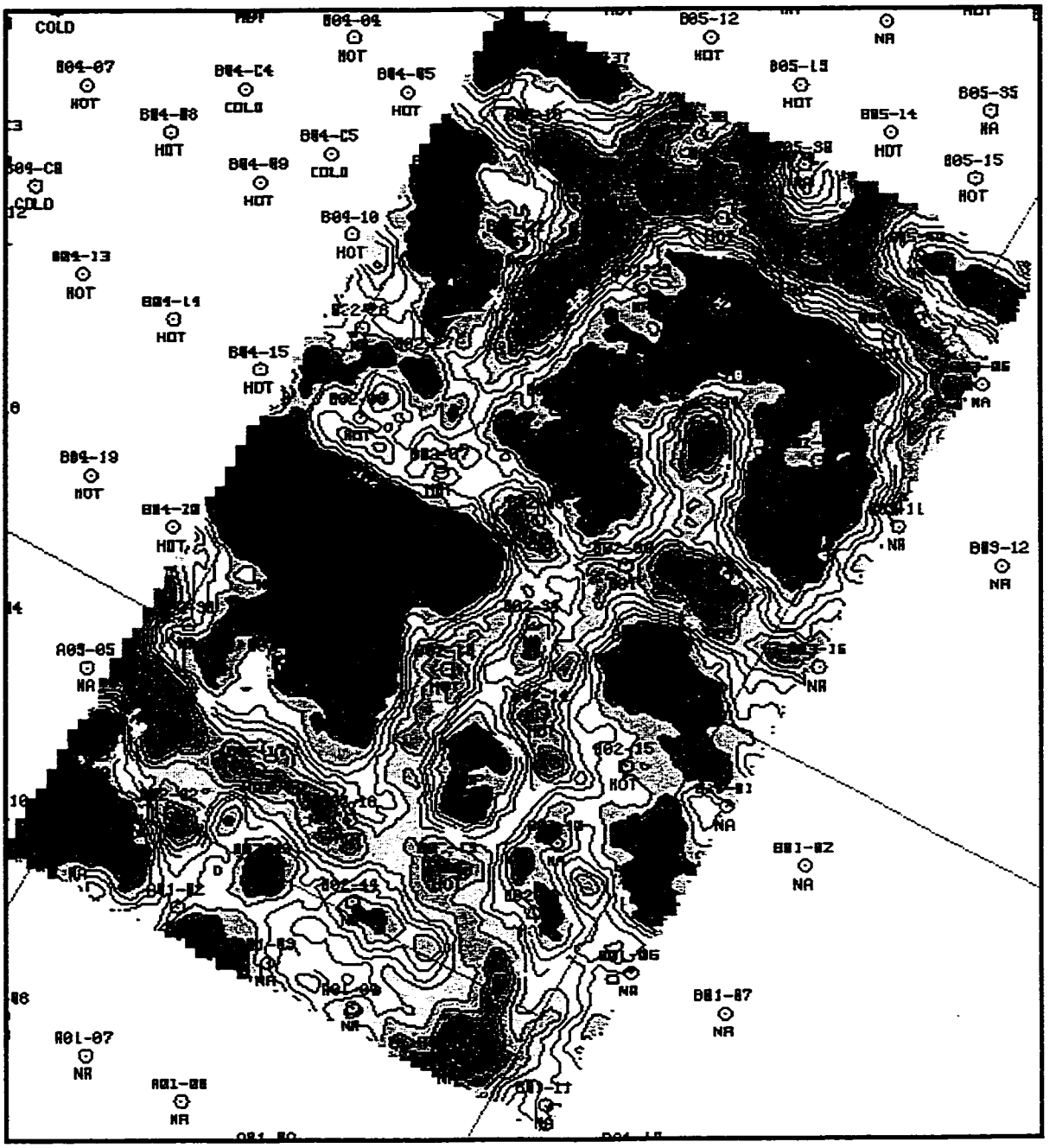

FIG. 5.26. Contour plot of the first principal component attribute of the 1995 survey extracted from joint seismic shape decomposition by merging surveys of the 1995 and 1997.

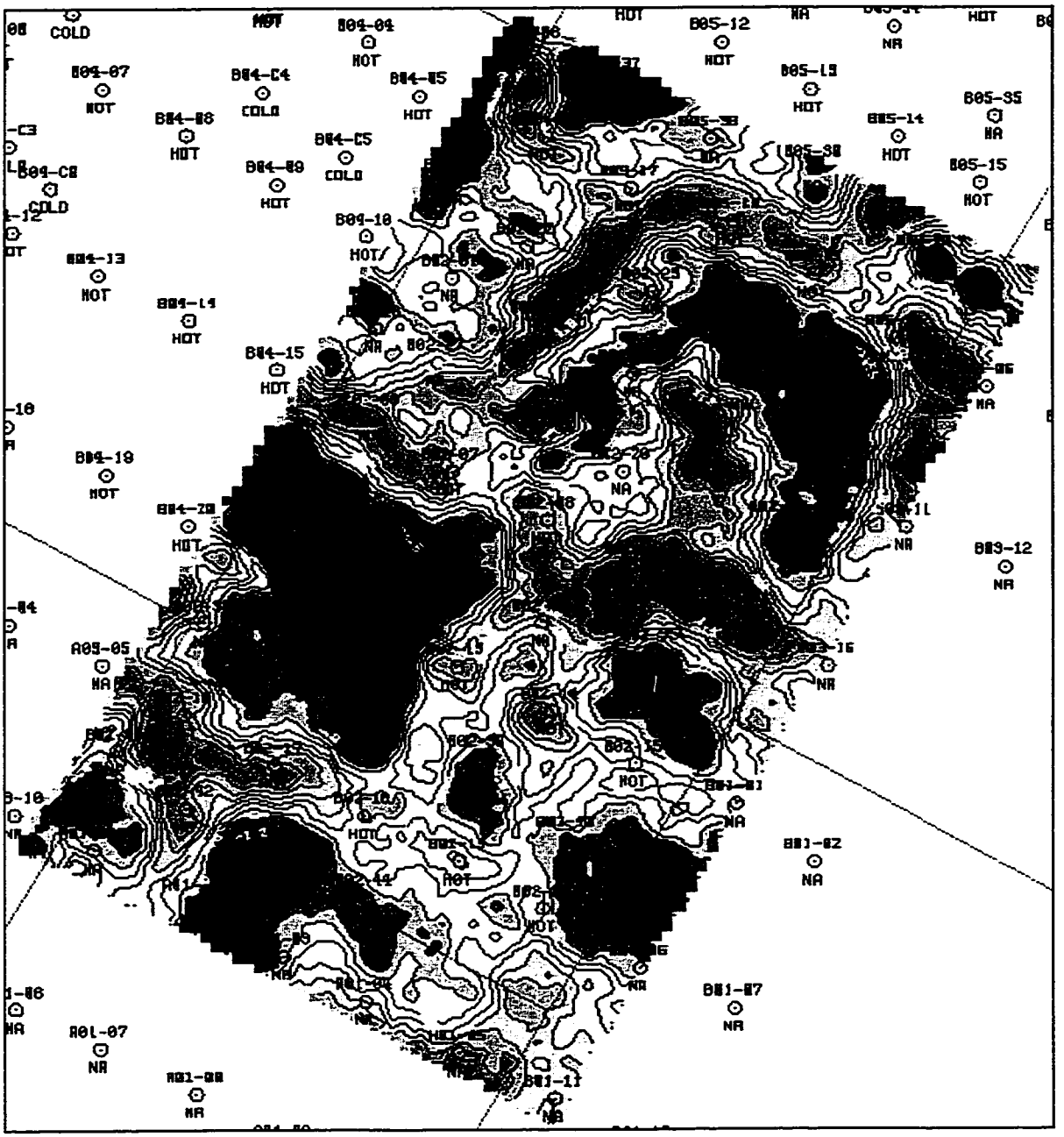

FIG. 5.27. Contour plot of the first principal component attribute of the 1997 survey extracted from joint seismic shape decomposition by merging surveys of the 1995 and 1997.

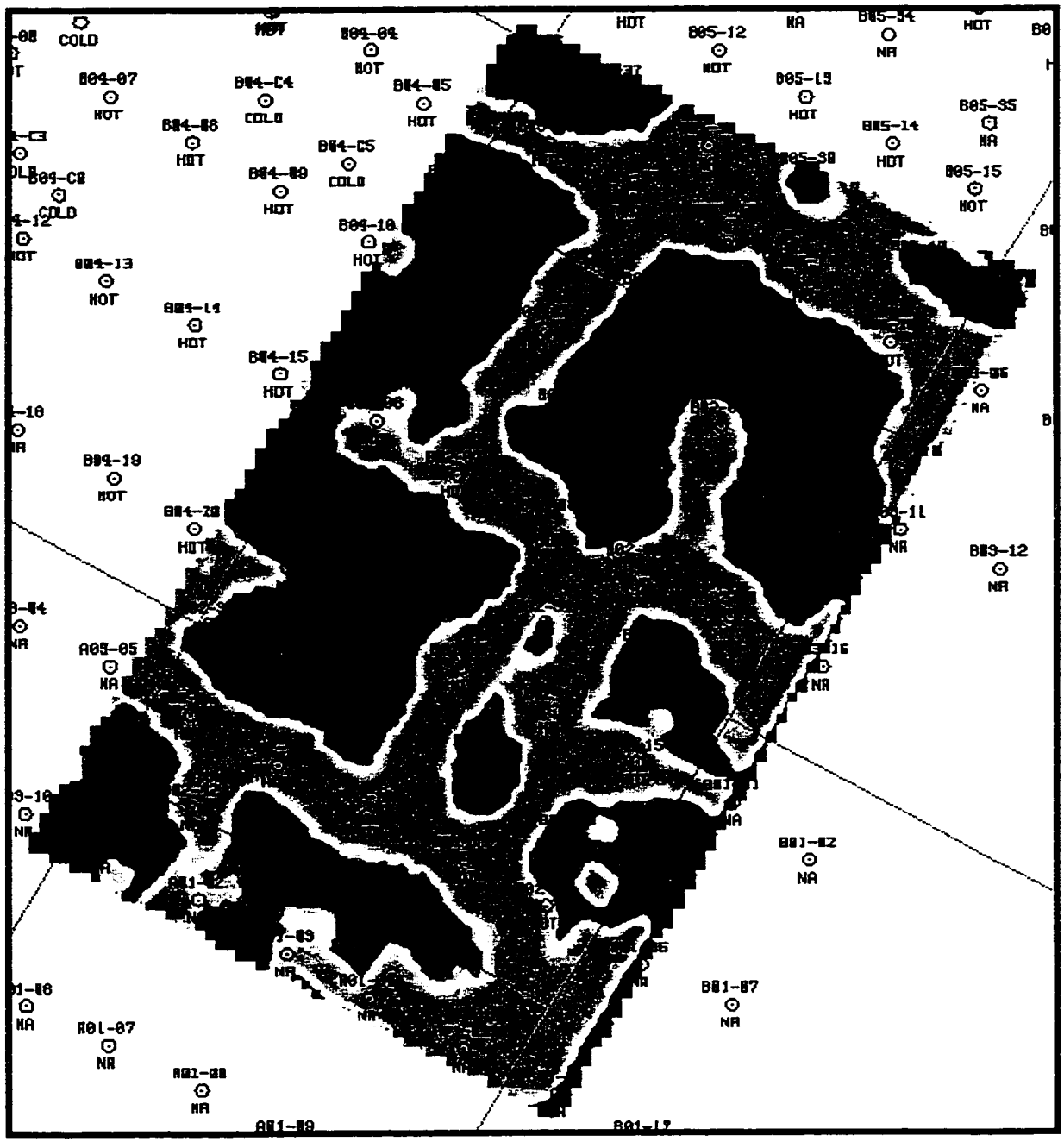

FIG. 5.28. B2 pad steam conformance of the 1995 survey through discriminant analysis of attributes extracted from independent seismic shape decomposition of the 1995 survey.

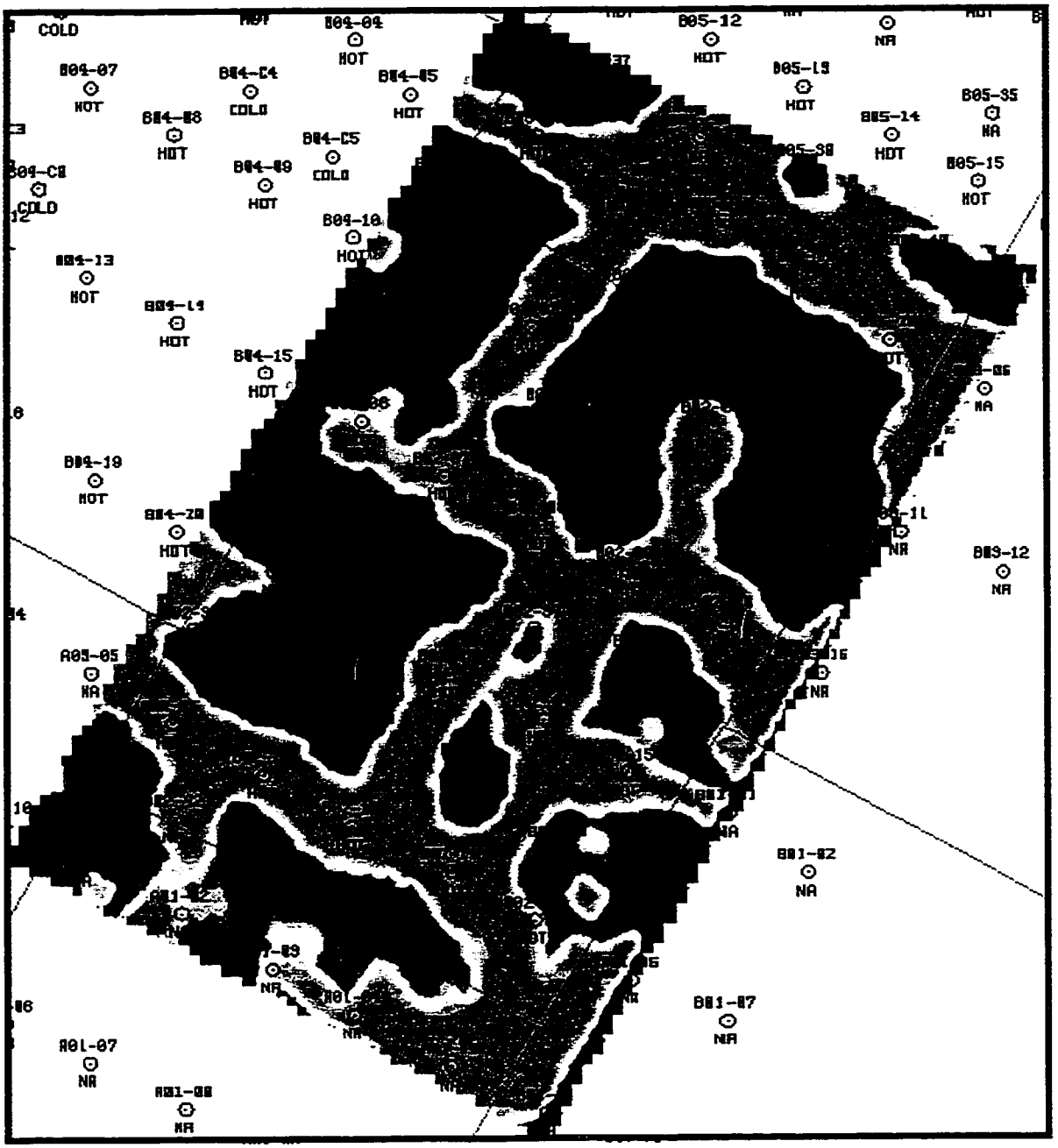

FIG. 5.29. B2 pad steam conformance of the 1995 survey through discriminant analysis of attributes extracted from joint seismic shape decomposition of the 1995 survey and 1997 survey.

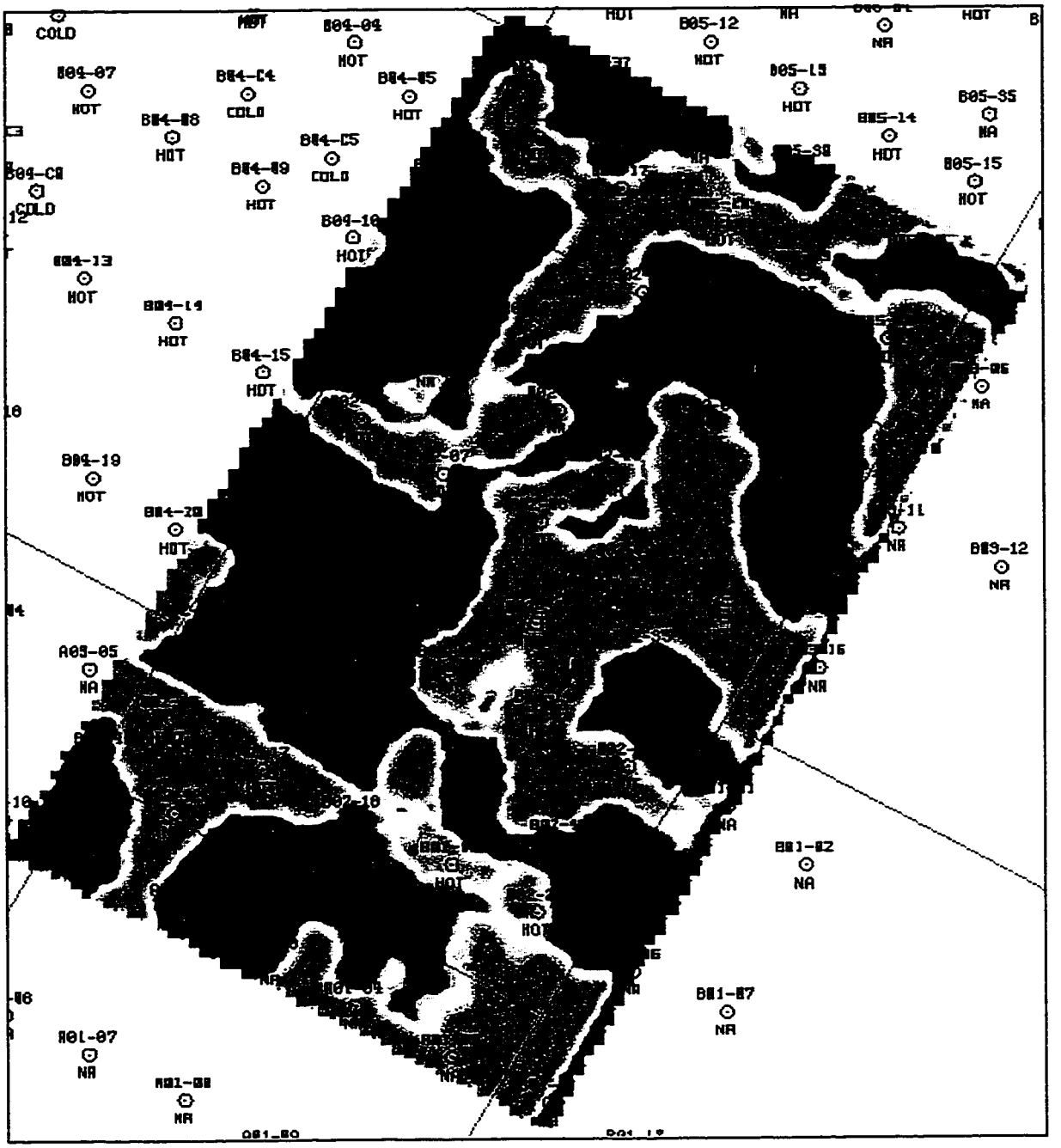

FIG. 5.30. The steam conformance of B2 pad of the 1997 survey from independent attributes extraction of principal component decomposition of 1995 and 1997 surveys (shapes are extracted separately on time-lapse data sets). Cross calibration was applied (the training set of 95 was applied to discriminant analysis of 97).

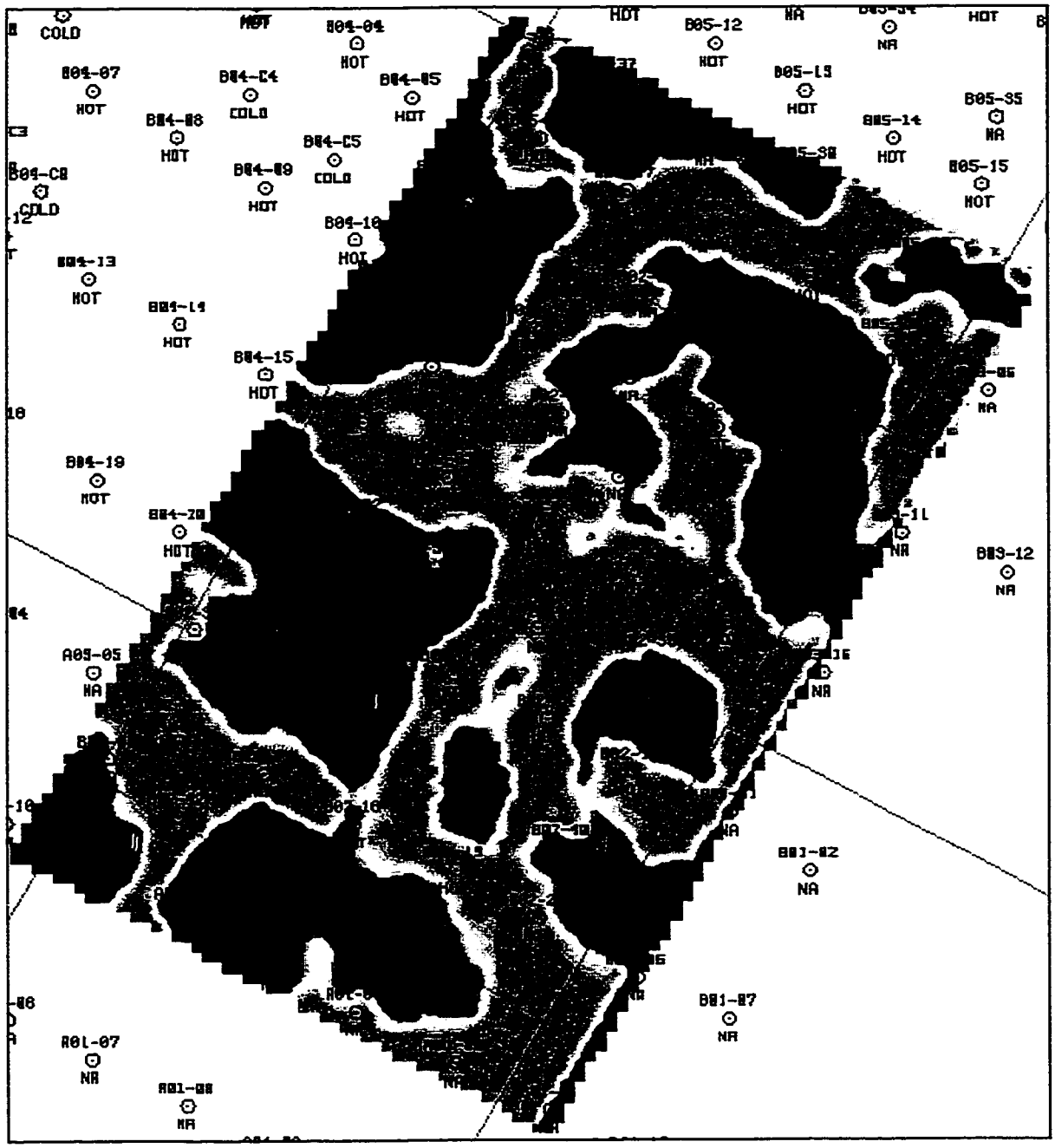

FIG. 5.31. The steam conformance of B2 pad of the 1997 survey from dependent attributes extraction of principal component decomposition of 1995 and 1997 surveys (shapes are extracted by merging time-lapse data sets). Cross calibration was applied (the training set of the 1995 was applied to discriminant analysis of 1997).

5.4 Conclusions and discussions

This study should be summarized as following points:

1. Principal component attribute analysis is well suited to multi-variant statistical analysis such as discriminant analysis with more than a single variable (attribute) as it simplifies the attribute selection process. No attribute modeling is required in this analysis. No concern of redundant information in discriminant analysis is necessary, as principal component attributes are orthogonal to one another; they are not correlated.

2. Better areal conformance mapping was obtained in both the A2/A4 and J1/J8 pads survey areas when the principal component attribute analysis was applied rather than the conventional attribute analysis in which the seismic facies are vertically consistent. Unlike conventional attributes principal component attributes are sensitive to the vertical position of the geological property. The reservoir property may vary vertically if a large area analysis is involved, thus the principal component attribute analysis may not be efficient and valid. To overcome this issue, the vertical sensitivity can be desensitized through phase rotation. To take advantage of this property, the vertical sensitivity may be able to help us work on the vertical conformance issue.

3. Statistically, the full set of non-zero principal component attributes gives the best well-to-seismic tie, in which 100% of the information (variance) is utilized. The low-variance end of the attributes (last few attributes in the hierarchy) can be noise dominant, however they may contain a signal of the reservoir property. Comparing this to the high-cut bandpass filtered seismic data, the data with full frequency content gives the best result. A future research direction is to find the upper limit of the frequency band that gives sufficient discrimination analysis.

4. In time-lapse analysis, where the cross-calibration between the surveys is required, independent seismic shape decomposition is invalid as the principal component attributes

are data set dependent and are not correspondent between the surveys. Principal component attributes extracted from shapes that are decomposed from the merged data set of the two surveys are able to help us avoid the data set dependent issue. Cross-calibration between the surveys becomes valid, and a new accurate steam conformance map is obtainable.

Chapter 6 – 3-D steam conformance and influence of sequence strata

6.1 Introduction

The previous two chapters have discussed seismic attributes (both conventional and principal component attributes) used to map areal steam conformance and developed a quantitative cross-calibration algorithm for analysis of time-lapse seismic surveys. A steam conformance map provides important input in terms of infill location and steam performance evaluation. Steam conformance in 3-D space would be the next potential advancement. In particular, mapping of steam conformance in the vertical dimension will provide insights into the rate at which steam moves vertically in the reservoir and the impact of lithologic influence on the heated zone or steam chamber. From a process perspective, this data will facilitate the determination of the relative impact of gravity drainage and fracturing on the growth of the heated zone. From a practical perspective the results will directly impact the selection, design and operation of follow-up processes.

To obtain steam conformance in 3-D space this chapter takes the approach of post-stack inversion. Using a numerical modeling method this chapter will start with discussions on factors such as AVO effects and wavelet extraction, which can affect inversion results. Time-lapse datasets (1995 *vs* 1997) from the B2456 survey area will be used for the inversion. One velocity model is built for inversion of both surveys with editing from the logs measured before steam injection.

The main focus of the chapter is the interpretation of inverted results. This includes tying sequence architecture or lithologic barriers to steam migration and studying the pattern of vertical conformance.

6.2 Description of the inversion process

Post-stack seismic inversion is the process of reconstructing the velocity or impedance structure of the earth via a reflectivity calculation from a stacked seismic trace. Figure 6.1 best describes the post-stack inversion process. To implement seismic inversion an initial velocity model and a wavelet are required to combine with the seismic data. The seismic inversion process begins with seismic data and well logs (sonic and density). A wavelet is extracted from seismic and well log data and used to generate a synthetic seismogram. Well logs are edited (stretch, squeeze, and redraw) through an iterative process of tying synthetic to seismic data, from which an initial velocity and impedance model is constructed.

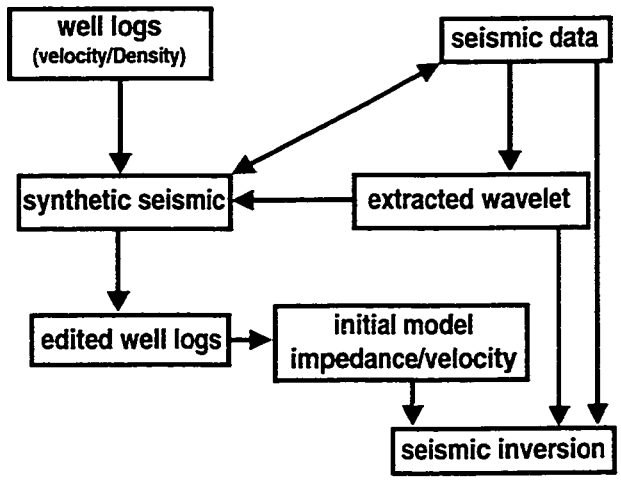

FIG. 6.1. Seismic inversion process.

6.3 Factors affecting inversion results

Seismic inversion is based on four assumptions: (1) the phase of the seismic data is correct, (2) the wavelet is constant, (3) the multiples are negligible, and (4) the *P*-wave is vertically incident on a reflection boundary.

The tie of VSP to surface data (see Chapter 2) suggests that the multiples are negligible and wavelet is relative constant on the Cold Lake data. The phase can be tuned according to VSP and synthetic. However, the *P*-wave is not vertically incident on a reflection boundary as traces of full offset are usually employed to obtain stacking power. The tradeoff is that an AVO (Amplitude Versus Offset) effect is introduced to the stacked seismic traces. Is the AVO effect serious enough to harm the inversion result? To answer this question an inversion was conducted on a series of limited offset stack traces which were generated form a AVO modeling of well B05-28. Figure 6.2 shows an AVO gather

from well B05-28 modeling with an offset from 0 meter to 800 meters using a Ricker 100 Hz wavelet. There are strong AVO effects shown at the top of the Grand Rapids, and at the middle of the Grand rapids. Some moderate AVO effects are evident at the top of the Clearwater formation, at the steam chamber inside the Clearwater reservoir formation, and in the lower Grand Rapids. Figure 6.3 shows the limited offset stacks of 0, 200, 500, 800 meters. The stack traces do look different due to the AVO effect, especially in the shallow section such as at the Grand Rapids top. A feasible change at the depth of the steam chamber can be observed. In this case the wavelet extraction is deterministic (Ricker wavelet 100 Hz). Limited offset stack traces are inverted using a model based generalized linear inversion algorithm (STRATA package by Hampson-Russell software Ltd.) to see the contribution of the AVO to the final inversion result. Figure 6.4 shows the inverted impedance for different limited offset stacks and comparison to the impedance

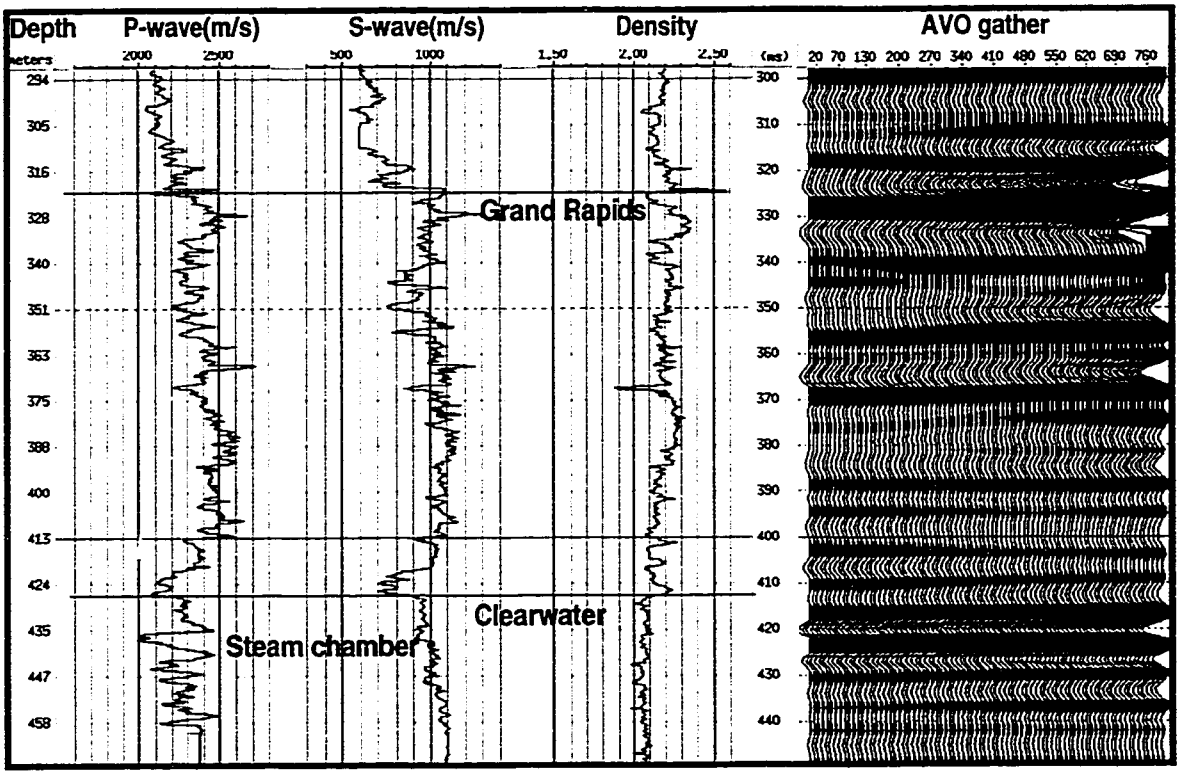

FIG. 6.2 Well logs of well B05-28 and a modeled AVO gather from offset of 0 meter to 800 meters.

log.

In general, the inverted results of all offsets agree well with the impedance log (Figure 6.4). Significant change or error of impedance appears at the top of Grand Rapids in time around 330 ms where a strong AVO effect exists. A zero-offset stack provides the inverted impedance closest to the impedance log. In the portion where steam chambers present (around 420-430ms in time) the results are very similar (Figure 6.4). In the other word, the AVO effect (moderate) of steam chambers at the reservoir level does not significantly affect the final inversion result.

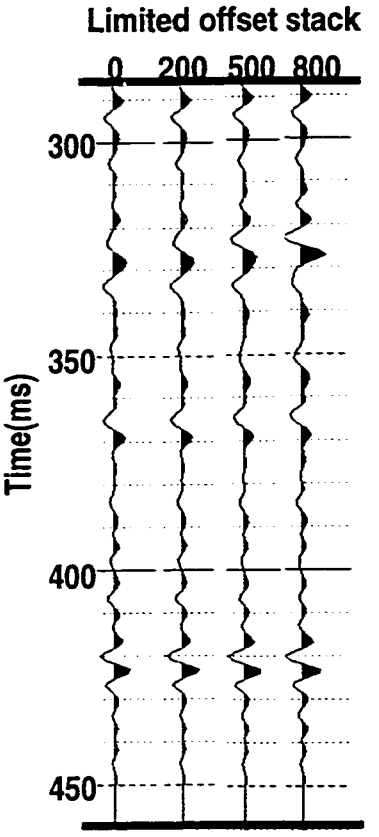

FIG. 6.3 Limited offset stack of modeling data from Figure 6.2

The above discussions have not yet involved the wavelet problem as the wavelet extraction was deterministic. In practice, the wavelet extraction in most cases is accomplished by combining seismic data with well logs or using seismic data alone (statistical wavelet extraction). To observe the wavelet effect on the inversion result, wavelets were extracted from different limited offset stack traces and applied to the inversion. Figure 6.5 shows the Ricker wavelet and its amplitude spectrum (top) and wavelets extracted from limited offset stack traces for a full time window (0-470ms). Extracted wavelets in time look very similar to the Ricker wavelet except for some high frequency side lobes on both sides. Amplitude spectra of all extracted wavelets in trend look similar to the amplitude spectra of the Ricker wavelet (they are not exactly the same due to side lobes and discrentization). Most importantly extracted wavelets of different offset stack traces look more or less the same though there are some minor changes in the amplitude spectra. Therefore, it is fair to draw the conclusion that wavelet extraction is insensitive to the AVO effect if the extraction window is large enough. If the

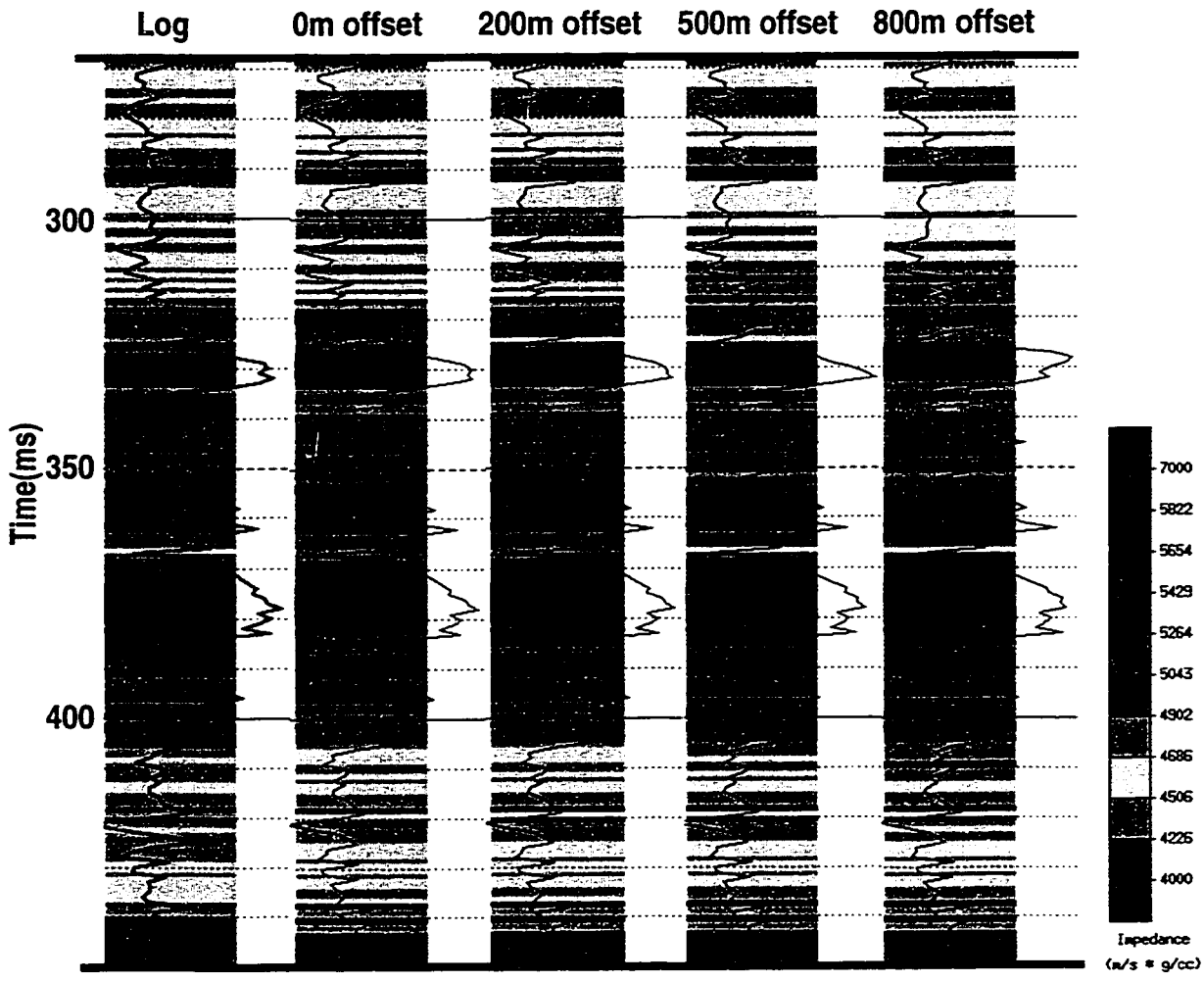

FIG. 6.4 Inverted impedance from different limited offset stack (Figure 6.3) and comparison to impedance log using the same Ricker wavelet (100 Hz).

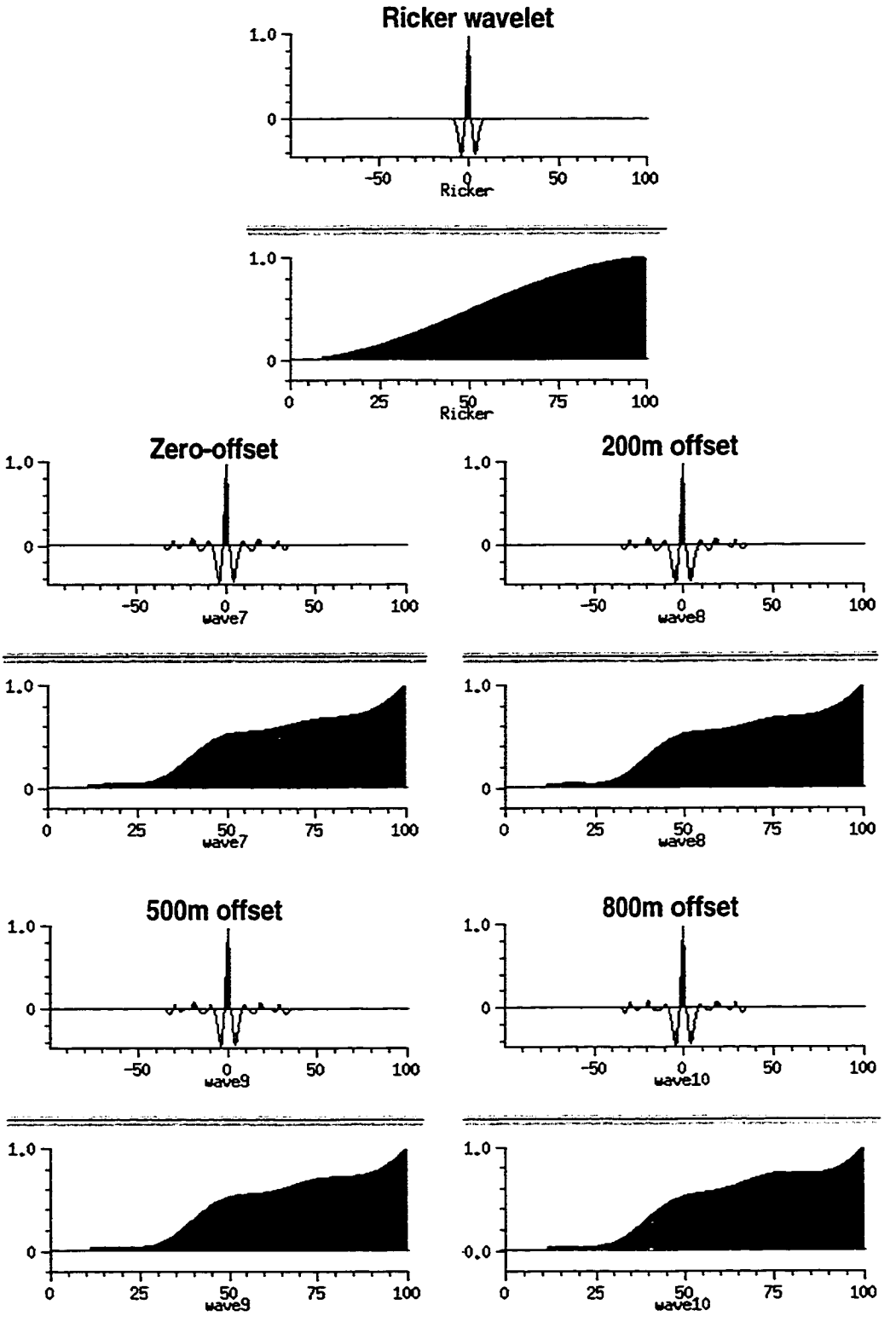

FIG. 6.5. The Ricker wavelet and wavelets extracted from different limited offset stack traces (see Figure 6.3) from the full time window (0-470ms).

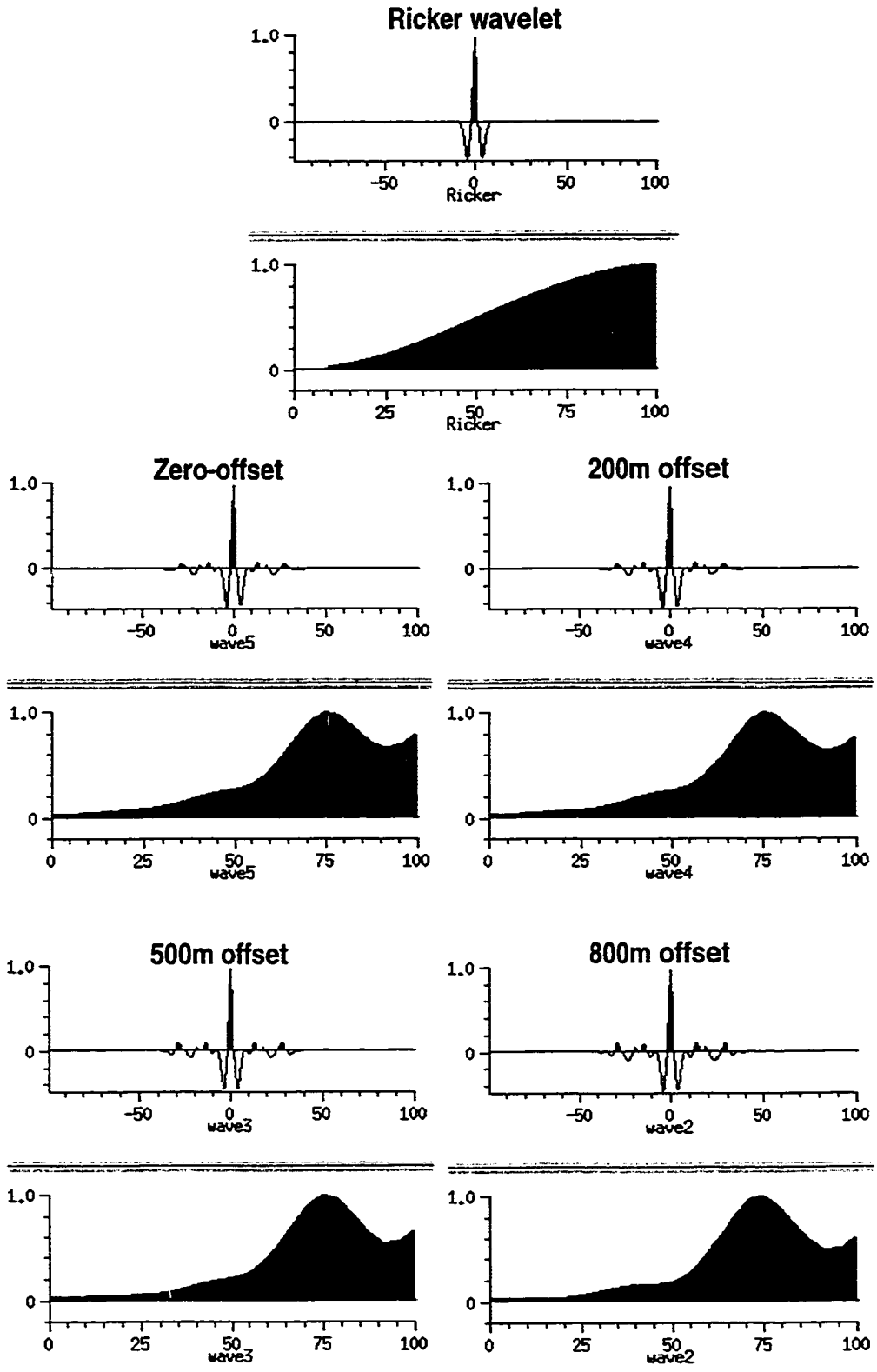

FIG. 6.6. Wavelets extracted from different limited offset stack traces (see Figure 6.3) of time window of 250 to 470 ms and comparison to the Ricker wavelet.

extraction window is reduced the lower portion of the trace wavelets become unstable. Figure 6.6 displays a similar layout of wavelets as in Figure 6.5 for a smaller extraction window (250-470ms in time). Wavelet from the zero-offset stack trace looks the best among the four. As the offset increases the extracted wavelet deteriorates: the side lobes get stronger with progressing time, and the similarity of the amplitude spectra to the amplitude spectrum of the Ricker wavelet is eroded. The amplitude of the low frequency portion also drops. Figure 6.7 shows a comparison of the impedance log and the inverted impedance logs from the zero-offset stack trace with different wavelets (Ricker wavelet, wavelet extracted from lower portion of the trace, and wavelet extracted from the whole data trace). In general, the results look similar. However, the better wavelet (extracted from time window of 0-470ms) provides the result that is closer to the impedance log, e.g. the magnitude of the impedance in the lower Grand Rapids (about 370-400 ms in time) is closer to the impedance log.

6.4 Velocity model using logs from time-lapse production drilling

The B2456 time-lapse seismic surveys were chosen for inversion (see Chapter 4 for a detailed description of the surveys). Figure 6.8 shows the wells with sonic and density logs available in the survey area overlain with the estimated steam areal conformance in 1995 (discussed in Chapter 4). A total of 11 wells were used to build the initial impedance model. Wells such as B02-08, B04-08, B05-08, and B06-08 were originally drilled when the reservoir was virgin (before any steam injection). The remaining locations are infill wells, which were drilled in 1996. As reservoir monitoring is a dynamic adjustments (or edit) have to be made to the sonic logs obtained before the 1995 seismic survey so it can be used for the inversion of the 1995 seismic survey. It is unnecessary to edit the density logs as the formation density remains almost unchanged before and after steam injection. Figure 6.9 shows the well-to-seismic tie to well B5-08, which was located in a hot steam zone when the 1995 seismic survey was acquired. Wavelet used in the synthetic was extracted from the 1995 seismic data. Overall, it is a good tie. The velocity in the steam zone has to be reduced to 1800 or 1900 m/s to tie to the seismic anomaly at the reservoir interval, which is the velocity for oil sand when

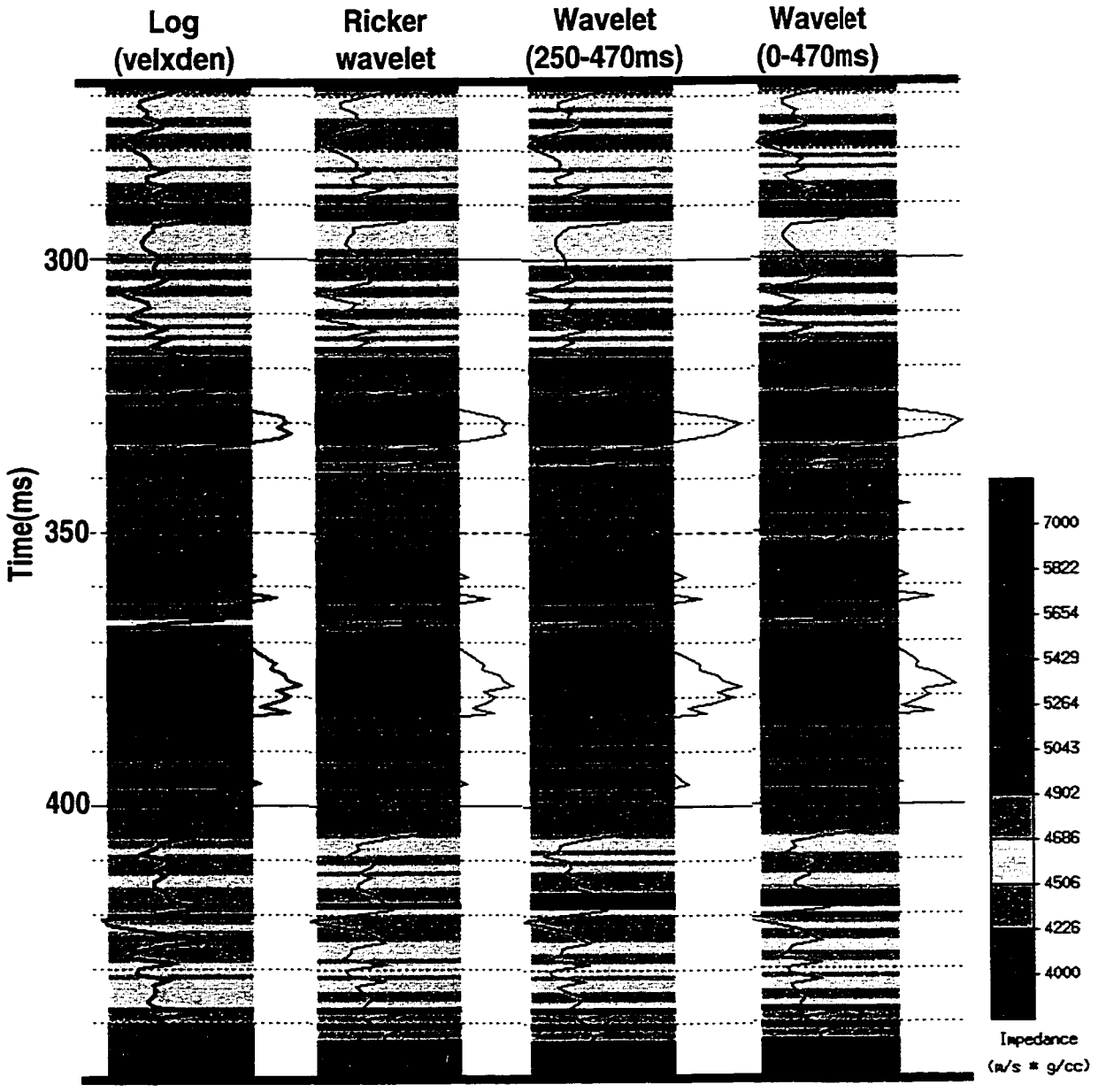

FIG. 6.7. Impedance log and inverted impedance from zero-offset stack trace using different wavelets (wavelet extracted from 250-470ms time window, wavelet extracted from 0-470 time window, and Ricker wavelet).

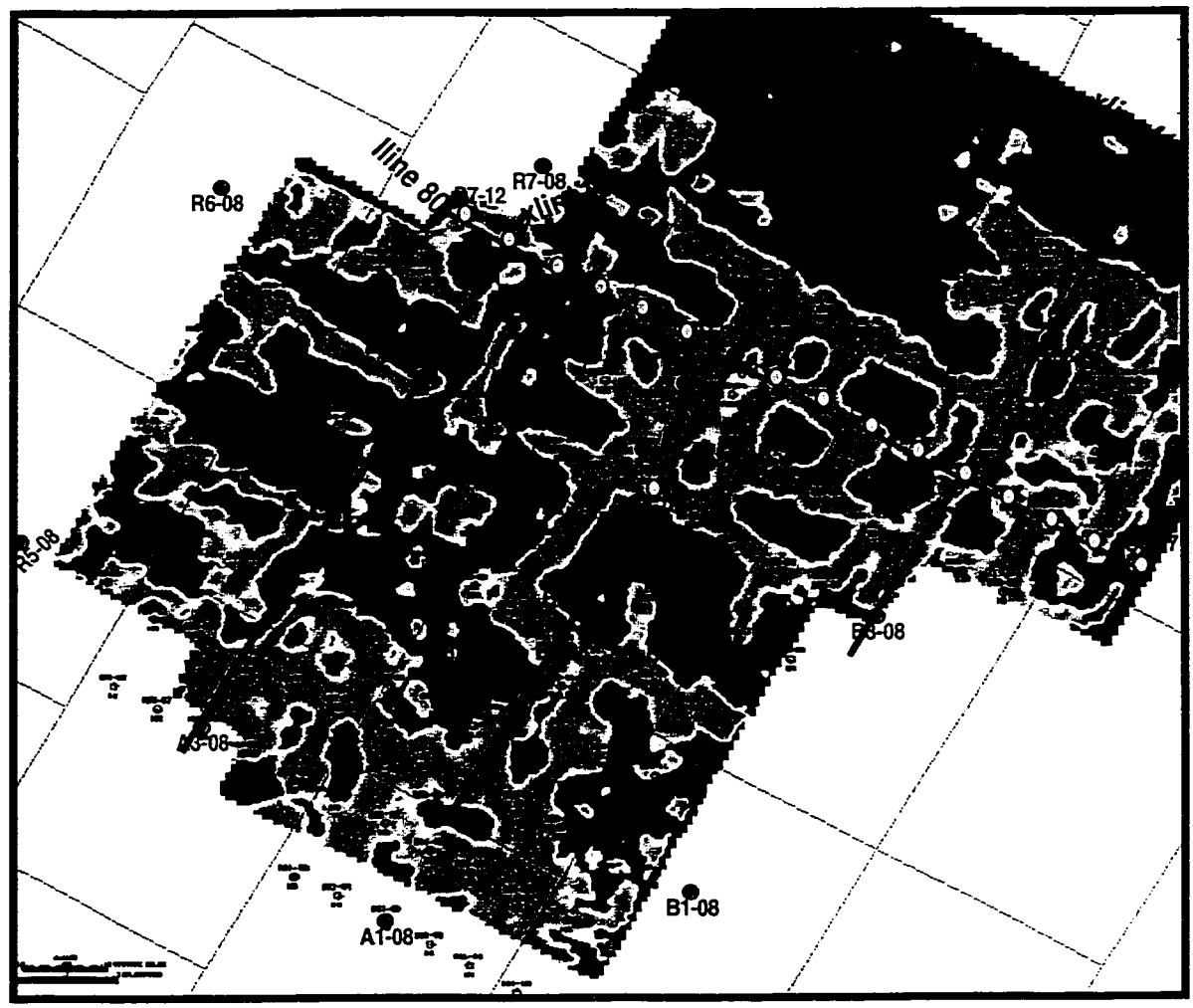

FIG. 6.8. Wells with sonic and density logs available (red dots) at B2456 time-lapse seismic survey area overlain with areal steam conformance of 1995.

heated by steam. To exactly tie the synthetic to the seismic characters in the reservoir interval, the velocity drop in steam zone requires two steps (see Figure 6.9). The velocity in the upper steam zone is lower than that in lower steam zone. Similar situations were encountered at wells B2-08 and B4-08. Most infill wells were drilled into cold reservoir locations based on estimated areal conformance as shown in Figure 6.8. Fewer wells were drilled into the hot steam zone for the purpose of collecting data. Shown in Figure 6.10 are the well-to-seismic ties for two hot infill wells (B5-38 and B5-33). Well B5-38 shows a significant velocity drop due to presence of steam. The velocity above and below the

steam zone is about 2300 to 2400 m/s while in the steam zone the velocity is reduced as low as 1500 m/s. The well log shows a much stronger response to steam than seismic data. The weaker response to the rock formation from the log above and below the steam zone may indicate an unbalanced amplitude due to the strong impedance contrast in the steam zone. In contrast, the seismic anomaly is much stronger in well B5-33 (Figure 6.10b). According to the well logs the velocities in the steam zone are mostly above 2200 m/s. There are very few points that fall below 2000 m/s. Interbeds probably have been broken through by steam injection. Hence evidence of steam appears in the seismic data but is not well reflected on the well log due to the limitation of the well log detection range.

Well B5-28 is a cold location and is close to the edge of steam channel as defined by areal conformance (Figure 6.8), but in fact steam traces can be seen on the well log with a velocity of 2000 m/s (Figure 6.11a). The boundary defining the areal conformance as hot and cold reservoir may not be the exact physical boundary; rather, it is a statistically weighted average (posterior probability, see Appendix A) boundary between hot and cold reservoir. Similarly, a trace of steam can be seen in the lower Clearwater formation in well B2-32 (see Figure 6.8 and Figure 6.11b). It is hoped that the post-stack inversion will provide a more detailed description for steam distribution in 3-D space.

Wells such as B2-28, B2-30, and B5-35 are in cold reservoir (see Figure 6.8) and respond mostly as cold. Also, the well logs show absolutely 'quiet' (Figure 6.12).

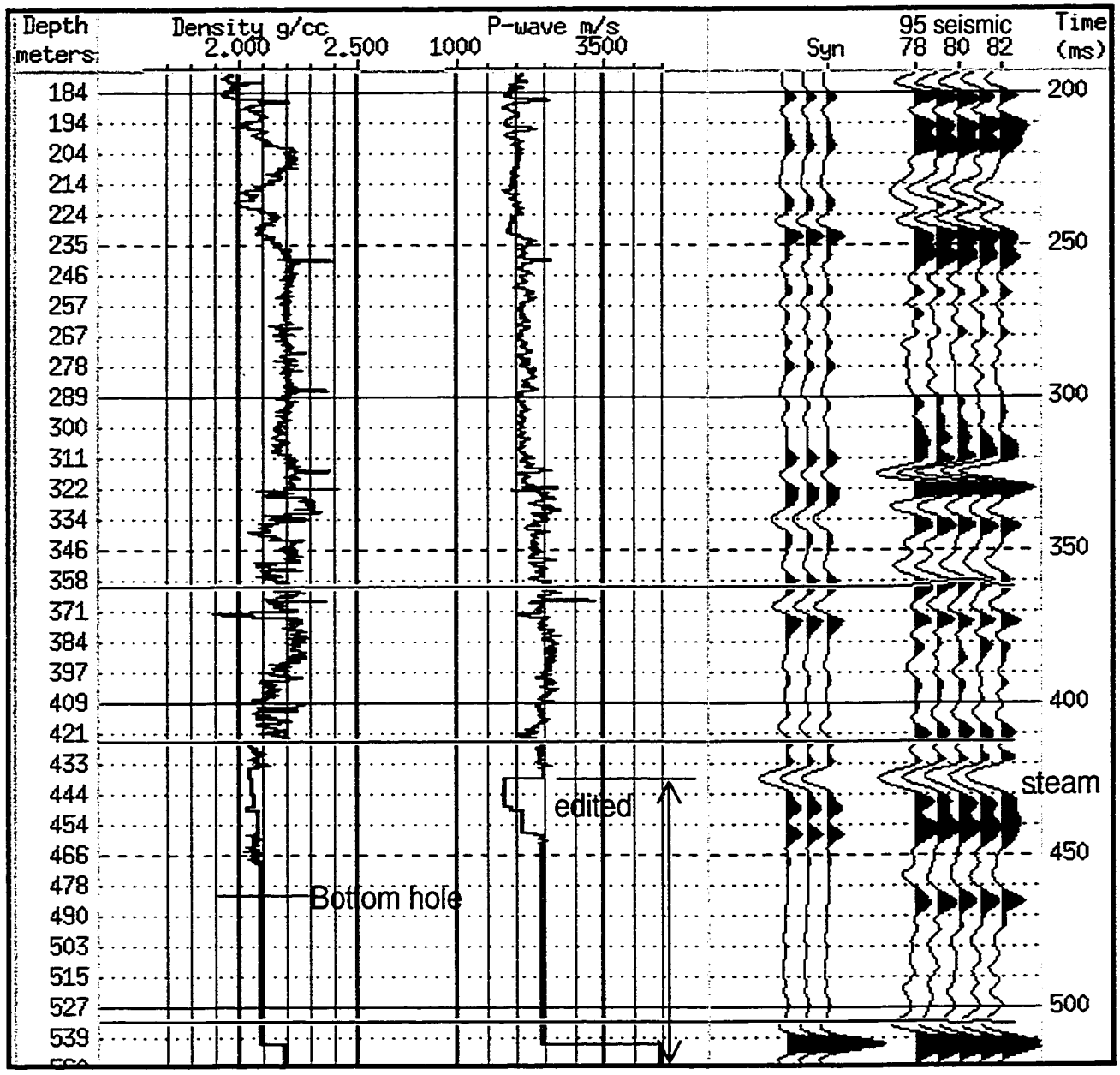

FIG. 6.9. B05-08 well logs tying to the seismic of 1995, sonic log edited at reservoir interval.

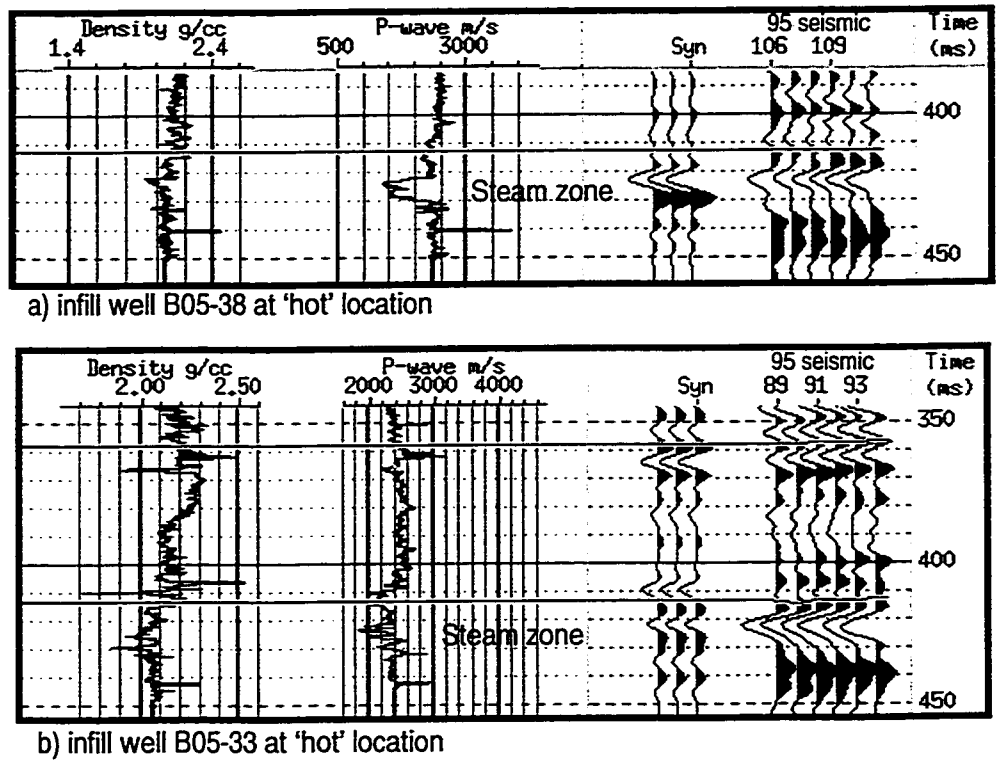

FIG. 6.10. Well-to-seismic tie at hot infill locations of the 1995 survey.

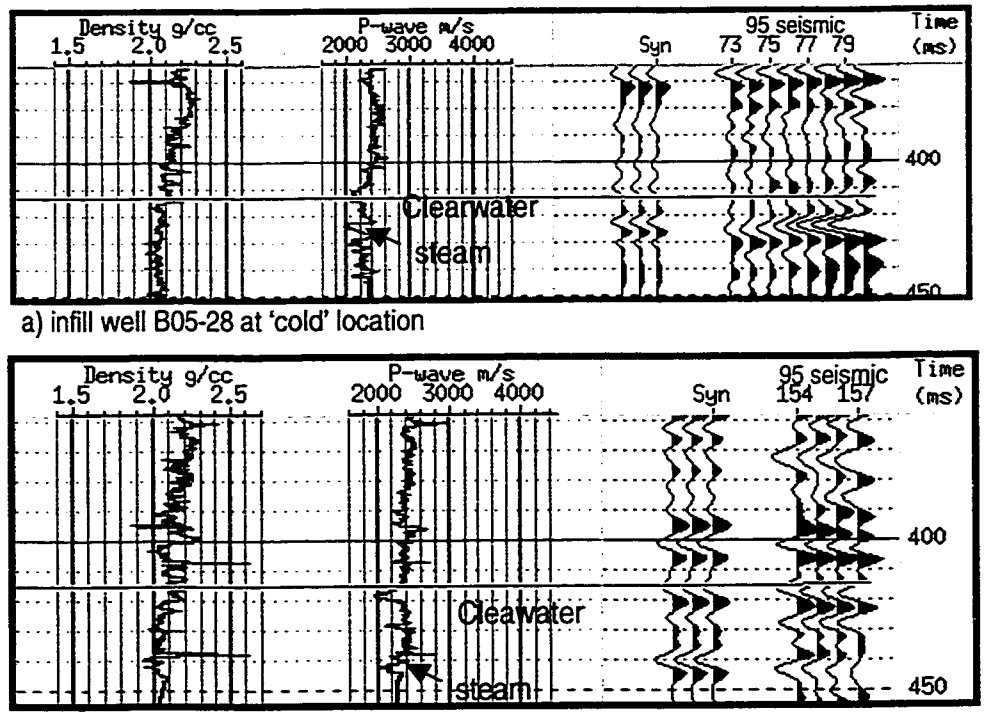

FIG. 6.11. Well-to-seismic tie at cold infill locations of the 1995 survey showing trace of steam.

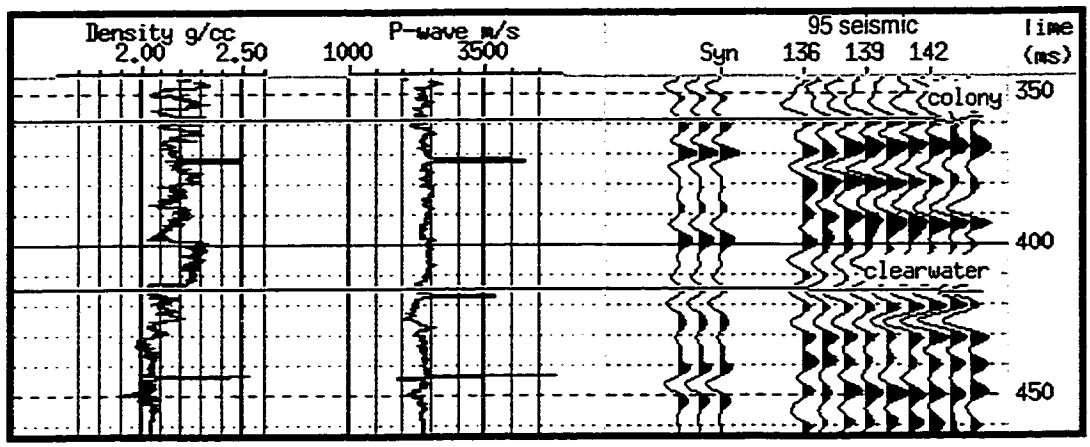

a) infill well B02-28 at 'cold' location

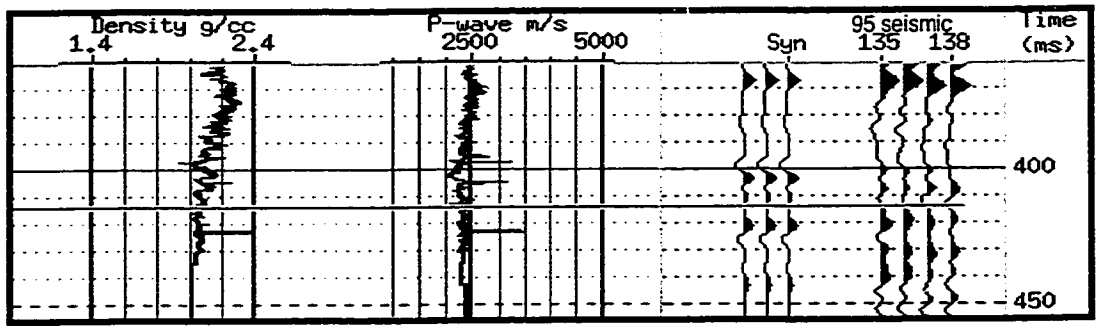

b) infill well B02-30 at 'cold' location

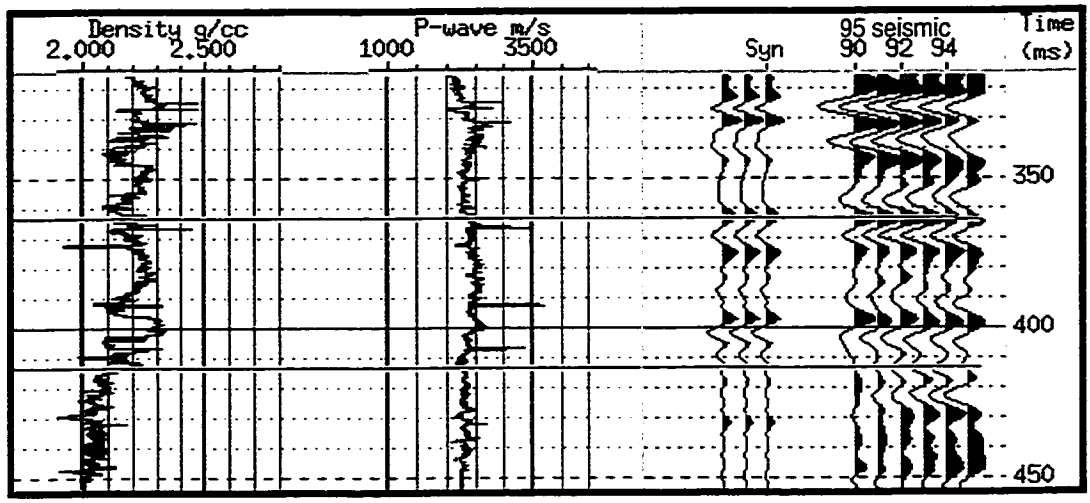

c) infill well B05-35 at 'cold' location

FIG. 6.12. Well-to-seismic tie at cold infill locations of the 1995 survey.

6.5 Results and interpretation

The time-lapse seismic inversion was carried out using STRATA inversion software, which uses a generalized linear inversion algorithm. Wavelets were extracted independently from two datasets and applied to the inversion of the correspondent dataset. However, the initial impedance model built for the 1995 seismic data, which includes the 1996 infill wells and pre-steam production wells with editing of the sonic logs, was used for inversions of both 1995 and 1997 seismic data. Even though this initial model may not be quite applicable for the 1997 seismic data as steam has been injected into the reservoir in cold infill locations, the intention was to let the inversion algorithm resolve the differences between 1995 and 1997. The inversions were implemented through 12 iterations with block size of 1 ms which is the same sample rate as was used for the seismic data. With such a block size the vertical resolution of the inversion reaches the uppermost resolution that such seismic data can provide.

The direct output from inversion is seismic impedance, which is the product of velocity and density. In order to tie the inversion output to the physical meaning of hot versus cold reservoir, seismic impedance is converted to velocity using the Gardner relation as the reservoir status of hot versus cold corresponds to a velocity change of approximately 1800 m/s versus 2400 m/s.

Figure 6.13 shows the vertical conformance of the 1995 survey along cross-line 90 (N-S, see Figure 6.8) crossing wells B5-08 to B2-18. This section is a profile along a steam channel. First of all, it agrees with the areal conformance presented in Figure 6.8 in terms of the lateral extension of the steam chamber. It can be observed that steam is mostly accumulated in the top 20 to 30 m portion of the reservoir. The cold region defined on that areal conformance map (Figure 6.8) via discriminant analysis may have horizontal fractures and provide a communication path between steam chambers. This cold region certainly is not as hot as the steam chambers; but it may not be totally cold and exists as a barrier between the hot steam channels. This evidence from seismic and its inversion confirms the steam injection phase of the CSS reservoir engineering process (see Chapter

1 for discussions), that is, during the steam injection phase the fluid injected creates horizontal fractures and dilates the formation.

Figure 6.14 displays a time-lapse vertical conformance crossing the steam channels (E-W) from both the 1995 and 1997 surveys along inline 80 which is a cross-section off well section R7-12 to C5-17 south 20 m. Comparing the upper panel (1995 survey) with Figure 6.8 and the lower panel (1997 survey) with Figure 4.28, the projection of the lateral steam distribution from the vertical conformance agrees well with the areal steam distribution mapped via discriminant analysis except that details such as the shape of the steam chamber and inter-well connections are missing on the areal conformance map. The vertical conformance shows that steam chambers have a 'V' shape (called gravity drainage driven) to the totally inter-well connected steam block (called later fracture driven). Since the 1995 seismic survey and drilling of infill wells drilled more steam has been injected into B2 pad and B4 pad (R7 pad affected) to balance the steam distribution for the whole area. Less steam was injected into B5 and B6 pad with the exception of IOI wells in B5 pad. This is reflected in the vertical conformance. More steam is evident on the west part of the section (wells R7-12 to R7-15) from the 1997 survey (see Figure 6.14 lower panel). Inter-well connections are evident between well R7-14 and R7-15 since the 1995 survey and 1997 survey.

The highest temperature is usually near the perforation location at the bottom of the steam chambers. This is shown in Figure 6.15 which ties the well temperature profile of B5-33, seismic, well logs and the vertical conformance from the 1995 survey all together. IOI well B5-34 was drilled at a warm location (white in color) as defined by areal conformance via discriminant analysis. In fact, steam was present in the bottom of the reservoir. The steam chamber as a whole is not as thick as in well B5-33. Even though the well log of well B5-33 does tie to seismic (discussed earlier in this chapter) inversion resolved the steam conformance properly from the seismic data.

Shown in Figure 6.16 is a slice of 3-D inverted velocity volume that is converted from impedance using the Garner relation. The slice is extracted with a time window of 5 ms centered at 430 ms (the middle of the reservoir). A velocity of 2050 m/s is the cutoff

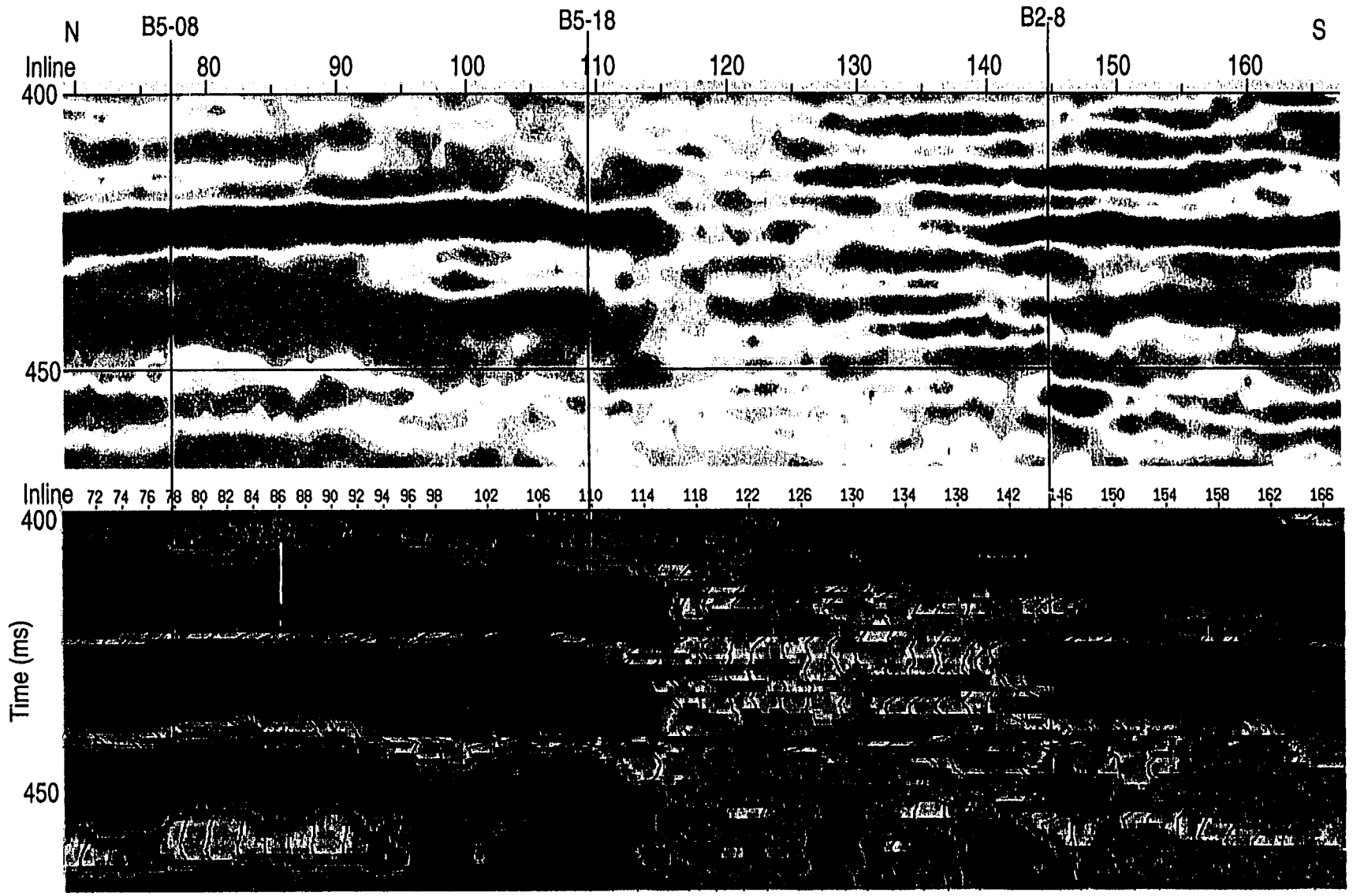

FIG. 6.13. The 1995 survey vertical conformance along wells B5-08 to B2-18 (cross-line 90), seismic data in upper panel, green represent hot and blue represent cold in lower panel.

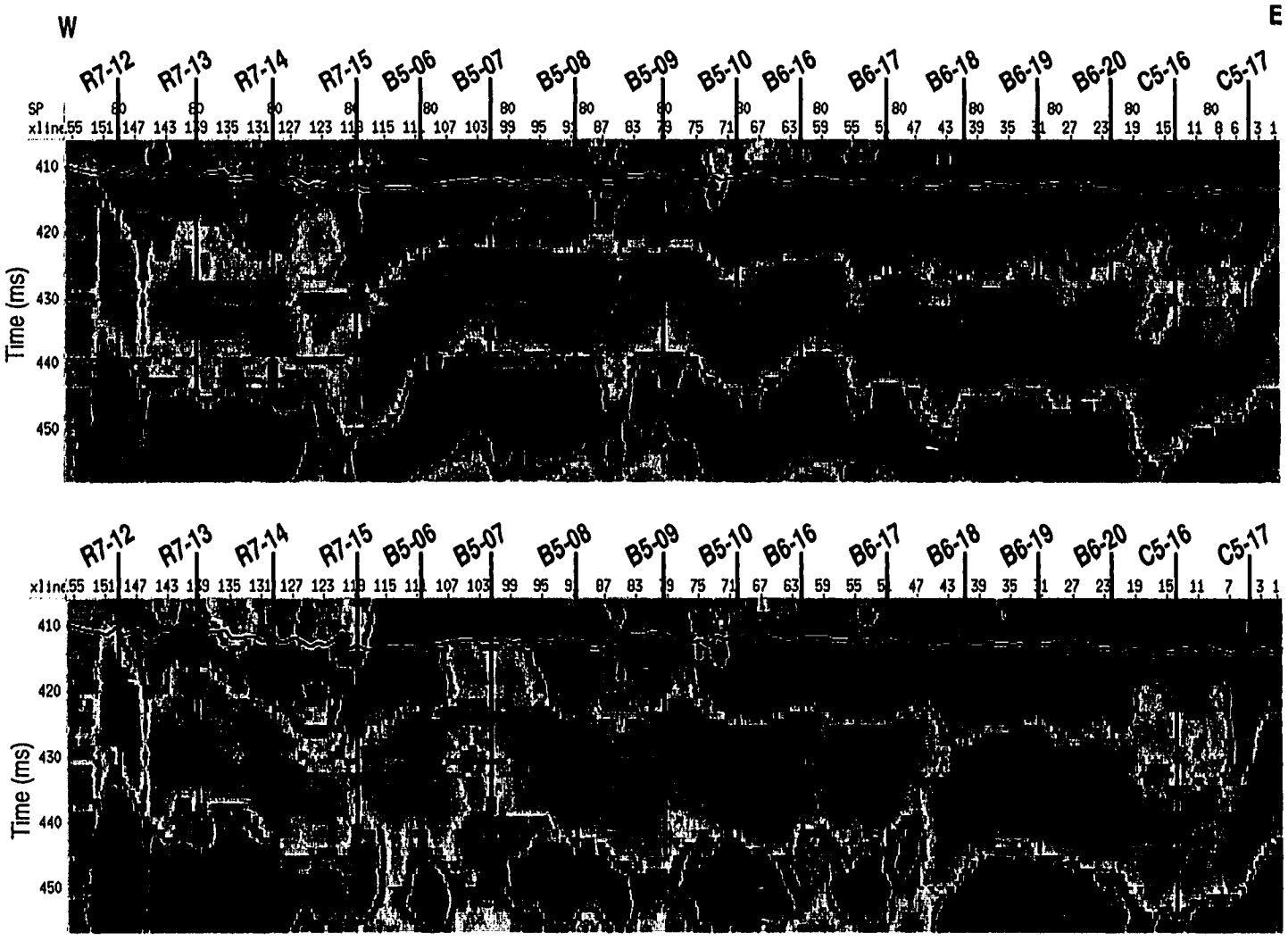

FIG. 6.14. Vertical steam conformance along wells R7-12 to C5-17 (inline 80) for time-lapse seismic surveys (1995-upper panel, 1997-lower panel).

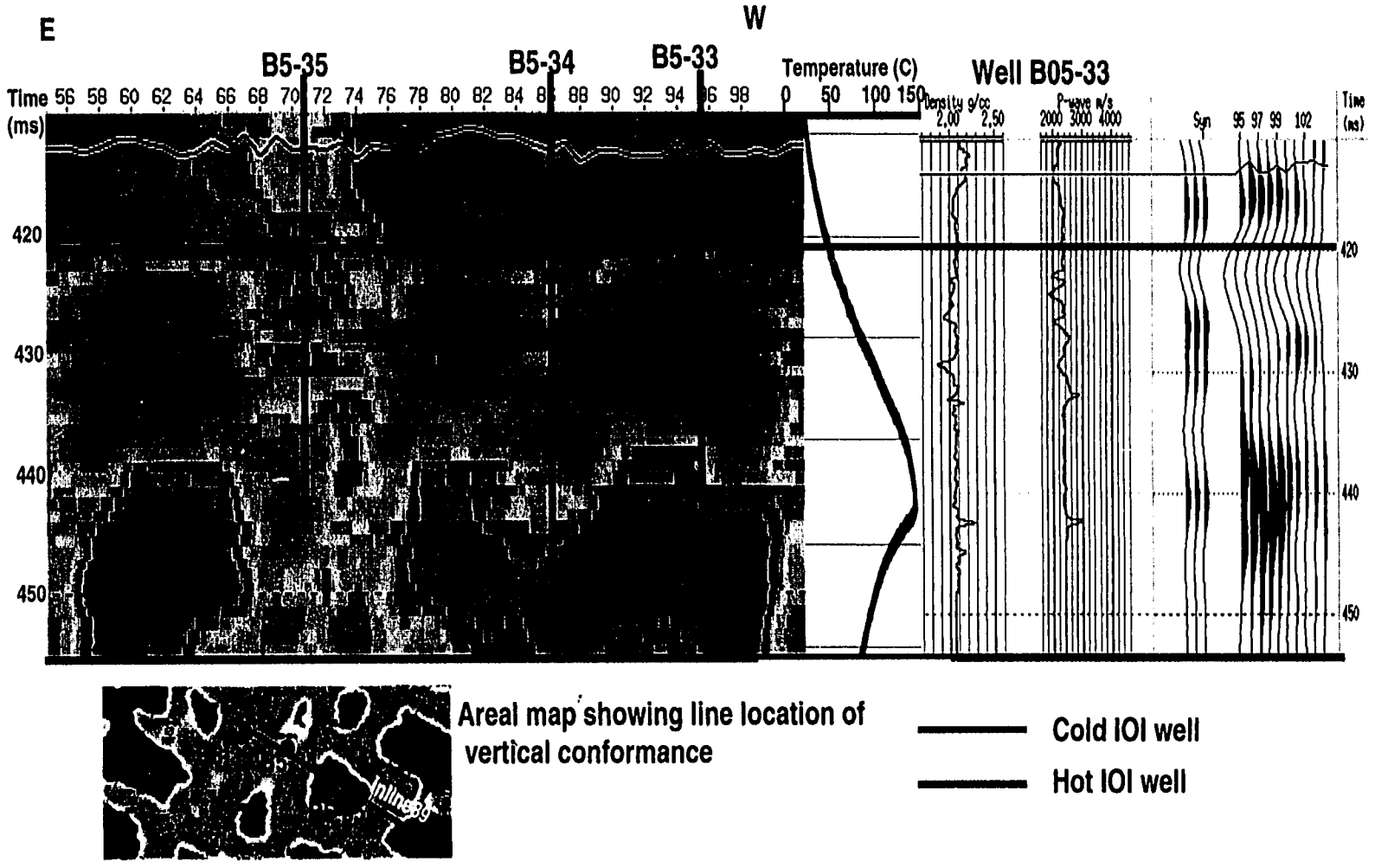

FIG. 6.15. Tie of vertical steam conformance along IOI wells B5-33 to B5-35 (inline 89) and well temperature profile for 1995 survey.

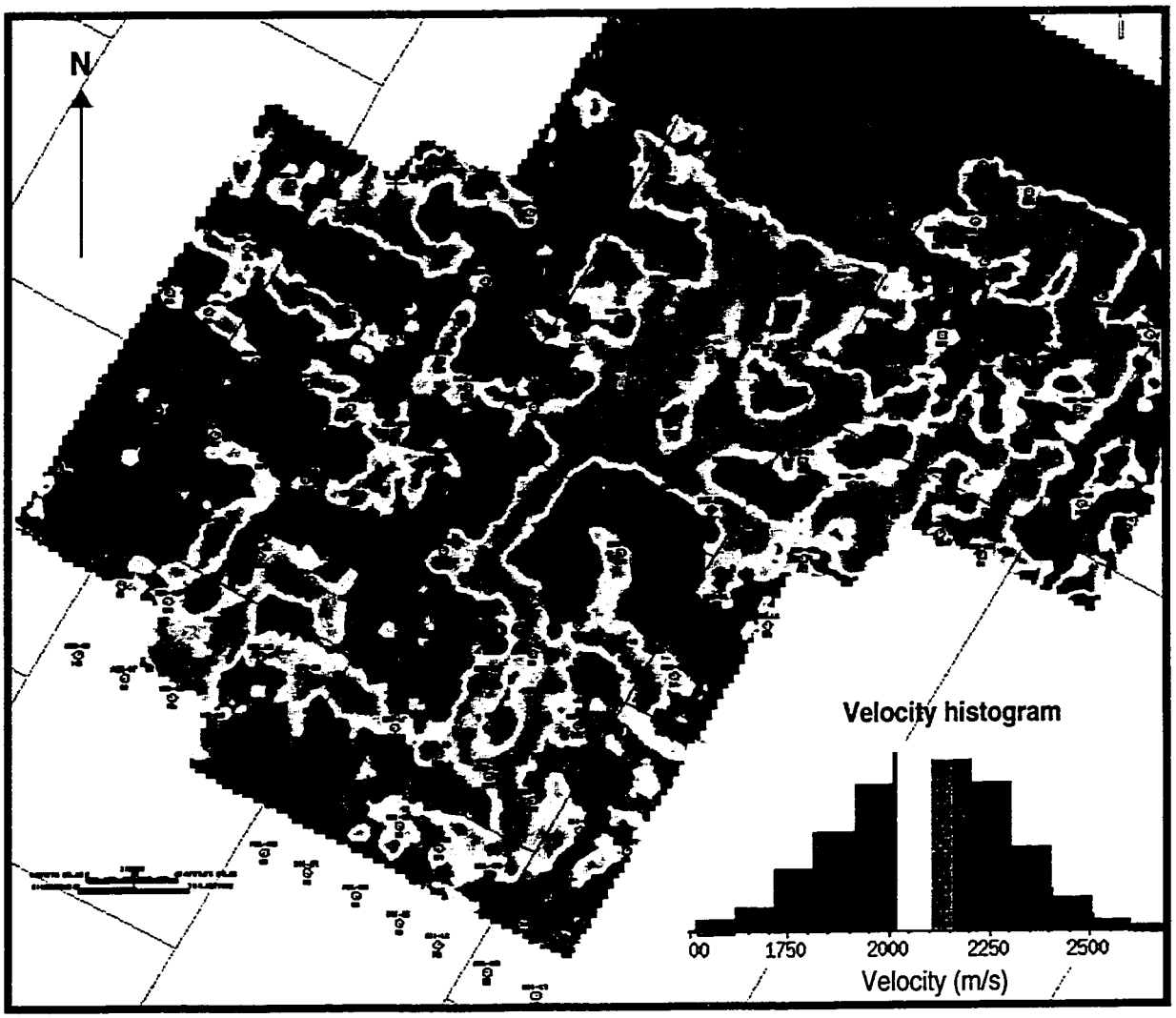

FIG. 6.16. Time slice from middle of 3-D steam conformance (inverted velocity) of 1995 survey, centered at 430 ms and averaged within 5 ms vertical window.

boundary between hot and cold reservoir. Figure 6.16 also indicates the velocity from cold to hot shows normal distribution (see lower right corner of the figure). The areal steam distribution shown in this slice is very similar to the areal distribution mapped by the seismic attribute analysis (Figure 6.8). As it is a slice from the middle of the reservoir a difference is expected when compared with the areal conformance map calculated from the entire reservoir interval (Figure 6.8). Steam chambers may be restricted by lithologic barriers, which control vertical steam distribution. Steam chambers are missing in the

center of B6 pad due to this reason. Figure 6.17 shows a cross-line section (xline 41, see Figure 6.8) of both the seismic and inverted impedance for the vertical conformance. It is clear that major lithology (or sequence, C70) boundary exists near well B6-08. The steam chamber stays in the lower sequence to the south of the well, while it gathers in a higher sequence to the north side of the well. It seems that steam has broken through the sequence boundary.

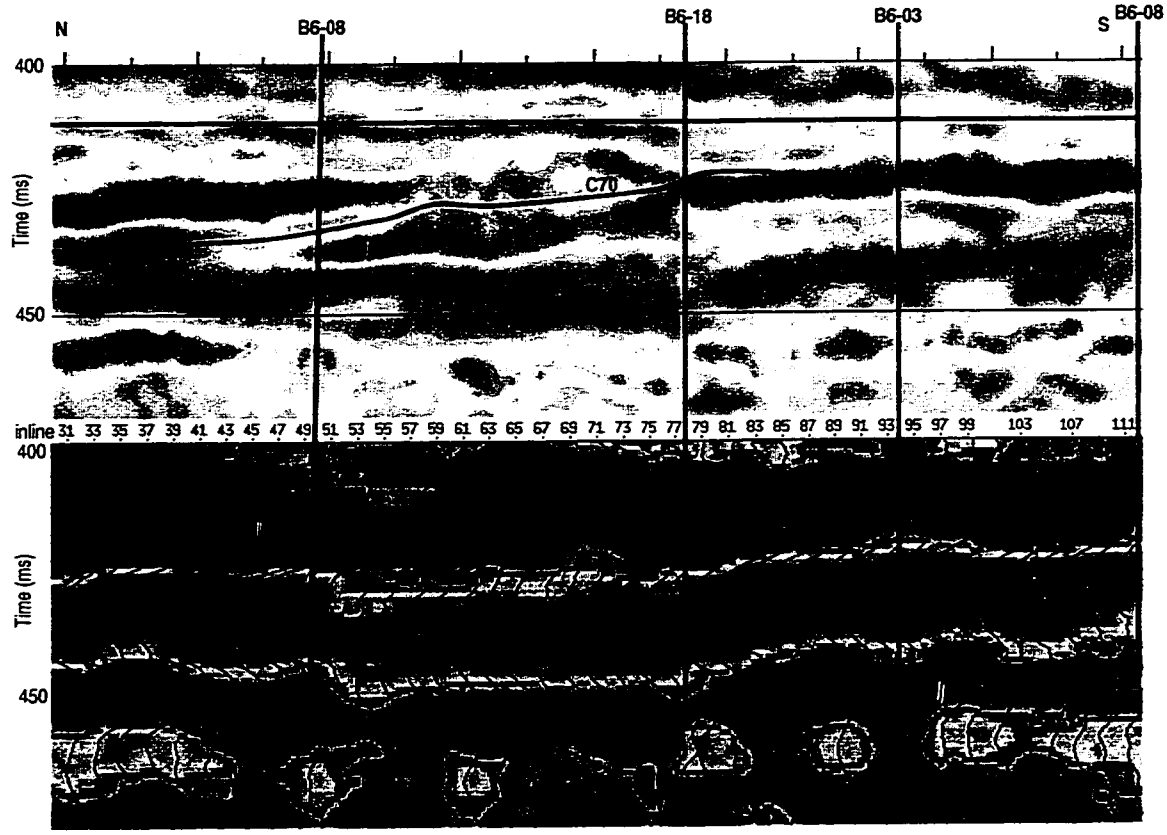

FIG. 6.17. Vertical conformance along cross-line 41 of the 1995 survey showing lithologic barrier of steam chambers.

Shown in Figure 6.18 is a similar time slice made for the 1997 survey, which is comparable to the areal conformance map in Figure 4.28.

In fact, the steam barrier discussed above is the C70 sequence boundary within the Clearwater formation. The upper part of the C70 is good quality reservoir while the lower part gets very shaley. This shaley boundary may not have enough impedance contrast to

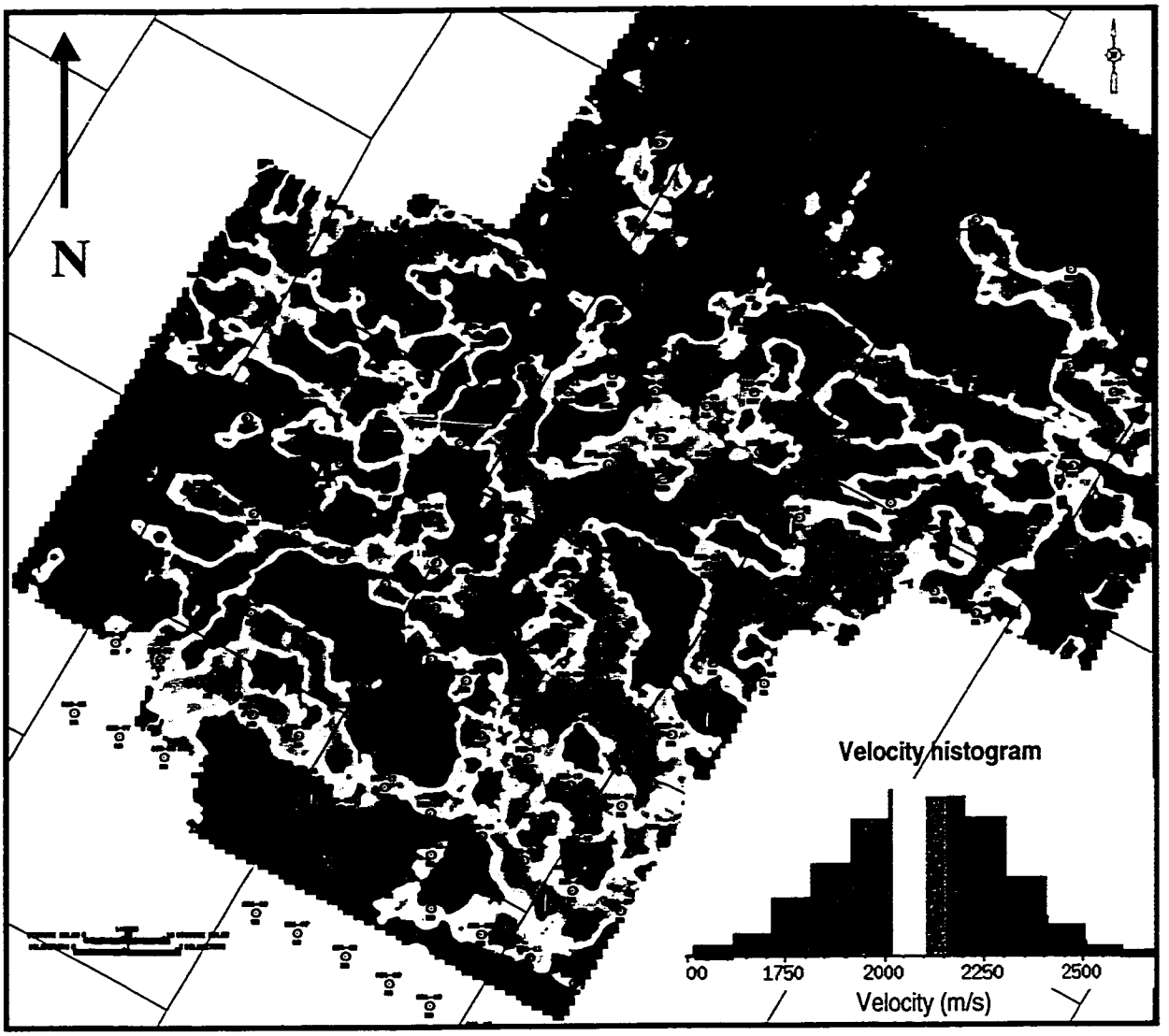

FIG. 6.18. Time slice centered at 430 ms and averaged within 5 ms vertical window from middle of 3-D steam conformance (inverted velocity) of 1997 survey.

act as a strong reflector on *P*-wave data. However, due to the steam disturbance above and below this boundary it can become a good reflector. The major reservoir unit at Cold Lake is sequence C50. The survey area is on the edge of sequence C50 (see Figure 6.19). As shown in Figure 6.19 sequence C50 is pinching out toward the north along cross-line 41. The C50 isopach indicates that there is a dramatic decrease in thickness of the C50 sequence from 30 m to 15 m or less from well B6-08 to the northern boundary of the

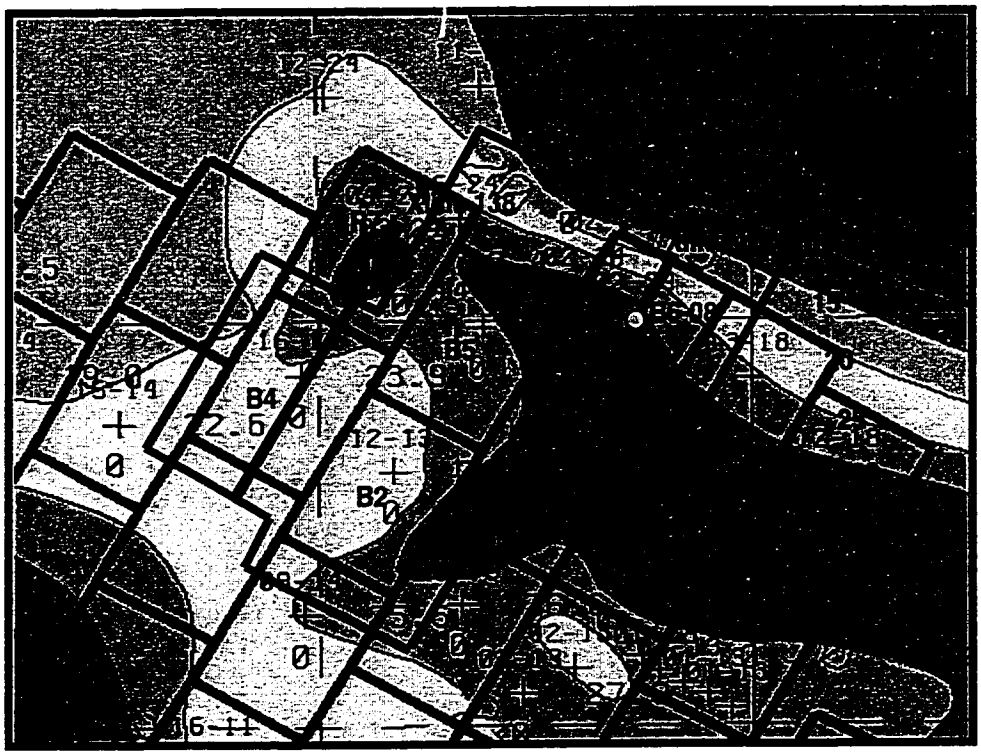

FIG. 6.19. The Clearwater Formation C50 sequence isopach in B2456 survey area. (courtesy of H.R. Feldman)

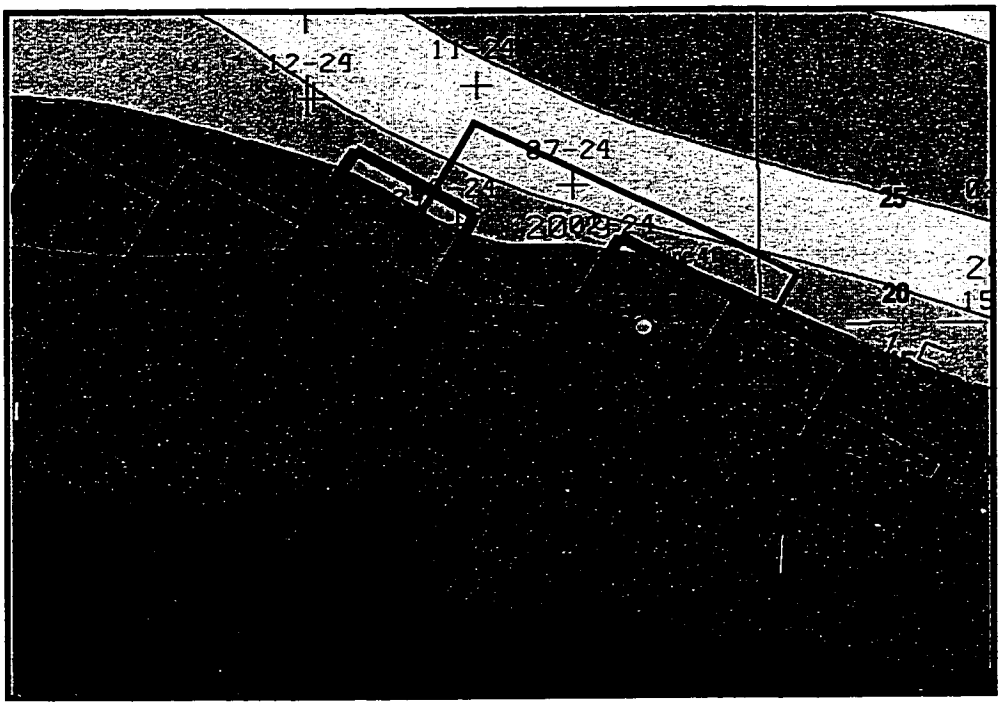

FIG. 6.20. The Clearwater Formation C70 sequence isopach in B2456 survey area. (courtesy of H.R. Feldman)

survey. In contrast, the thickening of sequence C70 is dramatic. The thickness of C70 increases from 10 m to 20 m from well B6-08 to the north boundary of the survey area (see Figure 6.20).

Of sequences C30, C40, C50, and C70, the C50 is composed of the cleanest sand. The sharp lower boundary of the steam chambers corresponds closely to the C50 sequence boundary. Apparently the mud content of the C30 and C40 prevented significant steam penetration. In the area where C50 is the dominant reservoir, steam usually breaks through some of barriers such as thin shaley boundaries in the later cycles of CSS. Steam chambers plot on vertical conformance show displays as blocks. Sequence boundaries may be damaged and not show reflections. However, in the area where C50 is reduced, steam chambers are restricted locally and areal communication channel networks are in the early stage. Sequence boundaries are preserved. The C70 overlies the C50 in the study area. This sequence is muddy at the base and sandy at the top. The muddy interval was a weak impediment to steam migration, but steam still penetrated the upper portions of the sequence in some areas.

Cross-line 138 is a section crossing the B4 and R7 pads in a north-south direction (see Figures 6.8, 6.19, and6.20). Figure 6.21 shows the tie of the sequence boundaries to the

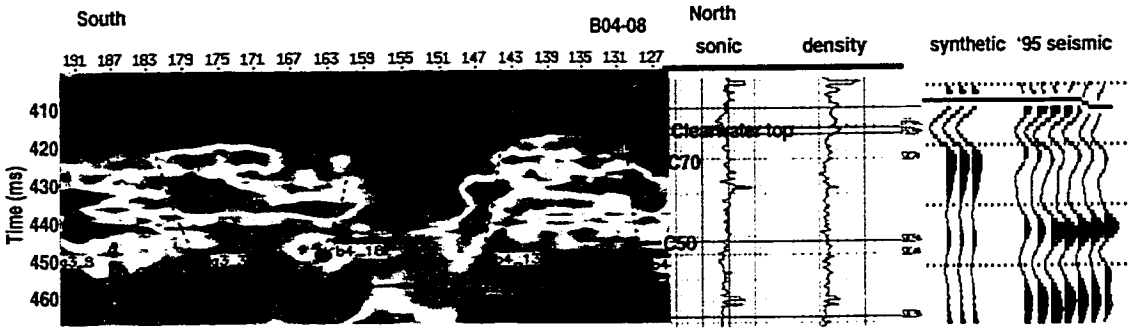

FIG. 6.21. Tie of the sequence boundaries to the vertical conformance texture for well B4-08. Red - hot steam chambers, blue - cold formation.

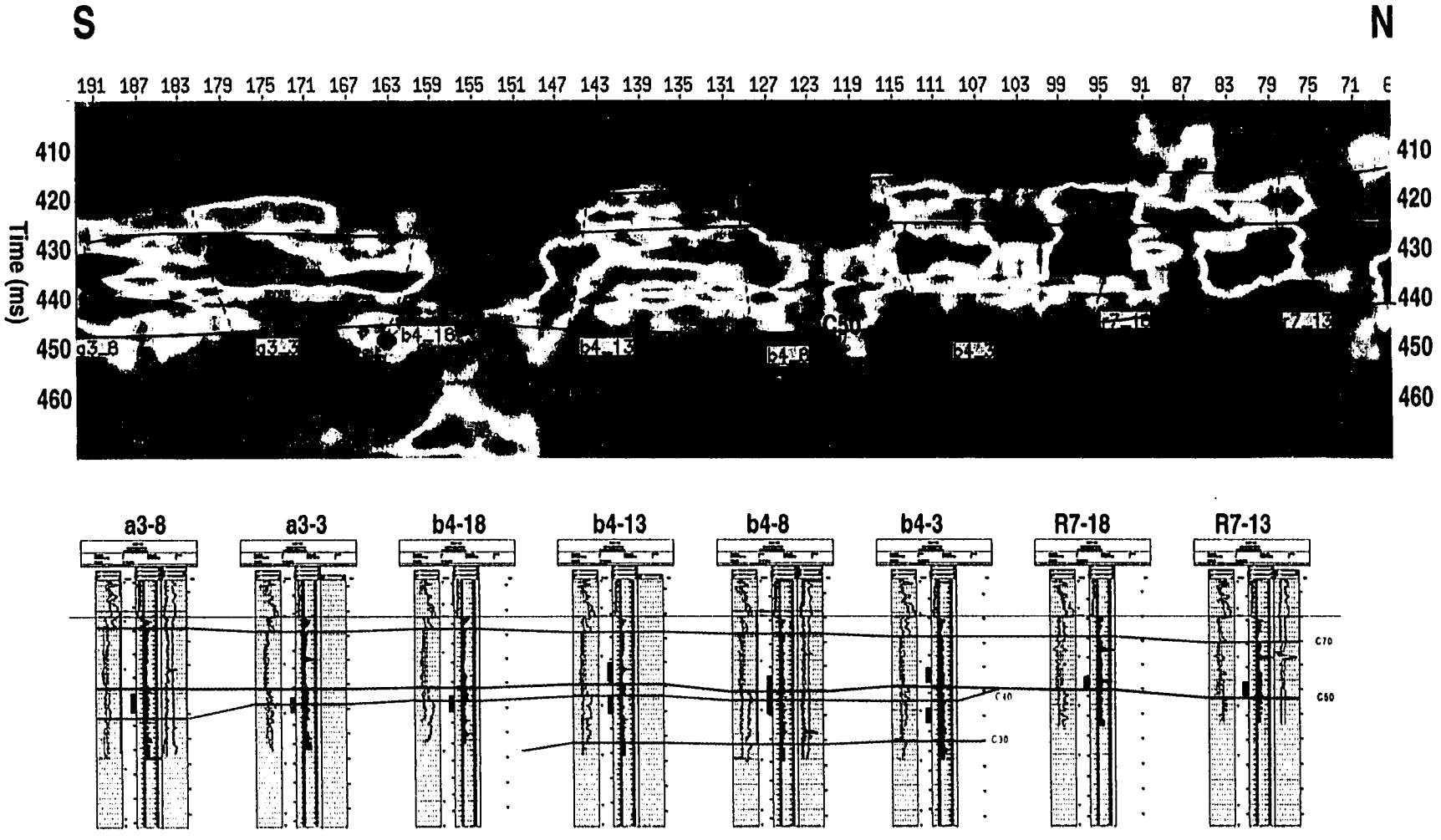

FIG. 6.22. Comparison of the sequence boundaries defined by well logs and the vertical conformance texture along a north-south section of wells R7-13 to A3-08 (cross-line 138).

vertical steam conformance texture. Apparently, the C70 sequence boundary acts as a steam communication barrier between the major sequence C50 and upper C70. A detailed sequence stratigraphy cross-section is built using well logs along cross-line 138. Shown in Figure 6.22 is the comparison of a well log cross-section with sequence boundaries mapped and the vertical steam distribution. The vertical steam texture confirms sequence boundaries defined by well logs. The general trend of C70 sequence thickening towards the north can be observed on the vertical conformance texture.

6.6 Conclusions and discussions

The advantage, when post-stack inversion is applied to time-lapse seismic datasets as a technique for reservoir monitoring, is that time-lapse data normalization is no longer required as wavelets are extracted independently from each data set.

Post-stack data, by nature, contains AVO effects, which can affect the final inversion results. The numerical modeling suggests that significant inversion error can be introduced when AVO effects are strong. The shallow section around the Grand Rapids Formation has strong AVO effects. In addition, steam disturbed reservoir has AVO effects. It is expected that inversion error can be introduced, but the modeling from well B5-28 suggest that this error is negligible. Wavelet extraction is insensitive to AVO effects if the extraction window is large enough. The extraction window should be 300 ms or larger.

As an initial velocity guide, one velocity model can be used and worked out for two time-lapse surveys. Logs obtained before steam injection need editing to be included in the velocity model.

The inverted results (impedance or velocity) provide more detailed information about steam conformance than an areal conformance map. The geometric description of steam is in 3-D space instead of being restricted to a 2-D lateral (areal) plan view. More detailed information such as the trace of steam (edge of steam chambers) or a minor steam pathway is also available. The areal conformance mapped via discriminant analysis is a

statistically weighted (average) probability of hot versus cold reservoir. The vertical conformance reveals that sequence architecture has a significant influence on steam migration. A sequence with high mud content tends to limit or slow both the vertical and horizontal migration of the steam chamber.

Chapter 7 – AVO inversion for reservoir heterogeneity and monitoring

7.1 Introduction

As discussed in chapter 2, further reservoir characterization can be carried out by integrating *P*- and *S*-wave information, compared with using *P*-wave information alone. These include reservoir heterogeneity studies such as lithology differentiation and fluid mapping. However, the availability of field measured shear-wave data is limited. Also, in some cases surface *P-S* wave data suffers near-surface attenuation; therefore it has lower resolution than *P*-wave data.

The purpose of this chapter is to introduce an 'in-house' shear-wave extraction method from pre-stack data, which is commonly known as AVO inversion. The extracted shear-wave is called a psuedo shear-wave. The mud-rock line constructed in chapter 2 will be used in the inversion process.

The chapter covers theoretical modeling to final application of reservoir heterogeneity study and reservoir monitoring. The theoretical studies and modeling define the best and sufficient theoretical model that is suitable for the Cold Lake Clearwater reservoir. Through modeling, the reflection angle and usable offset in the inversion is addressed.

2-D 3-component line 6y074 is chosen to explain the analysis of reservoir heterogeneity study. With the availability of both a single phone and an array of 6-phone recording, a comparison will be made on true amplitude processing and inversion result. Comparison will also be made between psuedo shear-wave and converted shear-wave. The final fluid factor will be tied to well information. D3 pad 3-D time-lapse seismic surveys (1990 versus 1992) are chosen for reservoir monitoring by applying this technique.

7.2 Theory

The variation of reflection and transmission coefficients with incident angles (or offsets) is referred to as offset-dependent-reflectivity and is the fundamental basis for amplitude versus offset (AVO) analysis. The equation used here is from Aki and Richards (1980) which is an approximated form for the *P-P* wave reflection coefficients (*Rpp*), simply parameterized in terms of the changes in density, P-wave velocity, and S-wave velocity across the interface.

$$R_{pp}(\theta) \approx \frac{1}{2}(1-4V_{sa}^2 p^2)\frac{\Delta\rho}{\rho_a} + \frac{1}{2\cos^2\theta}\frac{\Delta V_p}{V_{pa}} - 4p^2 V_{sa}^2 \frac{\Delta V_s}{V_{sa}} \qquad (7.1)$$

where

$\Delta\rho = \rho_2 - \rho_1$ the density difference across the interface,

$\Delta Vp = V_{P2} - V_{P1}$ the *P*-wave velocity difference across the interface,

$\Delta Vs = V_{S2} - V_{S1}$ the *S*-wave velocity difference across the interface,

$\rho = (\rho_2 + \rho_1)/2$ the average density,

$Vpa = (V_{P2} + V_{P1})/2$ the average *P*-wave velocity,

$V_{sa} = (V_{S2} + V_{S1})/2$ the average *S*-wave velocity,

$\theta = (\theta_2 + \theta_1)/2$ the average angle of incident angle θ_1 and transmitted angle θ_2,

$p = \frac{\sin\theta_1}{V_{P1}} = \frac{\sin\theta_2}{V_{P2}}$ the ray parameter.

In the AVO analysis, the reflection amplitude can be approximately treated as the reflection coefficient (*Rpp*), and the incident angles can be calculated via ray tracing. Usually there are more than three offsets in each CDP gather. Therefore, equation (7.1) provides more equations than unknowns ($\Delta\rho/\rho$, $\Delta Vp/Vp$, $\Delta Vs/Vs$), the inverse problem is over-determined. Without dropping any term, equation (7.1) can be further reformulated as (see Appendix A):

$$Rpp(\theta) \approx (1+\tan^2\theta)R_p - 8\frac{Vs^2}{Vp^2}R_s \sin^2\theta - (\frac{1}{2}\tan^2\theta - 2\frac{Vs^2}{Vp^2}\sin^2\theta)\frac{\Delta\rho}{\rho} \quad (7.2)$$

where *Rp* and *Rs* are approximated as follows (see Appendix A):

$$Rp \approx \frac{1}{2}(\frac{\Delta Vp}{Vp} + \frac{\Delta\rho}{\rho}) \quad (7.3)$$

$$Rs \approx \frac{1}{2}(\frac{\Delta Vs}{Vs} + \frac{\Delta\rho}{\rho}) \quad (7.4)$$

By solving equation (7.2) we can obtain the reflection coefficient of P-wave (*Rp*) and S-wave (*Rs*) and density gradient ($\Delta\rho/\rho$) as long as there more than three offsets in each CDP gather. However, the constants associated with each unknown can be different in second order magnitude. For example, for θ=20° and *Vp/Vs*=2.0, the constants are 1.13247, 0.23396, and 0.00775 respectively; and the first constant is 146 times bigger than third constant. Therefore, in most practical situations, solving equation (7.2) for three unknowns is unnecessary as the equation is ill-conditioned. The last two terms associated with $\Delta\rho/\rho$ can be dropped, especially when $\Delta\rho/\rho$ is small.

$$Rpp(\theta) \approx (1+\tan^2\theta)R_p - 8\frac{Vs^2}{Vp^2}R_s \sin^2\theta \quad (7.5)$$

Further, more aggressive approximation can be obtained by assuming *Vp/Vs*=2.

$$Rpp(\theta) \approx (1+\tan^2\theta)R_p - 2R_s \sin^2\theta \quad (7.6)$$

In the case where the incident angle is relatively small, the assumption of $\sin\theta = \tan\theta$ is used, and equation (7.2) is rewritten as:

$$Rpp(\theta) \approx R_p + (R_p - 8\frac{Vs^2}{Vp^2}R_s)\sin^2\theta - (\frac{1}{2} - 2\frac{Vs^2}{Vp^2})\frac{\Delta\rho}{\rho}\sin^2\theta\,. \quad (7.7)$$

As in equation (7.5) the last two terms associated with $\Delta\rho/\rho$ can be dropped.

$$Rpp(\theta) \approx R_p + (R_p - 8\frac{Vs^2}{Vp^2}R_s)\sin^2\theta \qquad (7.8)$$

Again, if we further assume *Vp/Vs*=2 in equation (7.8), we obtain the simplest format of approximation:

$$Rpp(\theta) \approx R_p + (R_p - 2R_s)\sin^2\theta\,. \qquad (7.9)$$

In most cases, however, equation (7.9) introduces a significant error to the estimations of *Rp* and *Rs*. To see the accuracy of different approximations a series of numerical calculations of the reflection coefficient has been carried out. Figure 7.1 shows blocked well logs of well B05-28. The first numerical modeling is to calculate the reflection coefficient of two different interfaces - Grand Rapids formation top (shallow one) with *Vp/Vs* ratio around 2.7 and the top of the steam zone (deeper one) with *Vp/Vs* ratio around 2. The physical parameters for the two interfaces are listed in Table 7.1. Figure 7.2 shows the plot of reflection coefficient versus incident angle (θI) for different approximations and their relative error to the Zoeppritz equation at the shallow interface. The relative error is defined as the absolute difference of reflection coefficient between an approximation and Zoeppritz equation divided by absolute value of reflection coefficient from Zoeppritz equation.

Table 7.1 Physical properties of two modeling interfaces.

Interfaces	Vp (m/s)	Density (kg/m3)	Vs (m/s)
Grand Rapids top	2268	2250	843
	2447	2260	1024
Top of steam zone	2310	2080	957
	2061	2070	957

It is seen from Figure 7.2 that the poorest approximation is under the assumption of *Vp/Vs*=2 and $\sin(\theta)=\tan(\theta)$, which is expressed by equation (7.9). It is nearly valid when the incident angle is less than 10°. It is almost impossible for pre-stack inversion to be carried out in shallow reservoir zone. For example, the Clearwater reservoir in Cold Lake is about 400 m in depth, and the approximated useful offset for inversion is about 70 m. With such limited offset the inversion result will be unstable, and the accuracy will be poor. In the shallow section usually the *Vp/Vs* ratio may not be 2. Following the case above if we keep the assumption of *Vp/Vs* ratio of 2 but not the assumption of

sin(θ)=tan(θ) the valid incident angle still remains the same (10°, see Figure 7.2). The second category of approximation is under the assumption of *sin(θ)=tan(θ)* or dropping the last two terms associated with $\Delta\rho/\rho$. Now the valid incident angle has been extended to 20° (see Figure 7.2b). The best approximation should make full use of all offsets before the critical angle. The results from Aki and Richards (equation (7.1)) and the new approximation (equation (7.2)) bring the error down significantly (see Figure 7.2) with approximately 10% error between 30° and 50° of incident angle or less for other incident angles. It is worth noting that dropping the last two terms in the new approximation makes the error even lower. This is because in some occasions dropping the last two terms can cancel the error brought by the previous approximation from Aki and Richards.

As depth increases *Vp/Vs* ratio gets close to 2. The assumption of *Vp/Vs*=2 does not bring as big an error as the assumption *sin(θ)=tan(θ)* does. Figure 7.3 shows the similar plot as Figure 7.2 except it is for the top of the steam zone. It is clear that any approximation associated with the assumption of *sin(θ)=tan(θ)* brings a significant error after an incident angle of 20° or higher. In this particular case dropping the last two terms associated with $\Delta\rho/\rho$ brings less than 4% error; still it is higher than the errors from the Aki and Richards approximation and the approximation by equation (7.2). The approximation with the assumption of *Vp/Vs*=2, in this particular case, brings the least error, which is due to a similar reason as dropping the last two terms in the previous case.

The above numerical calculations tell us that in the shallow situation the error mostly comes from the wrong assumption for the *Vp/Vs* ratio, and in the deeper situation the assumptions associated with incident angle such as *sin(θ)=tan(θ)* may cause significant error. In fact, the correct *Vp/Vs* of shallow (near surface) will help the ray tracing in the deep and resolve a more accurate incident angle. Therefore, an iterative pre-stack inversion process is introduced in this chapter.

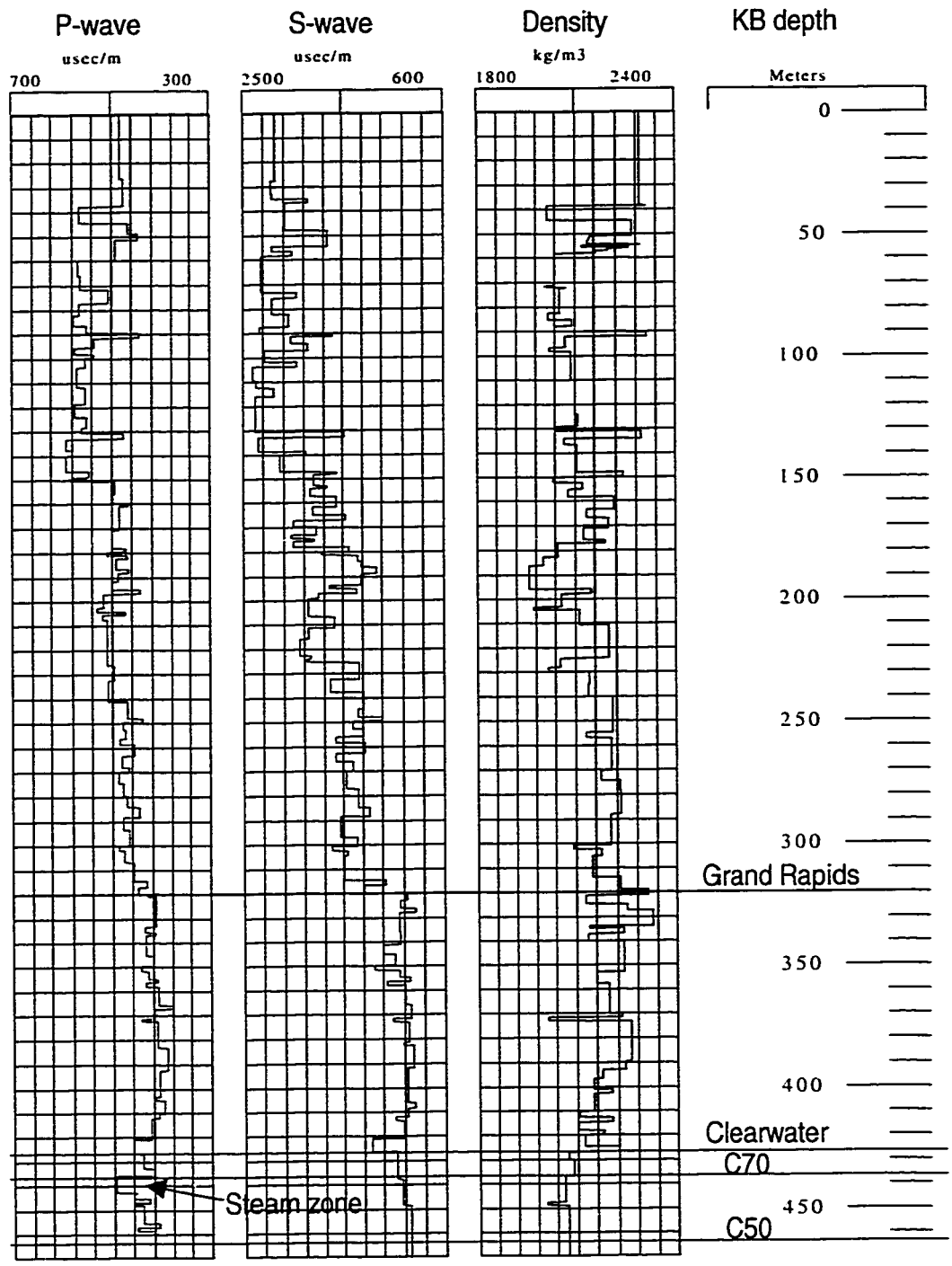

FIG. 7.1. Blocked well logs (P-wave slowness, S-wave slowness, and density) of well B05-28.

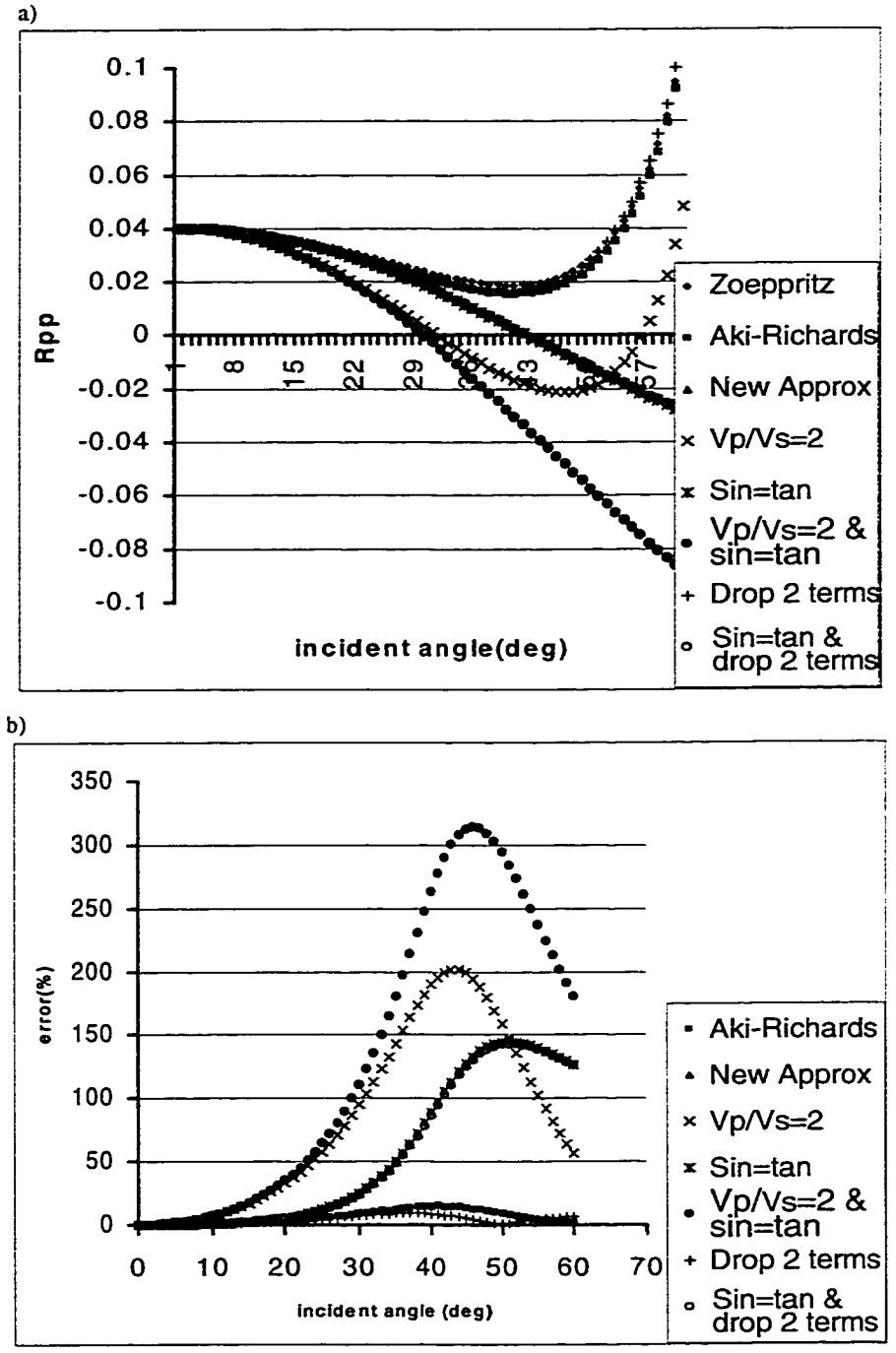

FIG. 7.2. *P-P* wave Reflection coefficients (a) calculated from the Zoeppritz equation and different approximations at the interface of the Grand Rapids formation top (FIG. 7.1) and their relative error (b) to the Zoeppritz equation.

a)

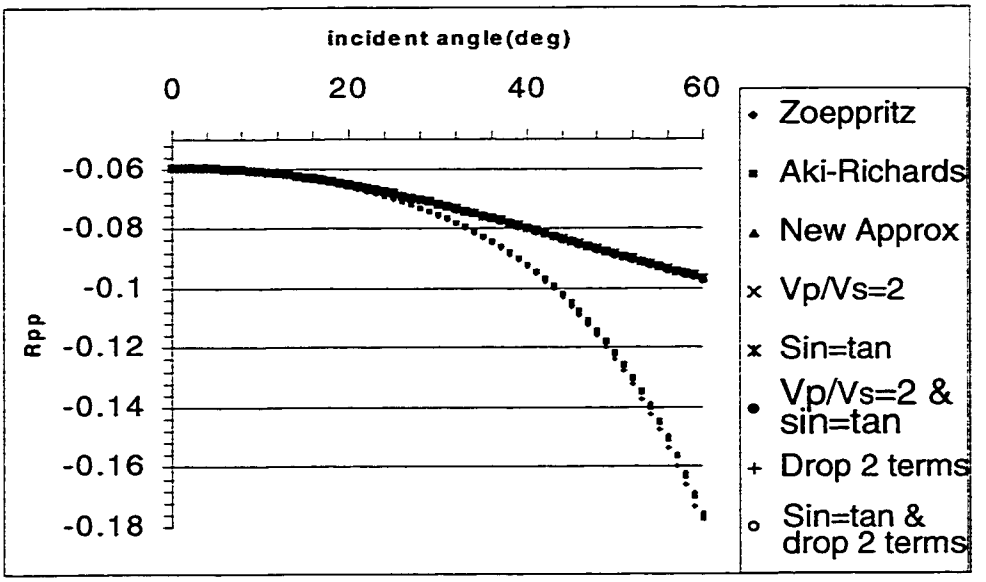

b)

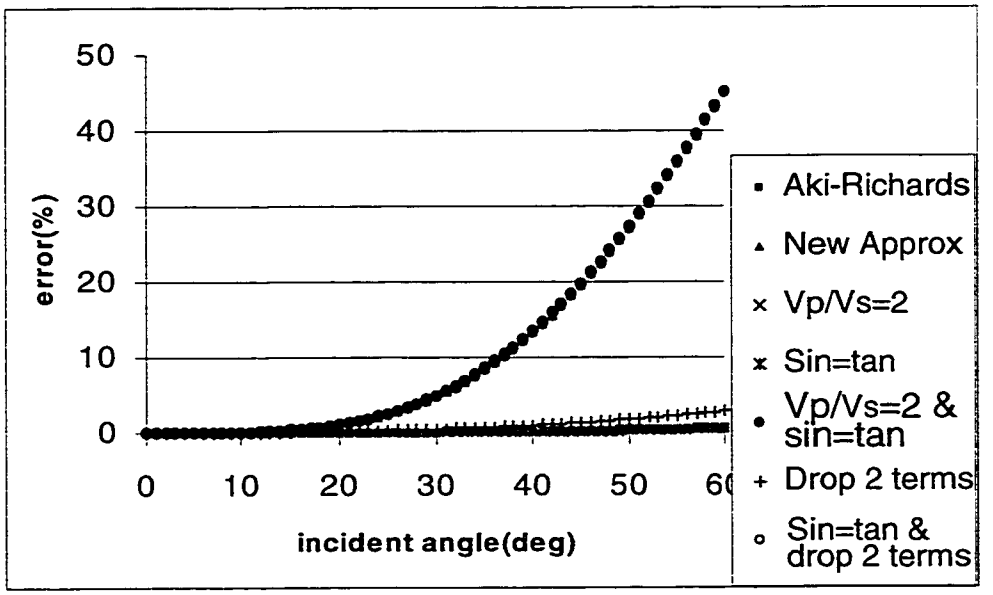

FIG. 7.3. *P-P* wave Reflection coefficients (a) calculated from the Zoeppritz equation and different approximations at the interface of the top of the steam zone (see FIG. 7.1) and their relative error (b) to the Zoeppritz equation.

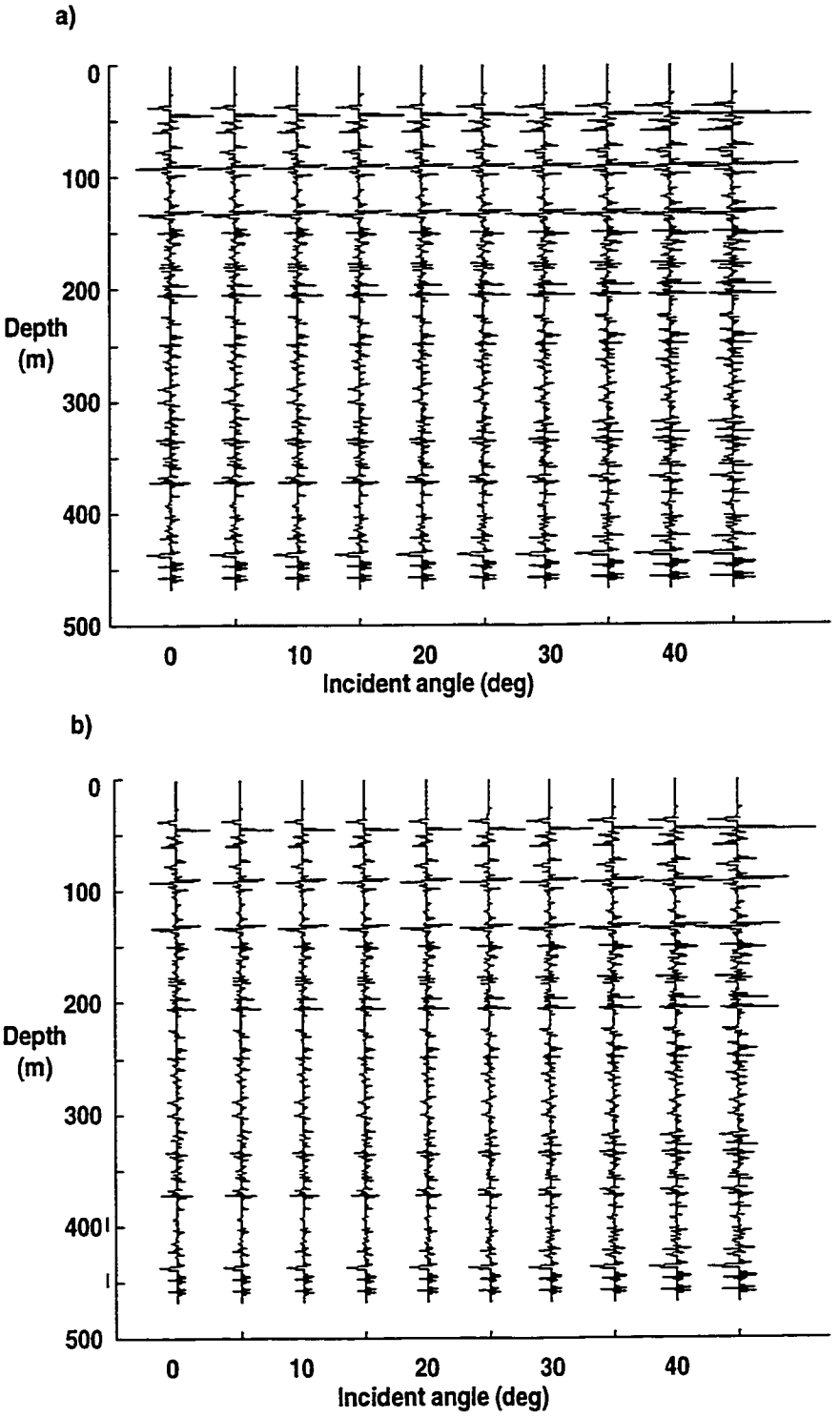

FIG. 7.4. *P-P* wave Reflection coefficients of well B5-28 (Figure 7.1) calculated from the Zoeppritz equation (a) and an approximation dropping the last two terms associated with $\Delta\rho/\rho$ (b) (equation 7.5).

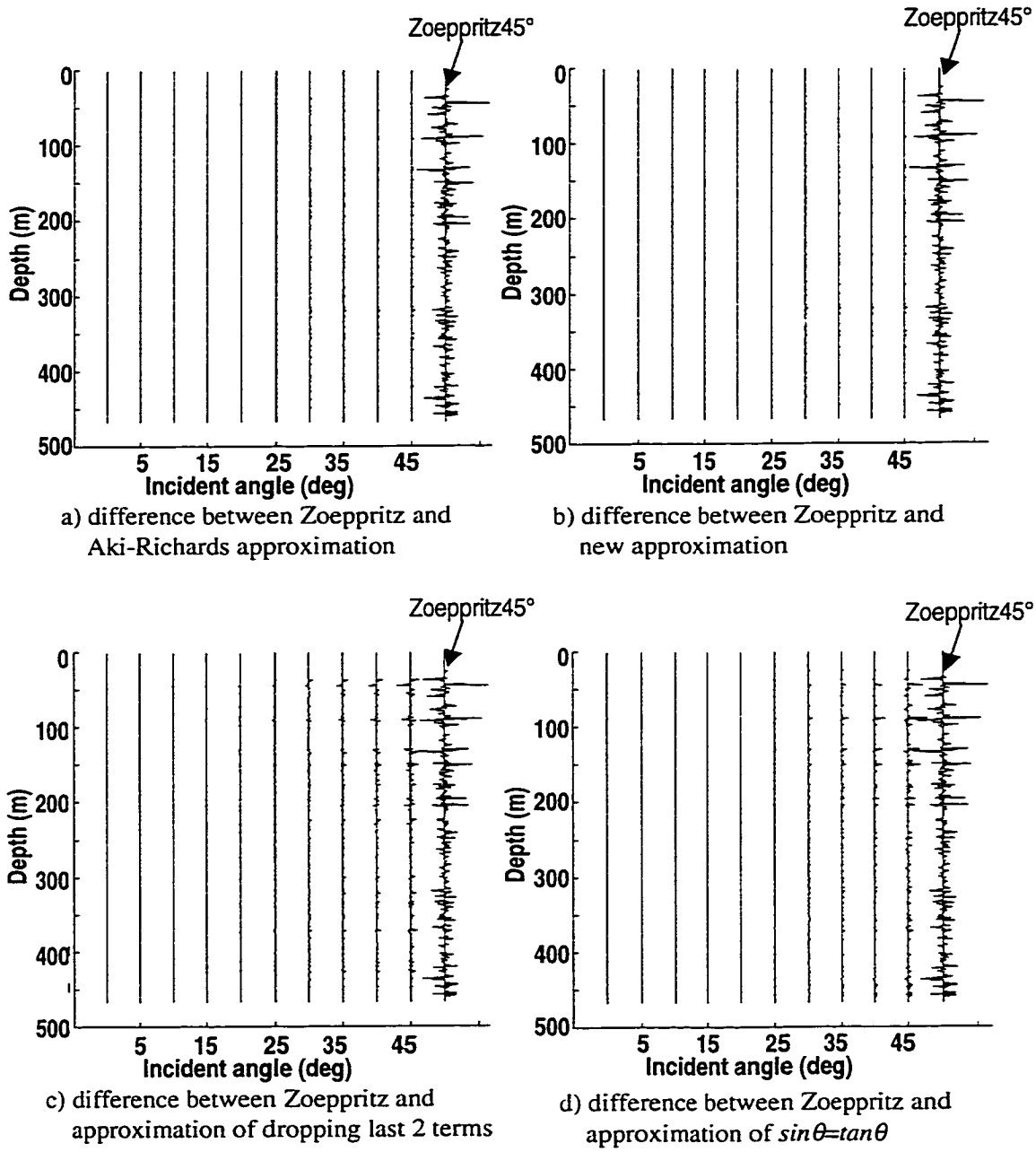

a) difference between Zoeppritz and Aki-Richards approximation

b) difference between Zoeppritz and new approximation

c) difference between Zoeppritz and approximation of dropping last 2 terms

d) difference between Zoeppritz and approximation of $sin\theta$=$tan\theta$

FIG. 7.5 a), b), c), and d) The difference of *P-P* wave Reflection coefficients of well B05-28 between the Zoeppritz equation and other approximations, Zoeppritz45° is the reflection coefficients from the Zoeppritz equation with incident angle of 45°.

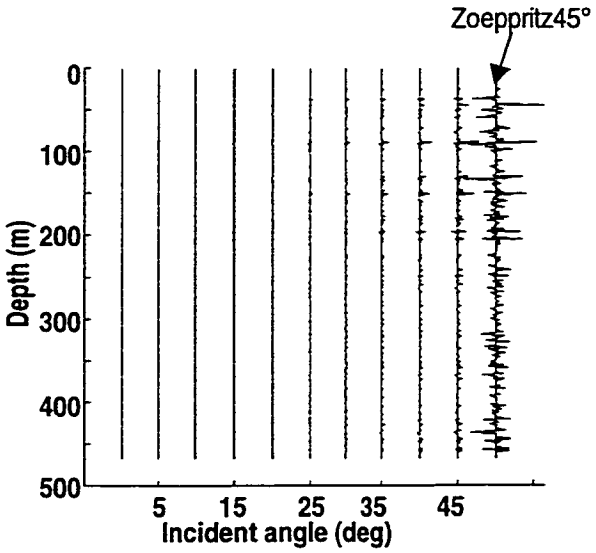

e) difference between Zoeppritz and approximation of drop last 2 terms & $sin\theta=tan\theta$

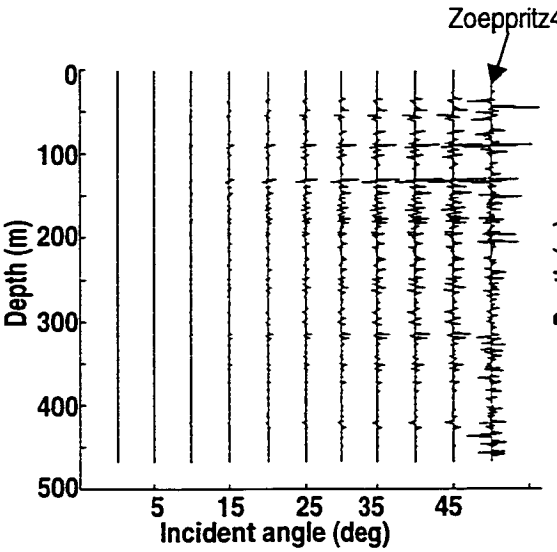

f) difference between Zoeppritz and approximation of Vp/Vs=2

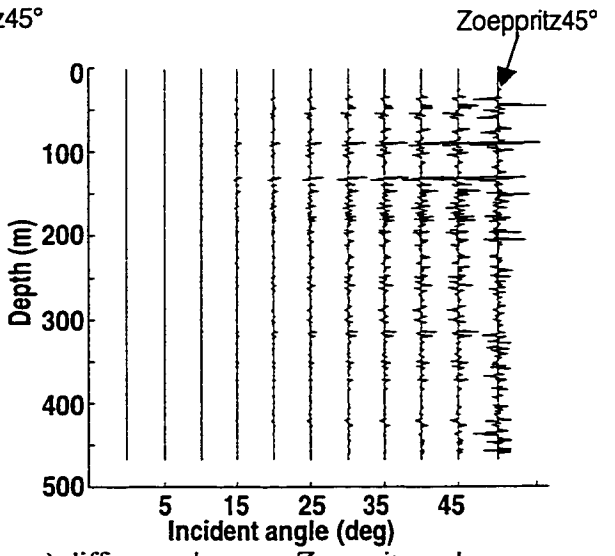

g) difference between Zoeppritz and approximation of Vp/Vs=2 & $sin\theta=tan\theta$

FIG. 7.5 e), f), and g) The difference of *P-P* wave Reflection coefficients of well B5-28 between the Zoeppritz equation and other approximations, Zoeppritz45° is the reflection coefficients from the Zoeppritz equation with incident angle of 45°.

Further quantitative error analysis is implemented by calculating the reflection coefficient both for different incident angles and in different depth, under various approximations. Figure 7.4a shows the *P-P* wave Zoeppritz reflection coefficient varied with incident angle of 0° to 45° for the entire well of B05-28 (see Figure 7.1). Similar calculations have been carried out for all types of approximations (equation 7.5 to 7.9), For example, Figure 7.4b shows the approximation of dropping last two terms associated with $\Delta\rho/\rho$ (equation 7.5).

Figure 7.5 shows differences (error bar) of reflection coefficient between the Zoeppritz equation and various approximations for the entire well B05-28. To make sure that all the difference plots are scaled the same, the largest in magnitude, (the reflection coefficients from Zoeppritz equation with incident angle of 45°), is attached and plotted in all difference plots. The observation of all seven plots leads to the following summary. The least error is from Aki and Richards (Figure 7.5a, equation 7.1) and the new approximation (Figure 7.5b, equation 7.2). The next best acceptable approximation is from dropping the last two terms in Equation (7.2) (see Figure 7.5c, equation 7.5). It seems that the error from the approximation of $\sin\theta = \tan\theta$ is comparable to the previous approximation (compare Figure 7.5d to 7.5c, see equation 7.7), but this error increases dramatically as the incident angle increases. It may be acceptable to assume $\sin\theta = \tan\theta$ and drop the last two terms in equation (7.2) if the data only contains offsets that make the incident angle less than 40° (see Figure 7.5e, equation 7.8). It is definitely improper to assume a *Vp/Vs* ratio of 2 as we can see a significant error is introduced (see Figure 7.5f, 7.5g, equation 7.9).

To summarize the experiment, we can conclude that the straight reformulated approximation (equation 7.2) from Aki and Richards provides the best estimation of reflection coefficient. However, the inverse process of solving equation (7.2) for all three unknowns (*Rp*, *Rs*, $\Delta\rho/\rho$) sometimes can be troublesome, and the solutions may not be stable. Solving equation (7.5) in which the two terms associated with $\Delta\rho/\rho$ are dropped is a practical and realistic way to resolve *Rp* and *Rs* for reservoir heterogeneity and fluid study.

7.3 The inverse problem and modeling

Historically, the inverse problem is simplified to solve equation (7.9). Without ray tracing (θ unknown) $\sin^2\theta$ is approximated by the square of offset over depth. This is possible since the depth is unchanged for the same time sample. Therefore, a cross-plot of reflection amplitude against offsets in each CDP gather is the way to determine the intercept (*Rp*) and the slope (*Rp-2Rs*) for linear equation (7.9). For the shallow reflectors, however, this is a very poor approximation as we can see from Figure 7.6. Here the approximation is only valid for $\sin^2\theta$ less than 0.05, which converts to an incident angle of 10°. In order to obtain stable and reliable inversion results it is necessary and advantageous to make full use of all offset data.

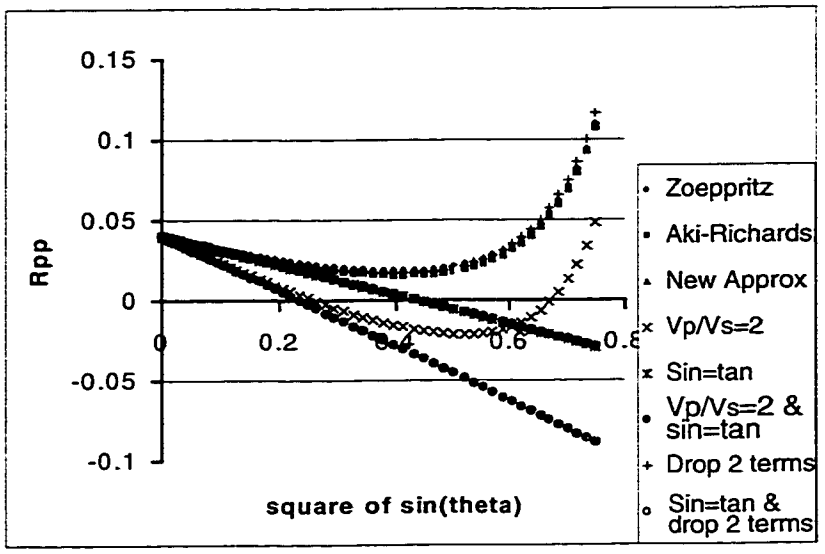

FIG. 7.6 Cross-plot of *P-P* wave Reflection coefficients against $\sin^2\theta$ from Zoeppritz equation and different approximations at the top of Grand Rapids formation.

The following linear system can be constructed if, in equation (7.5), we know the two constants a_{i1} and a_{i2} (θ can be obtained through ray tracing, *i* stands for offset number) in the front of *Rp* and *Rs*, and assume the reflectivity *Rpp* at a specific time sample is the amplitude at that specific time on a specific offset (corresponding to θ), and suppose that there exist *n* offsets.

$$\begin{bmatrix} a_{11} & a_{12} \\ a_{21} & a_{22} \\ . & . \\ . & . \\ a_{i1} & a_{i2} \\ . & . \\ . & . \\ a_{n1} & a_{n2} \end{bmatrix} [R_p \quad R_s] = \begin{bmatrix} R_{pp1} \\ R_{pp2} \\ . \\ . \\ R_{ppi} \\ . \\ . \\ R_{ppn} \end{bmatrix} \tag{7.10}$$

Let us use **A**, **R**, and **Rpp** to denote the three matrices above respectively. The inverse problem (Equation 7.10) is over determined for resolving two unknowns *Rp* and *Rs*. To optimize the solution equation (7.10) is manipulated and solved as follow:

$$\mathbf{R} = (\mathbf{A}^{\mathrm{T}}\mathbf{A})^{-1}\mathbf{A}^{\mathrm{T}}\mathbf{R}_{pp}. \tag{7.11}$$

The existence of a solution for equation (7.10) requires a minimum number of two offsets for each CDP gather. With high fold coverage (e.g. 20 fold or higher for Cold Lake data) this is not a problem at the target level. However, it may be a problem at the near surface, as the fold here is very low or zero fold. Figure 7.7 shows the offset aperture versus incident angle simulated for Cold Lake by using velocity data of well B5-28 (Figure 7.1), assuming maximum offset is 610 m. Below 0.1 second in time the offsets included in the inversion are large enough to stabilize a solution of equation (7.11).

As it is expected that the offsets get bigger as the time (or depth) increases for the same incident angle. For Cold Lake data it is usually safe if the inversion is applied to the time window of 100 ms and below. The offset range used for inversion can be as large as the incident angle reaches 60°. This is clear from Figure 7.8, which shows the critical incident angle or maximum reflection angle in Cold Lake calculated from a typical well B5-28.

An AVO gather (Figure 6.2) was created by using a single well (B5-28) information (*Vp*, *Vs*, Density). The inversion algorithm described above has been applied to this AVO gather. The relationship between *Vp* and *Vs* established in chapter 2 is used in the first iteration to get initial guide of *Vp/Vs* (equation 2.2). Figure 7.9 shows the cross-plot of *Rp* and *Rs* at time samples of 150 ms for the first iteration. Though equation (7.10) is over determined, the solution is optimized. There are about 20 offset traces included in the inversion, which gives 19 solutions; but the best solution is in the center (red solid dot, see Figure 7.9). After the first iteration a pair of *P*-wave (*Ip*) and *S*-wave (*Is*) impedance is obtained. The *Vp/Vs* ratio for the next iteration can simply use the relationship *Vp/Vs=Ip/Is*. This iterative procedure keeps updating the *Vp/Vs* ratio and thereafter improves the ray tracing result (θ). Figure 7.10 shows the comparison of inverted *Rp* and *Rs* at 150 ms through different iterations to the results of using actual *Vp* and *Vs*, including the result from the intercept-gradient method (equation 7.9, see Figure 7.11). It is clear that the iterations make the solutions of *Rp* and *Rs* approach the result from using actual logs.

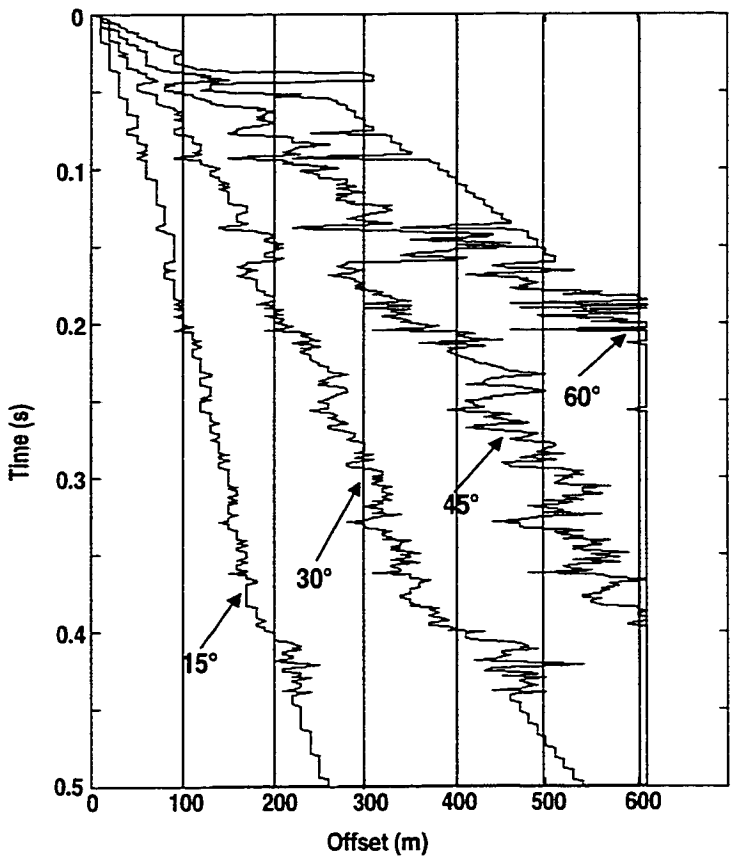

FIG. 7.7. Offset aperture for different incident angles of 15°, 30°, 45°, and 60° via AVO modeling of well B05-28 (Figure 7.1), assuming maximum offset of 610 meters.

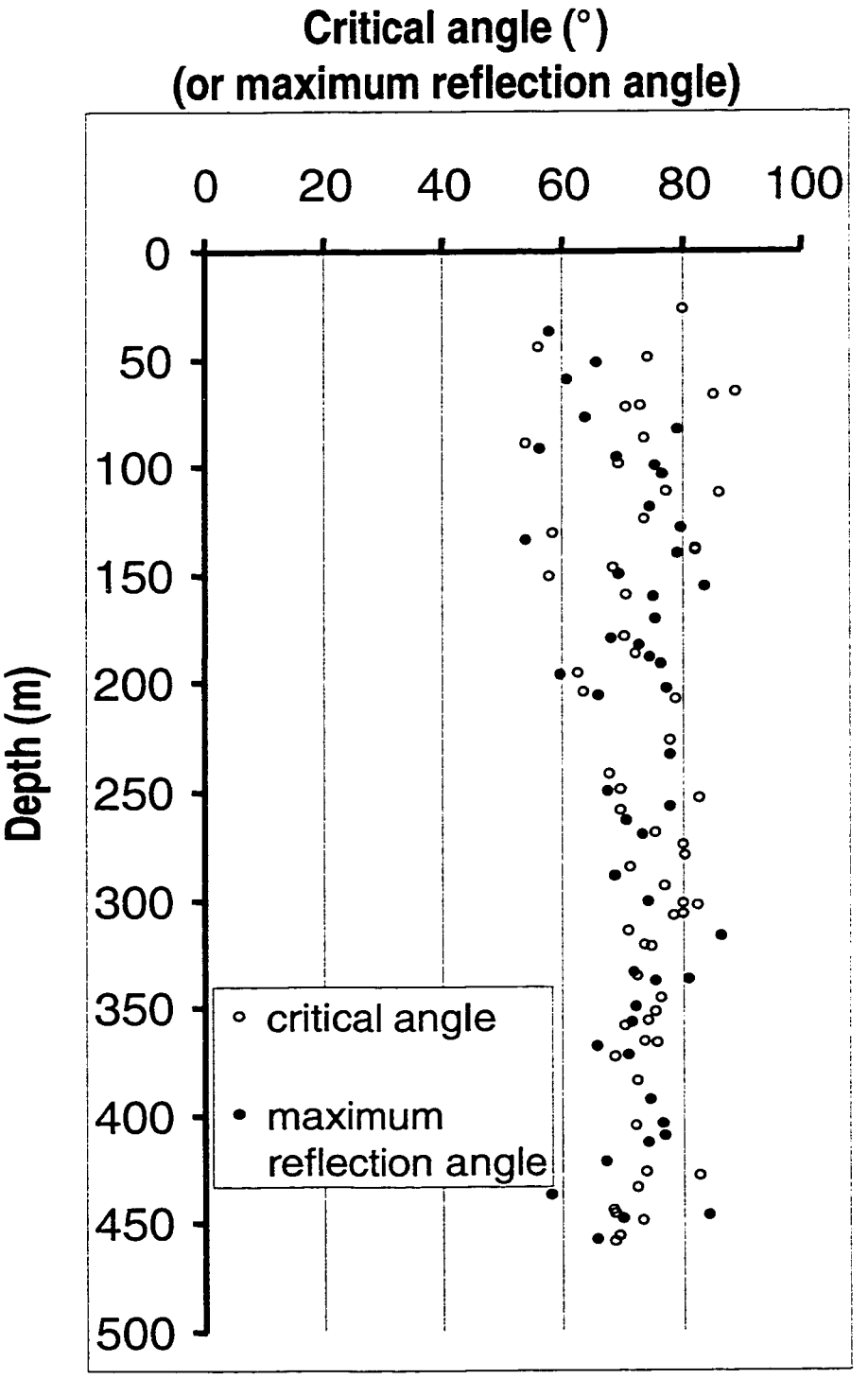

FIG. 7.8. Critical angle or maximum reflection angle (for reflection interface of upper velocity higher than lower velocity with maximum incident angle of 90°) for a typical Cold Lake well B05-28.

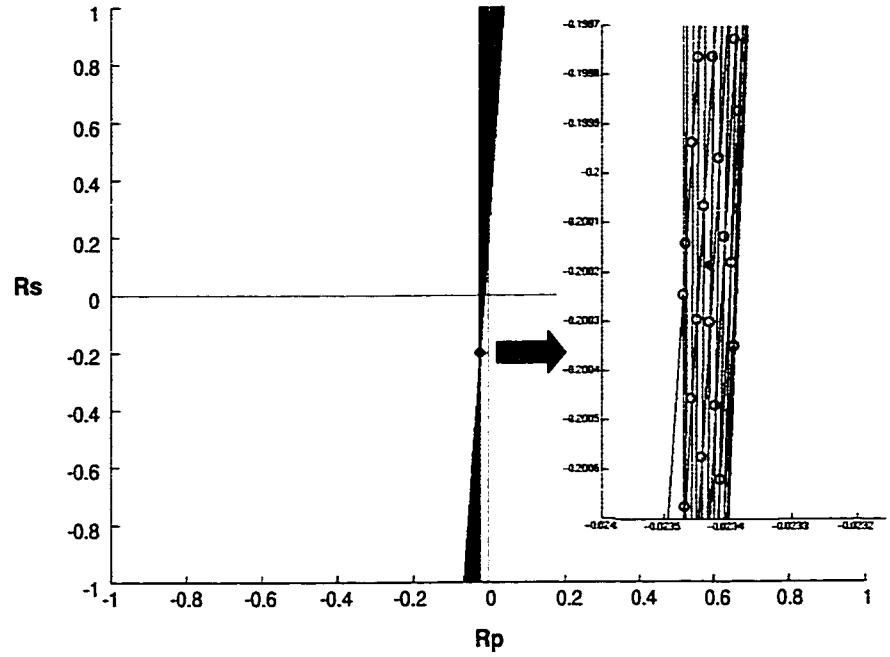

FIG. 7.9. Cross-plot of *Rs* versus *Rp* for first iteration of modeling data at time of 150 ms, showing optimized solution.

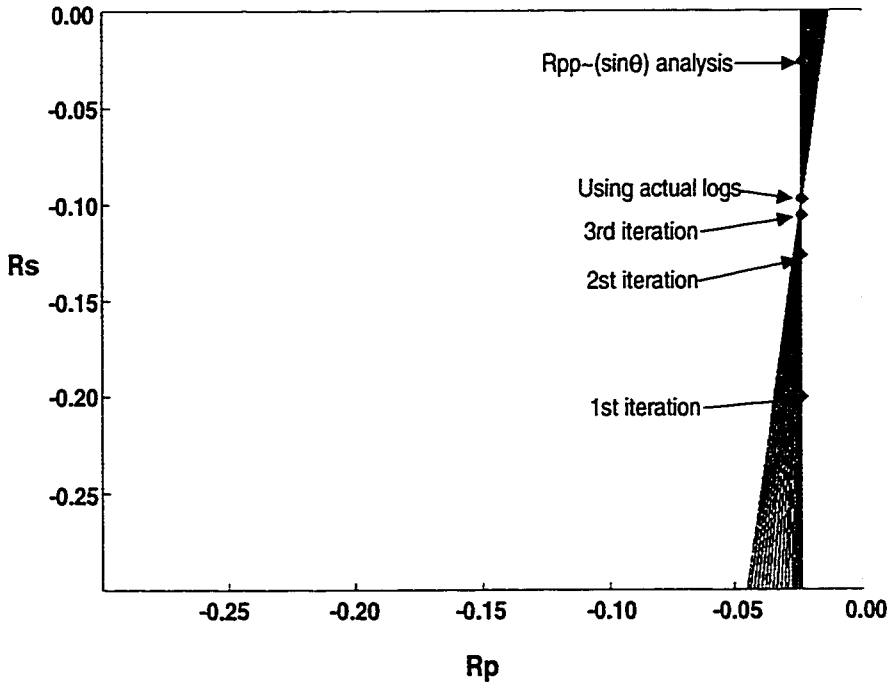

FIG. 7.10. Cross-plot of *Rs* versus *Rp* for inversion results of using actual logs with the results of all iterations, posted at the time of 150 ms, showing solution improvement through iterations.

It is very important to note that the shear-wave information (*Rs*) gets improved most through the iterations (see Figure 7.10), while the compressional-wave information (*Rp*) almost remains unchanged. Figure 7.11 shows that very little change of *Rp* has been made through the iterations. This is further illustrated by the inverted results for *Ip* and *Is* and their quality control plots (error plots). Figure 7.12 shows the inverted *P*-wave impedance through 3 iterations and the iteration using the actual log as a guide. All inversions are implemented using the same parameters and the same parameters for wavelet extraction. Figure 7.13 shows the comparison of inversion error through different iterations (each trace scaled individually). This illustrates that *P*-wave impedance almost remains unchanged through the iterations. However, the *S*-wave inversion result is significantly improved. Figure 7.14 and Figure 7.15 show similar plots as Figure 7.12 and Figure 7.13 for S-wave inversion. It is clear from the error plot (Figure 7.15) that the error bar is reduced through iterations.

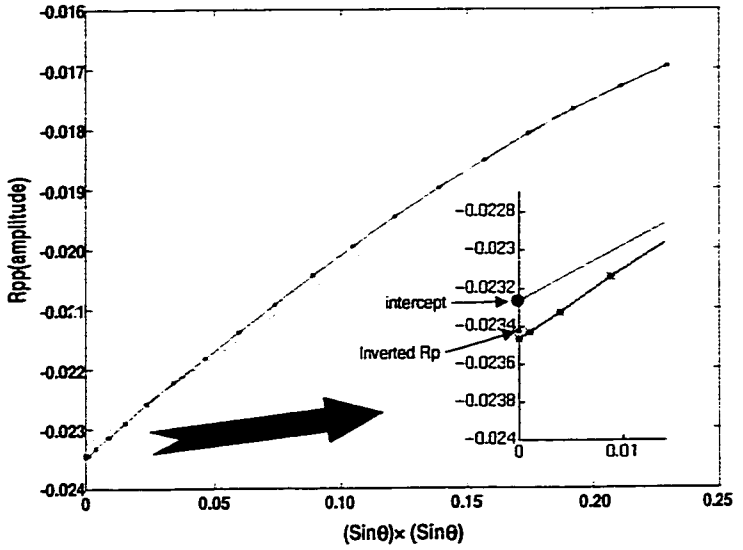

FIG. 7.11. Cross-plot of reflection amplitude versus $\sin^2\theta$ (or square of offset) shown by asterisks, the red line is the best fit line, the intercept (red solid circle) is the solution of *Rp* (see equation 7.9).

7.4 Reservoir heterogeneity study

The first case study presented in this chapter is a reservoir heterogeneity study. The concept of reservoir heterogeneity can be simply understood as reservoir quality. It is always in demand using seismic data to delineate shale or mud content in oil sand. In this reservoir heterogeneity study 3-C line 6y074 is used for zero-offset *P*-wave stack (R_p) and psuedo *S*-wave stack (R_s) inversion, to map reservoir quality. The inverted R_p and R_s are

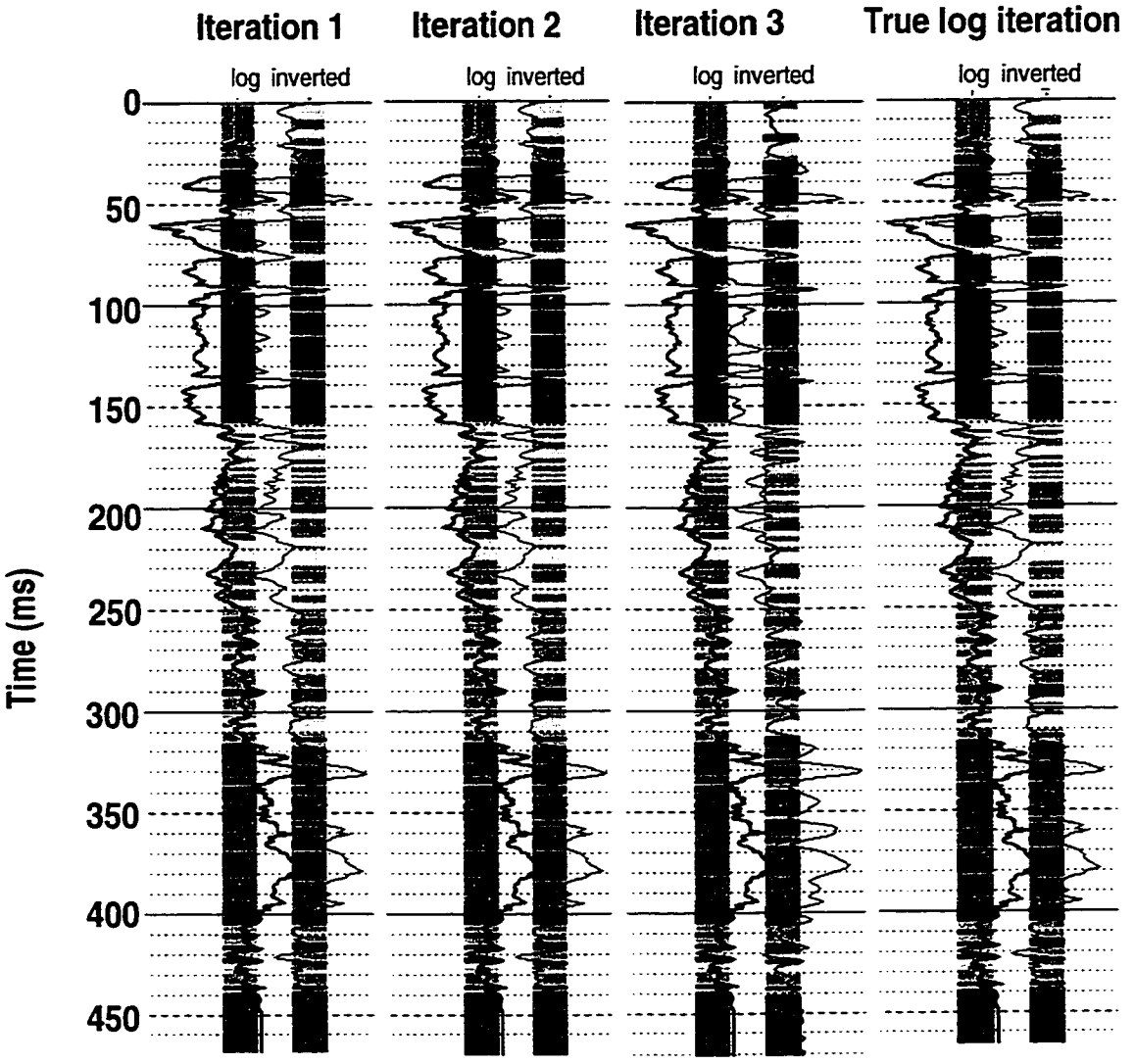

FIG. 7.12. Comparison of inverted P-wave impedance and impedance log through different iterations and an inversion using a real impedance log as a guide for modeling data.

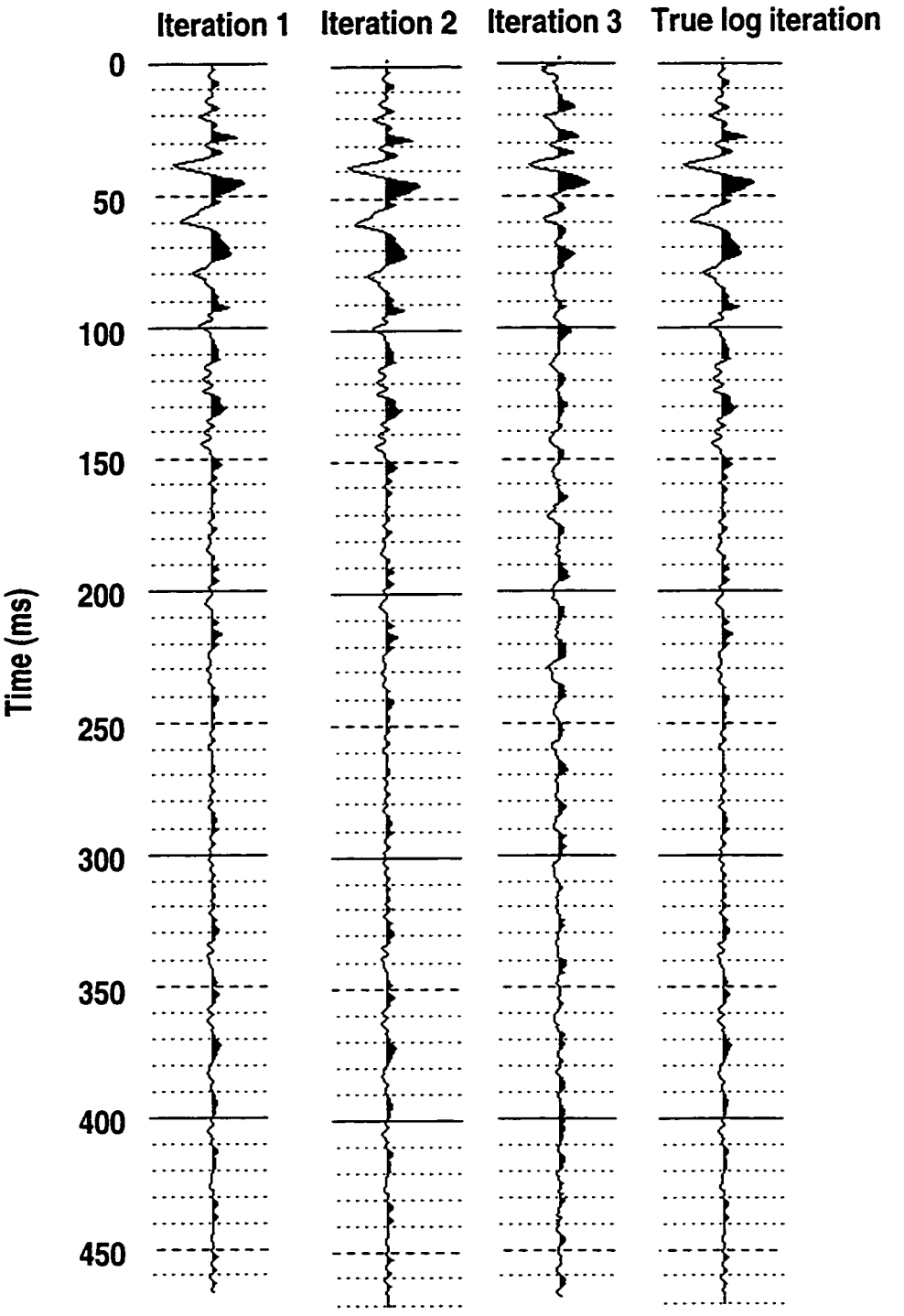

FIG. 7.13. Comparison of inversion error through different iterations; the error is calculated by subtracting *Rp* from a synthetic calculated from an inverted impedance.

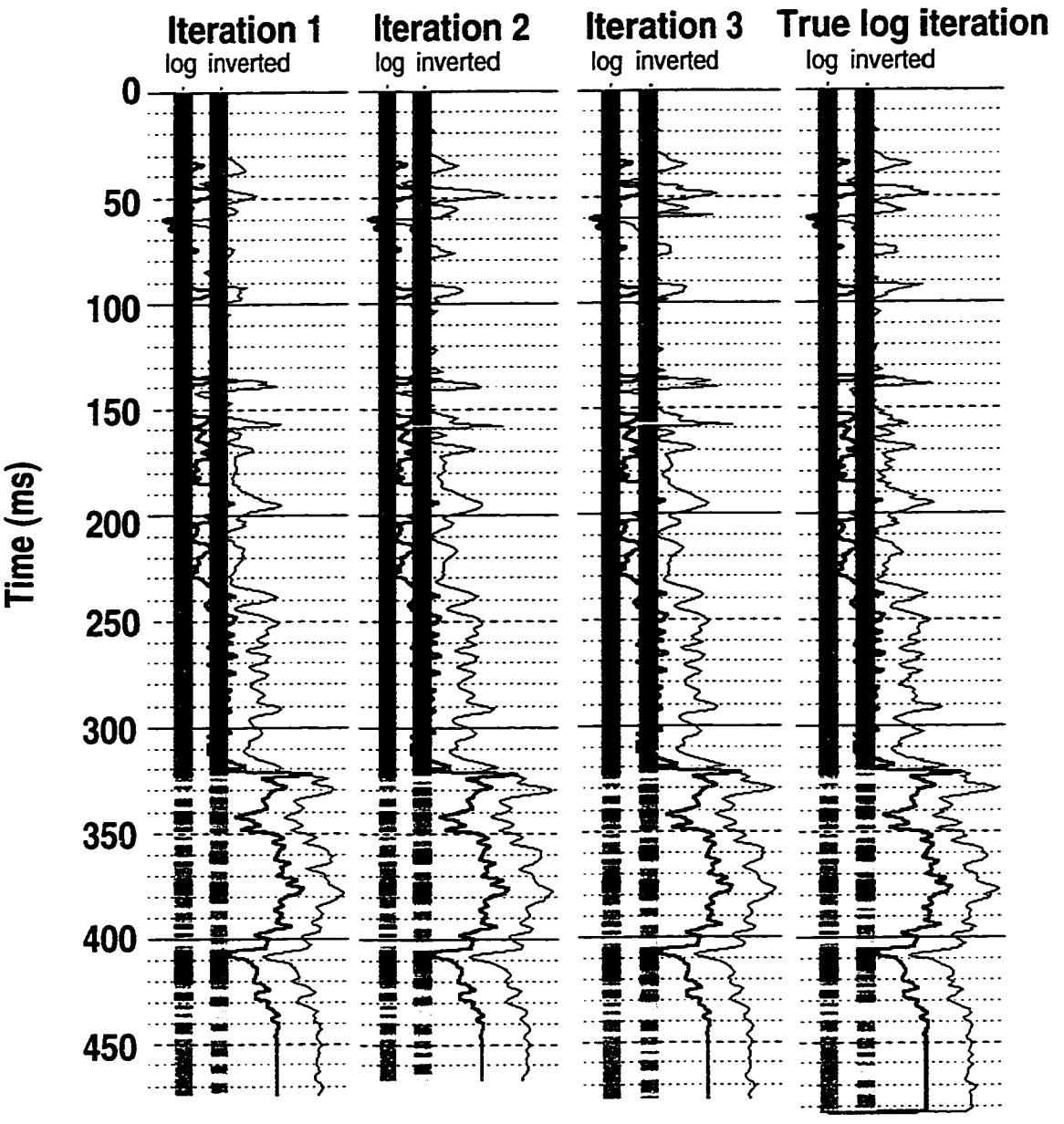

FIG. 7.14. Comparison of inverted *S*-wave impedance and impedance log through different iterations and an inversion using a real impedance log as a guide for modeling data.

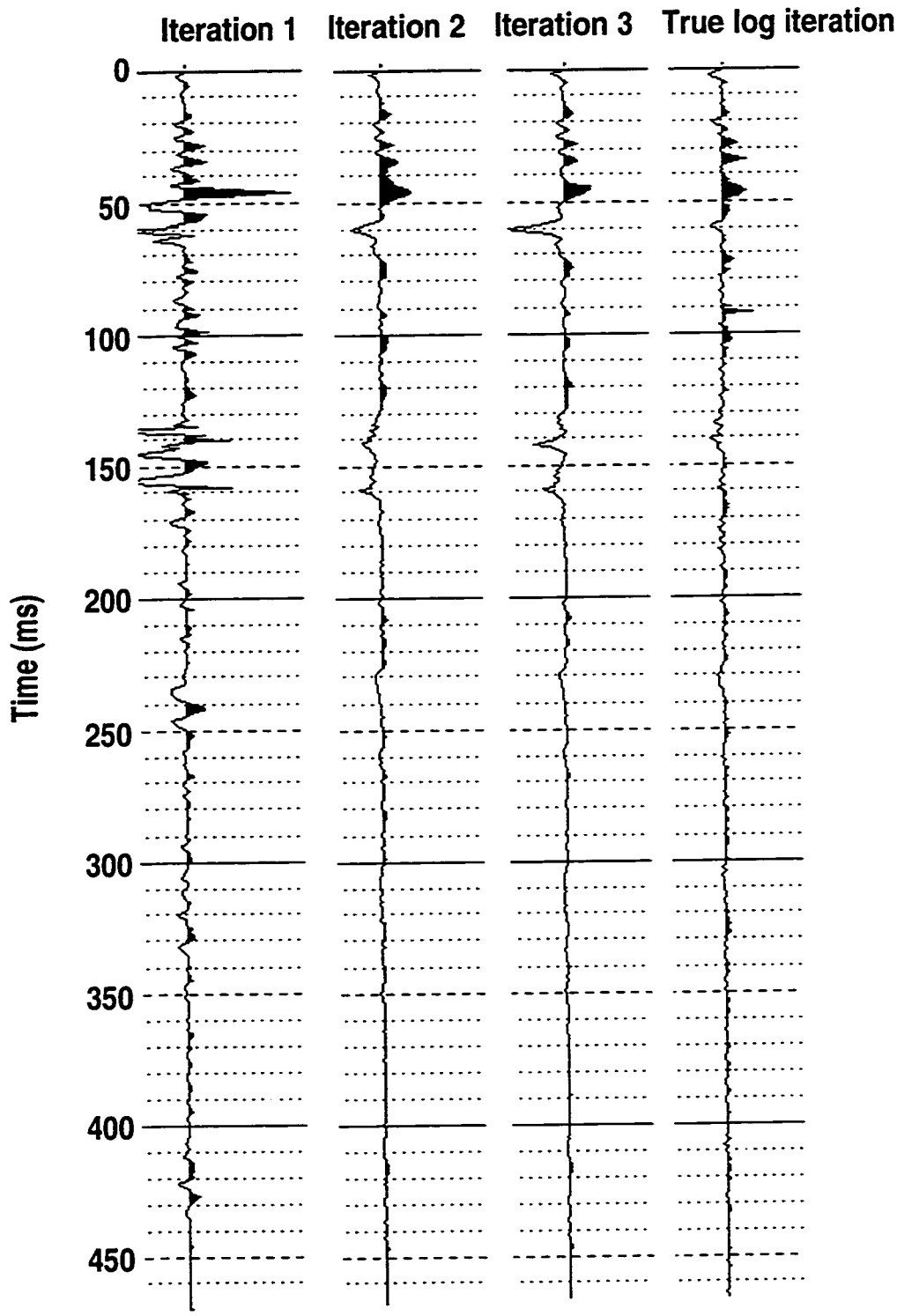

FIG. 7.15. Comparison of inversion error through different iterations; the error is calculated by subtracting *Rs* from a synthetic calculated from an inverted impedance.

compared to *P*-wave stack and converted shear-wave (*P*-*S*) stack. This 2-D line was also acquired with a conventional geophone array (an array of 6 geophones) for each station. Chapter 2 has detailed documentation of 3-C acquisition, processing, and interpretation. In this case study, comparison on AVO inversion will be made by using 3-C data versus conventional data.

7.4.1 True amplitude processing and geophone configurations

For AVO analysis true amplitude recovery on the pre-stack data is required. In fact, correct amplitude recovery is extremely important as the amplitude in each CDP gather significantly affects the final inversion results. Castagna (1993) summarized processing

Table 7.2. AVO true amplitude processing scheme.

1 True amplitude recovery
- Method: offset-varying spherical divergence correction
- Additional gain: 4dB/second

2 Surface consistent deconvolution
- Type: spiking
- Components: resolved: source, receiver, cdp, offset
  Applied: source, receiver
- Operator length: 80 ms
- Prewhitening: 0.01%
- Design window: 150-1300 ms at 0 m offset
  565-1345 ms at 690 m offset

3 Time-variant spectral whitening
- Balancing bandwidth: 2/8 - 200/220 Hz

4 Refraction statics
- Datum elevation: 600 m
- Replacement velocity: 1800 m/s
- Processing datum: floating
- Number of layers: 2

5 Velocity analysis

6 Surface consistent statics
- Method: stack power maximization
- Maximum allowed shift: 20 ms
- Correlation window: 250 - 1050 ms

7 NMO correction

8 CDP trim statics
- Trcaes in model: 7
- Maximum allowed shift: 8 ms
- Correlation window: 300-1000 ms

9 Surface consistent scaling

10 Shift to final datum

11 Construct AVO superbin
- 3 CDPs per bin, overlapping

12 AVO superbin stack
- Offset: 10-690 m
- Offset increament: 20 m
- Normalization: 1/sqrt(fold)

13 Bandpass filter (10/14 - 170/190 Hz)

14 Offset-invariant scaling (time-varying scalers computed from entire dataset)

schemes reported in the literature. Table 7.1 shows the processing sequence used for AVO data conditioning before inversion. It is similar to most processing sequences published in the literature. One step that is not often used in the literature is time-variant spectral whitening; and this is applied in the process (step 3) to retain the wide frequency bandwidth. Each CDP gather for AVO analysis was formed by 3 CDPs called a superbin, which has the lateral mixture of 10 m, while the original CDP interval was 5 m. Figure 7.16 shows 2 CDP superbin gathers of line 6y074 with and without TV spectral whitening applied. AVO effects can be seen on most reflection events. The high frequency content enables identification of reflections such as the C70. Though the offset collected in each CDP ranges from 10 to 690 m, poor data quality appears on the far-

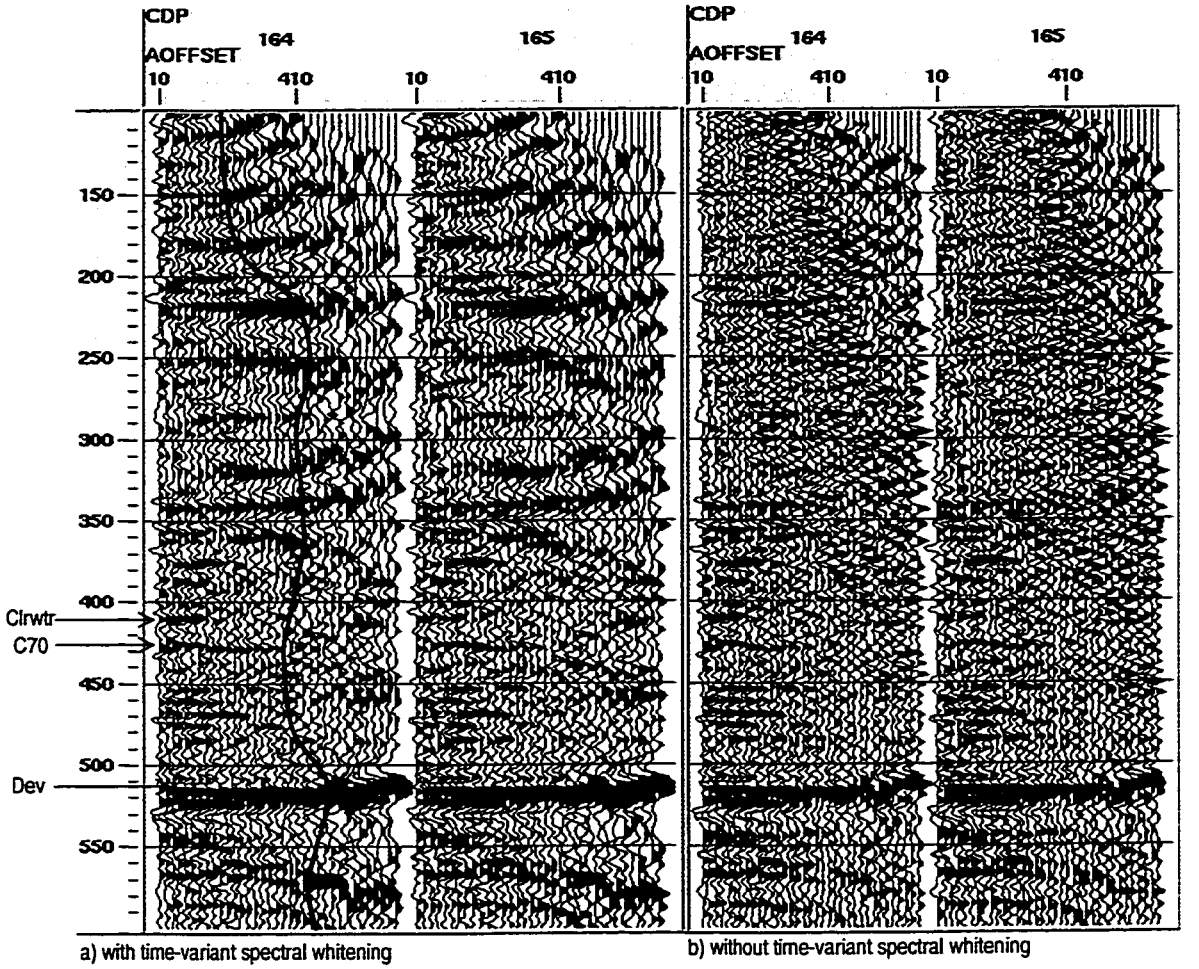

FIG. 7.16. Pre-stack AVO gathers from 3-C phones of line 6y074 with and without time-variant spectral whitening applied.

offset traces (right side of the blue line) due to NMO stretch or other factors such as anisotropy around the Colorado shale of the shallow section (see Figure 2.34). The gathers without time-variant spectral whitening looks noisier (ringing). In the lower part of the section the data with time-variant spectral whitening applied also looks better. It may not be safe to apply time-variant spectral whitening to the data for AVO analysis. It can alter the amplitude if the window of spectral whitening is too small. However, it can broaden the frequency bandwidth and cause no harm if the window is large enough.

The acquisition configuration allows us to make a comparison on effects of different geophone arrays. Conventional acquisition has a 6-geophone array for each station, while

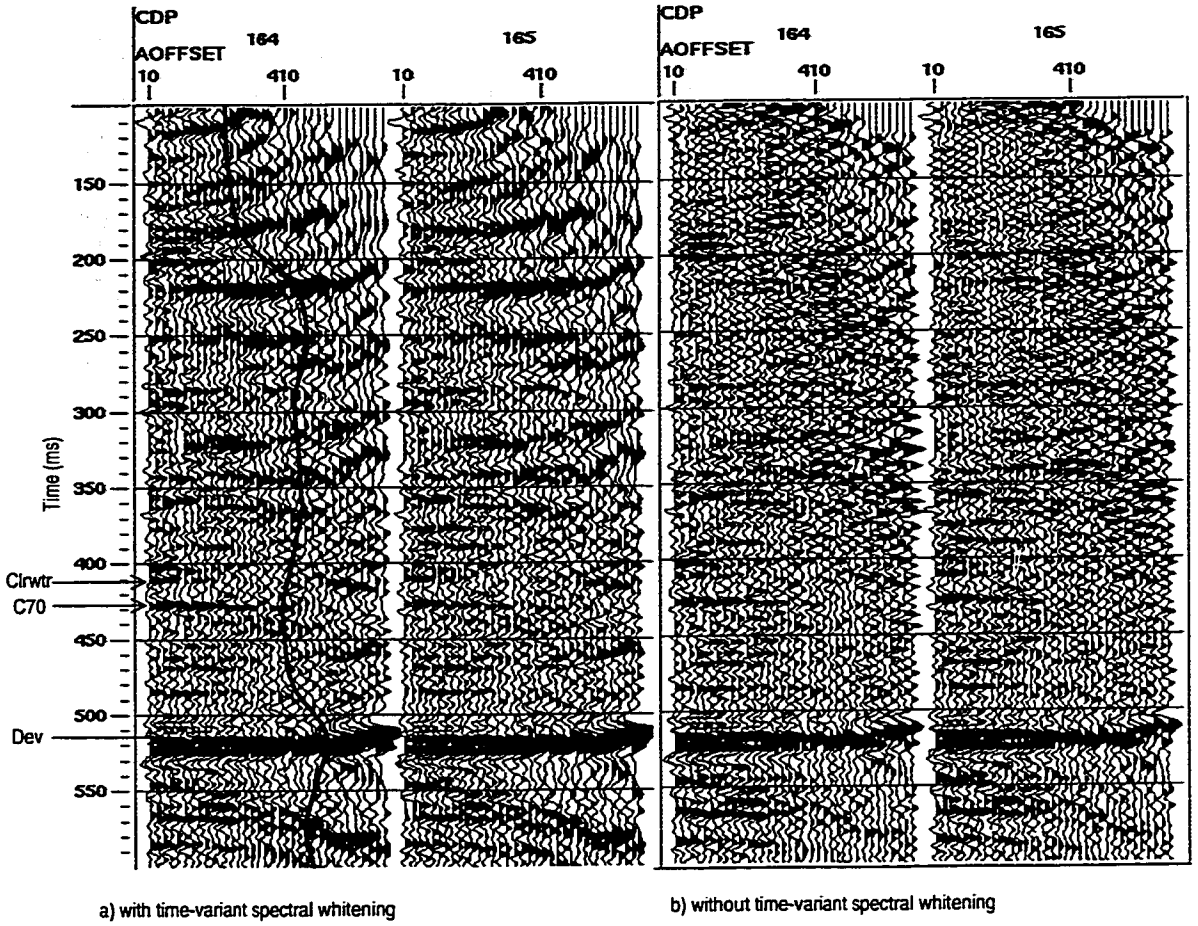

FIG. 7.17. Pre-stack AVO gathers from array of 6 phones of line 6y074 with and without time-variant spectral whitening applied.

3-component recording has a single geophone for each station. Figure 7.17 shows the AVO gathers from the same CDP locations as in Figure 7.16 using a 6-geophone array for

each station. A careful comparison indicates that conventional acquisition gives better signal-to-noise ratio. There is a subtle difference on frequency bandwidth. It seems that the 3-component acquisition provides higher frequency data (compare time window 300 to 500 ms).

If field acquisition geophone configuration makes a subtle difference on AVO gathers, processors can make a big difference by applying different processing streams and choosing different parameters. Figure 7.18 shows the same AVO gathers as in Figures 7.16 and 7.17 with true amplitude processing by a different processor. In this case there is

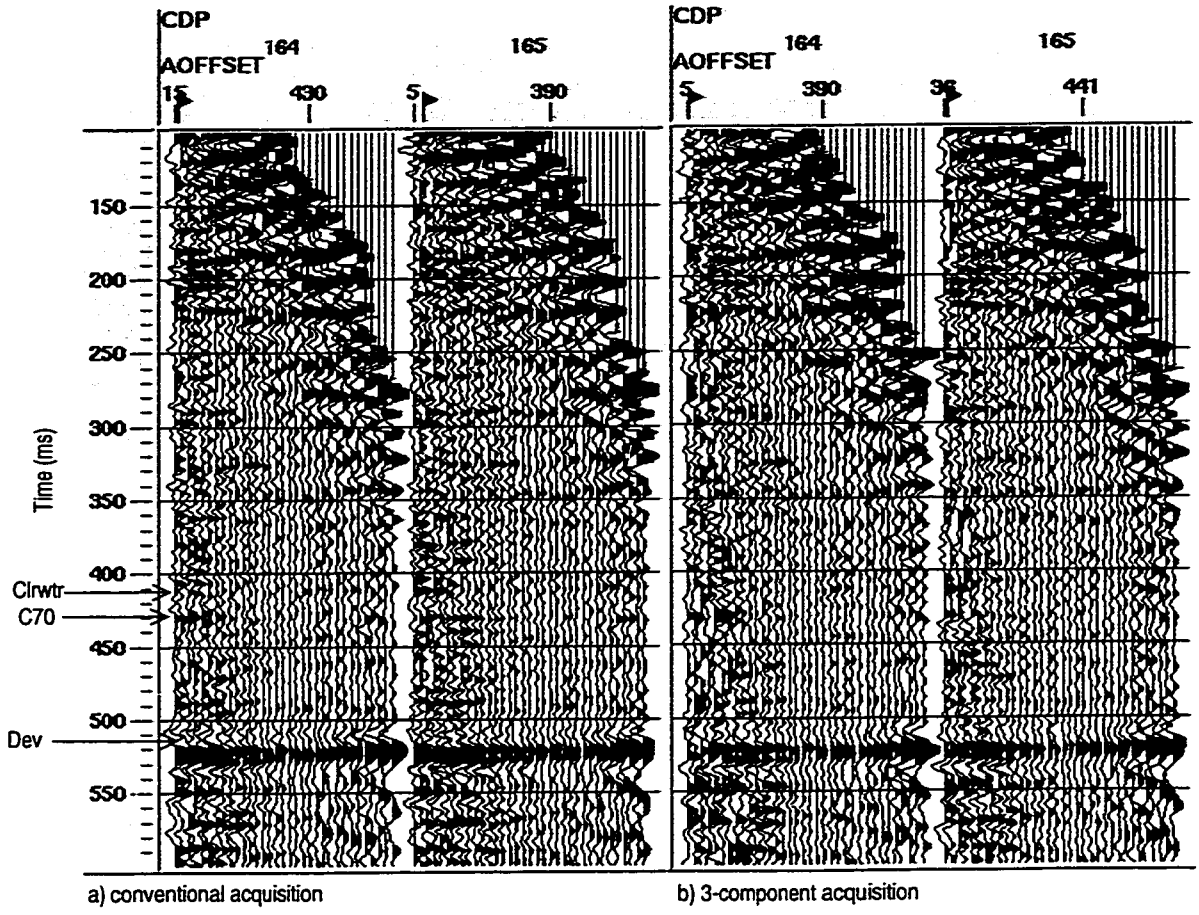

FIG. 7.18. True amplitude processing by a different processor for AVO gathers from array of 6 phones (a) and 3-component phones (b) of line 6y074 without time-variant spectral whitening applied.

a large difference between the conventional acquisition and the 3-component acquisition.

Near-offset noise (ground roll) on the 3-component acquisition was strong and not well handled. The amplitudes of most reflectors from 250 to 500 ms are not recovered. The frequency bandwidth is not as broad as previous processing.

7.4.2 Zero-offset *P*-wave stack (R_p) and psuedo *S*-wave stack (R_s) inversion

Following the algorithm discussed in section 7.3 of this chapter, equation (2.3) was used as the mud-rock line; inversions were tested with restriction of different incident angles (offsets) to be included in the inversion. On the one hand it is better and usually stablizes the solution to include more offsets when solving equation (7.10). On the other hand, far-offset data loses data quality as above discussed; final inverted results can be contaminated due to including poor quality far-offset traces. Figure 7.19 shows the inversion quality control test of different incident angles. As expected, by including more offsets (larger incident angle) both R_p and R_s show more continuous events and higher signal-to-noise ratio (see Figure 7.19 b and d). But more details are shown on the results using smaller incident angles (less offset traces included). This is easily seen within the Clearwater (clrwtr) formation (compare interval between clrwtr and C70). After a series of tests an incident angle of 38° was chosen for inverting all the data.

In reality, ray-tracing is implemented in the depth domain via time-to-depth conversion by using a velocity function. The horizontally layered media can be sampled as fine as one interface per time sample correspondent depth. This approach reaches the upper limit of the resolution in the data. It may take a much longer time for ray-tracing. Or the depth sampling can be coarser to two or more time samples correspondent depth. The difference of R_p stacks by using different sample intervals is relative subtle (see Figure 7.20). However, the difference of R_s stacks is larger (see Figure 7.21). Therefore, depth sampling is important to the final AVO inverted results, especially in getting better shear-wave information. The results from depth sampling of 2 time-samples correspondent depth interval in ray-tracing is as good as results from 1 time-sample correspondent depth interval. But the computing time is exponentially decreased; it took less than half of the

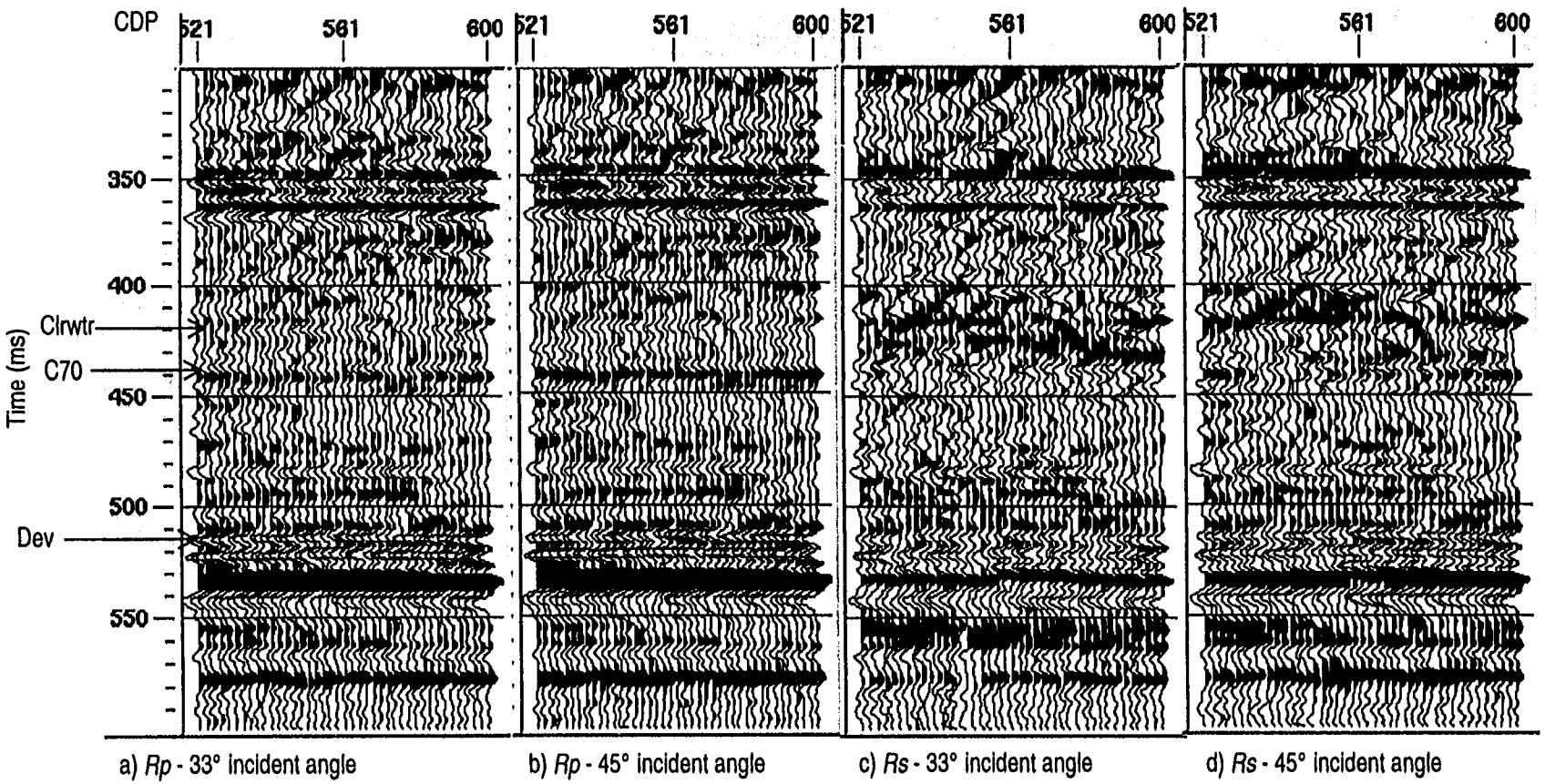

FIG. 7.19. Inverted R_p and R_s by using different incident angles for quality control.

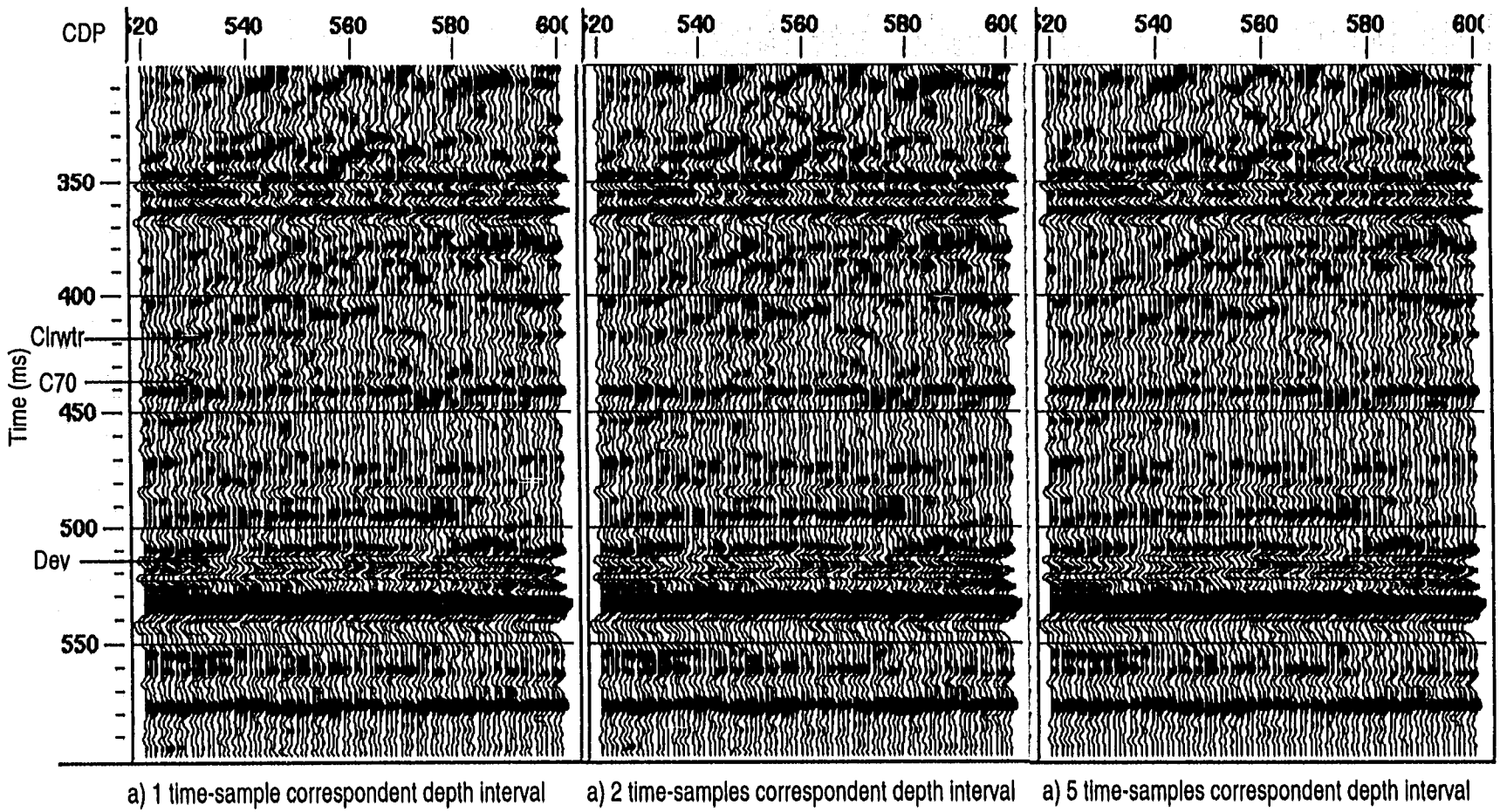

FIG. 7.20. Comparison of inverted R_p by using different depth sampling in ray-tracing.

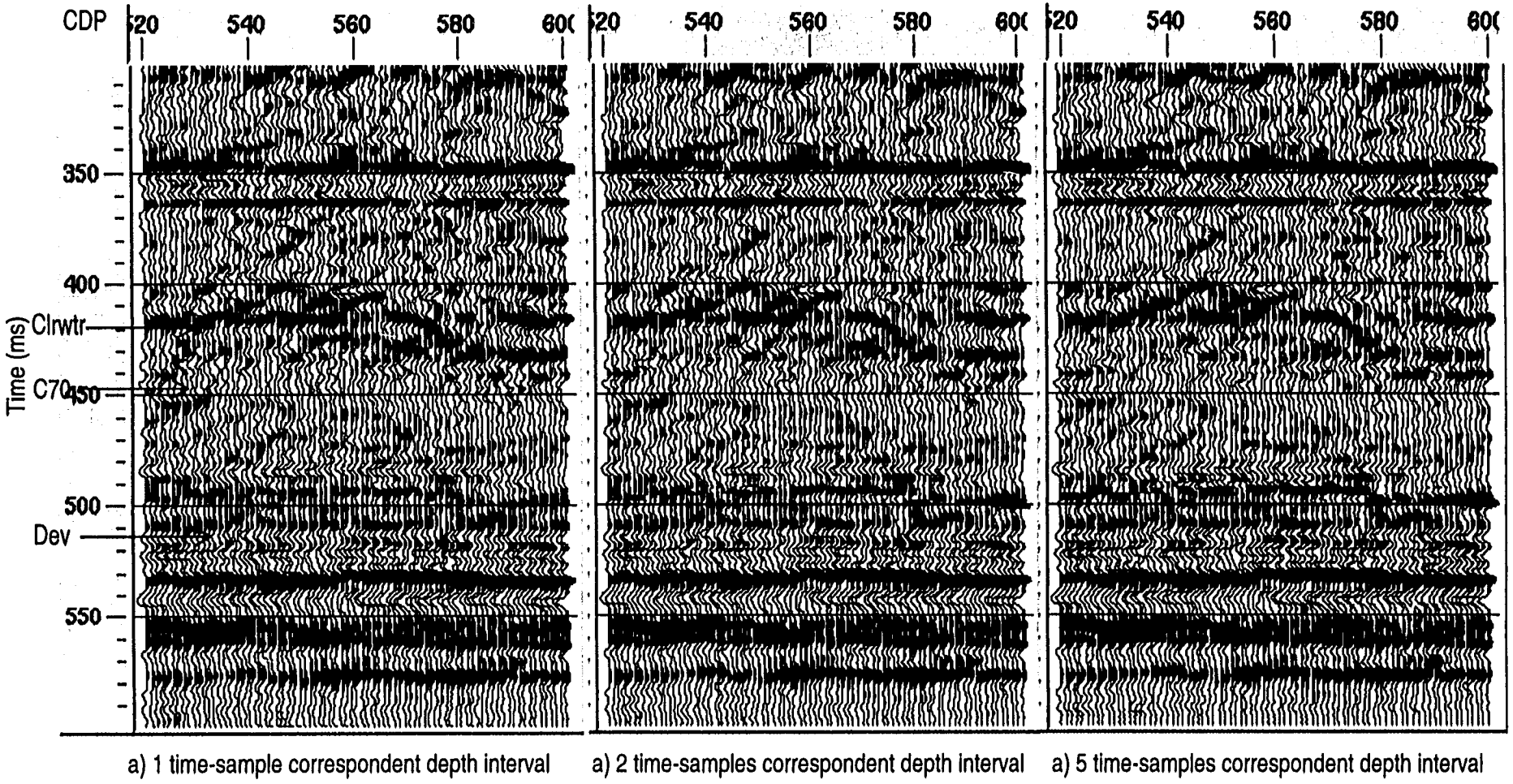

FIG. 7.21. Comparison of inverted R_s by using different depth sampling in ray-tracing.

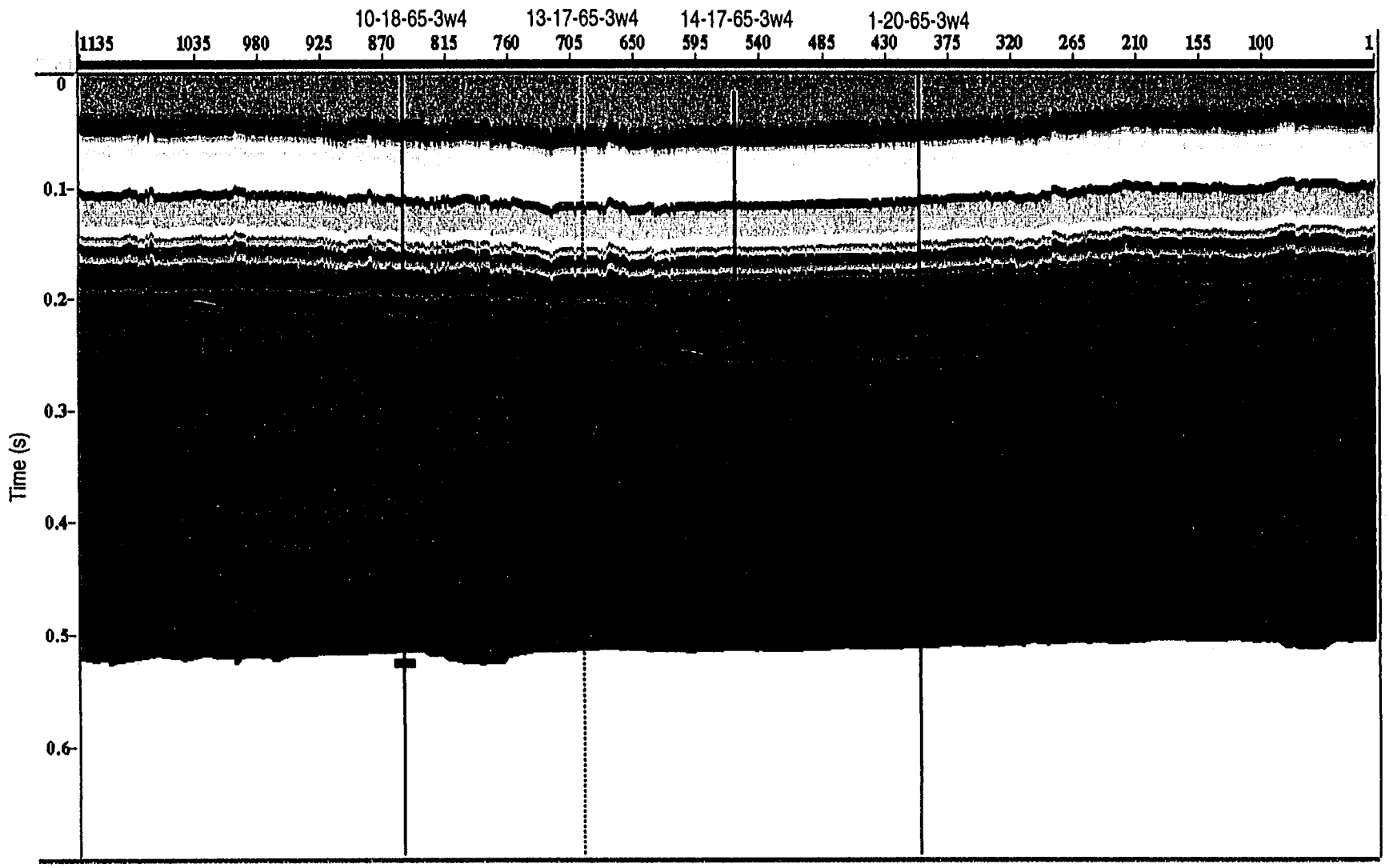

FIG. 7.22. Compressional-wave velocity model for AVO ray-tracing and inversion.

computing time to finish ray-tracing the model of sampling of 2 time samples correspondent depth interval. A velocity model was built using sonic logs from wells (see Figure 2.22). The quality control was made on sonic and density logs before they were tied to seismic interpretation. Velocity at each trace location was obtained by stratigraphic layer-wise interpolation of sonic logs. The interpolation was done using distance-based interpolation schemes - inverse distance weighted. All well interpolation weights decrease with the inverse distance and are exactly zero at the other well positions. The interpolation scheme relies on the x/y coordinates where the wells intersect the layers, which are used as centers for the inverse distance weighting.

Shown in Figure 7.23 are the *P*-wave stack sections from inversion (R_p, zero-offset stack) and regular processing (time shift due to 100 ms user statics applied). Major reflectors are

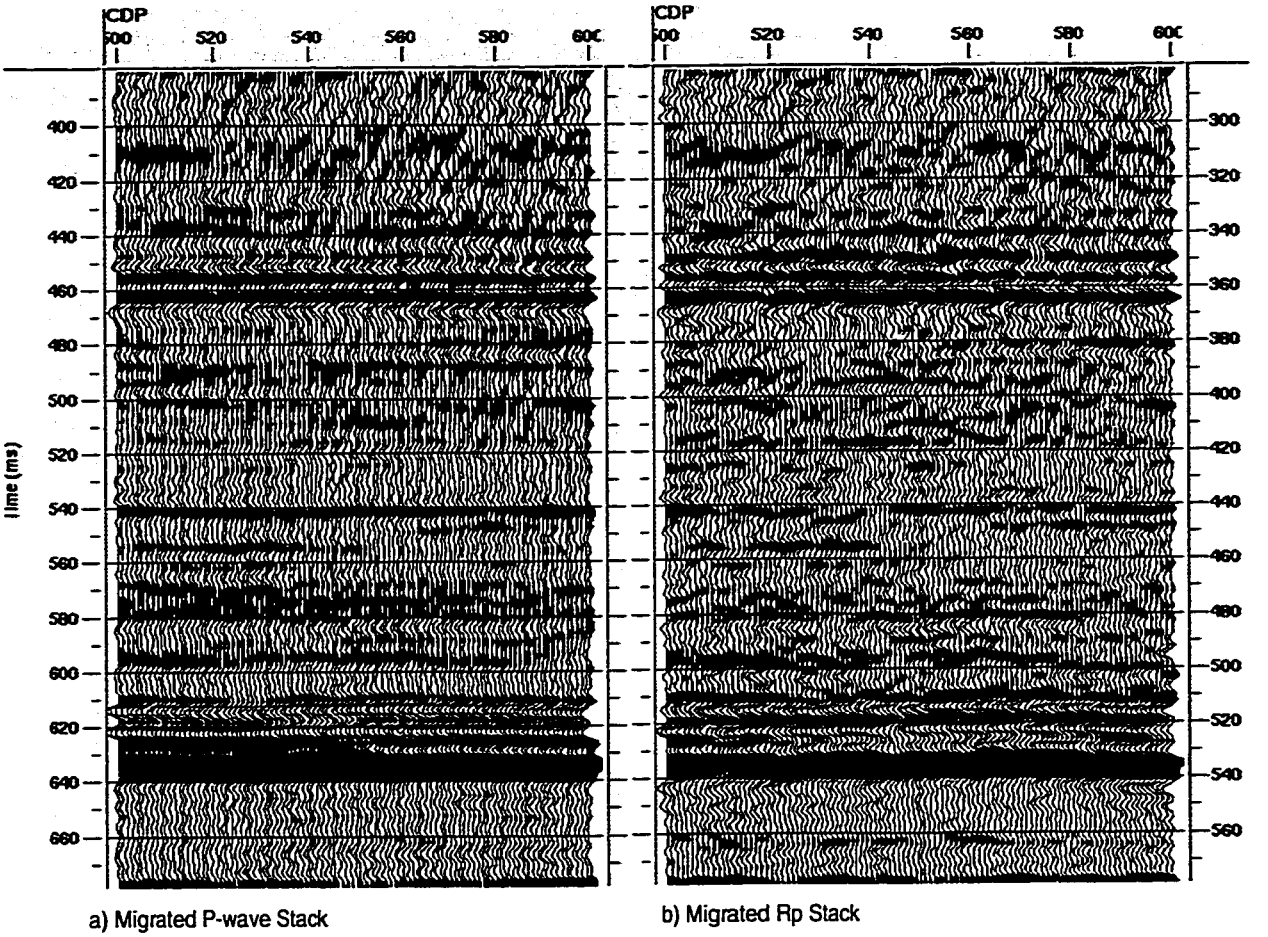

FIG. 7.23. Comparison of inverted zero-offset *P*-wave stack (R_p) with processed *P*-wave stack.

similar. Reflection events are more continuous on the processed stack than on the inverted stack. However, the inverted stack has a slightly higher resolution, which agrees, in theory, with the zero-offset stack (AVO effects were removed in stack). Figure 7.24 shows the comparison of inverted psuedo S-wave stack (R_s) with converted *S*-wave (*P-S*) processed from 3-component data. The appearance of the data looks very different as the frequency contents of the two panels are very different, and *P-S* wave is a processed field measurement of shear information, while R_s is a calculated one. But the major reflection events tie to each other fairly well. The advantage of inverting R_s is that it has direct tie to the *P*-wave data such as R_p. The disadvantage is that it is not a measured, but calculated. True amplitude processing, mud-rock line, velocity model, and other assumptions such as V_p/V_s ratio can potentially bring in errors and cause damage to the final results.

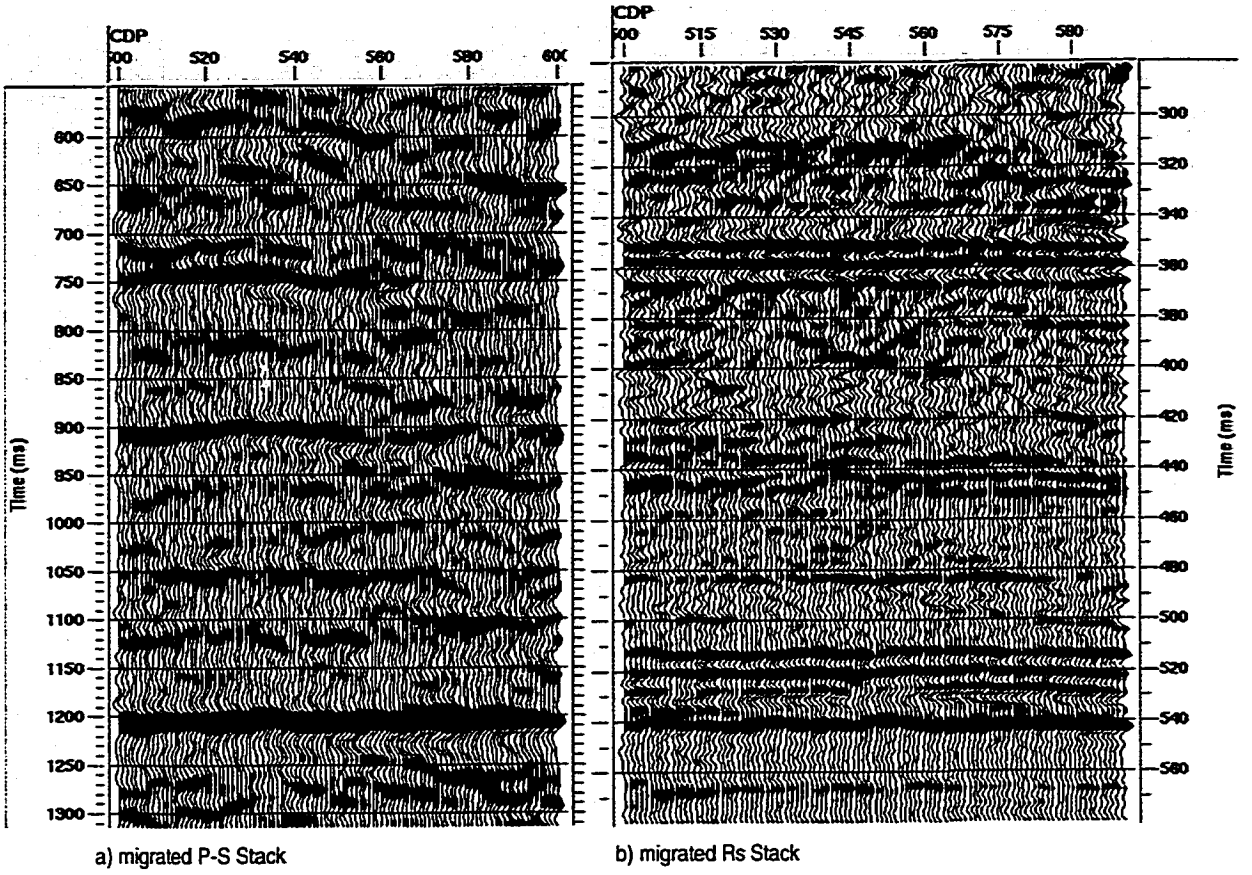

FIG. 7.24. Comparison of inverted zero-offset *S*-wave stack (R_s) with processed *P-S* wave stack.

7.4.3 Fluid factor and reservoir heterogeneity

Using mud-rock line by Castagna et al (1985), Smith and Gidlow (1987) define the fluid factor as:

$$\Delta F = \frac{\Delta V_P}{V_P} - 1.16\frac{V_S}{V_P}\frac{\Delta V_S}{V_S}. \tag{7.12}$$

Mud-rock line for Cold Lake (see chapter 2) can be generalized in the following format

$$V_P = CV_S^a. \tag{7.13}$$

Taking the derivative on both sides of equation (7.13), the following relation can be obtained

$$\Delta V_P = CaV_S^{a-1}\Delta V_S. \tag{7.14}$$

P-wave and *S*-wave velocity gradient are related as follows when dividing equation (7.14) by equation (7.13) on both sides

$$\frac{\Delta V_P}{V_P} = a\frac{\Delta V_S}{V_S}. \tag{7.15}$$

We note that regular Cold Lake clastic silicates should lie close to this line. Shale and steam invaded oil sand may deviate from this line, as shale has exceptional low shear velocity in such shallow reservoir and *P*-wave velocity is significantly reduced and *S*-wave velocity is hardly affected in the steam zone. The term 'fluid factor' was originally used by Smith and Gidlow to differentiate gas saturated sand from water-bearing sand. For reservoir heterogeneity study and reservoir monitoring, a similar convention is followed to define the Cold Lake 'fluid factor' as

$$\Delta F = \frac{\Delta V_P}{V_P} - a\frac{\Delta V_S}{V_S}. \tag{7.16}$$

To relate fluid factor to R_p and R_s an approximation can be made by using equations (7.3) and (7.4).

$$\Delta F \approx 2(R_P - a\,R_S) - (1-a)\frac{\Delta\rho}{\rho} \tag{7.17}$$

In the Clearwater reservoir interval, the densities of shale and oil sand are very close to each other. This density change can be ignored and the last term of equation (7.17) can be dropped, which indicates that the fluid factor can be easily obtained in such case.

Shown in Figure 7.25 is the 'fluid factor' from AVO inversion, assuming the density is unchanged, which is true in the reservoir interval. Green and yellow colors represent good permeable sand which is either reservoir (high resistivity) or water zone (low resistivity). Blue and brown (including white) colors represent shale or muddy zones. The SP and resistivity logs of well OV10-18-65-3w4 are tied to the 'fluid factor' section. It is clear that the 'fluid factor' identifies good reservoir (some of C70 and upper part of C50) where

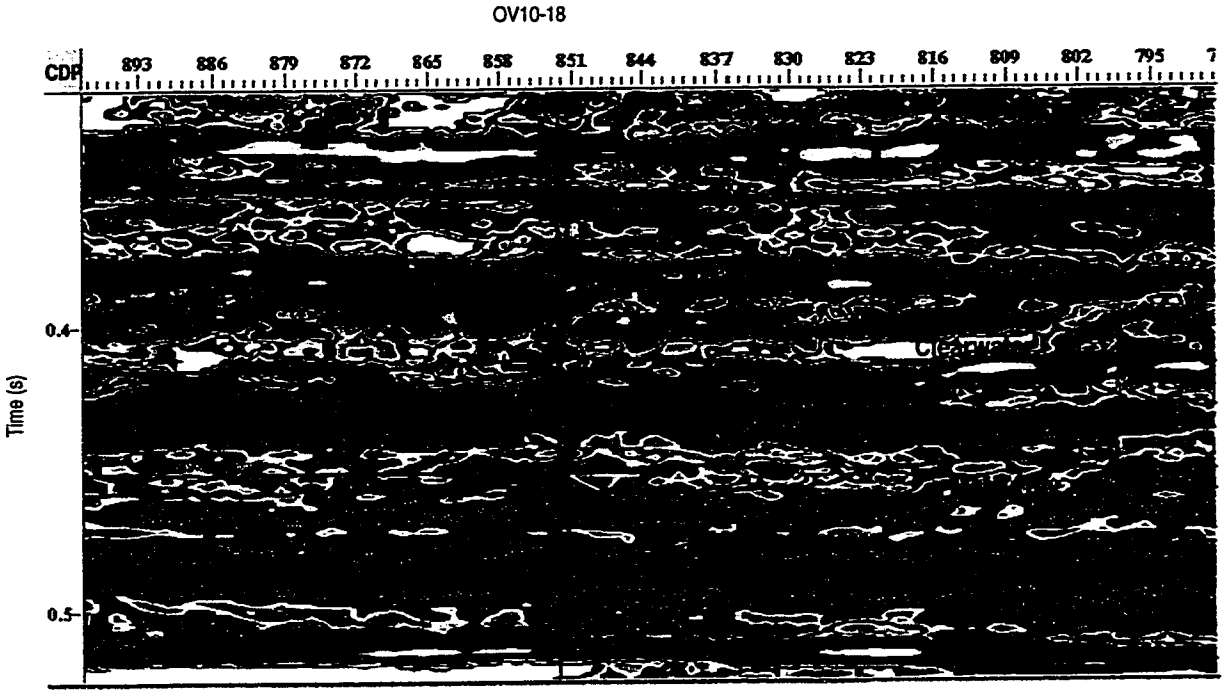

FIG. 7.25. 'Fluid factor' for the portion of line 6y074 around vertical well OV10-18-65-3w4. No post-stack processing applied. Red curve is SP log, and black curve is resistivity log.

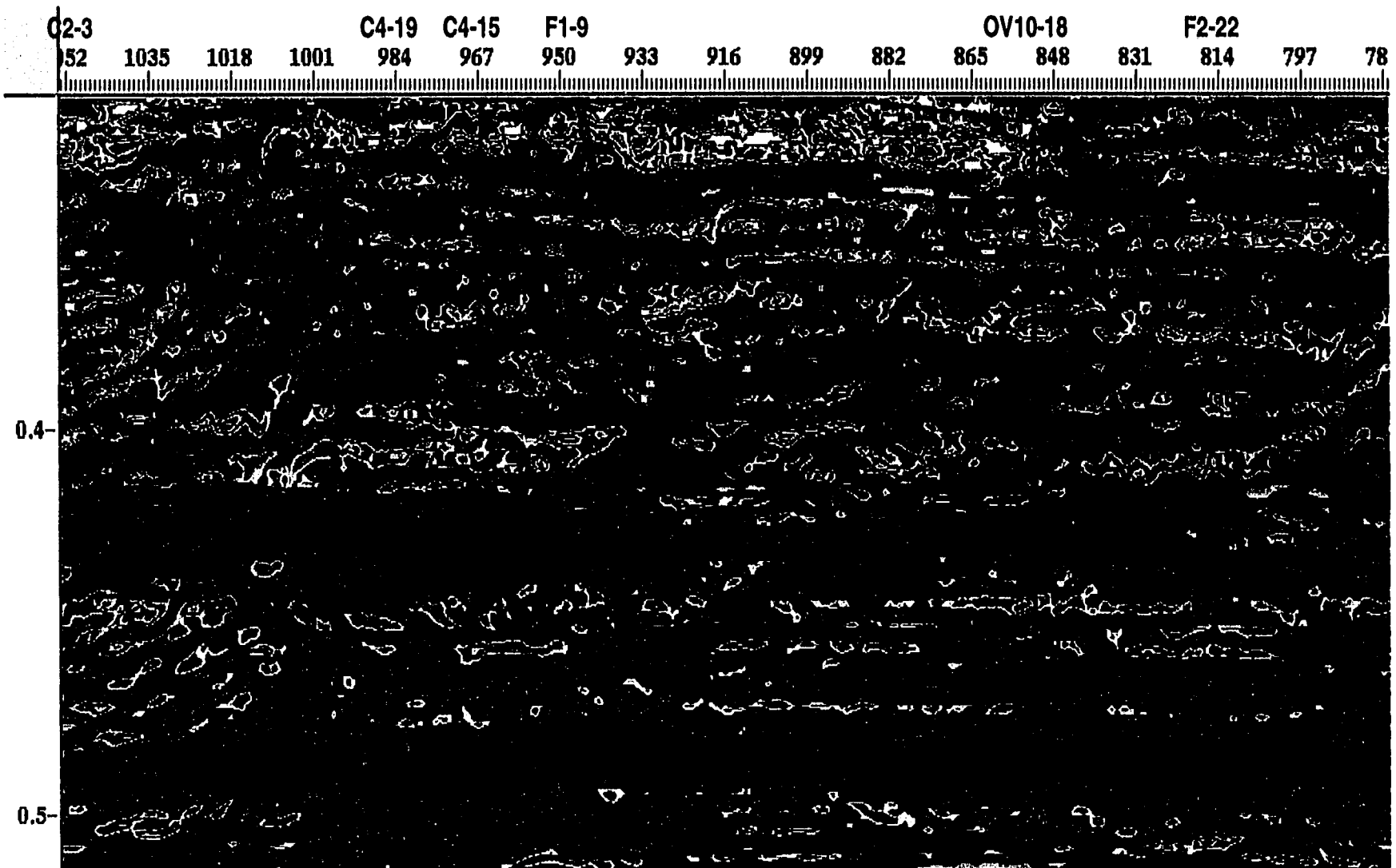

FIG. 7.26. 'Fluid factor' for the portion of line 6y074 with dense well control. Post-stack migration applied. Well-paths are out of section plane except OV10-18.

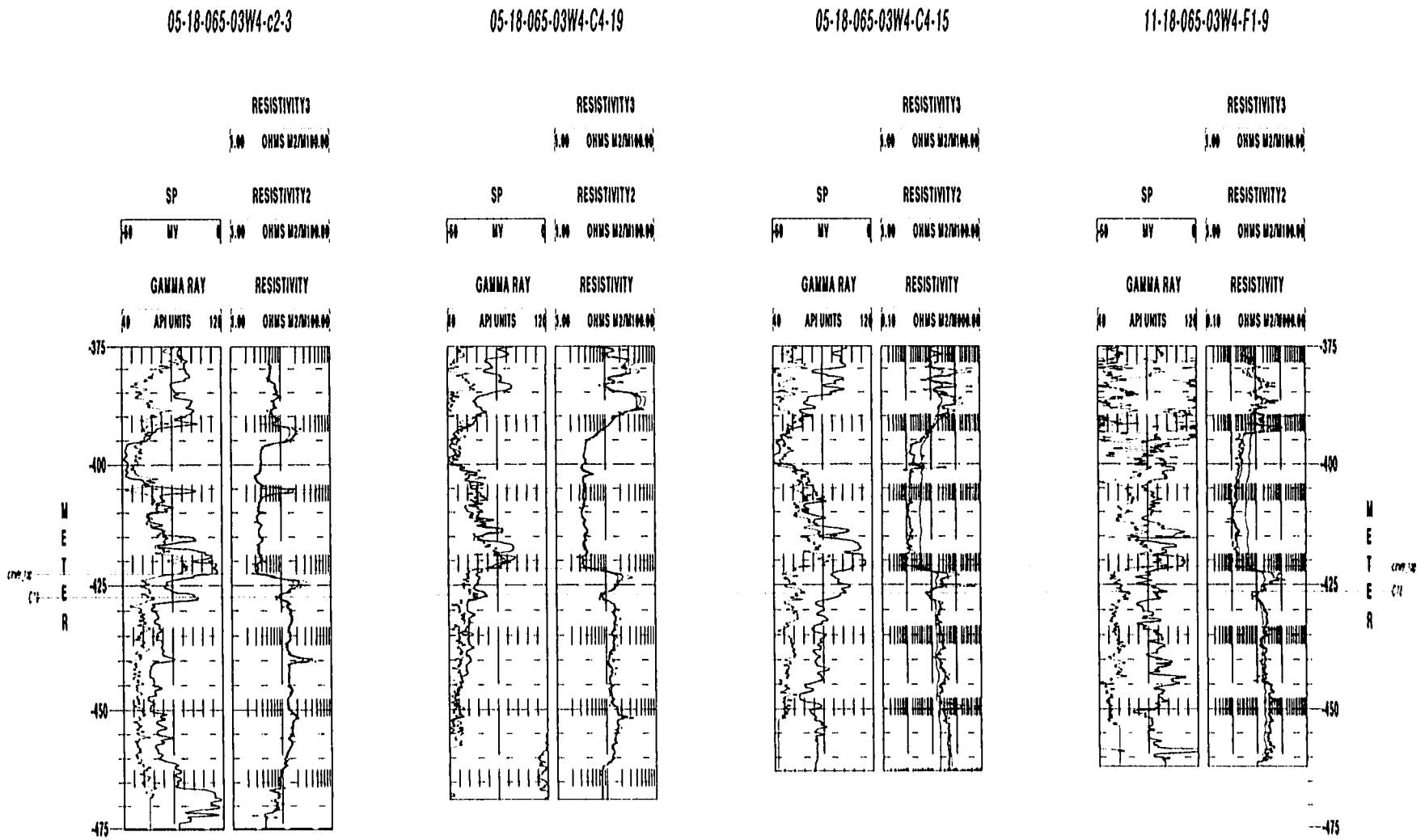

FIG. 7.27. SP, Gamma Ray, and resistivity logs for the four wells correspondent to the left four wells of Figure 7.26, showing reservoir is shaly in well F1-9.

the resistivity shows high values. Also, it ties to the McMurray water zone quite well where SP log shows permeability (anomaly) and resistivity is quiet (no anomaly). Figure 7.26 shows the tie of well to 'fluid factor' for the half of line 6y074 where wells are available from production pads (see Figure 2.16). According to the 'fluid factor' well F1-9 encountered poor reservoir quality. This was tied to the drilling results. Figure 7.27 shows a section built by using SP, Gamma Ray, and resistivity logs with left four wells included. The SP curve of well F1-9 certainly shows that it is shaley or muddy at that location.

7.5 Reservoir monitoring

AVO inversion technique is applied to time-lapse 3-D seismic surveys (1990 versus 1992) at D3 pad. D3 pad seismic surveys were the early pilot studies for time-lapse seismic monitoring in the Cold Lake Production Project.

The D3 pad surveys consisted of 296 geophones (buried to a depth of 10 m to improve the frequency bandwidth, experimental repeatability, and reduce surface noise) and 215 shot points (buried 12 m). The first survey was shot in April 1990, during the sixth cyclic steam stimulation (CSS) production phase. During the production phase reservoir pressure and temperature are at a local minimum. The second survey was shot in January 1992 during the eighth steam injection phase. During the steam injection phase reservoir pressure and temperature are at local maximum.

Rock physics analysis shows the velocities of a steam invaded zone significantly deviates from the Cold Lake mud-rock line (see Figure 2.8c). AVO inversion was conducted on the above time-lapse seismic survey data sets. A significant advantage of using AVO inversion for time-lapse seismic data analysis is that wavelets are removed independently from each data set. Data normalization is no longer an issue.

The velocity model was built by using sonic logs from observation wells D3-OB1 to D3-OB4 and production well D3-08 (see Figure 2.33) by applying similar interpolation schemes as discussed early in this chapter. All the wells with velocity data available are

restricted in the center of the survey area, but the survey area is small and the velocity model is probably valid for the whole area. There is no shear-wave log available in the survey area. The general mud-rock line for Cold Lake (see chapter 2 for detail) is used in this inversion.

The super CDP gather for AVO analysis at each CDP location was formed from 5-by-5

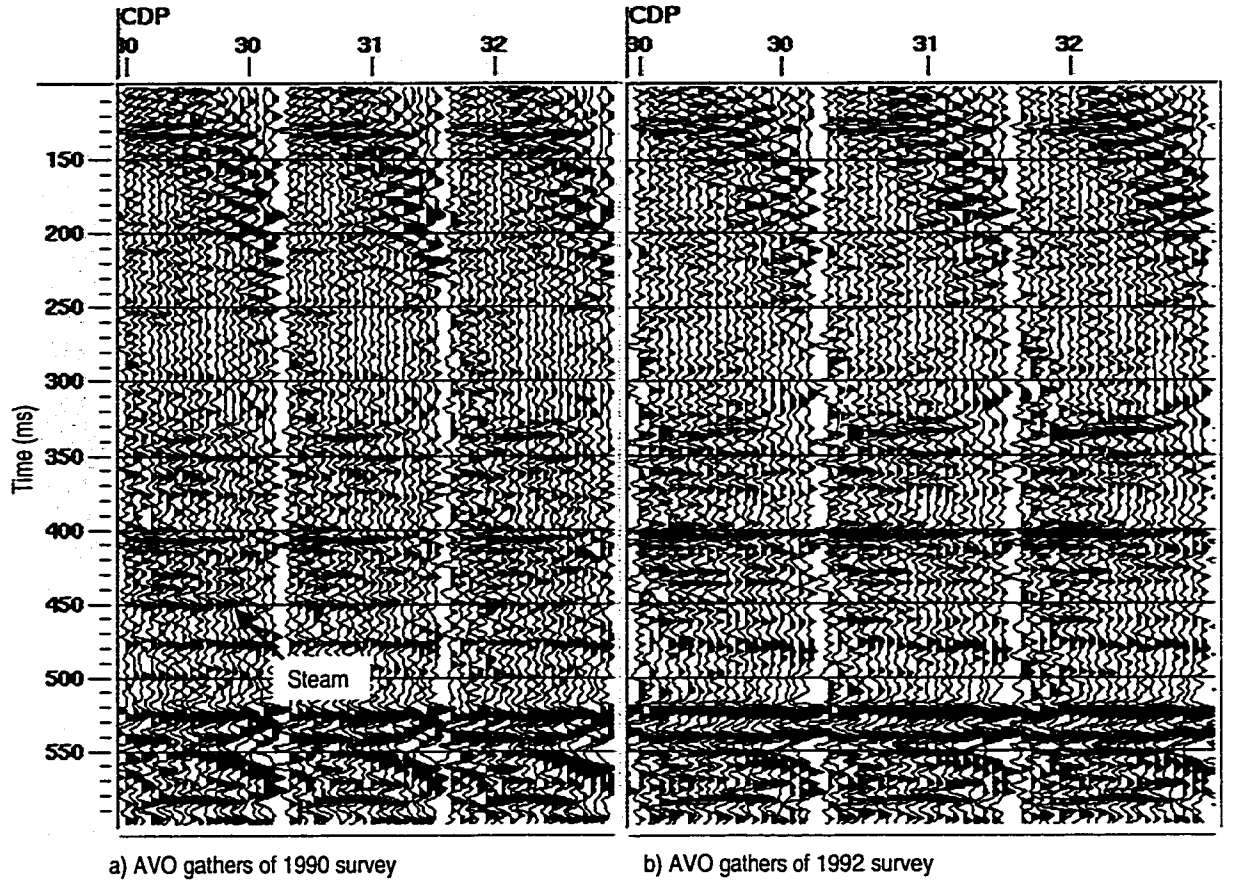

FIG. 7.28. Time-lapse AVO gathers from inline 48 of D3 pad surveys.

CDPs. Figure 7.28 shows time-lapse AVO gathers from inline 48. The amplitude anomaly labeled 'steam' shown on the survey of 1990, but not on the survey of 1992, is caused by a low velocity interval of heated reservoir.

Figure 7.29 shows a north-south cross-section of inverted fluid factor volume along wells D3-3, D3-8, D3-13, and D3-18 (see Figure 2.33). In the steam invaded zone, the *P*-wave

velocity is reduced, while the *S*-wave velocity remains almost the same. The velocity on V_p/V_s versus V_s cross-plot falls below the mud-rock line (see Figure 2.8c for details). As referred to equation (7.16), fluid factor is negative in value within Clearwater reservoir

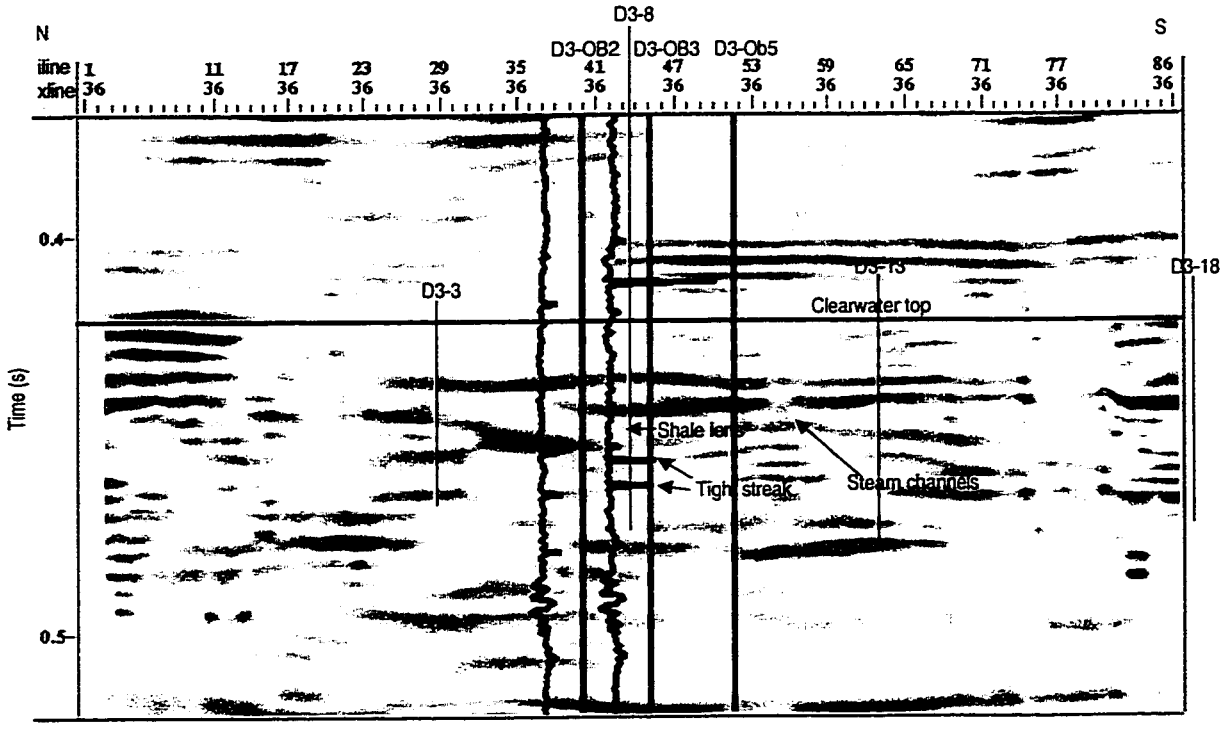

FIG. 7.29. Fluid factor section of 1990 survey along north-south direction of wells D3-3 to D3-18 (cross-line 36).

(black or gray color in Figure 7.29). In shale or muddy zones the *S*-wave velocity is decreased, while the *P*-wave velocity is hardly changed; therefore, the fluid factor is positive in value (see Figure 7.29). Velocities of tight streaks stay above the mud-rock line (see Figure 2.8c for details), therefore, the fluid factor of tight streaks is positive (see Figure 7.29).

Shown in Figure 7.30 is the same fluid factor section but from the 1992 survey (during the steam injection phase). It is plotted in the same scale as Figure 7.29. Though the magnitudes of the fluid factor between the two surveys are different, lithologic characteristics remain unchanged. However, steam channels no longer appear on the section.

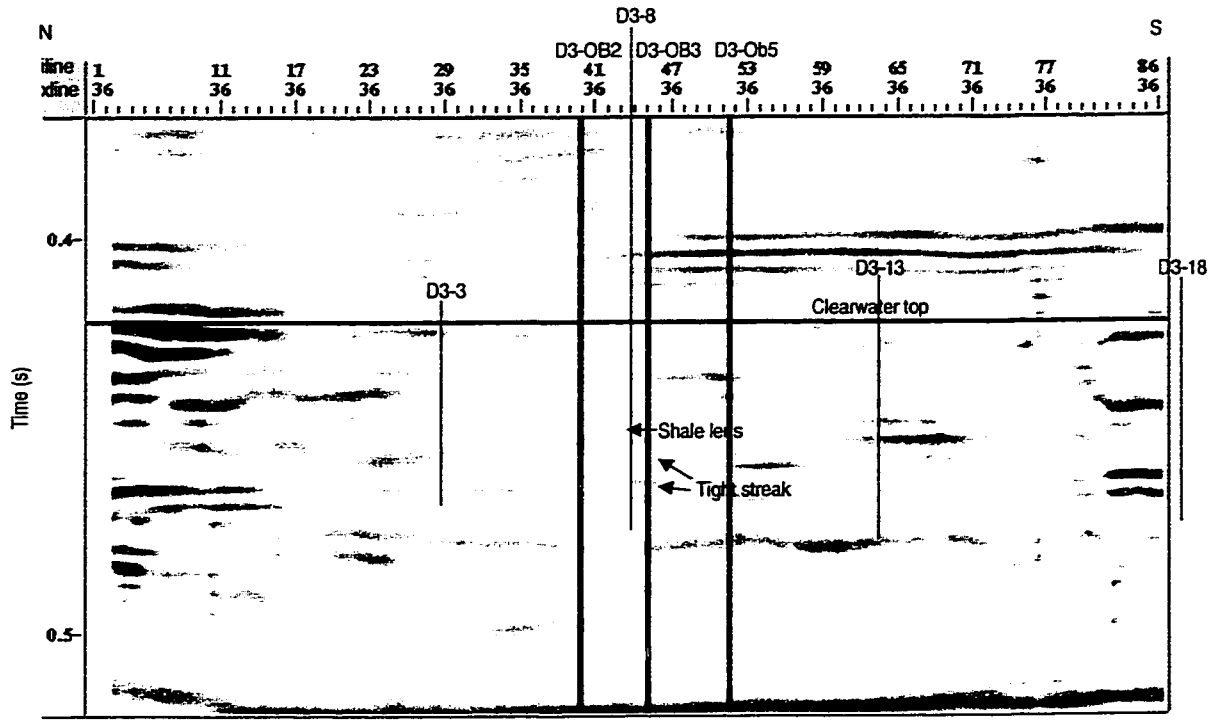

FIG. 7.30. Fluid factor section of 1992 survey along north-south direction of wells D3-3 to D3-18 (cross-line 36).

7.6 Conclusions and discussions

The theoretical studies and modeling suggest that the reformulated Aki and Richards' approximation of the Zoeppritz equation is sufficient for AVO inversion for the Cold Lake reservoir. For a shallow reservoir, such as the Cold Lake Clearwater formation, it is a very poor assumption to assume V_p-to-V_s ratio equals 2. A significant error is introduced in the estimation of zero-offset *P*-wave stack (R_p) and psuedo *S*-wave stack (R_s) when assuming that V_p-to-V_s ratio is 2 and $\sin\theta$ equals $\tan\theta$. Ray-tracing is required for obtaining proper incident angle and better inversion results.

In the inverse process the critical angle (or maximum reflection angle) at the reservoir level reaches as high as 65°, which indicates offsets of more 700 m can be included in the inversion. However, due to NMO stretch and anisotropy in the shallow, the maximum reflection angle used is 38°, which approximately corresponds to offsets between 400 m to 500 m at the reservoir depth.

Modeling suggest that iterative inversion through resolving *P*-wave and *S*-wave impedance can significantly improve the solution of R_s, which in turn improves the final inversion results.

In practice, true amplitude processing is the first key step for successful AVO inversion. However, different processors can make quite a difference. Large window time-variant spectral whitening can improve the signal and does minimum damage to the true amplitude recovery. In general, 3-component recording is as good as geophone array for AVO analysis. But the result using geophone array data is smoother.

The inverted *P*-wave is similar to the regular processed *P*-wave stack with slightly higher resolution, but not as continuous as the regular processed *P*-wave stack. However, the inverted psuedo *S*-wave has much higher resolution than the *P-S* wave data. With optimized mud-rock line and high frequency seismic data, reservoir heterogeneity can be well defined by fluid factor alone. The application of this technique to reservoir monitoring defines steam channels and identifies lithological barriers within the reservoir.

Chapter 8 – Conclusions and future work

8.1 Summary

The main goal of this dissertation has been to extend the current state of heavy oil reservoir monitoring and characterization.

Based on statistic (discriminant) analysis of conventional seismic attributes, a quantitative cross-calibration and cross-training stream has been developed for time-lapse seismic data analysis using data normalization as a bridge. This cross-calibration or cross-training provides better, more stable, and consistent results than independent training for reservoir monitoring. It was found that multi-trace operator derived from unchanged reservoir provides best data normalization.

To compensate for the redundancy of conventional seismic attributes, seismic attributes calculated from principal component decomposition of the seismic data are developed and used in the discriminant analysis for reservoir monitoring. These attributes produced better results than conventional attributes at A2A4 and J1J8 monitoring projects. To achieve this superior result, it was necessary to include a full set of principal component attributes. To minimize the dependence on the seismic data sets, time-lapse data sets were analyzed by merging two data sets together. The principal components were extracted from merged data set, and attributes were calculated separately from individual survey. A significant improvement has been made on time-lapse data analysis by applying this technique.

Since time-lapse data normalization is no longer required as wavelets are extracted independently from each data set, post-stack inversion is applied to time-lapse seismic datasets of B2456. The vertical conformance reveals that sequence architecture has significant influence on steam migration. A sequence with high mud content tends to limit or slow both the vertical and horizontal migration of the steam chamber.

Shear-wave information is useful for both reservoir characterization such as mapping heterogeneity and monitoring such as mapping fluid. Shear-wave information can be obtained in many ways: converted shear-wave and AVO inverted shear information. Integrated surface 2-D seismic and borehole VSP *P*- and converted *S*-wave studies have illustrated that the task of differentiating lithology and identifying fluid can be fulfilled by integrating *P*- and *S*-wave information. However, the resolution of surface *P-S* wave data is not high enough to resolve the detail required. 3-D 3-component VSP is the tool that will meet this need. The dissertation illustrated 3-D VSP survey design and processing technique.

3-D VSP binning has both characteristics of VSP and surface 3-D seismic. Surface geometry is used to determine the bin size and bin azimuth. The surface receiver interval (for RVSP) or shot interval (for VSP) is the key factor of influencing the bin fold. The number of downhole positions (either source or receiver) is the major parameter for the bin size. Changing the number of the downhole locations or the tool interval does not have much influence on the distribution of the bin fold. The analytical NMO correction and binning algorithm works reasonably well except for the shallow events. However, for the very shallow reservoir or structure area, a ray tracing binning, and stacking algorithm is required for a proper stack section.

The functional relation of *P*- to *S*-wave velocities, called mud-rock line, plays an important rule in extracting *S*-wave information from pre-stack data. The mud-rock line established from *in-situ P*- and *S*-wave velocity measurement is the optimized for Cold Lake clastic rocks. It is an exponential relationship between *P*- and *S*-wave velocity. This study provided insights on the feasibility of using AVO inversion to differentiate shale from sandstone and reservoir fluid monitoring. The inverted *P*-wave is similar to the regular processed *P*-wave stack with slightly higher resolution, but not as continuous as the regular processed *P*-wave stack. However, the inverted psuedo *S*-wave has much higher resolution than the *P-S* wave data. With optimized mud-rock line and high frequency seismic data, reservoir heterogeneity can be well defined by fluid factor alone.

The application of this technique to reservoir monitoring defines steam channels and identifies lithological barriers within the reservoir.

8.2 Future work

More work is needed to add into 3-D VSP processing techniques in Chapter 3 such as pre-stack time and depth domain migration. Since the signal-to-noise ratio of D3 pad RVSP data has been improved after f-x deconvolution. A comparison should be made between surface 3-D seismic and 3-D RVSP.

In the AVO analysis, pre-stack migration with amplitude preservation improves the inversion results in structured area. Cold Lake geology is relatively flat. It is believed that pre-stack migration will improve the reservoir heterogeneity study and steam monitoring.

References

Aki, K. and Richards P. G., 1979, Quantitative Seismology, W. H. Freeman & Co.

Aleotti, L., Gallori, A., Miranda, F., Craglietto, A., Persoglia, S., Poletto, F., Impact of drill-bit seismic method on explorative wells: Presented at the **56**th Ann. Mtg., Europ. Assn. Explor. Geophys., Vienna.

Batycky, J. P., Leaute, R. P., and Dawe, B. A., 1997, A mechanistic model of cyclic steam stimulation: SPE International Conference on Thermal Operation and Heavy Oil Symposium, Bakersfield, California, U.S.A., 1997.

Boone, T. J., Youck, D., and Sun, S. Z., 1998, Target steam injection using horizontal wells with limited entry perforations: SPE International Conference on Horizontal Well Technology, Calgary, Canada, 1998.

Cant, D. J., 1996, Sedimentological and sequence stratigraphic organization of a foreland clastic wedge, Mannville Group, western Canada Basin: Journal of Sedimentary Research, v. 66, p. 1137-1147.

Castagna, J. P., Batzle, M. L., and Eastwood, R. L., 1985, Relationship between compressional-wave and shear-wave velocities in clastic silicate rocks: Geophysics, **50**, p. 571-581.

Castagna, J. P., 1993, AVO analysis - Tutorial and review, *in* Castagna, J. P. and Backus, M. M., Eds, Offset-dependent Reflectivity - Theory and Practice of VAO Analysis: SEG, 3-36.

Chen, H. and McMechan, G.A., 1992, 3-D pre-stack depth migration for salt and subsalt structures using reverse-VSP data: J. Seis. Expl., **1**, 281-291.

Eaton, W. S. D., Stewart, R. R., and Harrison, M. P., 1991, The Fresnel zone for P-SV waves: Geophysics **56**, 360-364.

Eastwood, J., Lebel, P., Dilay, A. and Blakeslee, S., 1994, Seismic monitoring of steam-based recovery of bitumen, The Leading Edge, April, 1994

Eastwood, J.E., 1996a, Discriminant analysis for reservoir monitoring: CSEG 1996 National Convention, Calgary.

Eastwood, J.E., 1996b, Case history: Drilling 46 wells based on seismic monitoring at Cold Lake: CSEG 1996

Fournier, F., and Derain, J.-F., 1995, A statistical methodology for deriving reservoir properties from seismic data: Geophysics, **60**, 1437-1450.

Gardner, G. H. F., Gardner, L. W., and Gregory, A. R., 1974, Formation velocity and density - the diagnostic basis for stratigraphic traps, Geophysics 39, 770-780.

Gidlow, P. M., Smith, G. C., and Vail, P. J., 1992, Hydrocarbon detection using fluid factor traces: A case history: SEG/EAEG research workshop, 78-89.

Goodway, B., Chen, T., and Downton, J., 1997, Improved AVO fluid detection and lithology discrimination using Lame petrophysical parameters; "$\lambda\rho$", "$\mu\rho$", "λ/μ fluid stack", from P and S inversions: Presented at the **69**nd Ann. Intl. Mtg., Soc. Explor. Geophys., Dallas.

Graybill, F.A., 1969, Introduction to Matrices with Applications in Statistics, Wadsworth Publishing Co. Inc., Belmont.

Haldorsen, J. B. U., Miller, D. E., Walsh, J. J., and Zoch, H.-J., 1992, Multichannel approach to signature estimation and deconvolution for drill bit imaging: Presented at the **62**nd Ann. Intl. Mtg., Soc. Explor. Geophys., New Orleans.

Hardage, B.A., 1992, Reverse VSP and crosswell seismology: Geophysical Press.

Harrison, M. P., 1992, Processing of P-SV surface seismic data: Anisotropy analysis, Dip moveout, and migration: unpublished Ph.D. dissertation, University of Calgary.

Havig, S. O. and Krail, P. M., 1996, Vertical cable seismic applications: World Oil, May, 1996.

Hilterman, F., 1990, Is AVO the seismic signature of lithology? The Leading Edge, **9**, No 6, 15-22.

Hemon, C. and Mace, D., 1978, Use of the Karhunen-Loeve transformation in seismic data processing: Geophy. Prosp., **26**, 600-626.

Isaac, J. H., 1996, Seismic methods for heavy oil reservoir monitoring: unpublished Ph.D. dissertation, University of Calgary.

Jackson, P.J., Onions, K.R., and Westerman, A.R., 1989, Use of inverted VSP to enhance the exploration value of boreholes: First Break, **7**, 233-246.

Jardine, D. 1974, Cretaceous oil sands of Western Canada: CSPG Memoir **3**, 50-67.

Jones, M., 1991, On the analysis of a reverse VSP data set using a core-gun source: Presented at the Sixty-First Ann. Intl. Mtg. Soc. Expl. Geophys., Houston.

Kragh, J.E., Goulty, N.R., and Findlay, M.J., 1991, Hole-to-surface seismic reflection surveys for shallow coal exploration: First Break, **7**, 335-344.

Labonté, S., 1990, Modal separation, mapping, and inverting three-component VSP data: M.Sc. thesis, University of Calgary.

Leckie, D. A. and D. G. Smith, 1992, Regional setting, evolution, and depositional cycles of the western Canada Foreland Basin, *in* R. W. Macqueen and D. A. Leckie, eds., Foreland basins and fold belts: AAPG memoir 55, p. 9-46.

Lindsey, J. P., 1991, The Fresnel zone and its interpretive significance: Seismic interpretation series, 2, No. 13-14.

Lansley, R. M., 1994, 3-D seismic exploration: SEG continuing education, 1994

McCrimmon, G. and Cheadle, B., 1997, Tidal-fluvial facies of stacked incised-valley complexes in the Lower Cretaceous Clearwater Formation, Cold Lake, Alberta: CSPG core conference June 1-6, 1997, p. 335-354, Calgary, Canada.

Minken, F.D., 1974, The Cold Lake Oil Sands: Geology and a reserve estimate: CSPG Memoir **3**, 84-89.

Naville, C., Layotte, P.C., Serbutoviez, S., and Verdier, F., 1991, Uphole surveys digitally recorded and processed as multi-offset RVSP's: Presented at Ann. Mtg. Europ. Assoc. Expl. Geophys., Paris.

Parra, J. O. and Bangs, J. H., 1992, High-resolution reverse VSP and interwell seismic experiments at the Buckhorn test site in Illinois: Presented at the **62**nd Ann. Intl. Mtg., Soc. Explor. Geophys., New Orleans.

Pickett, G. R., 1963, Acoustic character logs and their applications in formation evaluation L J. Ter. Tech., **15**, 650-667.

Potocki, D. and I. E. Hutcheon, 1992, Lithology and diagenesis of sandstones in the Western Canada Foreland Basin: *in* R. W. Macqueen and D. A. Leckie, eds., Foreland basins and fold belts: AAPG memoir 55, p. 229-257.

Rennie, W., Leyland, W., and Skuce, A., 1989, Winterburn (Nisku) Reservoirs, in: Geophysical Altas of Western Canadian Hydrocarbon Pools, Anderson, N. L., Hills, L. V., and Cederwall, D. A., eds.: Can. Soc. of Expl. Geophys./Can. Soc. of Petrol. Geol. Joint Publication.

Rolheiser, P., 1998, Riddle of the sands: Imperial Oil Review, Summer 1998, p.8-11.

Smith, G. C. and Gidlow, P. M., 1987, Weighted stacking for rock property estimation and detection of gas: Geophysical Prospecting, **35**, p. 993-1014.

Stone, D. G., 1994, Designing Seismic Survey in Two and Three Dimensions: Soc. of Expl. Geophys.

Stewart, R. R., 1991, Rapid map and inversion of P-S waves: Geophysics, **56**, 859-862.

Stewart, R. R., Huddleston, P. D., and Kan, T. K., 1984, Seismic versus sonic velocities: A vertical seismic profiling study: Geophysics, **49**, 1153-1168.

Sun, Z. and Stewart, R. R., 1994, 3-D reverse VSP: CREWES Report, 1994.

Tatham, R. H., 1985, Shear wave and lithology, in Dohr, G. Ed., Seismic Shear Waves: Handbook of Geophysical Exploration, **15b**, 87-133.

Toksöz, M. N. and Stewart, R. R., 1984, Vertical seismic profiling, Part B: Advanced concepts: Geophysical Press, 1984.

Wang, Z. and Nur, A., 1989, Effect of temperatures on wave velocities in sands and sandstones with heavy hydrocarbons, *in* Nur, A. and Wang, Z., Eds, Seismic and Acoustics Velocities in Reservoir Rocks: SEG, 188-194.

Yilmaz, O., 1987, Seismic Data Processing: Soc. Explor. Geophys.

Zhang, Q., Sun, Z., Brown, R. J., and Stewart, R. R., 1994, VSP interpretation from Joffre, Alberta: CREWES Report, Vol. 6, Chapter 33.

Appendix A – Theory of data normalization filter

Let us consider two seismic traces shot at different times — $a_t(a_0,a_1,a_2,...)$ for earlier survey **A** and $b_t(b_0,b_1,b_2,...)$ for later survey **B**. The objective of data normalization is to find a filter that will transform an input (e.g. survey **A**) into an output (e.g. survey **B**). The Wiener-Levinson filter will meet the need. To illustrate mathematical principles, an analysis using 3-point seismic data can be used, i.e.

$$a_t = (a_0, a_1, a_2) \tag{A-9}$$

Let f_t be the normalization filter.

$$f_t = (f_0, f_1, f_2) \tag{A-10}$$

Let b_t be the seismic trace for a_t to be normalized to.

$$b_t = (b_0, b_1, b_2, ...) \tag{A-11}$$

Then, the actual output from the filtering can be calculated.

$$x_t = f_t * a_t$$

$$x_t = \sum_{\tau=0}^{2} f(\tau)a(t-\tau) \tag{A-12}$$

$$x_t = (f_0a_0, f_0a_1 + f_1a_0, f_0a_2 + f_1a_1 + f_1a_1 + f_2a_0, f_1a_2 + f_2a_1, f_2a_2) \tag{A-13}$$

The sum of the squares of the difference between the desired and actual results is as follow:

$$\begin{aligned} E = {} & (f_0a_0 - b_0)^2 + (f_0a_1 + f_1a_0 - b_1)^2 + (f_0a_2 + f_1a_1 + f_2a_0 - b_2)^2 \\ & + (f_1a_2 + f_2a_1 - b_3)^2 + (f_2a_2 - b_4)^2 \end{aligned} \tag{A-14}$$

To minimize the value, the partial derivative of the squared difference with respect to the filter values (f_0, f_1, f_2) is rearranged and set to zero. After some algebra operation following results are obtained:

$$\frac{\partial E}{\partial f_0} = (a_0^2 + a_1^2 + a_2^2) f_0 + (a_0 a_1 + a_1 a_2) f_1 + a_0 a_2 f_2 = a_0 b_0 + a_1 b_1 + a_2 b_2 \tag{A-15}$$

$$\frac{\partial E}{\partial f_1} = (a_0 a_1 + a_1 a_2) f_0 + (a_0^2 + a_1^2 + a_2^2) f_1 + (a_0 a_1 + a_1 a_2) f_2 = a_0 b_1 + a_1 b_2 + a_2 b_3 \tag{A-16}$$

$$\frac{\partial E}{\partial f_2} = a_0 a_2 f_0 + (a_0 a_1 + a_1 a_2) f_1 + (a_0^2 + a_1^2 + a_2^2) f_2 = a_0 b_2 + a_1 b_3 + a_2 b_4 \tag{A-17}$$

Equations A-15 through A-17 represent three linear equations with three unknowns (f_0, f_1, f_2), and can be expressed in matrix form as:

$$\begin{bmatrix} a_0^2 + a_1^2 + a_2^2 & a_0 a_1 + a_1 a_2 & a_0 a_2 \\ a_0 a_1 + a_1 a_2 & a_0^2 + a_1^2 + a_2^2 & a_0 a_1 + a_1 a_2 \\ a_0 a_2 & a_0 a_1 + a_1 a_2 & a_0^2 + a_1^2 + a_2^2 \end{bmatrix} \begin{bmatrix} f_0 \\ f_1 \\ f_2 \end{bmatrix} = \begin{bmatrix} a_0 b_0 + a_1 b_1 + a_2 b_2 \\ a_0 b_1 + a_1 b_2 + a_2 b_3 \\ a_0 b_2 + a_1 b_3 + a_2 b_4 \end{bmatrix} \tag{A-18}$$

The autocorrelation of the input a_t can be written as:

$$\phi_{aa}(\tau) = \sum_{t=0}^{2} a(t) a(t+\tau) \tag{A-19}$$

$$\begin{aligned} \phi_{aa}(0) &= a_0^2 + a_1^2 + a_2^2 \\ \phi_{aa}(1) &= a_0 a_1 + a_1 a_2 \\ \phi_{aa}(2) &= a_0 a_2 \end{aligned} \tag{A-20}$$

The crosscorrelation (ϕ_{ab}) between the desired output b_t and input a_t can be written as:

$$\phi_{ab}(\tau) = \sum_{t=0}^{2} a(t) b(t+\tau) \tag{A-21}$$

$$\begin{aligned} \phi_{ab}(0) &= a_0 b_0 + a_1 b_1 + a_2 b_2 \\ \phi_{ab}(1) &= a_0 b_1 + a_1 b_2 + a_2 b_3 \\ \phi_{ab}(2) &= a_0 b_2 + a_1 b_3 + a_2 b_4 \end{aligned} \tag{A-22}$$

Rewriting equation A-18 in the form of autocorrelation and crosscorrelation:

$$\begin{bmatrix} \phi_{aa}(0) & \phi_{aa}(1) & \phi_{aa}(2) \\ \phi_{aa}(1) & \phi_{aa}(0) & \phi_{aa}(1) \\ \phi_{aa}(2) & \phi_{aa}(1) & \phi_{aa}(0) \end{bmatrix} \begin{bmatrix} f_0 \\ f_1 \\ f_2 \end{bmatrix} = \begin{bmatrix} \phi_{ab}(0) \\ \phi_{ab}(1) \\ \phi_{ab}(2) \end{bmatrix} \tag{A-23}$$

The autocorrelation matrix is real and symmetric. Also, for autocorrelation $\phi_{aa}(i)$ equals $\phi_{aa}(-i)$ ($i = 0, 1, 2, \ldots$) sometimes equation A-23 is expressed as:

$$\begin{bmatrix} \phi_{aa}(0) & \phi_{aa}(1) & \phi_{aa}(2) \\ \phi_{aa}(-1) & \phi_{aa}(0) & \phi_{aa}(1) \\ \phi_{aa}(-2) & \phi_{aa}(-1) & \phi_{aa}(0) \end{bmatrix} \begin{bmatrix} f_0 \\ f_1 \\ f_2 \end{bmatrix} = \begin{bmatrix} \phi_{ab}(0) \\ \phi_{ab}(1) \\ \phi_{ab}(2) \end{bmatrix} \tag{A-24}$$

However, for crosscorrelation neither $\phi_{ab}(i)$ equals to $\phi_{ab}(-i)$ nor $\phi_{ab}(i)$ equals to $\phi_{ba}(i)$. In general case, for n-point seismic trace the equation can be written as follows (Wiener equation) that is similar as Yilmaz (1987).

$$\begin{bmatrix} \phi_{aa}(0) & \phi_{aa}(1) & \phi_{aa}(2) & \ldots & \phi_{aa}(n-1) \\ \phi_{aa}(1) & \phi_{aa}(0) & \phi_{aa}(1) & \ldots & \phi_{aa}(n-2) \\ \phi_{aa}(2) & \phi_{aa}(1) & \phi_{aa}(0) & \ldots & \phi_{aa}(n-3) \\ \cdot & \cdot & \cdot & \cdots & \cdot \\ \cdot & \cdot & \cdot & \cdots & \cdot \\ \cdot & \cdot & \cdot & \cdots & \cdot \\ \phi_{aa}(n-1) & \phi_{aa}(n-2) & \phi_{aa}(n-3) & \ldots & \phi_{aa}(0) \end{bmatrix} \begin{bmatrix} f_0 \\ f_1 \\ f_2 \\ \cdot \\ \cdot \\ \cdot \\ f_{n-1} \end{bmatrix} = \begin{bmatrix} \phi_{ab}(0) \\ \phi_{ab}(1) \\ \phi_{ab}(2) \\ \cdot \\ \cdot \\ \cdot \\ \phi_{ab}(n-1) \end{bmatrix} \tag{A-25}$$

Equation A-14 (sum of squared errors) can be rewritten for general case as follows:

$$E = \sum_t \left(b_t - \sum_\tau f(\tau) a(t-\tau) \right) \tag{A-26}$$

By expanding the square term in equation A-26,

$$E = \sum_t b_t^2 - 2 \sum_t b_t \sum_\tau f_\tau a_{t-\tau} + \sum_t \left(\sum_\tau f_\tau a_{t-\tau} \right)^2 . \tag{A-27}$$

By taking the partial derivatives with respect to filter coefficients (f_i) and setting them to zero,

$$\frac{\partial E}{\partial f_i} = -2\sum_t b_t a_{t-i} + 2\sum_t \left(\sum_\tau f_\tau a_{t-\tau} \right) a_{t-i} = 0 . \tag{A-28}$$

By setting autocorrelation (ϕ_{aa}) and crosscorrelation (ϕ_{ba})

$$\phi_{aa}(i-\tau) = \sum_t a(t-\tau)a(t-i) \tag{A-29}$$

$$\phi_{ba}(-i) = \sum_t b(t)a(t-i) \tag{A-30}$$

following relationship can be built

$$\sum_\tau f(\tau)\phi_{aa}(i-\tau) = \phi_{ba}(-i) , \tag{A-31}$$

or

$$\sum_\tau f(\tau)\phi_{aa}(\tau-i) = \phi_{ab}(i) . \tag{A-32}$$

Note that since $\phi_{ba}(-i)$ equals $\phi_{ab}(i)$ and $\phi_{aa}(i-\tau)$ equals $\phi_{aa}(\tau-i)$, equation A-31 and A-25 are the same. Therefore, equation A-25 holds for general case. Equation A-25 (or A-31) can be written as

$\mathbf{\Phi f} = \mathbf{\Psi}$, or (A-33)

$\mathbf{f} = \mathbf{\Phi}^{-1}\mathbf{\Psi}$ (A-34)

Appendix B – The approximation of *P-P* wave reflection coefficient

The approximation of *P-P* wave reflection coefficient from Aki and Richards (8.1) can be expanded (using ray parameter) as:

$$R_{pp}(\theta) \approx \frac{1}{2}\frac{\Delta\rho}{\rho_a} - 2V_{sa}^2\frac{\sin^2\theta}{V_{pa}^2}\frac{\Delta\rho}{\rho_a} + \frac{1}{2}(1+\tan^2\theta)\frac{\Delta V_p}{V_{pa}} - 4\frac{\sin^2\theta}{V_{pa}^2}V_{sa}^2\frac{\Delta V_s}{V_{sa}}$$

$$\approx \left[\frac{1}{2}\left(\frac{\Delta V_p}{V_{pa}} + \frac{\Delta\rho}{\rho_a}\right)\right](1+\tan^2\theta) - \frac{1}{2}\tan^2\theta\,\frac{\Delta\rho}{\rho_a}$$
$$-8\frac{V_{sa}^2}{V_{pa}^2}\sin^2\theta\left[\frac{1}{2}\left(\frac{\Delta V_s}{V_{sa}} + \frac{\Delta\rho}{\rho_a}\right)\right] + 2\frac{V_{sa}^2}{V_{pa}^2}\sin^2\theta\,\frac{\Delta\rho}{\rho_a} \qquad \text{(B-1)}$$

Substituting $\frac{1}{2}\left(\frac{\Delta Vp}{Vp} + \frac{\Delta\rho}{\rho}\right)$ with Rp and $\frac{1}{2}\left(\frac{\Delta Vs}{Vs} + \frac{\Delta\rho}{\rho}\right)$ with Rs we obtain following new approximation.

$$R_{pp}(\theta) \approx (1+\tan^2\theta)R_p - 8\frac{V_s^2}{V_p^2}\sin^2\theta\,R_s - \left(\frac{1}{2}\tan^2\theta - 2\frac{V_s^2}{V_p^2}\sin^2\theta\right)\frac{\Delta\rho}{\rho_a} \qquad \text{(B-2)}$$

Now, let's illustrate the approximation of zero-offset reflection coefficient (Rp).

$$R_P = \frac{V_{p2}\rho_2 - V_{p1}\rho_1}{V_{p2}\rho_2 + V_{p1}\rho_1} \approx \frac{1}{2}\left(\frac{\Delta V_p}{V_{pa}} + \frac{\Delta\rho}{\rho}\right) \qquad \text{(B-3)}$$

$$R_s = \frac{V_{s2}\rho_2 - V_{s1}\rho_1}{V_{s2}\rho_2 + V_{s1}\rho_1} \approx \frac{1}{2}\left(\frac{\Delta V_s}{V_{sa}} + \frac{\Delta\rho}{\rho}\right) \qquad \text{(B-4)}$$

In general, we have:

$$R_P = \frac{V_2\rho_2 - V_1\rho_1}{V_2\rho_2 + V_1\rho_1}$$

$$= \frac{V_2\rho_2 - V_2\rho_1 + V_2\rho_1 - V_1\rho_1}{V_2\rho_2 + V_1\rho_1}$$

$$= \frac{V_2 \Delta\rho + \Delta V \rho_1}{V_2 \rho_2 + V_1 \rho_1}$$

$$= \frac{V_2 \Delta\rho}{V_2 \rho_2 + V_1 \rho_1} + \frac{\Delta V \rho_1}{V_2 \rho_2 + V_1 \rho_1}. \tag{B-5}$$

Also, V_2 and ρ_1 can be reformulated as follows:

$$V_1 = V_2 - \Delta V \tag{B-6}$$

$$V_a = \frac{1}{2}(V_1 + V_2) \tag{B-7}$$

$$V_2 = 2V_a - V_1$$

$$= 2V_a - V_2 + \Delta V \tag{B-8}$$

$$V_2 = V_a + \frac{1}{2}\Delta V. \tag{B-9}$$

Similarly, we have:

$$\rho_1 = \rho_a - \frac{1}{2}\Delta\rho. \tag{B-10}$$

Therefore, we can rewrite $V_2 \rho_2 + V_1 \rho_1$ as follows:

$$V_2 \rho_2 + V_1 \rho_1 = 2V_a \rho_a + \frac{1}{2}\Delta V \Delta\rho$$

$$\approx 2V_a \rho_a \tag{B-11}$$

Substitute (A-9), (A-10) and (A-11) into (A-5) we have:

$$R \approx \frac{(V_a + \frac{1}{2}\Delta V)\Delta\rho}{2V_a \rho_a} + \frac{\Delta V (\rho_a - \frac{1}{2}\Delta\rho)}{2V_a \rho_a}$$

$$\approx \frac{1}{2}\left(\frac{\Delta\rho}{\rho} + \frac{\Delta V}{V}\right) \tag{B-12}$$